Montanuniversität Leoben

Department Metallurgie

Lehrstuhl für

Modellierung und Simulation

Metallurgischer Prozesse

Doktorarbeit

“A Study on Macrosegregation in Continuous Casting of Bronze“

“Makroseigerungsstudie im Strangguss von Bronze“

zur Erlangung des akademischen Grades

Dr.mont.

Eingereicht von DI Monika Gruber-Pretzler im WS 07/08

Betreuer:
Univ.-Prof. Dipl.-Phys. Dr.rer.nat. Ludwig Andreas
Univ.-Prof. Dipl.-Ing. Dr.mont. Clemens Helmut

Eidesstattliche Erklärung

Ich erkläre an Eides statt, dass ich die vorliegende Doktorarbeit selbständig verfasst und alle benutzten Quellen bzw. wörtlich und inhaltlich entnommenen Stellen erkenntlich gemacht habe.

Leoben, 25.03.2008 _____

DI Monika Gruber-Pretzler

Danksagung

Mit Dank möchte ich all die Hilfe und Unterstützung wertschätzen, die mir in der Zeit der Erstellung dieser Arbeit zuteil wurde.

Dabei möchte ich zuallererst meiner Familie danken, die mir immer mit ihrer Unterstützung zur Seite stand. Im Speziellen gilt dieser Dank meinen Kindern, die durch ihre Selbstständigkeit und ihr Verständnis den nötigen Freiraum zur Umsetzung meiner Doktorarbeit geschaffen haben.

Auch möchte ich mich im speziellen bei Herrn Prof. Andreas Ludwig, dem Hauptbetreuer meiner Dissertation, meinem Chef und gleichzeitig guten Freund, und damit auch beim Lehrstuhl für Modellierung und Simulation metallurgischer Prozesse für die Möglichkeit der Verfassung der Dissertation danken. Die fachliche Kompetenz und konstruktive Kritik, sowie die vielen Gespräche und Diskussionen haben sehr zum Gelingen dieser Doktorarbeit und zu meinem persönlichen Wachstum beigetragen. Vielen Dank auch Herrn Prof. Clemens Helmut für die Übernahme der Zweitbetreuung der Dissertation und Unterstützung der experimentellen Messungen. Daneben ist es mir auch ein Anliegen Herrn Prof. John Ågren von der KTH Stockholm für die Gespräche und Diskussionen bezüglich der experimentellen Arbeit zu danken.

Im Besonderen seien auch Wieland-Werke AG in Ulm/Vöhringen und die Christian Doppler Gesellschaft genannt, die gemeinsam die Finanzierung der Dissertation getragen haben. Hier möchte ich die überaus kooperative und fördernde Zusammenarbeit, die zwischen unserem Institut und Wieland-Werke AG möglich war, besonders hervorheben. Mein Dank gilt allen Beteiligten.

Ich möchte meinen Arbeitskollegen für die gute Zusammenarbeit und für den fachlichen Austausch, der immer auf freundschaftlicher Ebene stattfinden konnte, danken. Hier sei im speziellen DI Florian Mayer erwähnt, der mir neben der fachlichen Beratung auch ein sehr guter Freund geworden ist. Da in unserem Beruf die EDV einen wesentlichen Anteil hat, sei auch unserer EDV Abteilung ein herzlicher Dank gesagt. Nur durch ihre stetige Betreuung war es möglich diese Arbeit erfolgreich abzuschließen.

Contents

1 Abstract

Technical bronzes tend to form both macrosegregations and microsegregations during DC-casting due to the particular phase diagram situation, kinetics of phase transformation, and changes in the relative velocity between liquid and solid. As a result a heterogeneous cast microstructure forms. This can be observed after casting even in wrought alloys with a tin content from 4 to 8 wt.% Sn. Since the tin rich phases are brittle at room temperature as well as at hot working temperature, workability deteriorates. The intensity of macrosegregation in DC-casting can effectively be influenced by casting parameters like casting velocity, primary cooling or inlet geometry which in fact change the relative flow between the melt and the forming solid.

The aim of the presented work was to apply an already developed solidification model on continuous casting of technical bronze alloys. Since the thermodynamics of Cu-Sn-P is necessary as an input for the simulation of solidification, the ternary system has been studied by computational thermodynamics and experimental work.

For the thermodynamic data input it was necessary to validate already published data. Therefore, DSC (Differential Scanning Calorimetrie) -measurements and diffusion experiments have been performed for the binary, Cu-Sn and Cu-P, and the ternary, Cu-Sn-P, systems. For the binary systems the performed DSC measurements confirm the already published phase diagrams. In addition, performed diffusion experiments allow an estimation of diffusion coefficients for specific conditions. In the ternary system it is of special interest to define and confirm the ternary eutectic point which is thought to be responsible for specific rigidity changes in technical bronze alloys. The presented experimental work shows generally good agreement with already published phase diagrams and published numerical assessment work.

In order to understand influence and interaction of the related phenomena during solidification, simulation methods are applied to 2D and 3D geometries. The first step was to apply, adapt and further improve an already developed multiphase solidification model for continuous casting of bronze. For this the CFD (Computational Fluid Dynamic) software FLUENT was used in combination with UDF's (User Defined Functions). The solidification of the strand as well as the formation of macrosegregation are simulated with a two phase volume averaging model. Correspondingly, the velocity field of the melt flow is explicitly calculated by solving the momentum conservation equations. Within the mushy zone the local formation of microsegregation in the presence of feeding and buoyancy flow is estimated. The thermodynamics of the Cu-Sn system is accounted for in the binary simulations by linearization of the binary phase diagram and in the ternary calculations thermodynamics of Cu-Sn-P is included by a thermodynamic model. In both cases, it is distinguished explicitly between interface and average concentrations.

To investigate the influence of different flow phenomena (thermo-solutal buoyancy flow, feeding flow and forced convection) on the formation of macrosegregations, several case studies have been performed. Based on 2D axis symmetrical simulations with the binary alloy CuSn6, the results of several case studies are discussed by separating

the individual convection mechanisms: (i) considering only forced confection induced by injection at the inlet while ignoring feeding flow and thermo-solutal convection; (ii) considering only solutal buoyancy driven flow; (iii) considering only thermal buoyancy driven flow; and (iv) considering only feeding flow. In all 4 cases the same Blake-Kozeny-type mush permeability model was assumed. Finally, the case which combines forced convection, thermo-solutal buoyancy driven convection, and feeding flow is discussed. Additionally, similar cases have been repeated with a higher Blake-Kozeny-type mush permeability.

By comparing the above mentioned case studies, it is demonstrated how the different flow phenomena contribute to the final macrosegregation distribution. Besides, a study on the influence of the casting speed on macrosegregation is presented. Since, in case of low mush permeability, the results show that feeding flow is the most important mechanism for the macrosegregation destribution, a detailed discussion on the formation of macrosegregation is performed using this simulation results. A further step to as cast rectangular continuous casting is done by performing simulations for a 3D geometry in a laboratory scale and by applying the proposed model to the ternary alloy CuSn6P0.5. This was simulated with the 2D axis symmetric geometry in order to give qualitative predictions for both, P and Sn macrosegregations in a round strand. The validation of the macrosegregation distribution shows good qualitative agreement with experimental measurements.

Kurzfassung

Bei der Herstellung von technischer Bronze werden in der Industrie sowohl Mikro- wie auch Makroseigerungen beobachtet. Ausschlaggebend dafür sind das Phasendiagram, die Kinetik der Phasentransformation und Relativgeschwindigkeiten zwischen Schmelze und Festkörper. Resultierend daraus ergibt sich eine inhomogene Gussmikrostruktur, die selbst durch Glühen oder Kneten nicht entfernt werden kann. Sogar das Absenken des Zinngehaltes auf 4-8 wt.% kann diese Inhomogenitäten nicht verhindern. Zinnreiche Phasen sind sowohl bei Raum- wie auch Warmbearbeitungstemperatur spröde und mindern daher die Bearbeitbarkeit. Die Ausprägung der Makroseigerung im Strangguss kann nach Beobachtungen in der Praxis durch eine Veränderungen der Gießparameter, wie zum Beispiel Gießgeschwindigkeit, Stärke der primären Kühlung wie auch der Tauchrohrgeometrie beeinflusst werden. Diese Veränderungen führen meist zu einer Änderung in der Relativgeschwindigkeit zwischen Schmelze und Festkörper und damit zu Modifiktionen der Erstarrungsbedingungen.

Das Ziel der präsentierten Arbeit war es ein bereits vorhandenes Erstarrungsmodell auf den Stranggussprozess von Bronze anzuwenden und anzupassen. Nachdem die Thermodynamik des ternären Systems Cu-Sn-P notwendig ist um den Erstarrungsprozess genau zu beschreiben, wurden parallel zu der Simulationsarbeit Experimente durchgeführt.

Diese sollten in der Literatur vorhandene thermodynamische Beschreibungen evaluieren und ihre Anwendbarkeit für die Prozesssimulation überprüfen. Deshalb wurden DSC (Differential Scanning Calorimetrie) Messungen und Diffusionsexperimente für das System Cu-Sn, Cu-P und Cu-Sn-P durchgeführt. Die Messergebnisse bestätigen die publizierten binären Phasendiagramme. Außerdem war es möglich für die binären Systeme Diffusionskoeffizienten für bestimmte Bedingungen abzuschätzen. Im ternären System ist im Speziellen der ternäre eutektische Punkt von wissenschaftlichem Interesse, da durch diese Reaktion auch in industriellen Prozessen Cu_3P, eine sehr phosphorreiche Kupferphase auftreten kann. Diese wiederum ist sehr spröde und wird damit in gewissem Maße für die Sprödigkeit im erstarrten Strang verantwortlich gemacht. Generell zeigen die experimentellen Untersuchungen gute Übereinstimmung mit den veröffentlichten und auch numerisch berechneten Phasendiagrammen.

Um die Interaktion und den Einfluss der unterschiedlichen mit der Erstarrung im Strangguss auftretenden Geschwindigkeitsphenomäne zu studieren wurden numerische Simulationen für eine achsensymmetrische 2D Geometrie und eine rechteckige 3D Geometrie angewandt. Dafür war es vorerst notwendig das bereits entwickelte Mehrphasenmodell für die Anwendung an einem Strangguss zu modifizieren und weiterzuentwickeln. Dies geschah durch den Einsatz der Fluid Dynamik Software (CFD) FLUENT unter Einbeziehung von User Defined Functions (UDF's). Erstarrung wie auch Makroseigerungsverteilung werden mit einem Volume Averaging Modell berechnet. Dabei wird das Geschwindigkeitsfeld der Schmelze explizit durch das Lösen der Impulserhaltungsgleichung ermittelt. In der Mush (Zweiphasengebiet) wird Mikroseigerung im Zusammenhang mit Nachspeisungseffekten und thermo-solutaler Konvektion berechnet. Die Thermodynamik von Cu-Sn wird durch ein linearisiertes Phasendiagramm berücksichtigt, während für das ternäre System Cu-Sn-P ein thermodynamisches Modell ent-

wickelt wurde. In beiden Fällen wird explizit zwischen Oberflächenkonzentration (Grenzfläche zwischen Schmelze und Festkörper) und Durchschnittskonzentration in der Schmelze unterschieden.

Um den Einfluss der verschiedenen Geschwindigkeitsphenomäne (thermo-solutale Konvektion, Nachspeisung und Gießgeschwindigkeitsfeld) auf die Makroseigerung zu ermitteln wurden verschiedene Fälle studiert. Anhand von achsensymmetrischen 2D Simulationen mit der binären Legierung CuSn6 wurden verschiedene Fälle diskutiert, die die bereits genannten Einwirkungen auf das Geschwindigkeitsfeld, und damit auf die Makroseigerung, berücksichtigen: (i) nur das Geschwindigkeitsfeld verursacht durch die Geometrie und Gießbedingungen; (ii) zusätzlich zum Einfluss des Inlets (Tauchrohr) wird solutale Konvektion berücksichtigt; (iii) zusätzlich zum Einfluss des Inlets wird thermale Konvektion berücksichtigt; und (iv) zusätzlich zum Einfluss des Inlets wird Nachspeisungsinduzierte Konvektion berücksichtigt. Schließlich wurden auch noch Berechnungen durchgeführt, die alle genannten Konvektionsmechanismen miteinschließen. Dieselben Fälle wurden auch für eine zweite Mush Permeabilität durchgeführt. Zusätzlich wird der Einfluss weiterer Permeabilitätswerte und der Gießgeschwindigkeit auf die Makroseigerungsverteilung diskutiert. Die 3D Simulationen wurden für einen rechteckigen Laborstrangguss durchgeführt und zeigen ähnliches, wenn auch abgeschwächtes Makroseigerungsverhalten wie die achsensymmetrischen 2D Simulationen.

Der Vergleich der erwähnten Berechnungen zeigt wie die verschiedenen Konvektionsmechnismen auf die Makroseigerung wirken. Es wurde klar, dass für die verwendeten Randbedingungen der Nachspeisungseffekt und der Einfluss des Inletjets am wichtigsten sind. Hier führt die Nachspeisung zu positiver Seigerung an der Strangoberfläche und zu negativer im Zentrum des Stranges. Während direkter Kontakt der Mush mit dem Inletjet zu Ausspülung von Sn und damit zu negativer Seigerung an der Strangschale führt. Die durchgeführten ternären Berechnungen zeigen prinzipiell ähnliches Verhalten, wobei sowohl für P als auch für Sn Makroseigerungsverteilungen berechnet werden konnten.

2 Introduction

Bronzes and especially Phosphor bronzes are among the oldest engineering materials, intensively used from the 3rd to the 1st millennium B.C., called "Bronze Age", for manufacturing almost all articles for daily life such as bowls, sculptures, jewellery, weapons etc. in Europe, Asia, and North Africa [BRUNNER 90]. In America the oldest archaeological bronze findings were dated back to 600 A.C. Nowadays, Phosphor bronze is still used for many different applications, such as electrical connectors, contact springs, plain bearings, sieve wires, and musical instruments. The main reasons for the widespread popularity of Phosphor bronzes are their high mechanical strength, corrosion resistance, and good electrical as well as thermal conductivity.

The main alloying elements in Phosphor bronzes are Tin (Sn) and Phosphorus (P). Sn ensures excellent corrosion resistant properties while P lowers the viscosity of the melt and improves the filling capability during casting processes. The production of almost every product of bronze starts with casting. Since the most economical way to produce Phosphor bronze is continuous casting, the inhomogeneous distribution of the solute elements (macrosegrations) occurring in the solidified strand is one of the critical problems in bronze production [KUDASHOV 05].

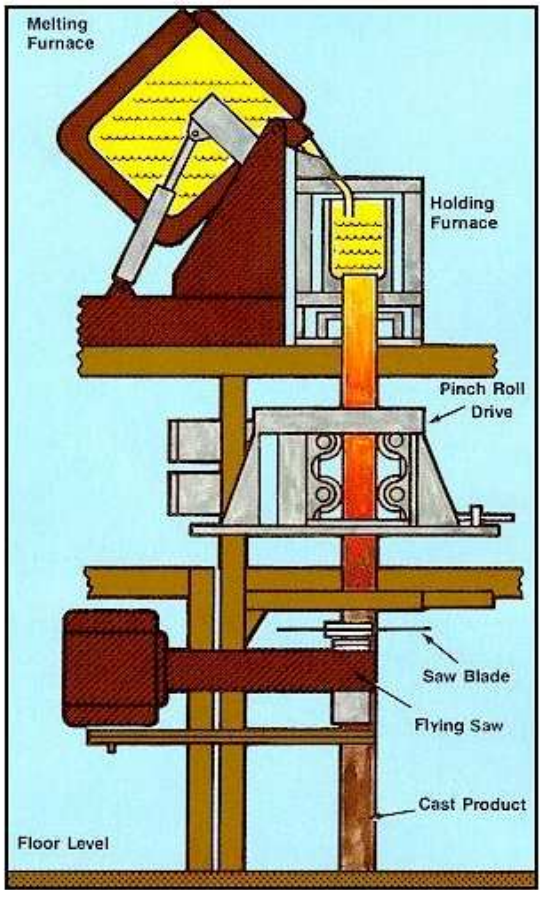

Figure 2-1: Schematical picture of a vertical continuous caster for bronze [ANCHOR-BRONZE 07].

Figure 2-1 shows a schematical sketch of a vertical continuous casting process. A vertical continuous casting machine consists mainly of the mold with a tundish or a melting furnace and the mechanical-hydraulic strand withdrawal mechanism. The melt is kept at casting temperature in the heated tundish from where it is flowing into the mold. The mold itself is holding and in addition extensively cooling the melt. This leads to the formation of a solidified shell at the beginning and finally to complete solidification of the strand. Since bronze is a metallic alloy with a solidification intervall of about 200 °C, dependent on the alloy composition, during casting a region is developing where both, liquid melt and solidifying dendrites are present. This region is called mushy zone where as the sump contains both, the liquid melt and the solidifying dendrites. The already solidified metal is then transported by the mechanical-hydraulic withdrawal mechanism to further production. Pronounced segregation takes place in Phosphor bronzes because of the slow diffusion of Sn in the solid and the wide solidification intervall [COOK 41, DIES 67].

Two types of segregations can be distinguished by the length scale of the solidified structures, namely microsegregation and macrosegregation. Microsegregation is occurring at the length scale of dendrite arm-spacing caused by thermodynamics which leads to a solute rejection at the solid-liquid interface. If there is a relative motion occurring at the solid-liquid interface enriched solute can be transported away into the melt or the mushy zone. In the used context the term “macrosegregation” means any deviation in the local average concentration from the original casting alloy concentration at the length scale of the casting. *Figure 2-2* shows a picture of positive macrosegregations found at the strand surface caused by exudation. These features appear if the strand is contracting at the beginning of solidification. This mechanism forces already enriched melt to move towards the surface, draining through the already partly solidified surface (so called inverse segregation). The presence of Sn rich phases at the strand surface leads to deterioration of the product during the further production steps. Therefore parts of the strand have to be displaced.

Figure 2-2: Exudations lead to the presence of high segregated Sn droplets at the surface of bronze strands in production of vertical continuous castings [RIEDLE 06].

In industry both, positive and negative macrosegregations are observed in the solidified continuous casting strand. Since the discussed alloy is either a Cu-Sn or a Cu-Sn-P alloy, positive macrosegregation occurs in parts where a higher content of Sn or P in comparison to the average alloy concentration is observed. Therefore negative macrosegregation specifies a locally decreased Sn or P content in the solid. In *Figure 2-3*

microsegregations are displayed, visible in a micrograph after metallographic specimen preparation.

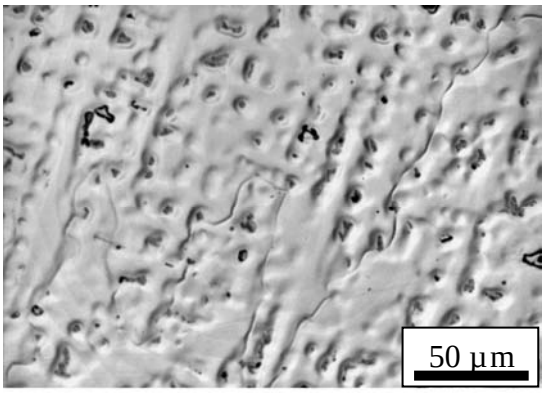

Figure 2-3: Etched microstructure of an as-cast CuSn8 alloy. Microsegregations are occuring in between the dendritic microstructure as dark areas [GRUBER 07A].

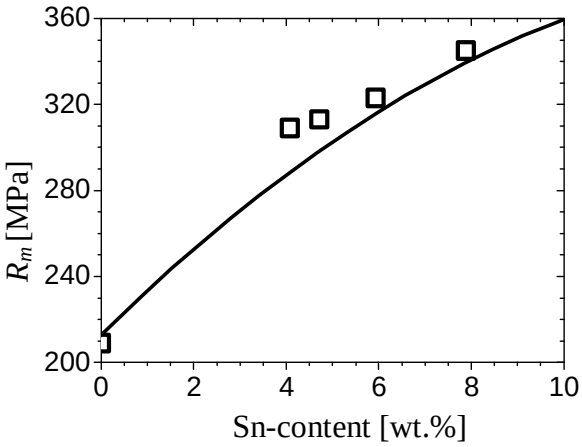

Figure 2-4: Ultimate tensile strength R_m depending on the Sn-content of chill castings. The ultimate tensile strength R_m is shown as a line [HANSON 51] and the squares indicate measured values for annealed Tin bronzes for varying Sn-content [HOFMANN 05].

According to European standards the Sn-content in bronze is limited to 9 wt.% Sn in wrought alloys and to 13 wt.% in cast alloys. Due to segregations in the as-cast state, the microstructure of the often used bronze CuSn8 consists of α phase (α) and the eutectoid of α phase and δ phase (δ). δ is present as interdendritic precipitate which leads to inhomogenities in the solidified material, but correspondingly, the strength of Cu-Sn alloys rises with increasing Sn-content. This is shown in *Figure 2-4* for the as-cast state [HANSON 51] as well as for strips which were finally heat treated. Micro hardness measurements give 2.5 times higher values for the eutectoid than for the Sn poor α (*Figure 2-4*) [HOFMANN 05]. *Figure 2-5* shows macroscopic concentration profiles in castings of different size, cross section, and average concentrations. The Sn-content measured by X-ray fluorescence spectroscopy changes over distances comparable to the dimension *d* of the casting. Generally, the Sn-content in the outer parts of the ingots is significantly higher than in the center. However, the so called inverse macrosegregation at the outer surface layer of the casting rots does not qualitatively depend on the dimension of the casting.

In general segregations are inhomogeneous and lead to ununiform distributions of mechanical properties. Based on *Figure 2-4* and *Figure 2-5*, the Sn-content depending deviation of the tensile strength R_m between the surface and the center of the ingot can be estimated with at least 20 MPa. Furthermore, by the enrichment of Sn towards the surface, interdendritic precipitation of the tin rich δ phase is pronounced. This uneven distribution of strength, hardness and brittleness of δ precipitations impedes the subsequent plastic deformation processes. Hence, undesirable segregations have to be removed. One possibility to handle this is to homogenize by heat treatment. But diffusion in the solid is too slow to remove macrosegregation and therefore it has to be minimized during solidification by choosing appropriate casting parameters.

Numerical calculations provide the possibility to check the influence of casting parameters on the macrosegregation distribution before doing experimental work. Besides, simulation offers the possibility to study the physics behind a process especially in important regions like the mushy zone, where measurement results are very difficult or not to obtain. In this respect, the experiments are used to evaluate the accuracy of the numerical model.

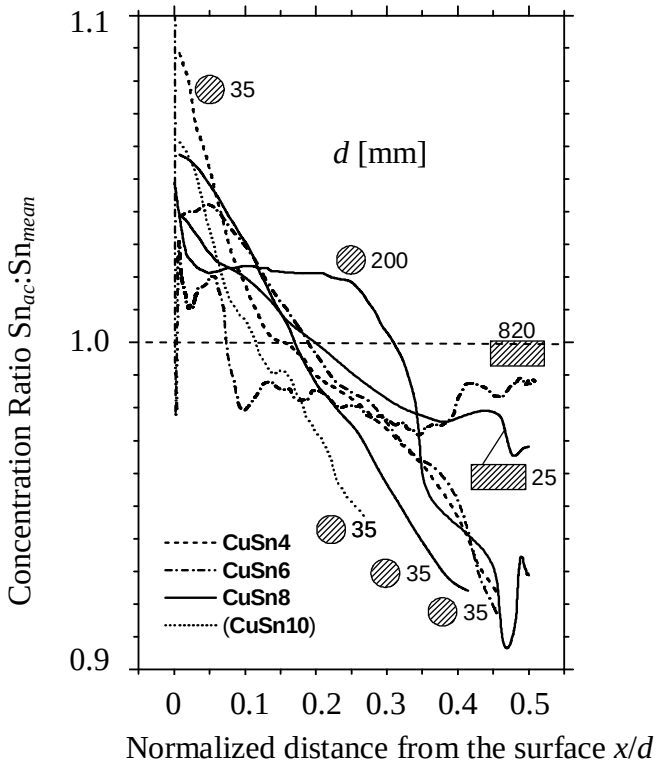

Figure 2-5: Segregation along crosssections in various bronze ingots of cylindrical and rectangular shape. The profiles show high concentrations at the wall and low concentrations in the center of the castings. d [mm]= dimension of the casting; x = position of chemical analysis measured from the surface; Sn_{mean} = average Sn-content of the ingot; Sn_{ac} = actual Sn-content at position x [modified after GRUBER 07A].

During the last decades much work has been performed to understand the formation of macrosegregation during solidification. Based on literature a general conclusion can be drawn [AMBERG 05, BECKERMANN 02, FLEMINGS 00, LAN 05, LUDWIG 05]: Macrosegregations are originated from mushy zone processes. They are caused by the relative mo-

tion between different phases with the mechanisms such as thermal-solutal convection, forced convection (inlet flow), feeding flow due to solidification (shrinkage), grain sedimentation, and exudation. There has been some modeling work carried out in order to visualize the main phenomena present in continuous (or direct chill) castings. Most of them are for Aluminum alloys [ESKIN 07, REDDY 97, ROUSSET 95, VREEMAN 00A, VREEMAN 00B] where Copper is often used as an alloying element. Moreover, due to the nature of the complexity of the multiphase phenomena involved, only partial success was achieved in the beginnings. The idea to treat the mushy zone as separated phases, i.e. the solidified dendrite and the interdendritic melt, started in later 1980's [BECKERMANN 93, RAPPAZ 87A, RAPPAZ 87B, RAPPAZ 90, VOLLER 89]. It is generally assumed that ideal diffusion occurs in the interdendritic melt, and the volume averaged concentration of the interdendritic melt (c_l) at the phase interface is equal to the equilibrium concentration ($\tilde{c}_l$). This approach was later extended [BECKERMANN 93] to consider more general non-equilibrium situation (for example $c_l \neq \tilde{c}_l$). A 3-phase model for mixed columnar-equiaxed solidification was developed based on the previous globular-equiaxed solidification approach [LUDWIG 02, LUDWIG 05, WU 03A, WU 03B, WU 06]. In this solidification model the morphologies of columnar and equiaxed phases are simplified as cylinders and spheres correspondingly, but the competitive growth of both columnar and equiaxed phases, melt convection, equiaxed grain sedimentation, and their influence on the species transport and macrosegregation are taken into account. This three phase model was applied for shape casting.

In the presented study, the model of [LUDWIG 02, LUDWIG 05, WU 03A, WU 03B, WU 06] is applied for two phase simulations that include columnar and liquid phase whereas nucleation and growth of the equiaxed phase are ignored. In this two-phase columnar solidification, the permeable mushy zone is assumed to be composed of cylindrical "dendrites" with a given primary dendrite arm spacing λ_1. The influence of feeding flow, as well as thermal and solutal buoyancy driven flow on the solute distribution especially throughout the mushy zone are studied. For the numerical solution the computational fluid dynamic software FLUENT (Fluent Inc. USA) is used in combination with user defined functions (UDF's).

Publications during the last three years discuss the formation of macrosegregations in continuous casting of bronze in detail [GRUBER 05, GRUBER 07A, LUDWIG 06A, LUDWIG 07]. By studying the influence of the different flow phenomena (feeding flow, thermo-solutal convection and forced convection) a deeper understanding of the formation of macrosegregations in the Sn bronze continuous casting was achieved.

For further development of the continuous casting process of bronze the following strategy is necessary. First of all, it is important to improve the knowledge about the properties and workability of the alloy. Secondly, simulation and modeling work has to be used to improve the understanding of the invisible physical processes taking place during solidification. The connection between these two strategies is kept by the comparison of experimental and simulation results. Most of the fundamental research related to bronze has been performed many years ago [DIES 67, HANSON 51, HANSON 58, RAYNOR 49, SCHUMANN 90, STEUDEL 60, VERÖ 53, VILLARS 97, WATSON 03]. During the last decades the improvement of experimental methods, and with that measurement accuracy, was remarkable. However, only little experimental work has been performed on thermodynamics of the system Cu-Sn-P, which is assumed to represent the thermo-

dynamic behaviour of common technical bronze alloys. Already published phase diagrams and assessment work for the binary systems Cu-Sn and Cu-P [EFFENBERG 07, MASSALSKY 86, MASSALSKY 90, MIETTINEN 01, SHIM 96, VILLARS 97, ZHANPENG 87] is based on experimental observations of the 1930's to the 1980's. Therefore it makes sense to validate those results with present measurement methods. The ternary system itself was assessed by [MIETTINEN 01] based on major publications on the binary and one experimental study on the ternary system [TAKEMOTO 87]. Mainly based on this publication, a database was implemented for the Cu-Sn-P system in the Cu rich corner by Thermo-Calc [THERMOCALC 03, THERMOCALC 05] for the presented computational thermodynamic description of the system. The numerical thermodynamic simulation of the software Thermo-Calc is based on the CALPHAD (Calculation of Phase Diagrams) approach [HILLERT 01, SAUNDERS 98, SUNDMAN 85, THERMOCALC 06]. The output of these calculations is used as thermodynamic input for the solidification simulation. Although direct coupling methods between a thermodynamic software (for example Thermo-Calc) and a fluid dynamic software (for example FLUENT) is still very time consuming, a model for ternary and higher order systems has been developed [LUDWIG 06B, LUDWIG 07].

The following studies were performed to gain information about the physical phenomena causing macrosegregations in continuous casting of bronze as a pre-step for studies on casting parameters like casting speed, casting temperature, cooling conditions and so on. In addition, information about almost unknown parameters like mush permeability and the flow field appearing during casting and solidification is gained from simulation work. As studied in this work, permeability is one of the most important parameter influencing the macrosegregation in continuous casting. The presented experimental work is used to verify the input for the thermodynamic data necessary for solidification simulation. And at the end verification of the simulation results is done by comparison with experimental measurements.

3 Thermodynamics in CuSnP Bronzes

In the following chapter basics of thermodynamics and applied experimental methods are given. This is followed by the performed thermodynamic description of the ternary Cu-Sn-P system, the performed experimental work, and the information gained by the presented investigation.

3.1 Basics and State of the Art

3.1.1 Thermodynamic Description of Phase Diagrams

Basics

Thermodynamic systems are defined as material objects that enable the observation of thermodynamic properties. These systems can be closed, open, or enclosed for exchange of matter, heat, and work with its surroundings. A thermodynamic system is composed of components and phases. Systems that have just one phase are homogeneous systems, whereas, systems with several phases are heterogeneous systems [THERMOCALC 06]. In metallurgy both kinds of systems are observed.

Thermodynamics deals with systems that are in equilibrium. This means that a system has reached a stable state against internal fluctuations in a number of variables, such as composition. The variables that show defined values or properties at the equilibrium state are called state variables. These are for example pressure (P), the chemical potential (μ), or temperature (T). A number of relations between these state variables are given by thermodynamics that enables the calculation of other variables of the system. The state variable can be either extensive or intensive. The value of an extensive variable depends on the size of the system, for example its volume, whereas the value of an intensive variable does not depend on the size of a system, as for example temperature (T) [THERMOCALC 06].

The chemical thermodynamics helps to define phase diagrams based on thermodynamic data. The “Gibbs Phase Rule” defines the number of phases in the different phase regions occuring in a system in equilibrium [FROHBERG 81, HILLERT 98, PREDEL 82]. The phase regions of a system itself are seperated by phase boundaries. The “Gibbs phase rule” correlates

- the number of independent chemical constituents, that are necessary to define the equilibrium system as components (C),
- the number of the present phases (P_p),
- the number of the state variables that can be varied independent of each other without disappearing of one of the phases as degrees of freedom (F),
- the number of linear independent reactions between the components of the system (R), and
- the number of additional conditions (B).

The ”Gibbs’s phase rule” is therefore defined as

$$F = (C\text{-}R\text{-}B)\text{-}P_p+2. \qquad (3\text{-}1)$$

In metallic alloys, R and B are usually assumed to be zero and therefore the equation turns to

$$F = C\text{-}P_p + 2. \tag{3-2}$$

According to the first and second law of thermodynamics, the change of the internal energy (U) of a system and with that the fundamental equation for thermodynamics, the Gibbs equation is defined [HILLERT 98]:

$$\mathrm{d}U = T\,\mathrm{d}S - P\,\mathrm{d}V + \sum_i \mu_i \mathrm{d}n_i, \tag{3-3}$$

where T is the temperature, S the entropy, V the volume, μ_i the chemical potential of phase i, P the pressure, and n_i the number of particles of phase i.

For the definition of the thermodynamic equilibrium the chemical potential μ_i of phase i is used. It is defined as [HILLERT 98]

$$\mu_i = \left(\frac{\partial U}{\partial n_i}\right)_{S,V,n_j}, \text{ with } j \neq i, \tag{3-4}$$

where ∂U is the change in internal energy, ∂n_i is the change in particle number of phase i at fixed entropy (S), fixed volume (V), and fixed number of other particles (n_j) of phase j. In thermodynamics two different phases that are in equilibrium at certain conditions have to have the same chemical potential (μ_i). Usually, phase diagrams are used to describe the phase distribution in thermodynamic equilibrium, therefore the chemical potential (μ_i) of the phases are connected by tie-lines. In binary systems tie-lines are parallel to the concentration axes. Phase boundaries between two phase regions are defined by Gibbs energy curves. The Gibbs energy (G_i) of phase i is related to μ_i by

$$G_i = \Sigma\, x_i \mu_i, \tag{3-5}$$

where G_i is the Gibbs energy of phase i, and x_i is the mole fraction. The change of the Gibbs energy of a system is defined by

$$\mathrm{d}G = -S\,\mathrm{d}T - V\,\mathrm{d}P + \sum_i \mu_i \mathrm{d}n_i. \tag{3-6}$$

For binary systems Gibbs energy curves are generally plotted versus weight fraction or atomic fraction of one of the elements. That means that in a heterogeneous system a phase is only stable if its Gibbs energy is lower than the Gibbs energy of the additional phases of the system (see *Figure 3-1*). *Figure 3-1* shows the correlation between the phase diagram and the Gibbs energy curves for four different temperatures for a eutectic binary phase diagram with marginal solubility. By using the common tangential method the phase regions for various temperatures are defined.

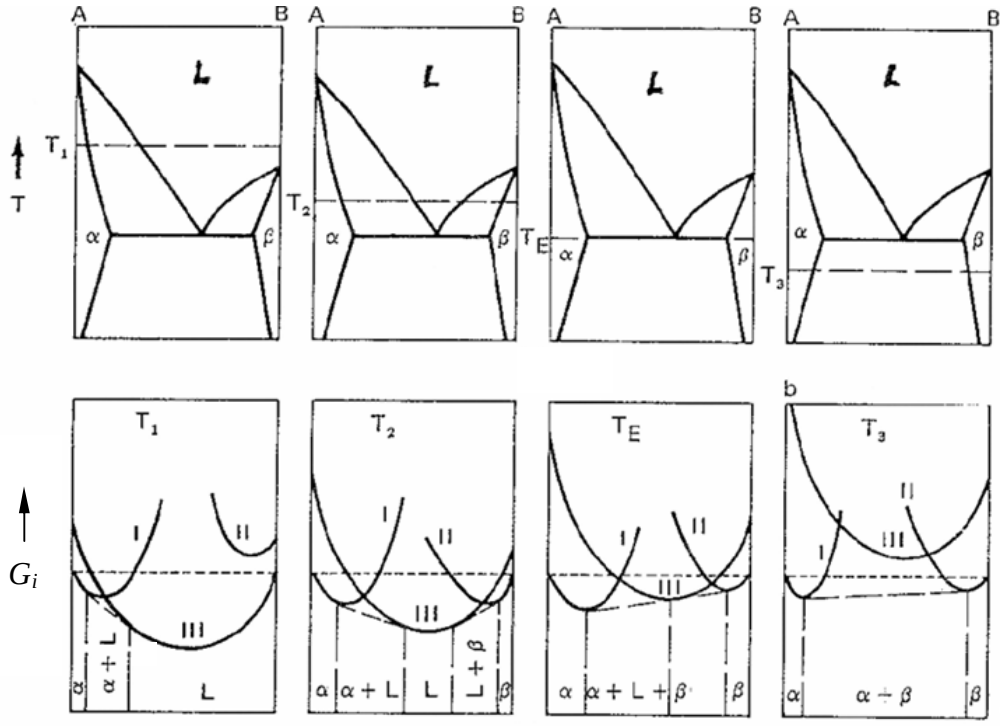

Figure 3-1: Molar Gibbs energy for a eutectic binary phase diagram with certain solubility. The common tangential method is applied for the definition of the phase regions for various temperatures. α, β, and L are appearing phases. G_i indicates the differential Gibbs energy values, I, II, III show the differential Gibbs energy curves for the phases α, β, and L [FROHBERG 81].

The phase diagram for ternary systems is a 3D construction with a triangle at the bottom showing the phase distribution at room temperature. The concentration of the three elements is plotted on the three sides of a triangle as mole or weight fraction and the temperature on a 4th axes perpendicular to the base area. *Figure 3-11* (see page 30) displays as an example the 3D ternary phase diagram of the Cu rich corner of the Cu-Sn-P system.

For ternary systems the tie-lines are in the plane of an isothermal section at a certain temperature. Therefore one chages from 2D to 3D diagrams, where there is one more degree of freedom. That is the reason that the temperature, in binary systems presented by a line, is extended to a planar projection. Therefore the isothermal section itself is located in a plane perpendicular to the concentration plane of a ternary phase diagram and is displaying the phase distribution occurring at one specific temperature in thermodynamic equilibrium. Again, phase boundaries between two phase regions are defined by Gibbs energy curves.

A ternary molar Gibbs energy (G_i) diagram is shown in three-dimensional diagrams (*Figure 3-2*) with a surface like a canopy at constant temperature (T) and constant pressure (P), plotted as function of mole fraction. For a stable phase it is convex everywhere downwards, as displayed in *Figure 3-2*. The tangential plane on the two plotted surfaces is also visible in *Figure 3-2*. The intersections of the tangential plane with the axes of the ternary system assign the chemical potentials. When the two Gibbs energy surfaces are displayed, this tangent plane is rolled under them and thus describes the different equilibrium situations each represented by one tie-line between two tangent points in

the plane [HILLERT 98]. In equilibrium the two stable phases reach the same value for the chemical potential of each component (μ_A, μ_B, μ_C). The general equilibrium condition in a ternary system is $G_A^{\alpha} = \mu_A = G_A^{\beta}$, $G_B^{\alpha} = \mu_B = G_B^{\beta}$, $G_C^{\alpha} = \mu_C = G_C^{\beta}$, where G_i^{φ} are the Gibbs energy values for element *i* and phase φ. These three equations leave one degree of freedom for the two-phase equilibrium since each phase can vary its composition by two degrees of freedom [HILLERT 98]. The contact points of the tangential plane with the Gibbs energy curves give then the concentrations at the phase boundaries in the alloy. For further details the reader is referred to literature [ATKINS 82, FROHBERG 81, HILLERT 98, MORAN 98, PREDEL 82, THERMOCALC 06].

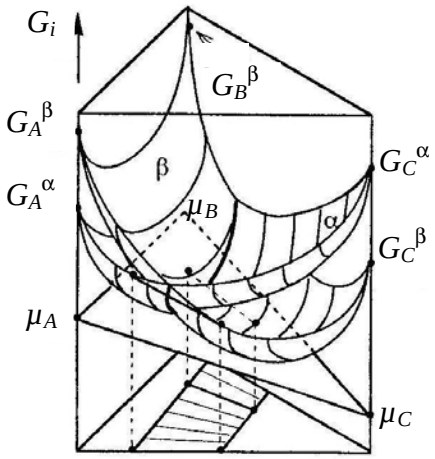

Figure 3-2: Molar Gibbs energy diagram for a two-phase equilibrium α and β in a ternary system. The phase regions are defined by the common tangential plane rolled under the two surfaces. μ_A, μ_B, μ_C: chemical potential of the phases, G_i^{φ} Gibbs energy values for element i and phase φ [HILLERT 98].

State of the Art

The two binary systems of Cu-Sn and Cu-P are described in literature [HANSON 58, MASSALSKY 86, RAYNOR 49, SCHUMANN 90, STEUDEL 60]. *Figure 3-3a* and *Figure 3-3b* show the phase diagram of Cu-Sn and Cu-P as proposed by [MASSALSKY 86]. The numerical assessment of the binaries have been performed by Shim et al. [SHIM 96] and by Mey and Spencer [MEY 90] respectively.

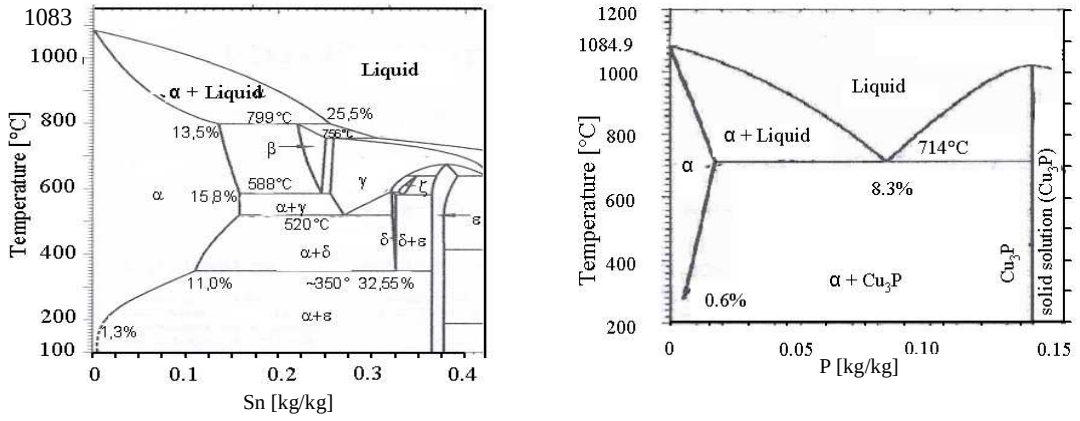

(a) *(b)*

Figure 3-3: (a) Phase diagram of the system Cu-Sn (modified after [MASSALSKY 86]). (b)Phase diagram of the system Cu-P (modified after [MASSALSKY 86]). Appearing phases: α = Cu (max. Sn 15.8 wt.%); $\beta \sim Cu_{17}Sn_3$; $\gamma \sim \gamma(Cu_3Sn\_D03)$; $\delta \sim Cu_{41}Sn_{11}$; $\varepsilon \sim Cu_3Sn$; $\xi \sim Cu_{10}Sn_3$ (Nomenclation taken from [EFFENBERG 07]).

After [SCHUMANN 90] Cu and Sn build substitutional crystalls. Applying technical heat treatment, the equilibrium phase distribution according to the phase diagram is not or just partly observed. The α phase (face cubic centered (fcc)) contains up to 15.8 wt.% Sn. At lower temperatures, the solubility of Sn is reduced and is expected to reach almost zero at room temperature. The large solidification interval (for example an alloy with 10 wt.% Sn solidifies from 1000 °C to 850 °C) is one of the reasons for strong macrosegregations often observed in bronze castings. In addition, diffusion of Sn in the solid is rather small, and therefore already formed segregations do not disappear naturely. Here Sn-poor, and therefore weaker dendrites, are imbedded in a Sn-rich, hard matrix. The β phase ($Cu_{17}Sn_3$, body cubic centered (bcc)), occuring above 588 °C has a body cubic centered structure and changes with further cooling to the γ phase [EFFENBERG 07]. Quenched γ (Cu_3Sn) is found as γ' (Cu_7Sn_2) as a metastable phase which has a martensitic form [EFFENBERG 07]. It is expected that the γ phase and the β phase have almost the same microstructure [SCHUMANN 90]. After [STEUDEL 60] the phase regions of these two phases are not well defined because of the fact that both phases tend to disolve after quenching. This leads to metastable morphologies that have a kind of martensitic structure [SCHUMANN 90]. γ reacts at 520 °C by a eutectoid reaction to α and δ phase ($Cu_{41}Sn_{11}$, which itself is a prototype). This tin rich phase increases the brittleness of the alloy. The formation of the ε phase below ~350 °C is not observed even with low cooling rates. [STEUDEL 60] proposes different phase diagrams depending on the kind of the casting in technical applications.

Since technical bronze alloys have a Sn-content up to 13 wt.% Sn and a P-content up to 1 wt.% P, the Cu rich corner of the ternary System Cu-Sn-P is of special interest for experimental studies. Steudel published concentration sections of the ternary system

after [STEUDEL 60, VERÖ 53]. In addtion parts of the ternary phase diagram Cu-Sn-P are described in [BAUER 30, CHADWICK 39, DIES 67, EFFENBERG 07, SHOWELL 51].
The strong advance in computer technology during the last few years enabled the connection of material science and thermodynamics with computer calculations and simulations. Over the same periode the CALPHAD approach for a comprehensive combination of thermodynamic and kinetic models was developed. This approach evolved from just performing complex equlibrium calulations relevant to materials science to simulating phase transformations involving diffusion. This enables to predict material composition, structures and properties resulting from various material processing. Since 1997, the Ringberg Workshops on Computational Thermodynamics have produced two reports on the status and evolution of "Applications of Computional Thermodynamics" [AGREN 02A, KATTNER 00]. Various publications on applications of computational thermodynamics are given in literature [AGREN 02B, COSTA E SILVA 06, HALLSTEDT 07, HILLERT 97, HILLERT 04, LARSSON 06]. Although the simulation of thermodynamic properties is based on experimental observations, the computational power helps to decide where particular experiments have to be performed in order to validate and improve already established thermodynamic information.

The assessment of the ternary system Cu-Sn-P for computational thermodynamics has been performed 2001 by [MIETTINEN 01] for the Cu rich corner up to 15 wt. % P and 40 wt. % Sn. The numerical thermodynamic description of the Cu-Sn-P system is based on one series of measurements in the ternary system, which itself is based on DTA (differential thermal analysis) measurements and SEM investigations, and literature for the binary systems [MIETTINEN 01, TAKEMOTO 87]. *Figure 3-4* shows two vertical sections (isopleth) at 5 wt.% P of the ternary phase diagram, *Figure 3-4a* shows the section based on experimental investigation where the points show DTA measurements ((Cu) = α) interpolated by lines [TAKEMOTO 87], and *Figure 3-4b* shows the calculated isopleths published by Miettinen (F = α, P = Cu_3P, B = β) [MIETTINEN 01]. The main difference between these two phase diagrams is that γ and with that the three phase regions containing γ have not been obtained by the experimental investigations [TAKEMOTO 87]. In this case the region of β extends further to both, lower Sn content and lower temperatures [MIETTINEN 01]. The red circles show that different phase distributions are given in the two phase diagrams.

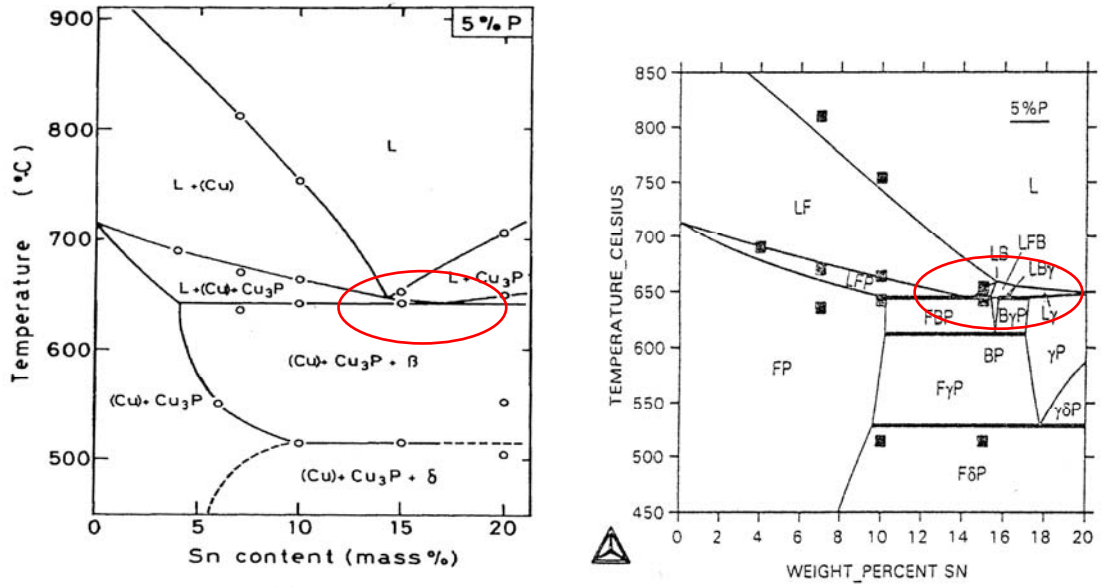

(a) *(b)*

Figure 3-4: (a) Vertical section (isopleths) of the ternary phase diagram Cu-Sn-P at 5 wt.% P based on the experimental investigation of [TAKEMOTO 87]. Displayed points show DTA measurements ((Cu) = α), and the lines show the interpolated expected phase regions [TAKEMOTO 87]. (b) Vertical section of the ternary phase diagram Cu-Sn-P at 5 wt.% P (isopleth) based on the numerical assessment work performed by [MIETTINEN 01]. The displayed dark small squares show DTA measurements [TAKEMOTO 87] and the lines show the calculated phase diagram (F = α, P = Cu_3P, B = β) [MIETTINEN 01]. The two phase regions LB and LFB in (b) have to be changed to LFB for LB and LB for LFB. Based on the binary phase diagrams γ is included in the numerical assessment although it was not observed in the experimental study of Takemoto [TAKEMOTO 87]. Red circles indicate the position around the ternary eutectic point of the system.

3.1.2 Diffusion in Bronze

Basics

The following chapter is mainly based on [GLICKSMAN 00]. In general, diffusion is a kinetic process that leads to homogenisation or uniform mixing of the chemical components in a system or phase. Although mixing of a fluid could occur in different length scales, diffusive mixing only occurs at microscopic scales by the motion of discrete entities (atoms, molecules, clusters, lattice vacancies). Such motions are caused by the fact that the system tries to reach the equilibrium statistical distribution of kinetic and potential energy among the atoms. The extent of homogenisation by diffusion increases with time and with that the level of mixing extends to macroscopic distances. Since diffusion results in a net transport of matter over such macroscopic distances, it is considered to be non equilibrium although thermodynamic equilibrium is achieved when the process is completed. For solid matter, diffusion can be described as a mass transfer over distances, which is bigger than lattice spacing. The single atoms move in a static translation. An atomic interpenetration is only possible, if the components are dissolvable into each other (mixed crystal system).

Diffusion is based on the chemical potential and is a process that starts optional and is not reversible. Because of the fact, that the chemical potential of a homogeneous phase depends on the concentration, a phase with a concentration gradient can not be in thermodynamic equilibrium - the atoms start to travel into the direction of the highest concentration gradient. In case of one dimensional diffusion, taking place for example in a stick, this leads to continuous diffusion of a quantity of the dissolved matter at an imaginary cross-section, which is proportional to the concentration gradient at this cross-section [GLICKSMAN 00].

The main diffusion mechanisms are interstitial diffusion, and substitutional diffusion, such as ring diffusion, and vacancy-assisted diffusion. Interstitial diffusion occurs if the diffuser atom is sufficiently small relative to the atom of the host lattice. At this point jumps can occur from one interstitial size to another where the interstitial sites are given by the host lattice. Even if the diffusion atom fits within the interstial site, it gets local repulsions from the nearby lattice atoms. These forces are getting stronger with increasing atomic displacement from the equilibrium interstital position. If the activation force is applied by the surrounding lattice to a diffuser, it will move from its mean equilibrium site to an adjacent interstitial site [GLICKSMAN 00].

If the size of the diffuser atom in respect to the host lattice increases and approaches or exceeds the size of the host lattice atoms, interstitial motion deminishes. In this case a different mechanism is necessary to move the atoms, the ring diffusion. This mechanism can lead to an exchange of atoms in a ring with the neighbor atoms. The ring or cyclic exchange diffusion mechanism proposes an arrangement for the diffuser which decreases the local lattice distortions but increases the amount of cooperative motion. Ring exchange occures rarely in crystalline structures because the energetics of cycle exchange are not favorable [GLICKSMAN 00]. Diffusion can also take place due to vancancy-assisted diffusion. Nowadays this mechanism is thought to be the dominan mechanism for mixing of substitutional atoms in close-packed metals at elevated temperatures. The origin of lattice vacancies can be thermal or stoichiometric. The Interchange of a vacancy with one of the neighbor atoms is based on local distortion of the lattice.

Since Sn and Cu are both metals with an atomic radius ratio of Cu:Sn = 0.8 [PERIODENSYSTEM 07, SEILNACHT 07, UNITERRA 07, WIKIPEDIA 07] it is thought that diffusion within these two metals takes place either by ring diffusion by vacancy-assisted diffusion. The ratio of the atomic radius of Cu to P is in the order of Cu:P = 1.1-1.3 and with that a little bit greater than 1 (here different values are published [PERIODENSYSTEM 07, SEILNACHT 07, UNITERRA 07, WIKIPEDIA 07]). In this case, diffusion of a non metallic element is taking place in a metallic matrix. Based on the fact that P has almost the same atomic size as Cu it is thought to diffuse by the same mechanism as Sn does.

Those mechanisms taking place in the atomic scale have to be described analytically. The laws of diffusion are mathematical relationships that associate the rate of diffusion with the concentration gradients occurring in the matter and therefore leading to net mass transfer. Such laws are considered to be phenomenological and are used to describe physical effects. The scientist Adolf Fick was the first one who reported the behaviour of a salt-water system undergoing diffusion. For his description the diffusion coefficient (D [$m^2 \cdot s^{-1}$]) as used in equation 3-7, is defined as material property [FICK 55A, FICK 55B]. The linear response between the applied concentration gradient and the diffusive mixing salt and water established an empirical fact. These observations help to predict the quantitative response of a system to an undergoing diffusion [GLICKSMAN 00].

Estimation of diffusion in binary systems can be done by using first Fick's law for one-dimensional diffusion shown in the vector form in equation 3-7.

$$\vec{J} = -D\nabla c\,, \tag{3-7}$$

where $\vec{J}$ [$mol \cdot m^{-2} \cdot s^{-1}$] represents the flux vector, a physical quantity, D [$m^2 \cdot s^{-1}$] is the diffusion coefficient, and ∇c (for 1 dimensional diffusion $\partial c/\partial x$ [$mol \cdot m^{-4}$]) the concentration gradient. The flux vector is parallel to the concentration gradient but opposite directed. Its magnitude is proportional to ∇c according to equation 3-7. The first Fick's law gives a quantitative expression for the statistic direction of the movement of the atoms and describes how many atoms of an element are moving through a part of a surface that is perpendicular to the diffusion direction in a specified time slot. The second Fick's law is the diffusion equation based on the continuity equation for flux:

$$\frac{\partial c}{\partial t} = -\nabla \vec{J}\,, \tag{3-8}$$

where $\partial c/\partial t$ is the time derivative of the concentration. Including equation 3-7 the formulation can be rewritten as

$$\frac{\partial c}{\partial t} = D\Delta c\,, \text{ or for 1 dimension } \frac{\partial c}{\partial t} = \frac{\partial}{\partial x}\left(D\frac{\partial c}{\partial x}\right). \tag{3-9}$$

The second Fick's law shows the connection between the temporal and local concentration gradient. Equation 3-9 is used for the description of time dependent diffusion whereas the first Fick's law describes the diffusive flux constant with time. For the equation analytical as well as numerical solutions are applied in literature [CARSLAW 59, EINSTEIN 05, FICK 55A, FICK 55B, GLICKSMAN 00, GRAHAM 29, GRA-

HAM 33, GRAHAM 50]. In case of one dimensional diffusion, the length of diffusion x for an alloying element in a matrix after a defined time t and at a certain temperature can be described by [GLICKSMAN 00]

$$x = \sqrt{2Dt}\,. \tag{3-10}$$

Based on an average value of the diffusion coefficient $D = 10^{-13}$ [$m^2 \cdot s^{-1}$] for CuSn20 at 648 °C, the path of diffusion of Sn in Cu can be approximated by $x = 2.98 \cdot 10^{-5}$ m per hour (equation 3-10). The interdiffusion of species in multicomponent alloys is a subject of considerable complexity, but very important in material science. The basic lows of multicomponent diffusion are not fundamentally different from those of binary diffusion. Although Fick's laws still apply, they have to be extended, as unusuall behaviors arise because each component flux, in general, depends on the gradient of every component. Therefore the extension of Fick's laws is proposed by literature [GLICKSMAN 00, MADELUNG 90, ONSAGER 31, ONSAGER 45] for unidirectional diffusion in ternary systems. According to [GLICKSMAN 00] Fick's first law in one spacial dimension can be rewritten by the interdiffusion flux $\vec{J}_i$ of component i expressed as a linear function of two independent concentration gradients. The expandet version for diffusion of Sn and P in Cu can be written for 1 dimensinal diffusion as

$$\begin{aligned} \vec{J}_{Sn} &= -D_{SnSn}\frac{\partial c_{Sn}}{\partial x} - D_{SnP}\frac{\partial c_P}{\partial x}, \\ \vec{J}_{P} &= -D_{PSn}\frac{\partial c_{Sn}}{\partial x} - D_{PP}\frac{\partial c_P}{\partial x}. \end{aligned} \tag{3-11}$$

In this case a matrix of 4 different diffusion coefficients is needed to describe the diffusion in the ternary system Cu-Sn-P mathematically since the interaction of the two alloying elements has to be taken into account. The derivative of Fick's second law is given by

$$\frac{\partial c_i}{\partial t} = -\frac{\partial \vec{J}_i}{\partial x}\,, \text{ with } i = \text{Sn, P.} \tag{3-12}$$

Fick's first law for a ternary alloy Cu-Sn-P in one spatial dimension may be substituted into equation 3-12 and with that the time dependend flux can be defined by

$$\begin{aligned} \frac{\partial c_{Sn}}{\partial t} &= -\frac{\partial}{\partial x}\left(-D_{SnSn}\frac{\partial c_{Sn}}{\partial x} - D_{SnP}\frac{\partial c_P}{\partial x}\right), \\ \frac{\partial c_P}{\partial t} &= -\frac{\partial}{\partial x}\left(-D_{PSn}\frac{\partial c_{Sn}}{\partial x} - D_{PP}\frac{\partial c_P}{\partial x}\right). \end{aligned} \tag{3-13}$$

State of the Art

Diffusion experiments in metallurgy are described in literature [BLUMENAUER 94, CIA-AN 87, KAWANAMI 97, MADELUNG 90, MÜLLER 97, ROUX 84, ZHANPENG 87]. Information gained from diffusion experiments is used to measure diffusion coefficients for different temperatures and concentrations. In addition, thermodynamic phase diagram information is obtained. However, the method applied for diffusion experiments depends especially on the used material.

[MÜLLER 97] describes the preparation of the samples as well as the experimental performance of diffusion experiemtents for the Ag-Zn system. In this case pure Ag and pure Zn were taken as diffusion partners. The samples itself had a cylindrical form where the Ag cylinder was put into the Zn tube and afterwards it was annealed. [ZHANPENG 87] used a cylindrical geometry, too. But in this case a ternary sysem was studied. The cylindrical samples, touching each other at one crosssection, were prepared by spotwelding for diffusion experiments of Ni-Co-Cr. [CIA-AN 87] proposes rectangular geometries for ternary diffusion experiments. In this case the diffusion couple specisms were prepared from a tungsten bar W for diffusion experiments with Cu and Ni. A rectangle hole was worked into a nickel board by line cutting. The blocks of W and Cu were grinded to suite the hole and pressed into it, so that all metals were touched closely.

It is still a big issue to prepare diffusion couples in a proper homogeneous way for Cu-Sn-P [PANZL 08]. Casting and homogenisation of binary Cu-Sn samples are well known up to a Sn content of about 20 - 25 wt.%, although the daily used materials contain mostly just up to 13 wt.% Sn. The task gets more difficult for the preparation of binary Cu-P samples and ternary samples. The P content in technical bronze alloys lies in a range of about 0.025 to 0.25 wt.% P. This is the main reason why there are no techniques available for casting and homogenisation of alloys with high P contents. This is still a challenge because P reduces the ductility of the alloy and makes it very porous. Therefore it was not possible up to now to achieve a fine homogeneous microstructure in ternary samples with higher P content. In addition, it has to be mentioned that P starts to evaporate at higher temperatures. The high rigidity of the ternary alloy CuSn20P6 leads to a porous surface and with that the diffusion interface between the diffusion partners is rather rough.

According to literature, diffusion coefficients (D [$m^2 \cdot s^{-1}$]) for Cu-Sn are in a range of $D = 10^{-11}$ to 10^{-18} [$m^2 \cdot s^{-1}$] depending on temperature, concentration and phase [COGAN 84, EBERLING 68, FIDOS 70, HISHINO 80, HISHINO 82, LUBYOVA 75, MADELUNG 90, OIKAWA 75, ONISHI 75, PRINZ 80, SPINDLER 76, STARKE 64, YOKOTA 80]. In the binary system Cu-P, for P a impurity diffusion coefficient was measured in Cu with $D = 1.5 \cdot 10^{-13}$ [$m^2 s^{-1}$] [MADELUNG 90]. Since the P is usually rather low in technical bronze alloys, the diffusion coefficient for impurities can be applied as first estimation for the diffusion time. The leakage of information at this point shows the importance of fundamental research in this area. For the ternary system Cu-Sn-P, diffusion gets more complicated because Fick's law has to be extended, as proposed by literature [GLICKSMAN 00, MADELUNG 90, ONSAGER 31, ONSAGER 45]. The diffusion coefficients of Sn in Cu and P in Cu are changing to a matrix of diffusion coefficients where the interaction of the different elements is taken into account. At the moment there are no diffusion coefficients available for the ternary system in literature.

Nowadays many people are working on proper models to describe diffusion by simulation work [AGREN 07, ANDERSSSON 92, DAYANANDA 89, DAYANANDA 96A, DAYANANDA 96B, DICTRA 05, GLICKSMAN 00, HELANDER 99, HILLERT 05, KULKARNI 05, LARSSON 06, THOMPSON 86]. Since there is no literature available for diffusions coefficients of the ternary Cu-Sn-P system up to now, it is not possible to use numerical techniques for the estimation of diffusion profiles.

3.1.3 Measurement Methodes for Phase Detection

Basics in DSC Measurments

DSC is a thermo-analytical technique for the detection of phase transformations. There are two types of DSC systems in common use, namely the Power-Compensation DSC and the Heat Flux DSC (*Figure 3-5*). For the Power Compensated DSC (*Figure 3-5a*) the temperatures of the sample and reference sample are controlled independently by using separate, identical furnaces. Since the temperatures of the sample and reference sample are kept identical by varying the power input to the two furnaces, the energy required to do this can be used to define the enthalpy or heat capacity changes in the sample relative to the reference.

In Heat Flux DSC (*Figure 3-5b*), the sample and reference are connected by a low-resistance heat flow path which can be, for example, a metal disc. The assembly is enclosed in a single furnace. The detected enthalpy or heat capacity change in the sample causes a difference in the temperature of the sample relative to the reference sample. The temperature difference is recorded and related to enthalpy changes in the sample using calibration experiments [BHADESHIA 02].

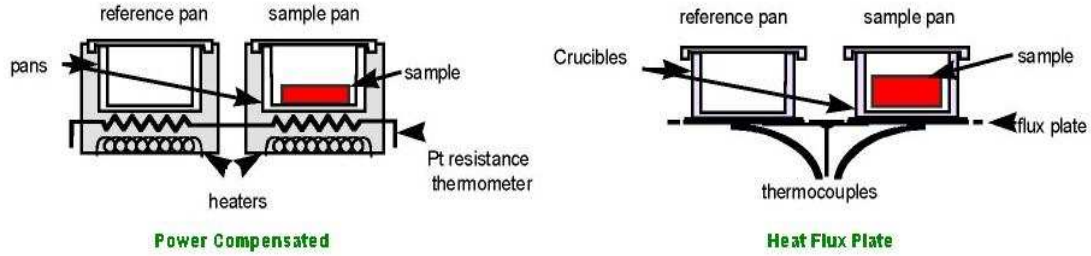

Figure 3-5: (a) Power Compensated DSC; (b) Heat Flux DSC [SAMUEL 07].

The direction of the heat flow depends on whether the process is exothermic or endothermic. For example, as a solid sample transits to the liquid stage it will require latent heat to melt. This endothermic process leads to a certain heat flux. In the opposite, exothermic processes (such as crystallization) will also cause a heat flux but in the other direction. To quantitatively evaluate a DSC measurement, such as shown in *Figure 3-6*, the enthalpy of transition can be expressed by

$$\Delta H = K_c \cdot A, \tag{3-14}$$

where ΔH is the enthalpy of transition, K_c is the calorimetric constant, and A is the integreated area of the measuring curve as shown in *Figure 3-6*. The calorimetric constant can vary from instrument to instrument, and therefore the DSC measuring device has to be calibrated by analyzing a well-characterized sample with known enthalpies of transition [PUNGOR 95]. In addition, the reference sample has to have a well-defined heat capacity in the interesting temperature range.

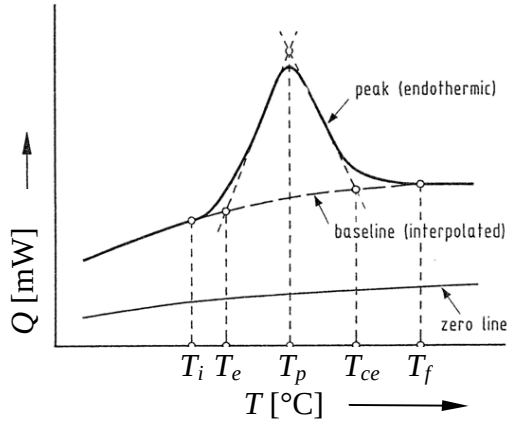

- T_i first deviation from the baseline
- T_e extrapolated peak onset temperature
- T_p max. interpolated baseline peak temperature
- T_{ce} extrapolated peak completion temperature
- T_f final peak temperature

Figure 3-6: Analysis of a DSC peak when Q [mW] is the heat flux, and T [°C] the temperature [HÖHNE 96].

The output of a DSC measurement is a heating and/or cooling curve that gives information about the enthalpies of transitions. Usually, the accuracy of the determined temperatures increases with lower cooling rate. To check this influence the measurements can be done with varying cooling rate and sample size. In addition the measurement can be influenced by the thermal conductivity of the sample, the mass and heat capacity of the sample, the structure of the sample (powder, granulates, foil,..), the microstructure (for example grain size), and the location of the sample in the crucible of the measurement system. Besides also the kind of gas in the cavity of the measuring system could influence the separation of closely adjacent peaks and therefore the resolution and the calibration [HÖHNE 96].

The analysis of the measurements is shown in *Figure 3-6* [HÖHNE 96]. The zero line is the curve measured either with the empty instrument, which means without samples and without sample containers, or with sample containers but still without samples. This curve shows the thermal behaviour of the measuring system itself. The repeatability of the measurement is direct proportional to the stability of this curve. The baseline is the line that connects the measured curve before and after the peak as if there would be no heat exchange. A peak in the measured curve appears always when a thermally activated heat production or consumption in the sample takes place. A peak begins at T_i which is the point of the first deviation from the baseline. T_p indicates the maximum temperature and correlates with the highest point of the peak. After this the peak merges into the baseline again in T_f. T_e shows the extrapolated peak onset temperature where the auxiliary line through the ascending peak slope intersects the baseline. T_{ce} shows the extrapolated peak completion temperature (same extrapolation like for T_e). Here the peak is completed [HÖHNE 96]. Since further detailed description of DSC measurements is out of the scope of this work, the reader is referred to literature [BHADESHIA 02, DEAN 95, HÖHNE 96, MASBERG 99, PUNGOR 95, SKOOG 98].

Basics in SEM Measurements

For the detection of phase and concentration distributions, diffusion and DSC measurements have to be combined with microscopy and SEM (Scanning Electron Microscope) measurements. Optical microscopy can be used to identify the phase distribution to a maximum resolution of approximately 500 nm, depending on the wave length of the used (visible) light. The resolution of SEM mesurements depends on diameter and penetration depth of the primary electron beam and can reach down to 1-6 nm [HUNGER 95]. A general picture of the construction of a SEM is shown in *Figure 3-7* [FLEWITT 94]. The heating of a tungsten wire (cathode) causes a primary electron beam (sated electron cloud), and the occuring high voltage (1-30 kV) between cathode and anode accelerates the electrons (Electron gun). This electron beam is focused by a control cylinder (wehnelt-cylinder). Electromagnetic inductors (two condenser lenses, one objective lens) bundle the primary electron beam to a focussed point on the surface. By using a XY-deflexion system the primary electron beam is sequentially scanning the surface of the sample.

The focused primary electron beam causes interactions with the electron sheath of the sample atoms, where back-scattered electrons and secondary electrons are emitted. This process has to take place in high vacuum to eliminate the possibilities of interactions of the primary electron beam with atoms and molecules of the air. The back-scattered, high energetic electrons are mainly reflected at the surface of the sample. The electrons with lower energy are generated by interactions of the primary electrons with the electron sheath in the atomic layers close to the surface. In this case the energy loss is induced by inelastic interactions of the primary electrons with the electron sheath of atoms. The slower secondary electrons are collected by a detector (Electron collector) and a scintillator causes light flashes on the detector for each electron that impinges. A photomultiplier (Amplifier) converts and amplifies the flashes to an electrical signal. This signal is then displayed on the monitor. Parts of the surface which emit a large number of secondary electrons look brighter than areas which emit less. With that information it's possible to create a picture of the surface (CRT–display (Cathode Ray Tube) / Camera). The picture itself is built by line-by-line scanning.

The two main measurement types for the element detection are EDS (Energy Dispersive X-ray Spectroscopy) and WDS (Wave length Distersive X-ray Spectroscopy) measurements. In case of EDS X-ray radiation is transformed by a detector crystal into an electric charge which is proportional to the energy of the radiation. A field effect transistor transforms the charge into voltage and amplifies it. For a low-noise signal it is necessary to cool down the crystal and the transistor with liquid nitrogen. The output signal is transformed into electromagnetic pulses. An analog/digital transducer assigns a digital value for each pulse depending on the level of the pulse. This information is sorted by a multi channel analyser and finally the number of pulses per channel builds the spectrum of the x-ray radiation on a monitor [HUNGER 95]. The combination of SEM and EDS enables semi-quantitative chemical analyses of the phases. *Figure 3-8* shows an example of a characteristic EDS spectrum of Cu-Sn-P bronze. The detection of P with EDS is rather difficult due to its small molecular weight, especially in combination with Cu or Sn which have a clearly higher molecular weight. In addition to that there is also some noise occurring during the measurements that leads to a certain error in the results. Therefore, for quantitative analysis of P, one has either to calibrate the EDS measurements or to use WDS calibrated with a standard for P. With WDS the angle of the reflected x-rays is detected, based on the Bragg's reflection of x-rays on crystalls. The

radiation that reaches the detector is only reflected if the distance of the atomic layers *d*, the reflexion angle Θ, and wavelength λ fulfill the condition

$$2d \sin\Theta = N\lambda, \tag{3-15}$$

where *N* is the diffraction order [HUNGER 95]. The calibration and comparison with the standard during the measurement increase the accuracy significantly. For further information about SEM measurements the reader is referred to literature [BLUMENAUER 94, FLEWITT 94, HUNGER 95].

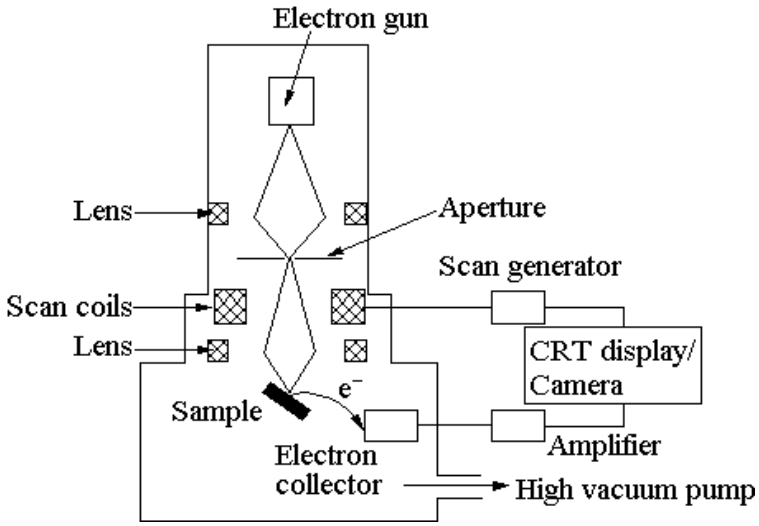

Figure 3-7: Schematical drawing of the construction of a SEM [FLEWITT 94].

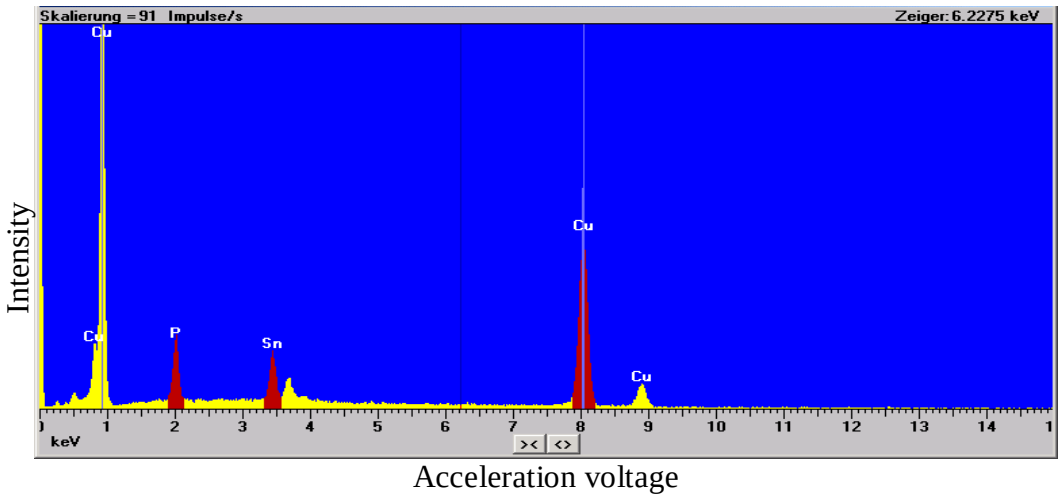

Figure 3-8: Characteristic EDS-spectrum of Cu, Sn, and P. Amplitudes of the peaks are related to the weight fraction of the corresponding element.

3.2 Thermodynamic Description of the System Cu-Sn-P

Although parts of the ternary system in the Cu rich corner are already described in literature [EFFENBERG 07, MIETTINEN 01, TAKEMOTO 87], the comparison of the experimental observations in the ternary system and the numerical results show some differences according the presence of some phases as for example the γ and ε phase. Therefore the basic aim of the following experimental investigation was to verify the known binary systems as well as ternary system. In the ternary system, the ternary eutectic point is of special interest for industry because its presence and temperature range is still questionable [EFFENBERG 07]. The presence of Cu_3P, occurring at the ternary eutectic point, influences the brittleness of the final bronze product.

The presented thermodynamic investigation includes numerical simulations of the ternary CuSnP system in the Cu rich corner with the thermodynamic software Thermo-Calc. In addition DSC measurements for the binary systems and diffusion experiments for both, binary and ternary alloys, have been performed.

3.2.1 Computational Thermodynamics

Based on literature [MIETTINEN 01, THERMOCALC 03] the numerical Cu-Sn-P database CuSn1 was implemented for the calculations performed within the scope of this work by Thermo-Calc. This database, in combination with the software Thermo-Calc, was used in the present work for the numerical description of the system. The binary Cu-Sn and Cu-P phase diagrams are displayed in *Figure 3-9a* and *Figure 3-9b* (calculated with database CuSn1 in Thermo-Calc). Further details on the phase distribution of the binary systems are given in chapter 3.2.2 in connection with the analysis of the DSC measurements.

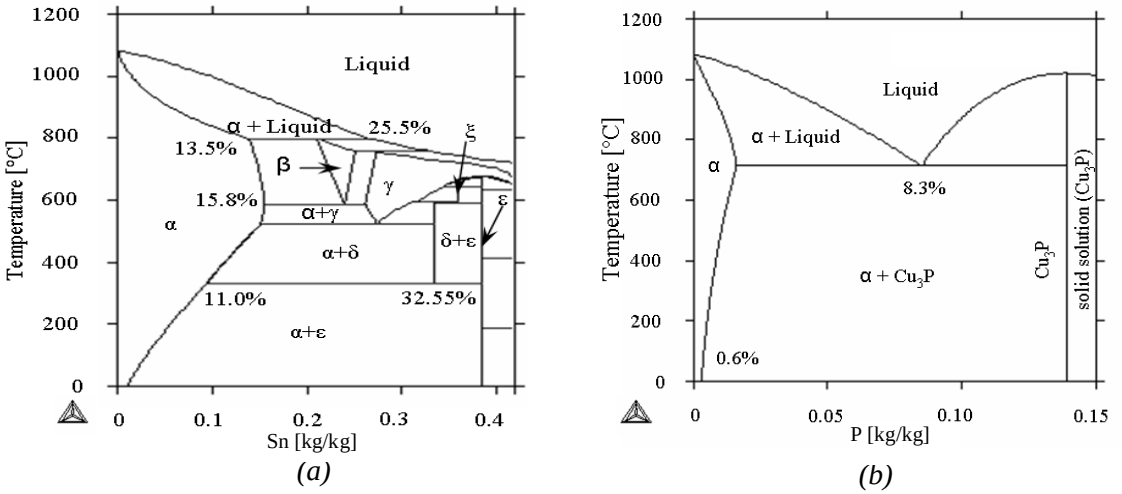

Figure 3-9: (a) Phase diagram for Cu-Sn calculated with Thermo-Calc (database CuSn1). (b) Phase diagram of Cu-P calculated with Thermo-Calc (database CuSn1). α = Cu (max. Sn 15.8 wt.%); β ~ $Cu_{17}Sn_3$; γ ~ Cu_3Sn; δ ~ $Cu_{41}Sn_{11}$; ε ~ Cu_3Sn; ξ ~ $Cu_{10}Sn_3$ (nomenclation taken from [EFFENBERG 07]).

Since the main scope of the experimental work is on the ternary system, in the following it is described in detail. *Figure 3-10* shows isothermal sections of the ternary Cu-Sn-P system for T = 1032, 1000, 900, 780, 700, 648, 645, 640, 600, 525, 400, and 300 °C.

The CuSn1 database is restricted to the Cu rich corner up to 15 wt.% P and about 40 wt.% Sn. Therefore the sections are calculated within this range.

Starting with 100 % liquid (L), the α phase (α, red regions, *Figure 3-10, T* = 1032 °C) forms after the melting point of Cu, T_{lCu} = 1085 °C is reached. The first isothermal section was chosen a little below T_{lCu} (*Figure 3-10, T* = 1032 °C). The one-phase regions α and L are separated by the two phase region α-L according to the Gibbs phase rule (equation 3.1). Below the melting point of the compound Cu_3P (appears as a point in the isothermal sections) T_{lCu3P} =1022 °C, the two phase region Cu_3P-L is present in the isothermal section (*Figure 3-10, T* = 1000 °C). With decreasing temperature the one phase region of α and the two phase regions of α-L and Cu_3P-L are increasing (*Figure 3-10, T* = 900 °C).

In the isothermal section at *T* = 780 °C, β is present as a result of the peritectic reaction L + α → β starting at *T* = 799 °C. With solidification of the third phase, the three phase region α-β-L (bright blue triangle, *Figure 3-10, T* = 780 °C) can be observed. In the isothermal section at *T* = 700 °C, γ is occuring in addition to the already mentioned phases as a result of the peritectic reaction L + β → γ at *T* = 756 °C, and with that the three phase region β-γ-L (orange triangle) appears. Besides, the eutectic groove between α and Cu_3P is reached and the three phase region α-Cu_3P-L is visible (dark green triangle, *Figure 3-10, T* = 700 °C).

Further cooling leads to a decrease of the L region to a small area at *T* = 648 °C which is even smaller in the isothermal section at *T* = 645 °C. At slightly lower temperature, namely at approximately *T* = 644.1 °C, the ternary eutectic point is reached at a concentration of 15 wt.% Sn and 5.5 wt.% P (red point, number I, *Figure 3-11*).

At *T* = 648 °C the decreasing of the liquid phase leads to the presence of two more three phase regions, namely Cu_3P-γ-L (black triangle) and Cu_3P-ε-γ (purple triangle). The ε phase (ε) is located at ~38 wt.% Sn in the binary phase diagram and therefore its one phase region (appearing as a point in the isothermal section) is not visible in the presented ternary sections. In the isothermal section at *T* = 640°C the ξ phase (ξ) occurs in the three phase region Cu_3P-γ-ξ as a result of the peritectoid reaction ε + γ → ξ. Since ξ has a Sn content of approximatley 36 wt.% Sn the one phase region of the binary system is also not visible in the ternary sections.

The liquid phase has already disappeared at *T* = 640°C but four three phase regions are present, namely Cu_3P-ε-ξ (pink triangle), Cu_3P-γ-ξ (brown triangle), Cu_3P-β-γ (gray triangle) and Cu_3P-α-β (middle blue triangle). The calculations with Thermo-Calc indicate a two phase region Cu_3P-ξ where, after Gibbs phase rule, a three phase region is expected. Since ξ is handled as a compound in the thermodynamic calculation the two phase region is reduced to a line.

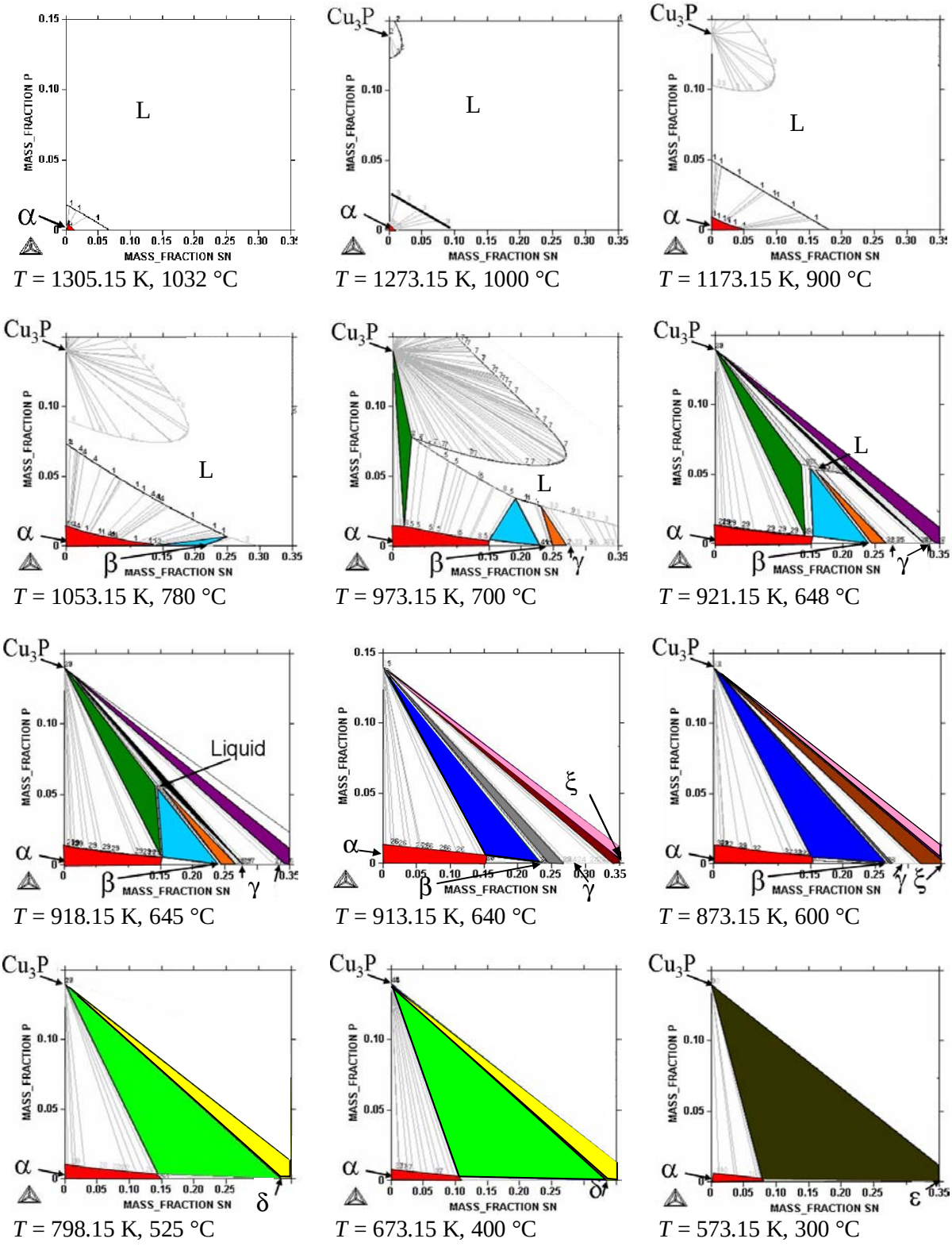

T = 1305.15 K, 1032 °C | *T* = 1273.15 K, 1000 °C | *T* = 1173.15 K, 900 °C

T = 1053.15 K, 780 °C | *T* = 973.15 K, 700 °C | *T* = 921.15 K, 648 °C

T = 918.15 K, 645 °C | *T* = 913.15 K, 640 °C | *T* = 873.15 K, 600 °C

T = 798.15 K, 525 °C | *T* = 673.15 K, 400 °C | *T* = 573.15 K, 300 °C

Figure 3-10: The presented isothermal sections of the ternary phase diagram of Cu-Sn-P in the Cu rich corner are calculated with Thermo-Calc (database CuSn1). α = Cu (max. Sn 15.8 wt.%, P 2 wt.%); β ~ $Cu_{17}Sn_3$; γ ~ Cu_3Sn; δ ~ $Cu_{41}Sn_{11}$; ε ~ Cu_3Sn; ξ ~ $Cu_{10}Sn_3$ (nomenclation taken from [EFFENBERG 07]).

At T = 600 °C the same phases are stable as at T = 640 °C, but position and size of the phase regions change. At T = 525 °C the δ phase (δ) has already appeared while ξ disappeared caused by the peritectoid reaction $\xi + \gamma \rightarrow \delta$. In this section the three phase regions of Cu_3P-δ-ε (yellow triangle), and Cu_3P-α-δ (bright green triangle) are present. β disappeared due to the eutectoid reaction $\beta \rightarrow \alpha + \gamma$ at T = 588 °C. With further cooling only the solibilty of Sn in α is decreasing and therefore at T = 400 °C the same phases are stable as at T = 525 °C.

Further decrease of the temperature leads to the eutectoid reaction $\delta \rightarrow \alpha + \varepsilon$ at T ~ 350 °C and therefore δ is not present in the isothermal section at T = 300 °C. At this temperature the stable phases Cu_3P, α, and ε are connected by the three phase region Cu_3P-ε-α (dark green triangle).

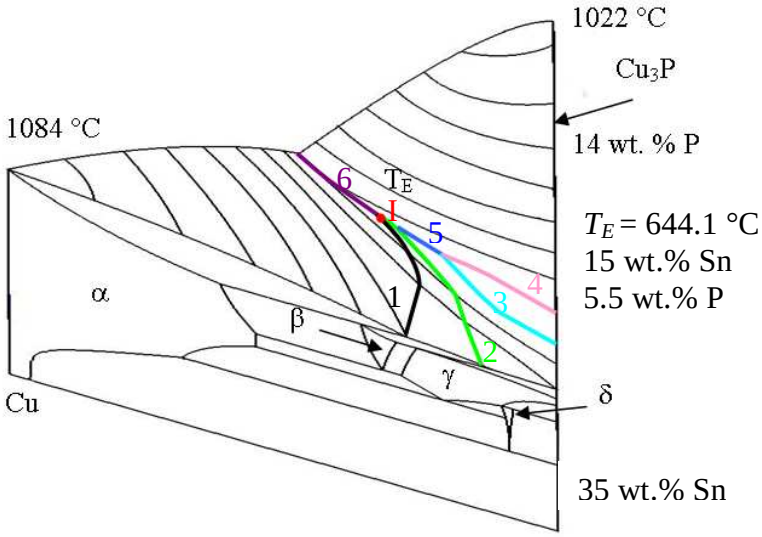

Figure 3-11: 3D liquidus surface of the ternary phase diagram Cu-Sn-P in the Cu rich corner up to 35 wt.% Sn and 14 wt.% P based on calculations with Thermo-Calc (database CuSn1). The colored lines show the monovariant lines of the liquidus surface and the front view the binary system Cu-Sn. Black line (1): monovariant line corresponding to the peritectic reaction $L + \alpha \rightarrow \beta$, green line (2): monovariant line corresponding to the peritectic reaction $L + \beta \rightarrow \gamma$, bright blue line (3): monovariant line corresponding to the peritectic reaction $\gamma + L \rightarrow \varepsilon$, pink line (4): monovariant line corresponding to the eutectic reaction $L \rightarrow Cu_3P + \varepsilon$, blue line (5): monovariant linecorresponding to the eutectic reaction $L \rightarrow Cu_3P + \gamma$, purple line (6): monovariant line corresponding to the eutectic reaction $L \rightarrow Cu_3P + \alpha$, red point (I) is the ternary eutectic point.

Figure 3-11 shows a 3D projection of the liquidus surface of the ternary phase diagram Cu-Sn-P in the Cu rich corner where the front view shows the binary Cu-Sn phase diagram up to 35 wt.% Sn. The isothermal lines (black fine lines) and mono variant lines (colored lines) of the liquidus surface are drawn based on the calculations performed with Thermo-Calc. The black line (number 1) is the monovariant line corresponding to the peritectic reaction $L + \alpha \rightarrow \beta$, the green line (number 2) the monovariant line corresponding to the peritectic reaction $L + \beta \rightarrow \gamma$, whereas the bright blue line (number 3) is the monovariant line corresponding to the reaction $\gamma + L \rightarrow \varepsilon$. The pink line (number 4) is the monovariant line of the eutectic reaction $L \rightarrow Cu_3P + \varepsilon$ and the blue line (number 5) the monovariant line of the eutectic reaction $L \rightarrow Cu_3P + \gamma$ which ends in

the ternary eutectic point (red, I). The purple line (number 6) represents the monovariant line of the eutectic reaction $L \rightarrow Cu_3P + \alpha$.

Figure 3-12 displays the vertical section (isopleths) at 5 wt.% P of the ternary phase diagram calculated with database CuSn1. The area marked with the red circle corresponds to the area also marked in the presented isopleths of [MIETTINEN 01, TAKEMOTO 87].The calculated isopleth generally complies with the published one of [MIETTINEN 01] but it differs in both, phase distribution and phase transformation temperature from the experimental study of [TAKEMOTO 87] especially due to the absence of γ in the experimental work.

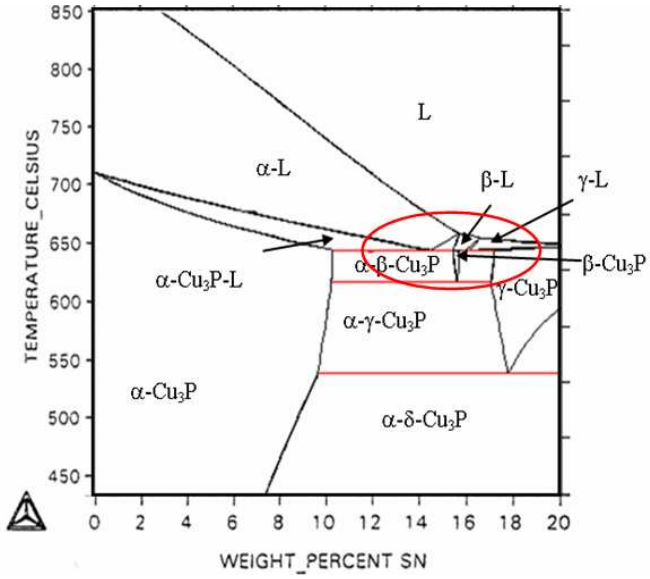

Figure 3-12: Vertical section (isopleth) of the ternary phase diagram Cu-Sn-P at 5 wt.% P calculated with Thermo-Calc (database CuSn1). It is possible to reproduce the published isopleth of [MIETTINEN 01] (see Figure 3-4b, page 17). Based on the binary phase diagram Cu-Sn, γ is included in the numerical assessment although it was not observed in the experimental study of [TAKEMOTO 87]. Red circles indicate the position around the ternary eutectic point of the system.

3.2.2 DSC Mesurements

The samples for the DSC measurements have been prepared by Wieland Werke AG with the following binary concentrations. *Figure 3-13* shows micrographs of the seven samples. The nominal concentration is applied for the sample name and the detected concentration of wet-chemical analysis is given in brakets:

1. Cu (99.991 wt.% Cu)
2. CuP2 (2.03 wt.% P)
3. CuSn4 (3.62 wt.% Sn)
4. CuSn10 (9.75 wt.% Sn)
5. CuSn20 (19.7 wt.% Sn)
6. CuP5 (4.84 wt.% P)
7. CuP8.3 (8.2 wt.% P)

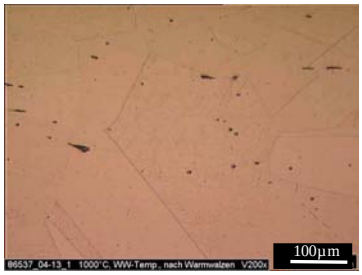

Nr. 1: Cu

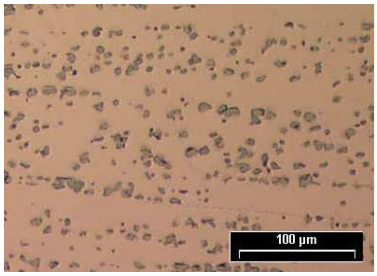

Nr. 2: CuP2

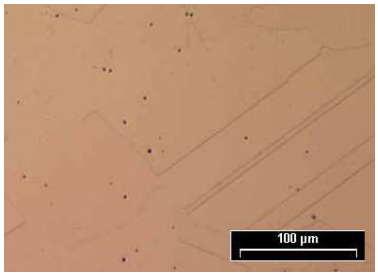

Nr. 3: CuSn4

Nr. 4: CuSn10

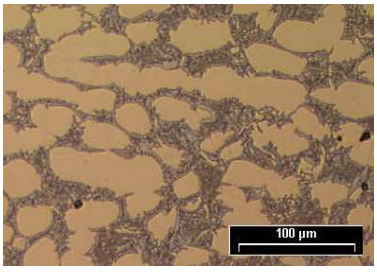

Nr. 5: CuSn20

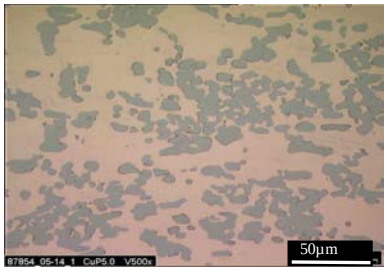

Nr. 6: CuP5

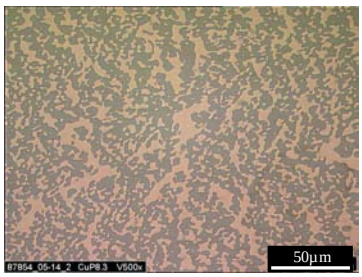

Nr. 7: CuP8.3

Figure 3-13: Micrographs of the pure Cu sample, the binary CuSn and the binary CuP samples [RIEDLE 04].

Experimental Description

The DSC measurements have been performed by the "Austrian Foundary Institut Leoben", by Heat Flux DSC. To ensure high measurement accuracy the measurements were done with low (2 $Kmin^{-1}$) and high (20 $Kmin^{-1}$) cooling rate and with varying sample size. The samples were first heated above the liquidus temperature of the alloy and afterwards cooled to room temperature.

The DSC was calibrated using Al (99.999 wt.% Al, Goodfellow Metals, Cambridge, UK, with a heating/cooling rate of 2 $Kmin^{-1}$), Au (99.995 wt.% Au, "NETZSCH Kalibrierset, NETZSCH Gerätebau, Selb, D, with a heating/cooling rate ot 2 $Kmin^{-1}$), and Cu (sample No. 1 (OFE-Nr.1), with a heating/cooling rate of 2 $Kmin^{-1}$). According to the calibration results, the DSC measuring device has a deviation of ΔT_{Al} = -0.1 °C, for super purity Al at melting temperature. The deviations from the melting point for Au was ΔT_{Au} = -2.4 °C and for pure Cu ΔT_{Cu} = -2.5 °C. The deviations have been compensated by the calibration. The negative ΔT values are negative deviations of the measuring device from defined reference values as given in literature [MASSALSKY 90]. DSC investigations were carried out by using pure Cu (sample Nr. 1) and the binary samples CuSn4, CuSn20, CuP2, and CuP5 (sample Nr. 2, 3, 5 and 6). For the temperatures around 660 °C the accuracy of the measurements is expected to be in a range of ΔT = +/-2 °C and for the temperatures around 1000 °C in a range of ΔT = +/-4 °C. As

an example *Figure 3-14* shows the cooling and heating curve of the DSC measurement of CuP5 (sample Nr. 5). SEM and microscopy was applied for phase detection. For that EDS measurements have been performed at the "Department of Metallurgy" of the Montanuniversity of Leoben.

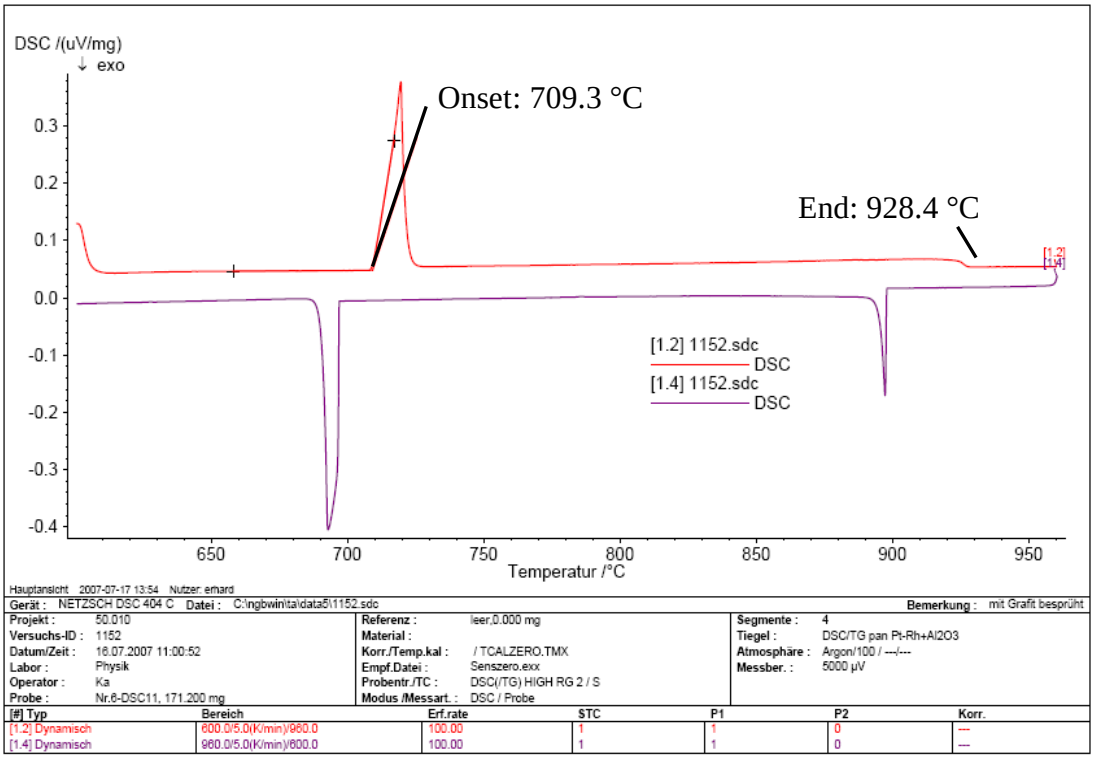

Figure 3-14: Cooling (violet line) and heating (red line) curves of the DSC measurement for CuP5 (sample Nr. 5) [KASCHNITZ 07].

Measurement Data

Two series of measurements have been performed, in 2005 and 2007. The second series of measurements was carried out to check the obtained transition temperatures in 2005. In *Table 1* and *Table 2* the obtained temperatures of phase transformation are presented whereas *Table 3* and *Table 4* show the detailed measurement data. The deviations obtained in the measurments are lying within the measurement accuracy.

Sample	***Name***	***1. PT***	***2. PT***	***3. PT***	***4. PT***	***Date***
Nr. 1	Cu	1084				28.01.05
Nr. 2	CuP2	1034	709			28,30.01.05;04.02.05
Nr. 3	CuSn4	1059	956			01,02,07.02.05
Nr. 5	CuSn20	898	793	576	518	03,07,09.03.05
Nr. 6	CuP5	922	709			04,08,10.03.05

Table 1: Temperatures [°C] of phase transformation of the DSC measurements in 2005.

Sample	***Name***	***1. PT***	***2. PT***	***3. PT***	***4. PT***	***Date***
Nr.5	CuSn20	906	794-801			16.07.07
Nr.6	CuP5	928	709			17.07.07

Table 2: Temperatures [°C] of phase transformation of the DSC measurements in 2007.

Sample	*Date*	*Weight [mg]*	*Cooling rate [K/min]*	*T-Range [°C]*
Cu_DSC 1	28.01.05	40.8	2	1050/1100
	28.01.05		2	1100/1000
	28.01.05		2	1000/1100
	28.01.05		2	1100/1000
CuP2_DSC 1	28.01.05	40.9	20	20/1100
	28.01.05		20	1100/20
	28.01.05		2	900/1100
	31.01.05		2	1100/900
	31.01.05		20	600/1100
	31.01.05		2	1100/600
CuP2_DSC 2	04.02.05	31.8	20	20/1100
	04.02.05		20	1100/600
	04.02.05		2	600/1100
	04.02.05		2	1100/20
CuSn4_DSC 1	01.02.05	41.9	20	20/1100
	01.02.05		20	20/800
	01.02.05		2	800/1100
CuSn4_DSC 2	02.02.05	44.2	2	800/1100
	02.02.05		20	20/1100
CuSn4_DSC 3	02.02.05	184.7	2	800/1100
	02.02.05		20	20/1100
CuSn20_DSC 1	03.03.05	45.1	20	20/1100
	03.03.05		20	1100/100
	03.03.05		2	100/1100
	03.03.05		2	1100/100
CuSn20_DSC 2	07.03.05	33.1	20	20/1000
	07.03.05		20	1000/300
	07.03.05		2	300/1000
	07.03.05		2	1000/300
CuSn20_DSC 3	09.03.05	179.7	20	20/1000
	09.03.05		20	1000/300
	09.03.05		2	300/1000
	09.03.05		2	1000/300
CuP5_DSC 1	04.03.05	38	20	20/1100
	04.03.05		2	100/1100
	04.03.05		20	1100/100
	04.03.05		2	1100/100
CuP5_DSC 2	08.03.05	40.6	20	20/1000
	08.03.05		20	1000/600
	08.03.05		2	600/1000
	08.03.05		2	1000/600
CuP5_DSC 3	10.03.05	173.1	20	20/1000
	10.03.05		20	1000/600
	10.03.05		2	600/1000
	10.03.05		2	1000/600

Table 3: DSC measurements performed in 2005.

Sample	*Date*	*Weight [mg]*	*Cooling rate [K/min]*	*T-Range [°C]*
CuP5	17.07.07	183.9	2	600/960
	17.07.07	183.9	2	960/600
CuSn20	16.07.07	171.2	2	450/980
	16.07.07	171.2	2	980/400

Table 4: DSC measurements performed in 2007.

Phase Detection

SEM and microscopy have been applied to define the phase distributions of the samples after DSC measurements. In the following the obtained phase distributions (by picture analysis in vol.%) are compared with the theoretical ones. *Figure 3-15a* shows the phase diagram for Cu-P and *Figure 3-15b* a micrograph of CuP2 (sample 2). The red line shows the average sample concentration. In the micrograph eutectic ($\alpha + Cu_3P$) (1) and α (2) are visible. The measured average concentration of α was 1 wt.% P, for Cu_3P 13 wt.% P and for the eutectic 10 wt.% P. Since the detection of P for the binary samples was performed by EDS, the variation of the P content lies within a range of ± 1 wt.%. The following percentages of the different phases are qualitativley estimated according to the phase diagram information in wt.% and the visible phase distribution in the micrographs. According to the phase diagram of Cu-P 92 wt.% α crystallizes during cooling untill the eutectic temperature is reached. At the eutectic temperature, eutectic, consisting of 55 wt.% Cu_3P and 45 wt.% α is formed. The phase distribution changes at lower temperatures due to a decrease of solibility of P in the secondary α. In the experiment 14 vol.% eutectic is observed (*Figure 3-15b*, gray-brown regions, (1)).

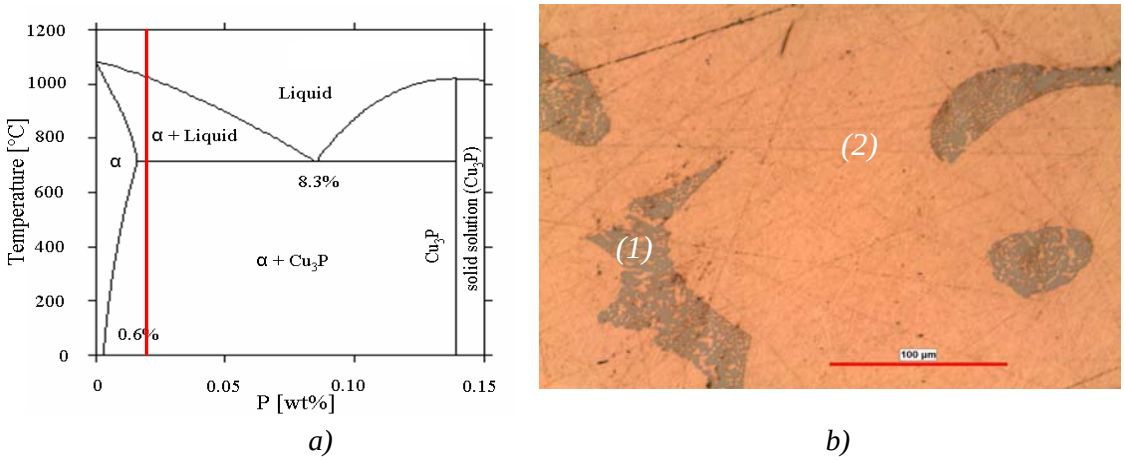

a) *b)*

Figure 3-15: a) The calculated phase diagram for Cu-P is displayed up to 15 wt.% P. b) A micrograph of CuP2 (sample Nr. 2) shows (1) the eutectic (α+Cu_3P) and (2) α. About 14 vol.% eutectic is observed in the sample.

Figure 3-16a shows the calculated phase diagram for Cu-P, wheras *Figure 3-16b* displays a micrograph of CuP5 (sample 6) after the DSC measurements. Here eutectic ($\alpha + Cu_3P$) (1) and α phase (2) are visible. The measured average concentration of α is 1 wt.% P, and of Cu_3P 14 wt.% P. The SEM measurements of the eutectic phase give a concentration of 9 wt.% P, slightly above the expected concentration. According to *Figure 3-16*, 42 vol.% α has crystallized before reaching the eutectic temperature. The phase diagram shows that 50 wt.% eutectic (*Figure 3-16b*, gray-brown regions, (1)) is formed at the eutectic temperature which consists of 55 wt.% Cu_3P and 45 wt.% α.

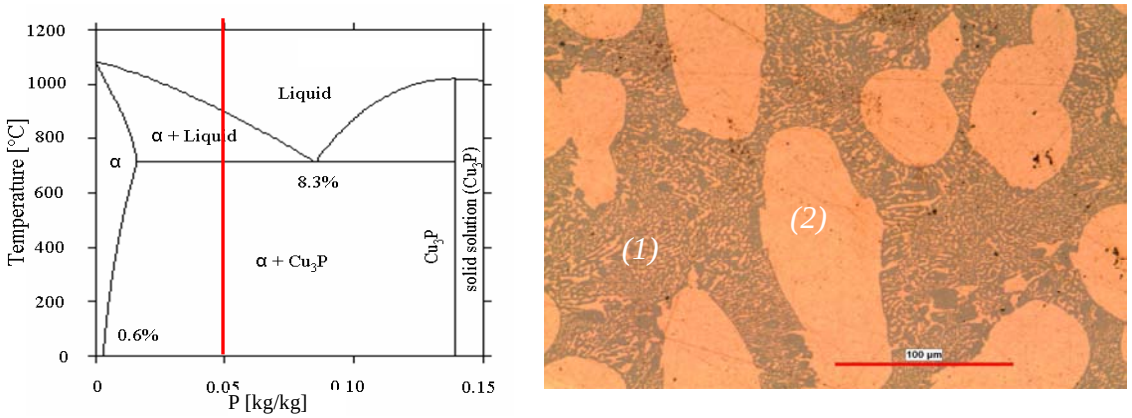

Figure 3-16: a) The calculated phase diagram for Cu-P is displayed up to 15 wt.% P. b) A micrograph of CuP5 (sample Nr. 6) shows (1) the eutectic (α+Cu_3P) and (2) α. Roughly 42 vol.% eutectic are observed in the sample.

Figure 3-17a shows the calculated Cu-Sn phase diagram and *Figure 3-17b* a micrograph of CuSn4 (sample 3) after the DSC measurements. Here 100 % α is observed. According to *Figure 3-17a*, the whole liquid crystallizes as α. Due to the fact that the solubility of Sn decreases to 1.3 wt.% Sn, the tin rich ε phase should occure at room temperature. But in the investigated samples it was not possible to identify ε, neither in the micrographs, nor in the SEM investigations.

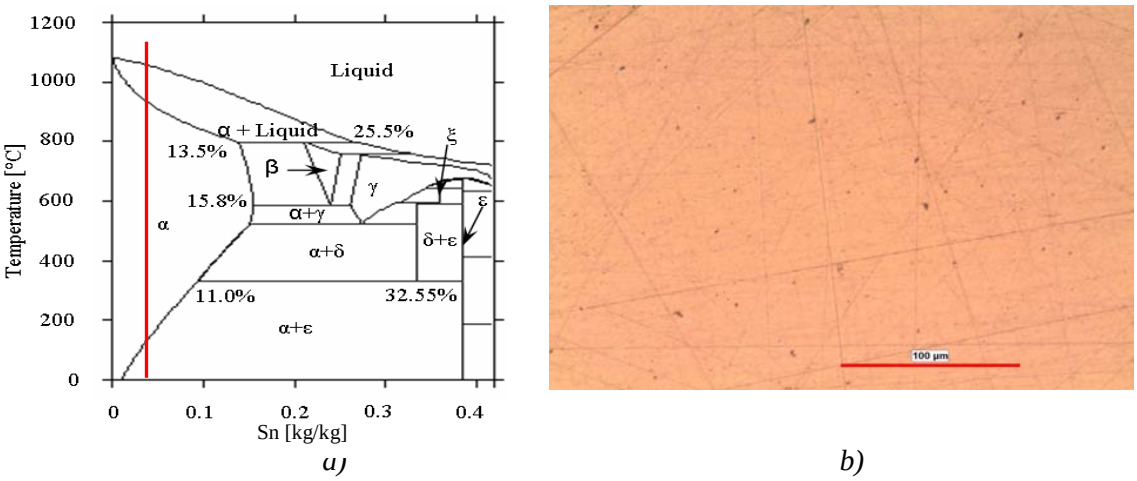

Figure 3-17: a) The calculated phase diagram for Cu-Sn is displayed up to 45 wt.% Sn and in b) a micrograph of CuSn4 (sample Nr. 3) is presented. Here 100 % α is observed.

Figure 3-18a shows the phase diagram for Cu-Sn and *Figure 3-18b* displays a micrograph of CuSn20 (sample 5) after the DSC measurements. The detected average concentration of α is 16 wt.% Sn, for δ 34 wt.% Sn, and for the eutectiod 28 wt.% Sn. The volume fraction of the eutectoid is 29 vol.%. According to the phase diagram, 50 wt.% α crystallizes during cooling until a temperature of 799 °C is reached. Further cooling leads to growth of β due to the peritectic reaction $\alpha + L \rightarrow \beta$. Reaching 588 °C 70 wt.% β is built-up whilst α is reduced to 30 wt.% and with that phase distribution changes to about 50 wt.% α and 50 wt.% β due to the reduced solubility of Sn. Further cooling leads to the transformation of β to α and γ due to the eutectoid reaction

$\beta \rightarrow \alpha + \gamma$, where the eutectoid consists of 10 wt.% α und 90 wt.% γ. Further cooling changes the composition to 60 wt.% α and 40 wt.% γ. At 520 °C, the eutectoid reaction, $\gamma \rightarrow \alpha + \delta$, leads to a composition of 70 wt.% α and 30 wt.% δ. At 350 °C the last eutectoid reaction, namely the transformation of δ in α and ε takes place. Hence, 70 wt.% α and 30 wt.% ε is expected at room temperature. Due to the fact that the solubility of Sn decreases to 1.3 wt.%, the volume fraction of the Sn rich ε should increase during cooling to room temperature. Therefore a final composition of 1.3 wt.% primary α and 98.7 wt.% eutectoid (50 wt.% α, 50 wt.% ε) is expected according to the phase diagram. However, it was not possible to detect ε (see also CuSn4) by SEM. The measured concentrations indicate mainly α (*Figure 3-18b*, brown regions, (2)) and eutectoid (δ with α) (*Figure 3-18b*, grey regions, (1)). The measurement data of the SEM investigation is listed in [GRUBER 07A, PANZL 08] of the binary DSC samples.

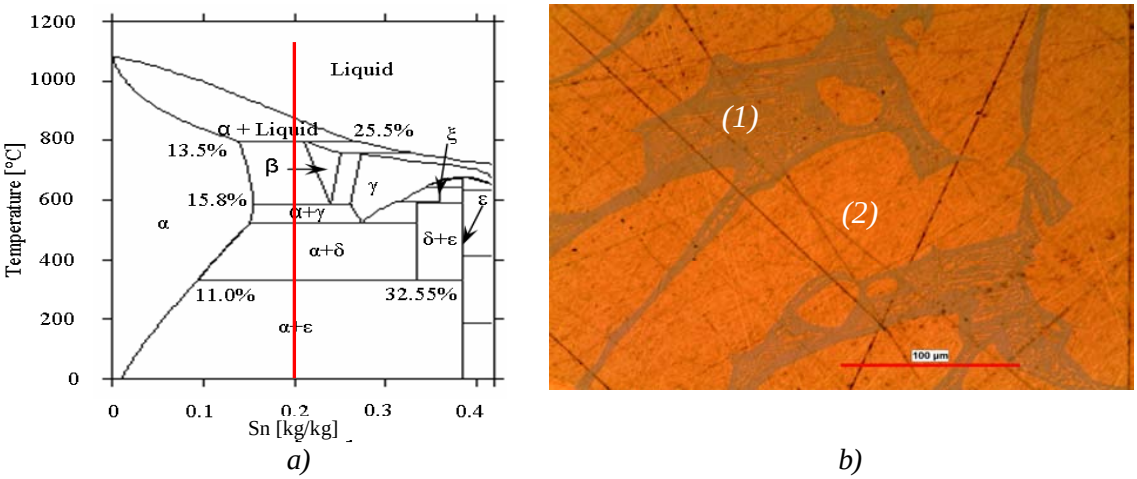

Figure 3-18: a) The calculated phase diagram for Cu-Sn up to 45 wt.% Sn and b) a micrograph of CuSn20 (sample 5) is displayed. (1) assigns the eutectoid (α+δ) and (2) α. 29 vol.% eutectoid is present in the sample.

3.2.3 Diffusion Experiments

Experimental Description

The experimental performance is described in detail in the bachelor work of Panzl [PANZL 08] which was performed in the frame of the present project. Therefore only some information is given here. *Figure 3-19* shows the test arrangement containing the furnace, the used digital multimeter and the position of the sample during annealing [PANZL 08]. According to test measurements the furnace holds the temperature with a deviation of ΔT = +/-1 °C. Radial symmetrical diffusion is approximated by an axis symmetric geometrie as schematically demonstrated in *Figure 3-20*. Since P tends to evaporate, a cylindrical geometry is used consisting of a outer tube (about 2 mm extension and a radius of about 8 mm) of Cu or Cu-Sn (*Figure 3-20*, bright brown) and of a core made of Cu-P or Cu-Sn-P (*Figure 3-20*, blue).

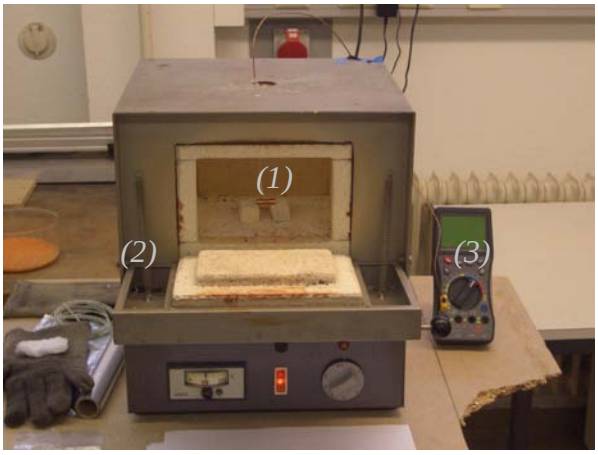

Figure 3-19: The test arrangement consist of (1) the sample, (2) the furnace and (3) the digital multimeter [PANZL 08].

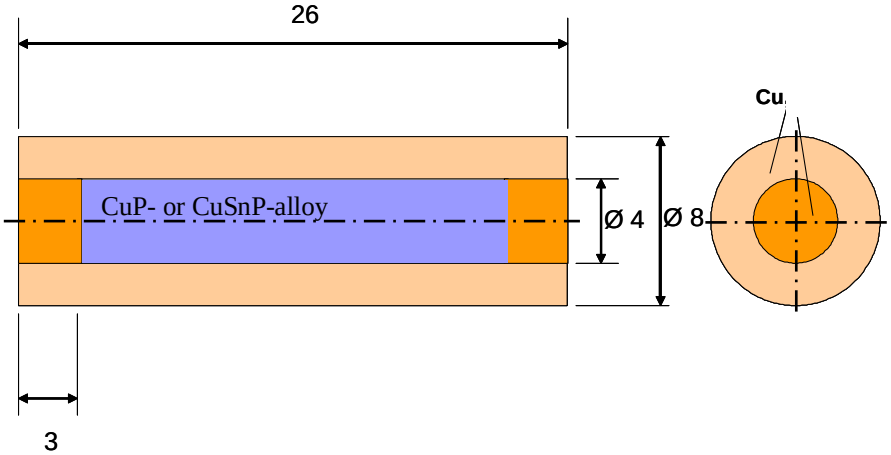

Figure 3-20: The cylindrical geometry applied for the diffusion experiments [RIEDLE 06] is shown. The outer tube consists of Cu or CuSn (light brown) and the inner cylinder of CuSnP or CuP (light blue). Cu pieces at the top and the bottom pieces close the sample. Dimensions are given in [mm].

In addition, the sample was closed at the top and at the bottom by Cu pieces as displayed (Figure 3-20, orange) to avoid evaporation of P [Riedle 06]. For further information about the sample preparation as well as details to the experimental performance the

reader is referred to [Panzl 08]. SEM and microscopy was applied for phase detection. Here, EDS measurements have been performed at the "Department of Physical Metallurgy & Materials Testing" of the Montanuniversity of Leoben and at "Wieland Werke AG" and WDS measurements at the "Chair of Mineralogy&Petrology" of the Montanuniversity of Leoben. The detailed measurement data obtained by SEM investigations for the diffusion experiments is listed in [GRUBER 07B] whereas in the following the results are shown and the discussion is given in the corresponding chapter 3.3.

Binary Diffusion Studies

The presented binary diffusion experiment was performed with two samples, namely CuSn20 and CuP8.3, at T_a = 648 °C for t_a = 3 days. After annealing, the sample was quenched in cold water and prepared for further measurements. *Figure 3-21* displays the ternary isothermal section of the system Cu-Sn-P at T_a = 648 °C (+/-1 °C) in the Cu rich corner, whereas the red arrows mark the sample concentrations.

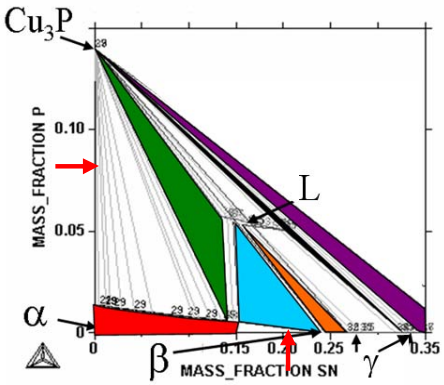

Figure 3-21: The isothermal section for T = 648 °C of the Cu rich corner for CuSnP as displayed in Figure 3-10. The red arrows mark the sample concentrations.

Figure 3-22 shows a micrograph of the used reference sample before annealing. The matrix of CuP8.3 (*Figure 3-22*, cylinder in the middle, *(1)*) is slightly gold-red imbedding the fine dispersed gray compound Cu_3P. According to the binary phase diagram these two phases are forming the Cu_3P-α eutectic. The outer tube consists of the CuSn20 α-δ eutectoid (*Figure 3-22*, less red-gold matrix with bright gray regions, *(2)*). *Figure 3-23* displays a micrograph of the binary diffusion sample after annealing. In the inner cylinder Cu_3P-α eutectic is observed, but the microstructure especially in the outer tube has changed due to the formation of α-β peritectic. At the contact interface, both, the Cu_3P-α eutectic and α-β peritectic are not visible any more *(I)*. The depleted area is marked by the white broken line.

In this zone the change of concentration due to diffusion is visible. These regions are depleted in Sn and P and therefore the concentration reaches the values of α (up to 15 wt.% Sn and 2 wt.% P) and eutectic/eutectoid is not stable any longer. The detailed measurement data for the SEM investigations of the reference and diffusion couple is listed in [PANZL 08, GRUBER 07B] whereas average concentrations are given in the following.

The detected average concentration of CuP8.3 of the reference sample is 9.5 wt.% P and the average concentration in an equivalent region of the annealed sample is 11.6 wt.% P. In both samples α has a concentration of about 1.5 wt.% P and Cu_3P 14.5 wt.% P. The detected average concentration of CuSn20 of the reference and the annealed sample is 21.4 wt.% Sn. The concentration of α is 15.6 wt.% Sn, the concentration of the α-δ eutectoid and the concentration of the α-β peritectic are almost the same, that is 25.5 wt.% Sn. The measured concentrations are in the expected range according to published phase diagrams.

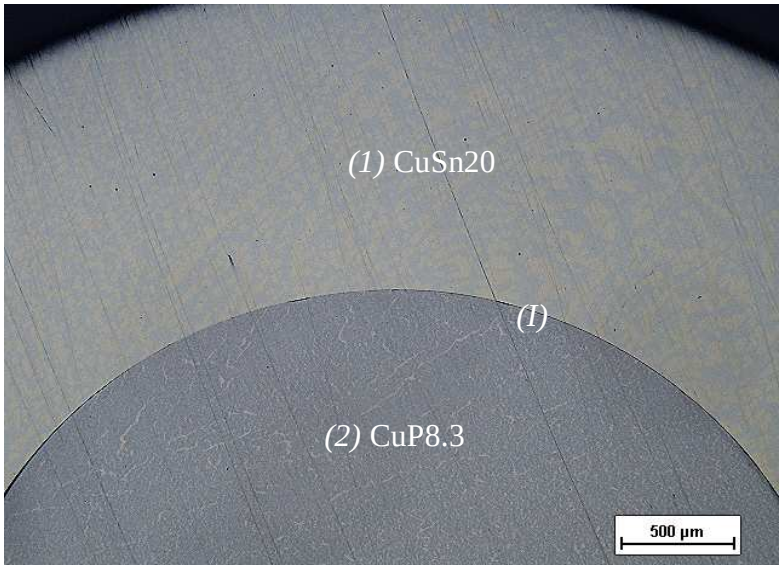

Figure 3-22: In the micrograph of the binary reference sample (1) marks the CuSn20 tube consisting of α-δ eutectoid, (2) the CuP8.3 cylinder consisting of Cu_3P-α eutectic, and (I) the contact between the two samples.

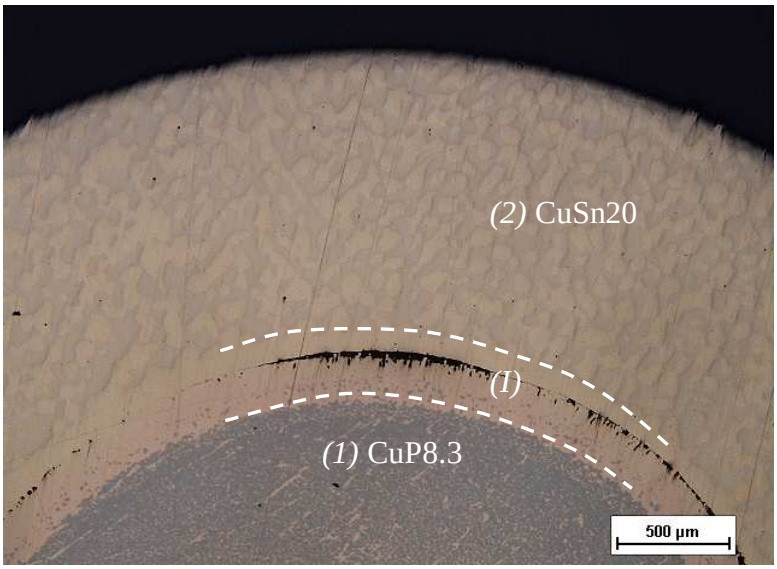

Figure 3-23: In the micrograph of the binary diffusion sample after annealing at 648 °C displays (1) the CuSn20 tube showing α-β peritectic, (2) the CuP8.3 cylinder consisting of Cu_3P-α eutectic, and (I) the contact area between the two samples with pores. White broken line indicates the Sn and P depleted region.

Ternary Diffusion Studies

For the ternary diffusion experiments, geometry, preparation and annealing were performed as described for the binary experiments. The core of the sample was prepared with CuSn20P6 and combined with a pure copper casing. Temperature range and sample concentrations for the experimental study were chosen to gain more information about the ternary eutectic point which is still questionable and discussed [EFFENBERG 07].

The experiments have been performed at (i) T_a = 648 °C for t_a = 6 days, (ii) T_a = 644 °C for t_a = 20 days, and at (iii) T_a = 642 °C for t_a = 20 days with a measured average deviation of the temperature during annealing of ΔT_a = +/-1 °C. After annealing, the samples were quenched into cold water and prepared for SEM investigations. Detailed description of the experimental performance is given in [PANZL 08].

Figure 3-24 to *Figure 3-26* display SEM pictures of the unnealed ternary sample. It seems to be unavoidable that, after sample preparation, there is still a small gap between the Cu tube (*Figure 3-24, (1)*) and the CuSn20P6 core (*Figure 3-24, (2)*). In addition, the CuSn20P6 core still features remarkable porosity which is caused by the rigidity of this ternary alloy. The fine structured matrix with dendrites of Cu_3P is visible in *Figure 3-25 (i)* which shows the region marked in *Figure 3-24* by the red area with a higher magnification. Cu_3P dendrites (gray phase, *Figure 3-24*) can be identified imbedded in light gray regions. *Figure 3-26* displays the red marked area of *Figure 3-25* with a higher magnification. In this picture it can be seen that the matrix imbedding the Cu_3P dendrites has eutectic microstructure containing δ-Cu_3P eutectoid (*Figure 3-26*). The detected average concentrations for the different phases are 31.6 wt.% Sn for δ and 14.6 wt.% P for Cu_3P. The detected average concentration of the ternary sample is 18.5 wt.% Sn and 6.9 wt.% P and of the δ-Cu_3P eutetoid 28.3 wt.% Sn and 3.8 wt.% P. These measurements have been performed by EDS and WDS. As expected by published phase diagrams, δ does not contain any P and Cu_3P no Sn.

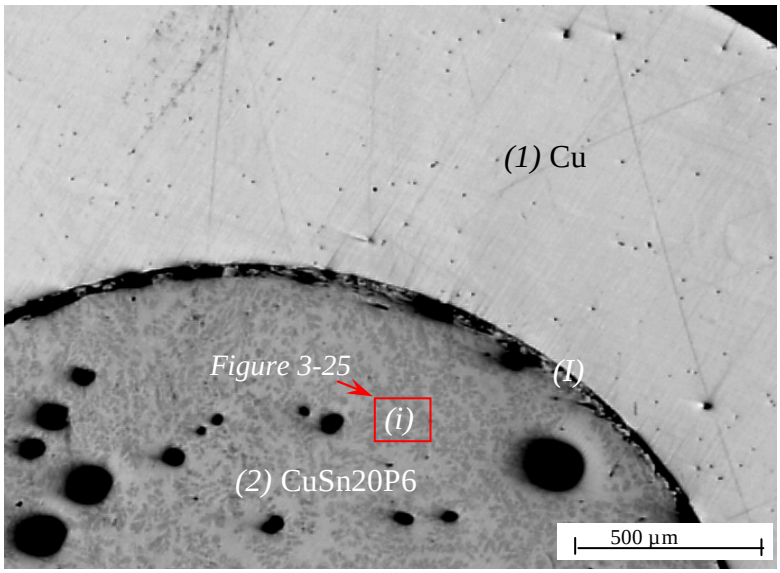

Figure 3-24: In the SEM picture of the unnealed sample (1) marks the Cu tube, (2) the CuSn20P6 core, and (I) the position of the interface between the different materials.

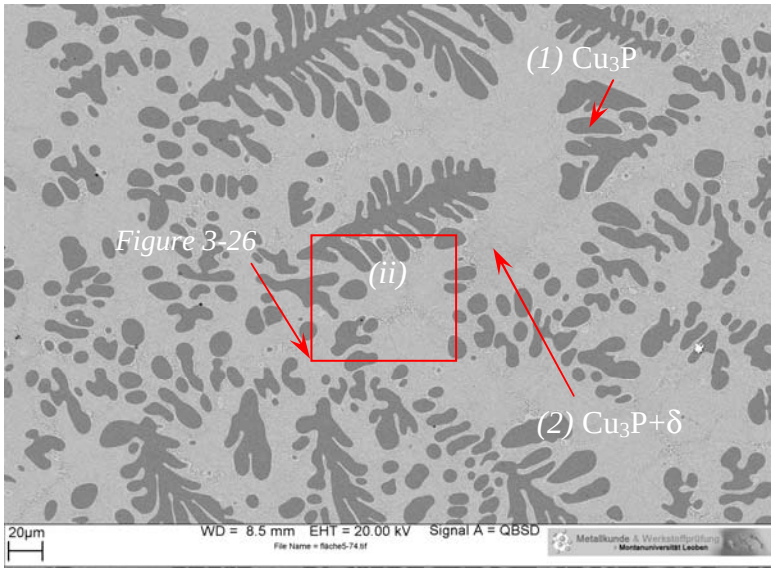

Figure 3-25: SEM picture of the unnealed sample in CuSn20P6 (Figure 3-24 (i) with higher magnification). Point (1) marks Cu_3P dendrites in the δ-Cu_3P eutectoid matrix (2).

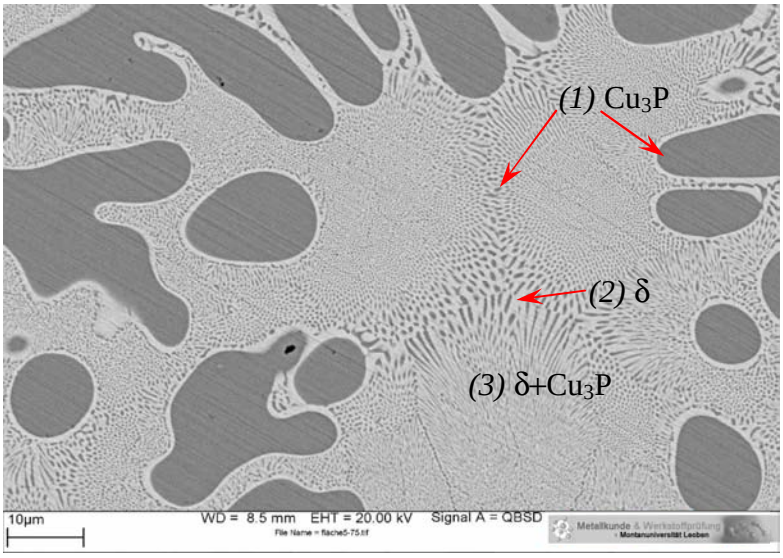

Figure 3-26: SEM picture of the unnealed sample (Figure 3-25 (ii) with higher magnification). Eutectoid microstructure is observed where (1) indicates the Cu_3P dendrites (dark gray), (2) δ (light gray), and (3) δ–Cu_3P eutectoid.

(i) Diffusion: T_a = 648 °C, t_a = 6 days

Figure 3-27 demonstrates a SEM picture of a cross section of the diffusion sample after annealing at T_a = 648 °C and t_a = 6 days. The outer tube consits of α^* (= pure Cu *(1)*) and the inner cylinder of the ternary CuSn20P6 alloy *(2)*. The interface between the two sample partners is thought to be at the position of the pores marked with *(I)* in *Figure 3-27*. In addition there are also some cracks visible in the center of the inner sample. The pores observed in the core of the reference sample are not visible anymore.

It is possible to distinguish four different regions, namely *(i)* the one phase region of the outer Cu ring (middle gray) which has increasing Sn content in the region close to the interface between the samples (defined by the red broken line), *(ii)* the two phase region

following the one phase region where a bright matrix is imbedding dark gray dots, and *(iii)* a slightly darker region with a relatively homogeneous matrix. This region is appearing twice: once attached to the two phase region in the lower part of the picture and in addition in the center of the sample *(iv)*.

Regions *(i)* and *(ii)* are displayed with a higher magnification in *Figure 3-28*. The black regions are pores that are thought to be close to the original sample boundary *(I)*.The gray level increases in brightness from the outer tube (α^* *(1)*, *Figure 3-28*) to the center while α (*(2)*, *Figure 3-28*) shows raising Sn content. As soon as the P content raises above the solubility of P in α (~2 wt.% P) Cu_3P is formed and the two phase region $Cu_3P+\alpha$ appears (*(3)*, *Figure 3-28*). The form of the Cu_3P within the α-matrix seems to be neither eutectic nor dendritic.

Figure 3-29 displays area *(iii)* from *Figure 3-27* and shows the next change in the microstructure moving further on to the center of the sample. A certain change from the relatively coarse two phase region to a fine structured area is observed. Attached to the big Cu_3P "grain" marked in *Figure 3-29 (1)*, a small two phase region with eutectic growth (*(2)*, *Figure 3-29*) is visible close to a fine structured region (*(3)*, *Figure 3-29*) that is slightly brighter than the surrounding areas.

This fine structured region can be again divided into a two phase region (*(3)*, *Figure 3-29*, *Figure 3-30*, *Figure 3-31*, and *Figure 3-32*) and a three phase region (*(4)*, *Figure 3-29*, *Figure 3-30*, *Figure 3-31*, and *Figure 3-32*). After "Gibbs phase rule" a one phase region is always touching a two phase region followed by either a one phase or a three phase region. The phase of the one phase region has to occur in the attached two phase region and again in a following three phase region. In addition, two phase regions always have to be separated by a one or a three phase region. Measurements in the two phase region marked in *Figure 3-32 (2)* identify α-Cu_3P eutectic. *(3)* in *Figure 3-32* shows the slightly brighter β in eutectic formation with Cu_3P (dark gray). The three phase region *(4)* marked in *Figure 3-32* contains β (bright gray), α (middle gray) and Cu_3P (dark gray). The same three phases are observed in *Figure 3-33*, *Figure 3-34*, and *Figure 3-35* according to the "Gibbs phase rule". The fine microstructure observed in *Figure 3-35* shows different concentrations for Sn and P than the corser microstructure shown in *Figure 3-34*.

The detected average concentrations for the different phases are 13.2 wt.% P for Cu_3P, 12.5 wt.% Sn and 2 wt.% P for α, 23.5 wt.% Sn and 2.2 wt.% P for β. The P content of β is high in comparison to published data, where almost no P is expected. Since the regions containing β show a fine phase distribution (~1 µm) the measurement accuracy is limitated. The detected average concentration of the three phase region Cu_3P-α-β in the center of the sample (*(iv) Figure 3-27*), is 16.5 wt.% Sn and 4.4 wt.% P, of the Cu_3P-α region (*(ii) Figure 3-27*), is 10.7 wt.% Sn and 4.6 wt.% P, of the Cu_3P-β region (*(3) Figure 3-32*) is 17 wt.% Sn and 4.7 wt.% P, and of the three phase region Cu_3P-α-β displayed in *Figure 3-34* 14.7 wt.% Sn and 4.6 wt.% P. These measurements have been performed by EDS and WDS.

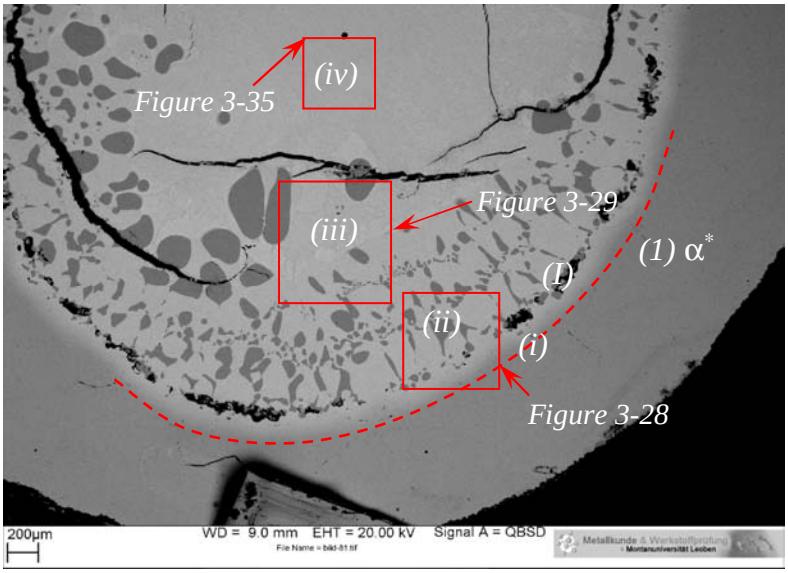

Figure 3-27: SEM picture of the annealed sample at T_a = 648 °C, t_a = 6 days. (1)marks the Cu tube, (2) the inner cylinder consisting of CuSn20P6, (i) the one phase region, and (ii) the two phase region (Cu_3P: dark gray, α: bright gray). Sn diffusion is observed up to about ~150 µm into the outer Cu tube. (iii) indicates a region where both, two and three phase regions (α, β Cu_3P) touch each other. (iv) shows the three phase region in the center of the sample (α, β Cu_3P) whereas (I) assigns pores as indicator for the sample boundaries). The red windows dessignate the position of Figure 3-28, Figure 3-29, and Figure 3-35. The diffusion depth of Sn is marked by the red broken line.

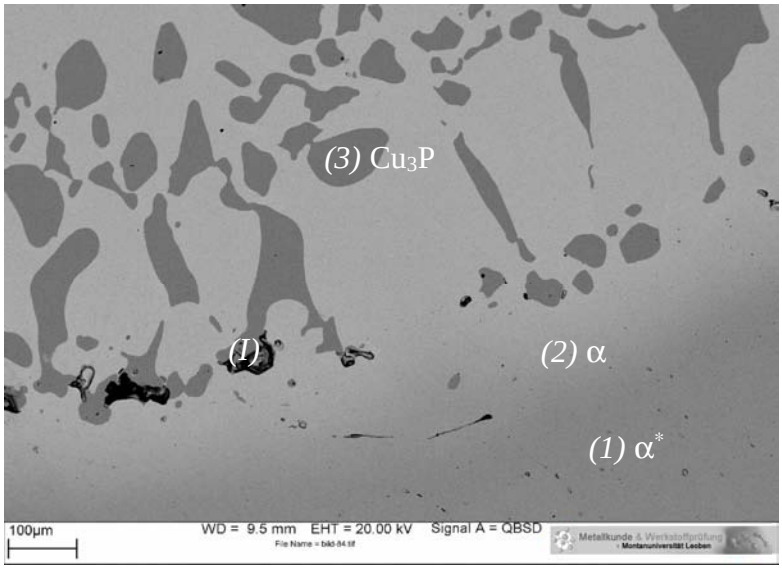

Figure 3-28: SEM picture of the annealed sample at T_a = 648 °C, t_a = 6 days of the red window (ii) shown in Figure 3-27 with higher magnification. Here the transition from the outer one phase region ((1) α (= pure Cu), (2) α to the two phase region ((3) Cu_3P: dark gray, α: bright gray) is visible. (I) marks pores as indicator for the sample boundaries.*

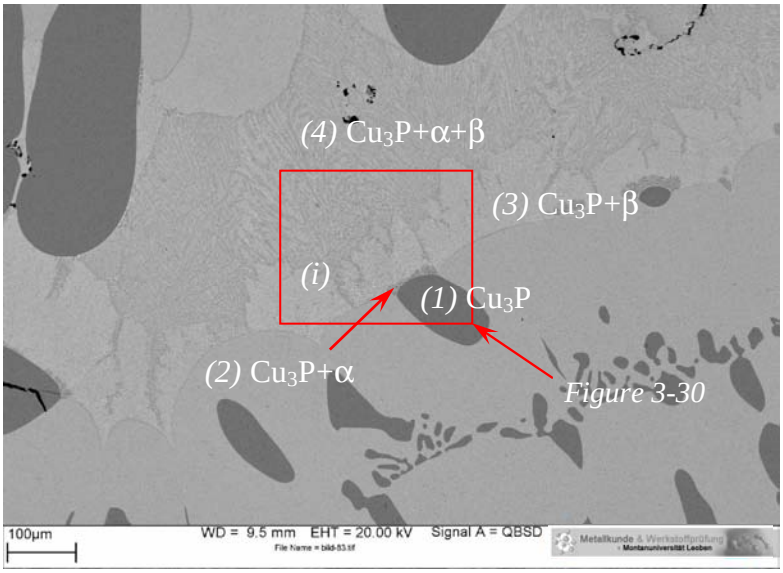

Figure 3-29: SEM picture of the annealed sample at T_a = 648 °C, t_a = 6 days of the red window shown in Figure 3-27 (iii) with a higher magnification. (1) marks Cu_3P (dark gray), (2) the two phase region with the eutectic α-Cu_3P (α: middle gray), (3) the two phase region of β-Cu_3P (β: bright gray), and (4) the three phase region of α-β-Cu_3P.

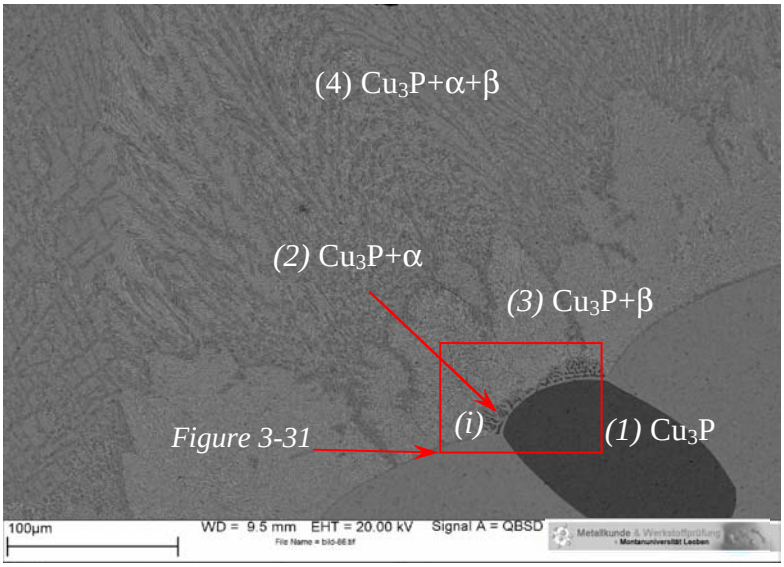

Figure 3-30: SEM picture of the annealed sample at T_a = 648 °C, t_a = 6 days of the red window (i) shown in Figure 3-29 with a higher magnification. (1) marks Cu_3P (dark gray), (2) the two phase region of α-Cu_3P (α: middle gray), (3) the two phase region of β-Cu_3P (β: bright gray), and (4) the three phase region oft α-β-Cu_3P. The big Cu_3P grain (dark region) in the right corner is surrounded by α (middle gray) on three sides, and by the two phase eutectic α-Cu_3P on the fourth side.

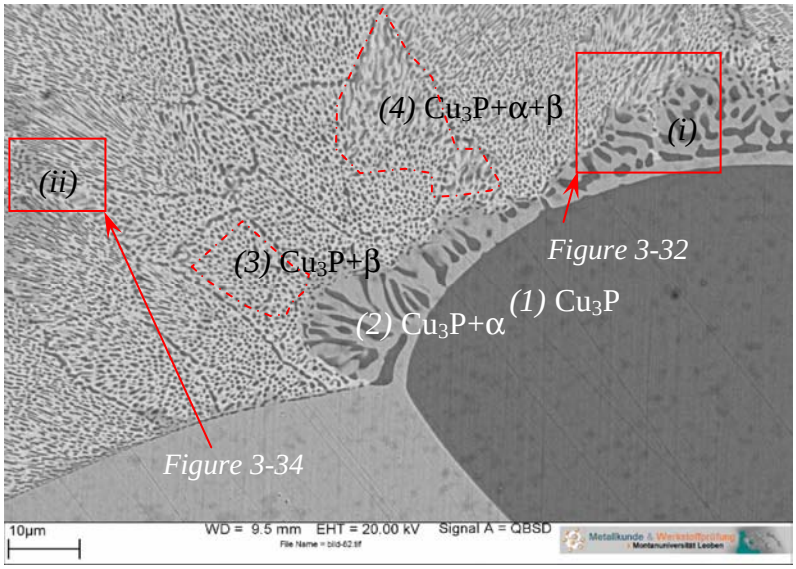

Figure 3-31: SEM picture of the annealed sample at T_a = 648 °C, t_a = 6 days of the red window (i) shown in Figure 3-30 with a higher magnification. (1) indicates Cu_3P (dark gray), (2) the two phase region of α-Cu_3P (α: middle gray), (3) the two phase region of β-Cu_3P (β: bright gray), and (4) the three phase region of α-β-Cu_3P.

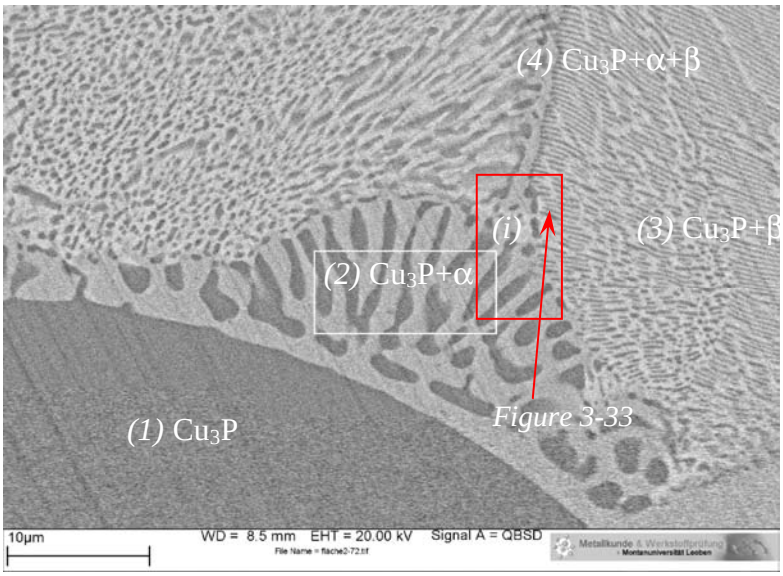

Figure 3-32: SEM picture of the annealed sample at T_a = 648 °C, t_a = 6 days of the red window (i) in Figure 3-31 with a higher magnification. (1) marks Cu_3P (dark gray), (2) the two phase region of α-Cu_3P (α: middle gray), (3) the two phase region of β-Cu_3P (β: bright gray), and (4) the three phase region of α-β-Cu_3P.

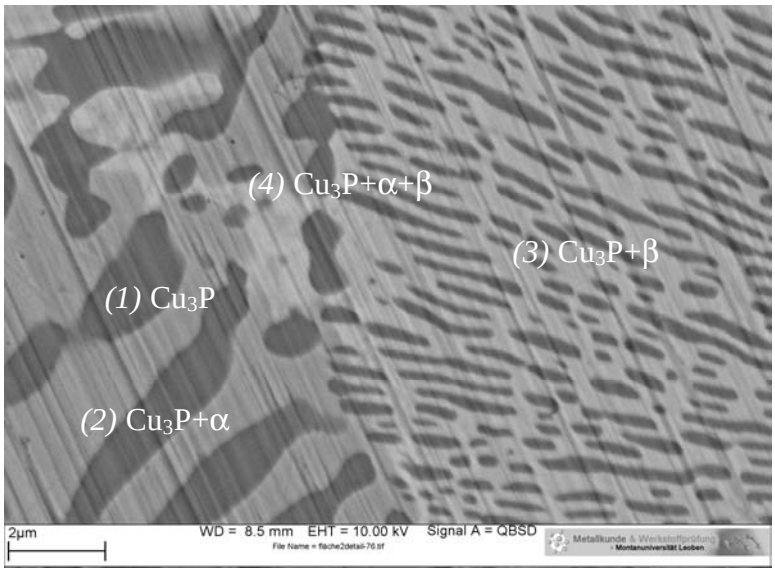

Figure 3-33: SEM picture of the annealed sample at T_a = 648 °C, t_a = 6 days of the red window (i) in Figure 3-32 with a higher magnification. (1) assigns Cu_3P (dark gray), (2) the two phase region of α-Cu_3P (α: middle gray), (3) the two phase region of β-Cu_3P (β: bright gray), and (4) the three phase region of α-β-Cu_3P.

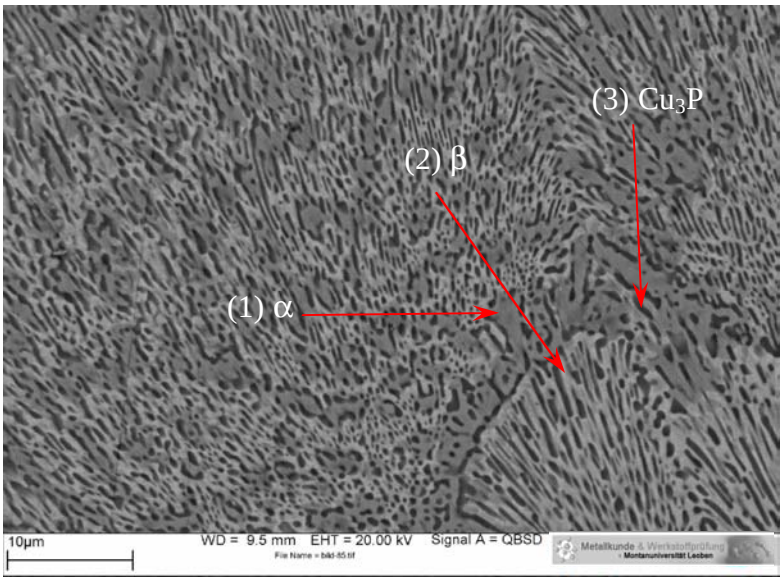

Figure 3-34: SEM picture of the annealed sample at T_a = 648 °C for t_a = 6 days of the red window (ii) displayed in Figure 3-31 with a higher magnification. The three phase region consists of approximately (1) 30 vol.% α (middle gray), (2) 35 vol.% β (bright gray), and (3) 35 vol.% Cu_3P (dark gray). The detected average concentration of this area is 14.7 wt.% Sn and 4.6 wt.% P. Both, observed volume fraction and phase concentrations show good agreement with the phase diagram as displayed in Figure 3-47 (page 60).

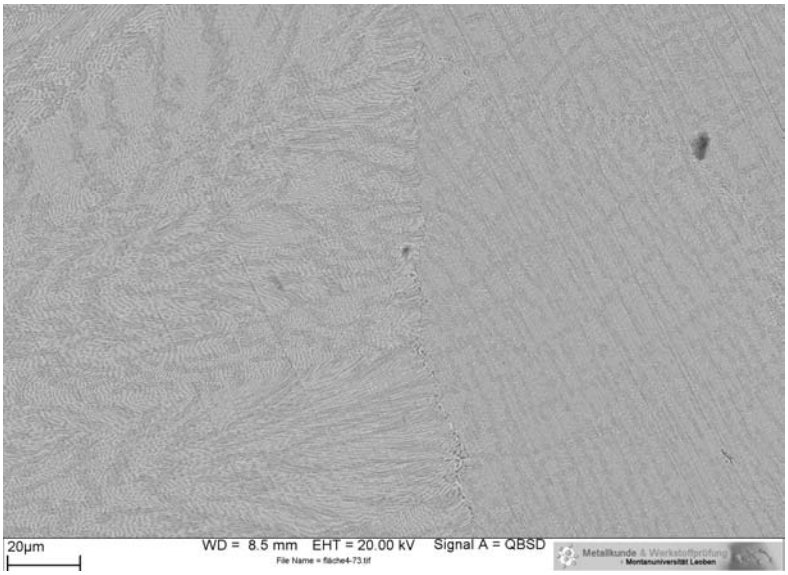

Figure 3-35: SEM picture of the annealed sample T_a = 648 °C for t_a = 6 days of the red window in Figure 3-27 (iv) with a higher magnification. It shows fine ternary eutectics in the center of the diffusion sample. This three phase region consists of about 25 vol.% α (middle gray), 45 vol.% β (bright gray), and 30 vol.% Cu_3P (dark gray). The detected average concentration in this area is 16.5 wt.% Sn and 4.4 wt.% P. Both, observed volume fraction and phase concentrations show good agreement with the phase diagram as displayed in Figure 3-47 (page 60).

(ii) Diffusion: T_a = 644 °C, t_a = 6 days

Figure 3-36 shows a micrograph of the sample annealed at T_a = 644 °C for t_a = 20 days, whereas *Figure 3-37* and *Figure 3-38* display SEM pictures of the same sample. Diffusion of Sn can be obtained in *Figure 3-36* up to ~300-350 µm *(3)* by the color change in the Cu tube *(1)*. The diffusion interface between the ternary sample (inner cylinder, *(2)*) and the Cu outer tube has pores *(I)* which seem to collect Cu_3P and are therefore enriched in P (up to 7 wt.% P) but depleated in Sn (~6 wt.% Sn). Attached to the interface a two phase region of Cu_3P-α is observed. The boundary between the two phase region and the attached three phase region is not very clear defined but indicated by the white broken line in *Figure 3-36*. It is thought that the Sn depletion at the interface region between Cu and CuSn20P6 leads to the presence of the two phase region α-Cu_3P according to the phase diagram. *Figure 3-37* displays the red window *(i)* in *Figure 3-36* where the three phase region α-β-Cu_3P (Cu_3P (dark gray, *(1)*), α (middle gray, *(2)*), β (bright gray, *(3)*)) appears. Adjacent to this, a second two phase region, namely β-Cu_3P is obtained. Here about 55 vol.% β (bright gray) and 45 vol.% Cu_3P (dark gray) are observed. The detected concentrations of the appearing phases confirm the previous measurments. The average concentration in the center of the sample is 15.5 wt.% Sn and 5.6 wt.% P.

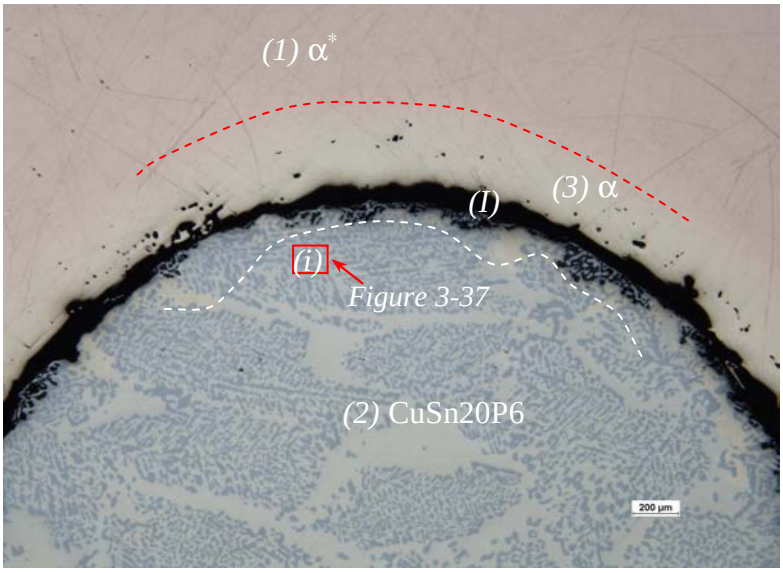

Figure 3-36: Micrograph of the annealed sample at T_a = 644 °C, t_a = 20 days. The brown region at the top is the Cu tube (α (1)) and the gray/brown region at the bottom the ternary sample CuSn20P6, where a two phase region of Cu_3P-β is visible (2). Sn diffusion occurs at the boundary into the Cu tube up to a depth of ~300-350 µm. The red broken line indicates the Sn diffusion into the outer tube whereas the white broken line marks the depletion zone of Sn in the ternary sample. The boundary between the two samples still shows pores (I).*

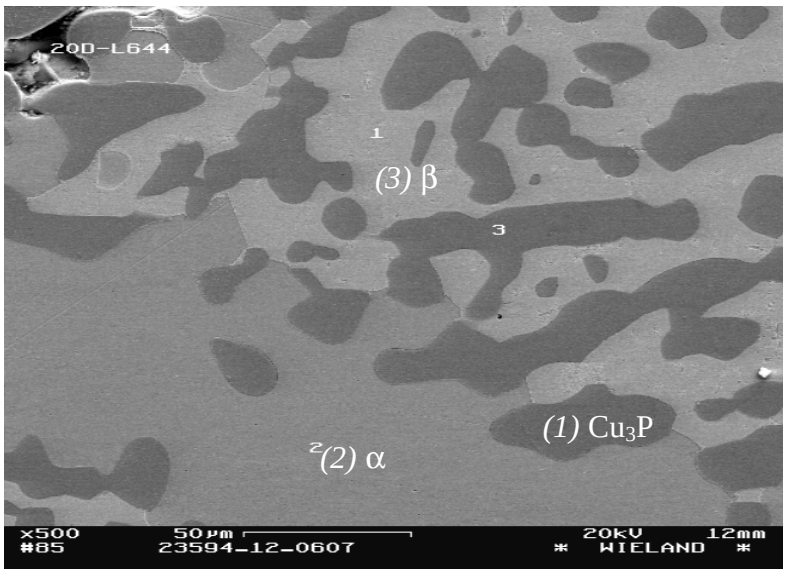

Figure 3-37: SEM picture of the diffusion sample at T_a = 644 °C for t_a = 20 days of the red window (i) in Figure 3-36 with a higher magnification. The observed three phase region consists of (1) Cu_3P (dark gray), (2) α (middle gray), and (3) β (bright gray).

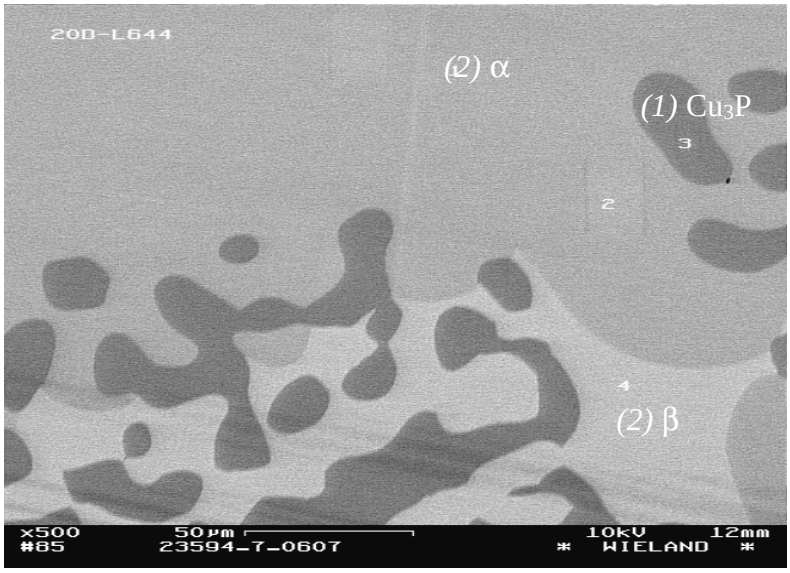

Figure 3-38: SEM picture of the diffusion sample annealed at T_a = 644 °C for t_a = 20 days. The Sn depleted region as shown in Figure 3-37 is displayed with a higher magnification. The three phase region ((1) Cu_3P (dark gray), (2) α (middle gray), and (3) β (bright gray)) is observed.

(iii) Diffusion: T_a = 642 °C, t_a = 6 days

Figure 3-39 shows an overview of the annealing sample T_a = 642 °C and t_a = 20 days whereas *Figure 3-40* and *Figure 3-41* allow a look at the microstruture at two different magnifications. *Figure 3-42* displays a SEM picture of a region attached to one Cu_3P "grain" at higher magnification (red window in *Figure 3-41*).

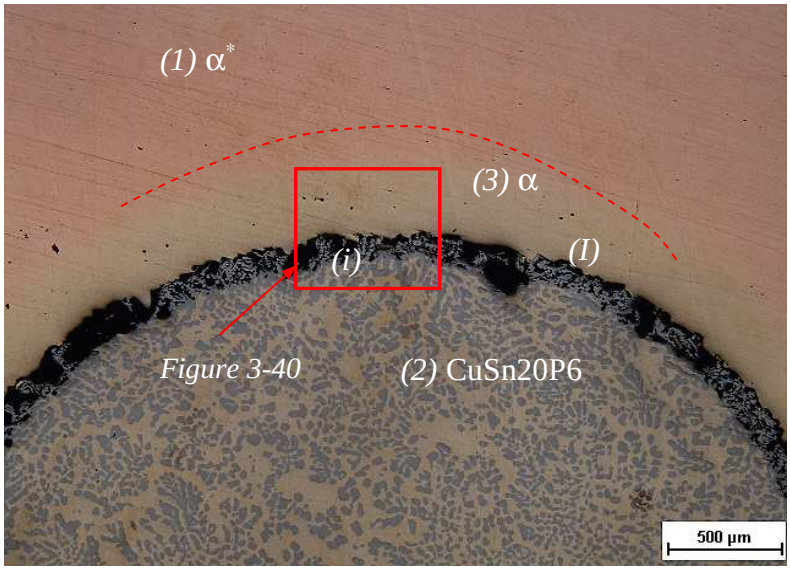

Figure 3-39: Micrograph of the diffusion sample annealed at T_a = 642 °C for t_a = 20 days. (1) shows the Cu (= α) sample, and (2) the ternary sample CuSn20P6. (3) indicates the one phase region α where Sn diffusion is observed up to ~350-400 µm into the outer tube. (I) shows the position of the pores at the boundary between the two samples. The red broken line shows the depth of Sn diffusion into the outer tube.*

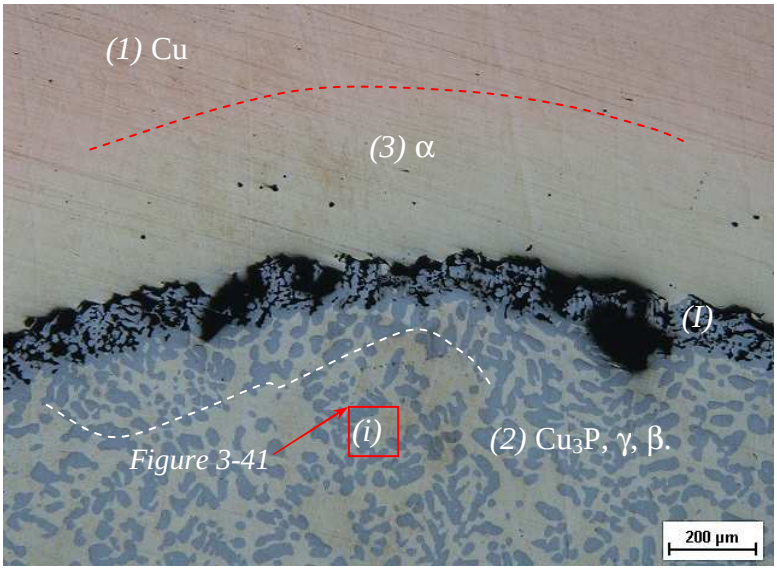

Figure 3-40: Micrograph of the diffusion sample annealed at T_a = 642 °C for t_a = 20 days of the red window shown in Figure 3-39. (1) indicates pure Cu, and (2) the ternary sample CuSn20P6, where the gray phase is Cu_3P and the brown matrix consists of γ and β. (3) shows the α region where Sn diffusion is observed into the outer tube. (I) indicates the position of the pores at the boundary between the two samples. The red broken line shows the depth of Sn diffusion into the outer tube whereas the white broken line indicates the depletion of Sn in the ternary sample.

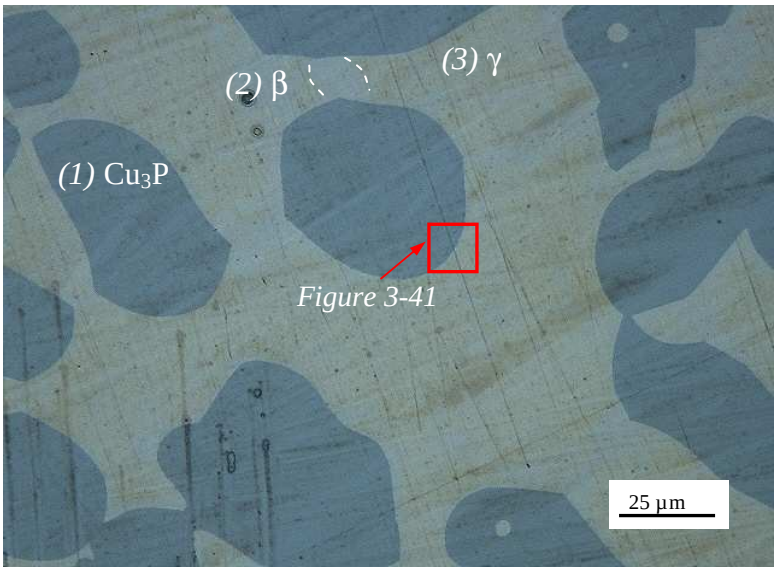

Figure 3-41: Micrograph of the diffusion sample, annealed at T_a = 642 °C for t_a = 20 days as indicated by the red window in Figure 3-40 (i). (1) marks Cu_3P(dark gray), (2) β (bright brown, between the white broken lines), and (3) γ(brown) in the ternary cylinder.

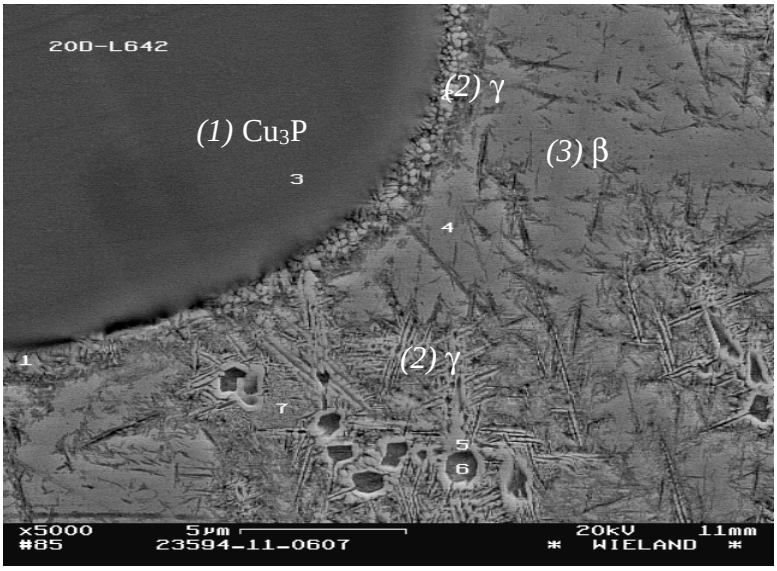

Figure 3-42: SEM picture of the diffusion sample annealed at T_a = 642 °C for t_a = 20 days indicated by the red window in Figure 3-41. Here a complex microstructure is visible after etching. (1) marks a Cu_3P corn at the left hand side of the picture, (2) γ, which shows a "needle" structure, and (3) β, which appears to be a little bit darker color than γ. The small numbers 1-7 show the position of the different measurement points as described [GRUBER 07B]. Measurement point 6 is located in a deeper etched area, shows relative low Sn content and appears with that darker.

The upper part of the picture in *Figure 3-39* is the Cu tube *(1)* where the lower part is the inner CuSn20P6 cylinder *(2)*. The brighter region attached to the inner cylinder can be identified as the diffusion area of Sn into Cu *(1)*. Here α *(3)* occurs and Sn is observed to a depth of ~350-400 µm of the Cu tube (indicated by the red broken line). According to the phase diagram the sample should not melt during annealing. The micrograph in *Figure 3-41* shows fine deviations in the color of the matrix between the Cu_3P grains which allows to differetiate between slightly brighter regions *(2)* and slightly darker ones *(3)*.

The SEM picture (the sample was etched, *Figure 3-42*) illustrates the complex microstructure of this sample. Here the gray scale difference, as well as the structure of the different phases is strengthened by etching. The Cu_3P corn (*Figure 3-42 (1)*) is visible at the left hand side of the picture. Attached to it, a region with 25.5 wt.% Sn and 0.7 wt.% P (*Figure 3-42 (2)*) can be seen. According to literature [EFFENBERG 07, MIETTINEN 01] this could be γ which shows a needle-like structure. The region marked with *(3)* is a little bit darker and has more or less a uniform matrix. It has a slightly lower concentration, that is 24 wt.% Sn and 0.5 wt.% P *(3)*, than the surrounding regions. The detected phase concentrations of this sample are in the same range as already measured. The average concentration in the center of the sample is 14.2 wt% Sn and 6.2 wt.% P, where the observed phase fractions of the three phases are γ 20 % (bright gray), β 25 % (bright gray), Cu_3P 45 % (dark gray).

3.3 Discussion

3.3.1 Comparison of the Calculated Phase Diagrams with Literature

Based on literature [MIETTINEN 01, THERMOCALC 03] the numerical Cu-Sn-P database CuSn1 was implemented by Thermo-Calc [THERMOCALC 03]. This database, in combination with the software Thermo-Calc, is used in the presented work for the numerical description of the system and with that for the comparison of published phase diagrams with the calculated ones as already shown in *Figure 3-3*, *Figure 3-4*, *Figure 3-9*, *Figure 3-10*, and *Figure 3-12*. The calculated phase diagrams are simplified for phase δ, ε and ξ in the Cu-Sn system by handling these phases as compounds (*Figure 3-9*). Besides, the calculations performed with Thermo-Calc show good agreement with the published phase diagrams but the liquidus line of L-α is slightly lower in the calculated ones in comparison to the published ones according to [MASSALSKY 86] (*Figure 3-3*, *Figure 3-4*). However, the phase transformation temperatures are almost the same in the published and the calculated diagrams. *Figure 3-12* presents the vertical section (isopleth) 5 wt.% P calculated with the database CuSn1. The isopleth shows, as expected, good agreement with the published phase distribution of [MIETTINEN 01] (*Figure 3-43*).

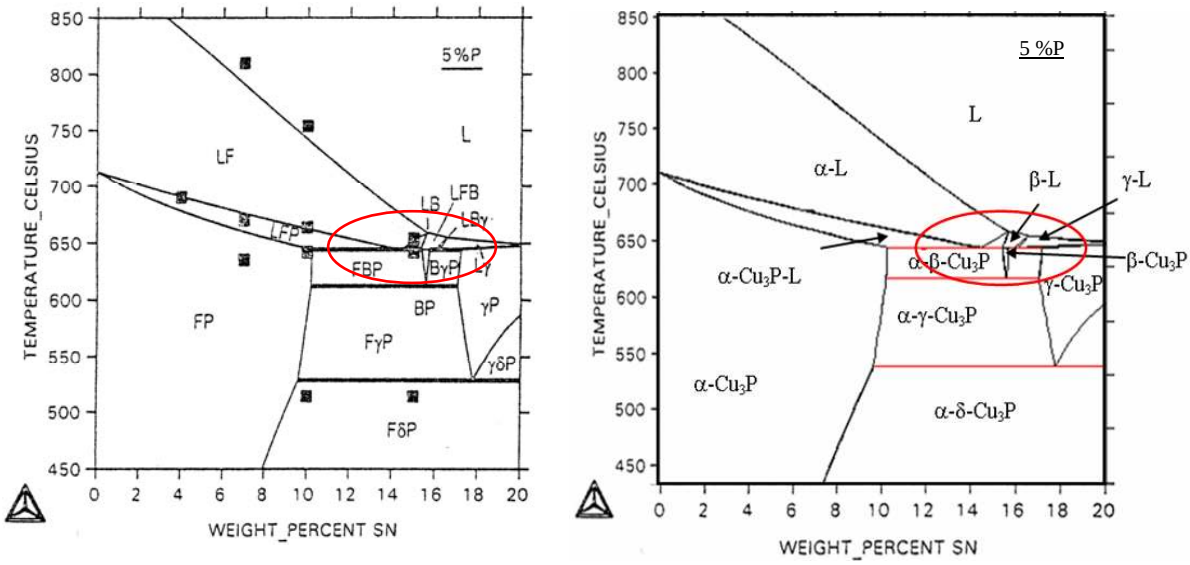

(a) *(b)*

Figure 3-43: (a)) Vertical section of the ternary phase diagram Cu-Sn-P at 5 wt.% P (isopleth) based on the numerical assessment work performed by [MIETTINEN 01]. The displayed dark small squares show DTA measurements [TAKEMOTO 87] and the lines show the calculated phase diagram (F = α, P = Cu_3P, B = β) [MIETTINEN 01]. (b)Vertical section (isopleth) of the ternary phase diagram Cu-Sn-P at 5 wt.% P calculated with Thermo-Calc (database CuSn1). It is possible to reproduce the published isopleth of [MIETTINEN 01]. Red circles indicate the position around the ternary eutectic point of the system. The calculated isopleth shows good agreement with the published one of [MIETTINEN 01].

Although the γ phase is taken into account in published binary Cu-Sn phase diagrams, the experiments performed by [TAKEMOTO 87] did not show the presence of γ and ε. However, [MIETTINEN 01] includes the γ phase in his assessment work for the ternary phase diagram. γ is thought to establish based on a kind of a martensitic transi-

tion out of β [DIES 67, SCHUMANN 90]. The absence of this phase in the experimental observations of [TAKEMOTO 87] could have several reasons. Besides experimental performance, a reason for missing of the γ phase could be explained by very rapid transition which unabled a detection after the DTA measurements by SEM or by the low concentration difference between β and γ [EFFENBERG 07]. ε was not detected in the experimental work. This could be explained by the fact that according to literature [DIES 67, SEITH 55, SCHUMANN 90] ε is thought to establish after very long diffusion times in the order of months or years. This might be a sufficient reason to ignore this phase for the estimation of phase distributions during continuous casting of bronze.

It has to be stated that the calculations performed with Thermo-Calc by using the database CuSn1 show problems in the area of the ternary eutectic point and some of the three phase regions including ξ and ε. Here, two phase regions are labeled in regions, where according to "Gibbs phase rule", a three phase region is expected. This was observed in the proposed three phase regions (i) Cu_3P-ε-ξ (pink triangle) and (ii) Cu_3P-δ-ε (yellow triangle) (see *Figure 3-10*). However, the present implementation shows good agreement with the published results of [MIETTINEN 01] in the region of interest for solidification simulation of bronze alloys.

3.3.2 Discussion of the DSC Measurements

The analysis of the DSC measurements shows temperature differences as listed in *Table 5* and *Table 6* in column ΔT_{min}. ΔT_{min} is defined by the minimum temperature difference observed by taking the measured DSC value minus the appropriate value from literature or Thermo-Calc. The phase transformations for all different phases of the binary phase diagram CuSn have been observed except of the one of ε.

	DSC	MASS.86	ΔT_{min}		DSC	MASS.86	ΔT_{min}
CuSn4	**3.6 wt.% Sn**			**CuP2**	**2 wt.% P**		
T_l	1059 °C	1062 °C	-3	T_l	1034 °C	1030 °C	+4
T_s	956 °C	960 °C	-4	T_s	709 °C	714 °C	-5
T_ε		260 °C					
CuSn20	**19.7 wt.% Sn**			**CuP5**	**5.4 wt.% P**		
T_l	898 - 905 °C	906 °C	-1	T_l	922 - 928 °C	907 °C	+15
T_β	793 - 795 °C	799 °C	-4	T_s	709 °C	714 °C	-5
T_γ	576 - 577 °C	588 °C	-11				
T_δ	518 - 522 °C	520 °C	+/-2				
T_ε		350 °C					

Table 5: Comparison of the measured DSC phase transformation temperatures and the expected temperatures after [MASSALSKY 86]. T_l: liquidus temperature, T_s: solidus temperature, T_β ,T_γ, T_δ and T_ε: phase transformation temperatures. $\Delta T_{min} = T_{DSC} - T_{Massalsky}$.

	DSC	TC	ΔT_{min}		DSC	TC	ΔT_{min}
CuSn4	**3.6 wt.% Sn**			**CuP2**	**2 wt.% P**		
T_l	1059 °C	1060 °C	-4	T_l	1034 °C	1030 °C	+4
T_s	956 °C	941 °C	+5	T_s	709 °C	715 °C	-5
T_ε		481 °C					
CuSn20	**19.7 wt.% Sn**			**CuP5**	**5.4 wt.% P**		
T_l	898 - 905 °C	878 °C	+20	T_l	922 - 928°C	874 °C	+48
T_β	793 - 795 °C	798 °C	-3	T_s	709 °C	715 °C	-5
T_γ	576 - 577 °C	582 °C	-5				
T_δ	518 - 522 °C	520 °C	+/-2				
T_ε		330 °C					

Table 6: Comparison of the measured DSC phase transformation temperatures and the expected temperatures based on calculations with Thermo-Calc (TC), database CuSn1. T_l: liquidus temperature, T_s: solidus temperature, T_β ,T_γ, $T_\delta$and T_ε: phase transformation temperatures. $\Delta T_{min} = T_{DSC} - T_{TC.}$

Although, the SEM investigations of the DSC samples have been performed with EDS and are therefore semi-quantitative, both, measured concentrations and phase distribution, generally agree with literature [MASSALSKY 86] and thermodynamic calculations with Thermo-Calc**.** Generally, it can be stated that the deviations lie within an acceptable range according to the expected measurement accuracy, based on the fact that in literature for example the melting point of pure Cu lies within a certain accuracy of values between T = 1083.5 °C and T = 1085 °C. There are four measurement points that show big deviations: T_γ for CuSn20 and T_l for CuP5 in the comparison with [MASSALSKY 86] and T_l for CuSn20 and CuP5 in comparison to calcuations with Thermo-Calc. Here, it has to be mentioned, that the two temperatures that show deviations from [MASSASKY 86] show rather small peaks. As also mentioned in literature the transformation between β and γ is difficult to obtain. Having this in mind, the deviations are,

still, in an acceptable range. And according to the calculations with Thermo-Calc, there seems to be a certain error in the calculation of the liquidus curve in both binary diagrams. However, due to the fact that the numerical study will not have very high Sn or P contents, this error can be accepted for the recent study.

It was not possible to detect the Sn rich ε phase by SEM or DSC investigations. It is known from literature [STEUDEL 60] that ε needs more time to form than the other phases (up to weeks or months). Therefore, the limited heating rate in the DSC measurements could be one reason for its absence.

3.3.3 Discussion of the Diffusion Experiments

Binary Diffusion Experiments

For the binary diffusion experiments, the detected concentrations as reported in chapter 3.2.2 show good agreement with published values [MASSALSKY 86]. Slightly higher average concentration of P in the diffusion sample in comparison to the reference sample was obtained. But due to the rigidity, the preparation of the samples with high P content is difficult and the casted alloy is rather inhomogenuous. This has to be kept in mind when comparing the reference sample and the annealed sample.

Figure 3-44: Concentration measurements in the binary diffusion sample for Sn (brown) and P (blue) at the diffusion interface. The Sn concentration shows a smooth distribution whereas the P concentration has big jumps. The red broken lines correlate the depth of diffusion according the SEM investigations with the observed microscopic structure change in this area.

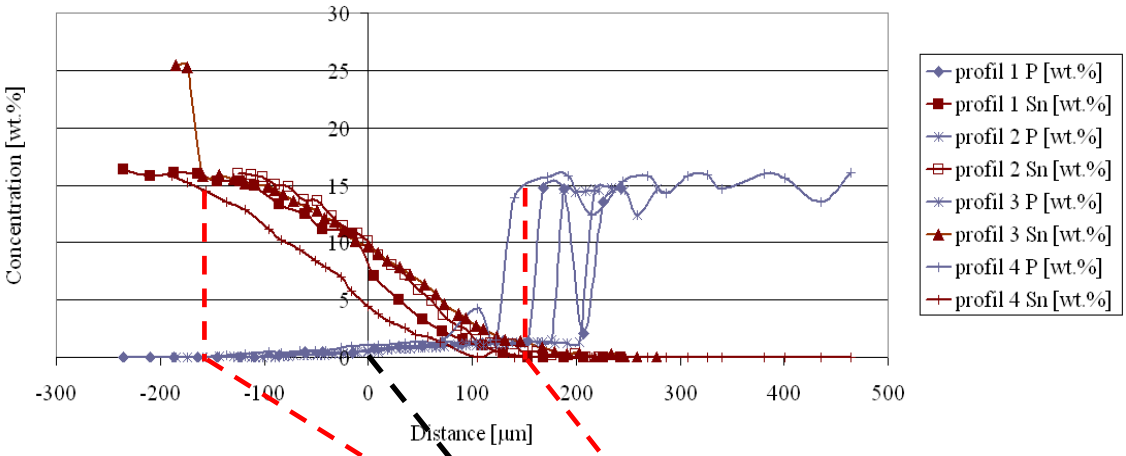

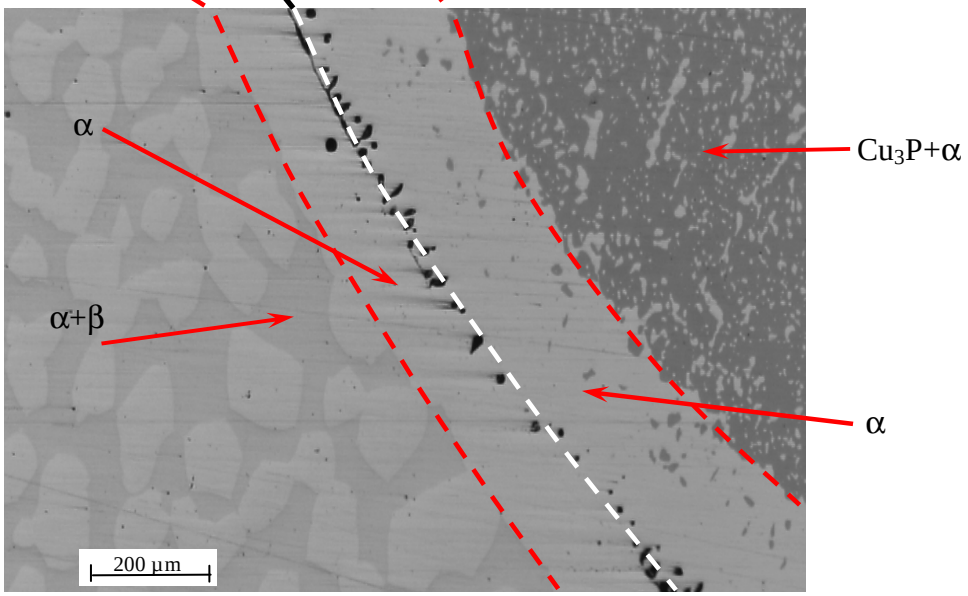

Figure 3-45: Micrograph of the binary diffusion sample in the diffusion area. The red broken lines mark the boundaries between the two and one phase regions whereas the white broken line indicates the expected boundary between the diffusion partners.

Figure 3-44 displays the concentration distribution along four measured profiles starting in the CuSn20 sample, crossing the boundary of the two diffusion partners, and ending in the CuP8.3 sample. *Figure 3-45* shows a micrograph of the diffusion sample in the

diffusion area. The two red broken lines mark the boundaries between the two and one phase regions whereas the white broken line assigns the boundary between the two diffusion partners in the miroscopic picture. These lines are used to visualize the location of the profiles displayed in *Figure 3-44* relative to the sample.

As shown in *Figure 3-45* the samples are connected at the interface although a certain amount of pores is still present after annealing. The jumps in the detected concentrations in both, the CuSn and CuP sample, are caused by the fact that the measurement series has been performed as point measurement and therefore sometimes the Sn and P rich phases themselves are detected. The low P content detected in α corresponds to its solibilty according to the shown phase diagrams. It seems that this low solubility slows the diffusion of P down towards the boundary and leads to diffusion towards the centre of the CuP sample where more Cu_3P is built. Here higher P concentrations are detected (up to 14 wt. % in the measured profile) in comparison to the reference sample.

Based on the SEM measurements rough diffusion coefficients can be estimated for the temperature of 648 °C according to the measured profiles for Sn in the α region with about $D_{Sn\alpha} \sim 10^{-13}$ $m^2 \cdot s^{-1}$ and for P in the α region with about $D_{P\alpha} \sim 3 \cdot 10^{-14}$ $m^2 \cdot s^{-1}$. The value observed for Sn lies in a range as proposed by literature for binary CuSn diffusion. Since for P just a diffusion coefficient for impurities is available in literature, no comparison is possible for the diffusion in Cu with 8.3 wt.% P.

Ternary Diffusion Experiments

The ternary eutectic point of the Cu-Sn-P system is of major interest and therefore the presented experimental work was performed. Calculations with Thermo-Calc proposed the ternary eutectic point at T_E = 644.1 °C. After [EFFENBERG 07] the range of the transformation temperature for a reaction of L+α→β+Cu_3P is from 642 °C to 655 °C which demonstrates that a ternary eutectic reaction is not expected based on published work, therefore diffusion experiments were performed at 648 °C, 644 °C, and 642 °C with a CuSn20P6 alloy.

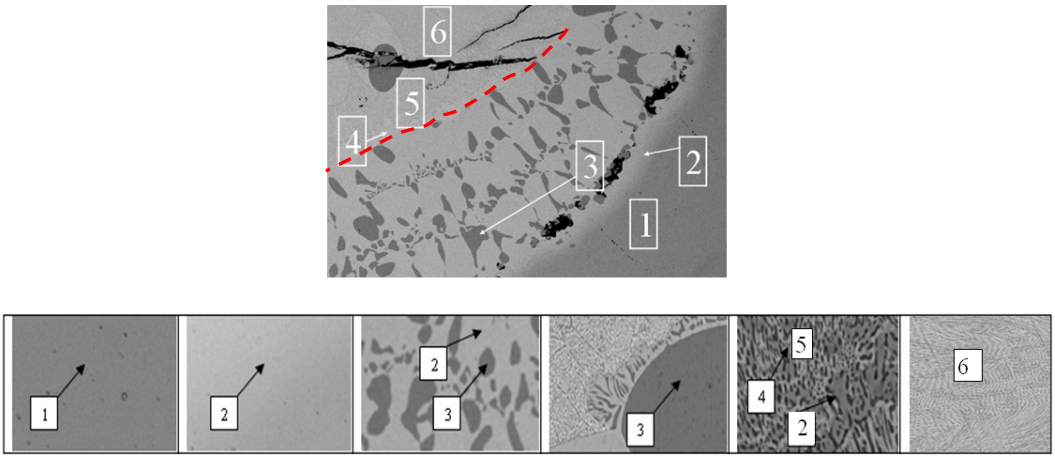

Figure 3-46: The upper picture shows a SEM picture of the diffusion sample at 648 °C. The numbers indictate the position of the different phase regions displayed in the phase sequence at the bottom of the figure. The observed phases are: (1) Cu, (2) α, (3) Cu_3P, (4) β. (5) indicate the three phase region (CuSn14.7P4.6), and (6) the three phase region (CuSn16.5P4.4) (modified after [PANZL 08]). The red broken line marks the expected boundary of the liquid region.

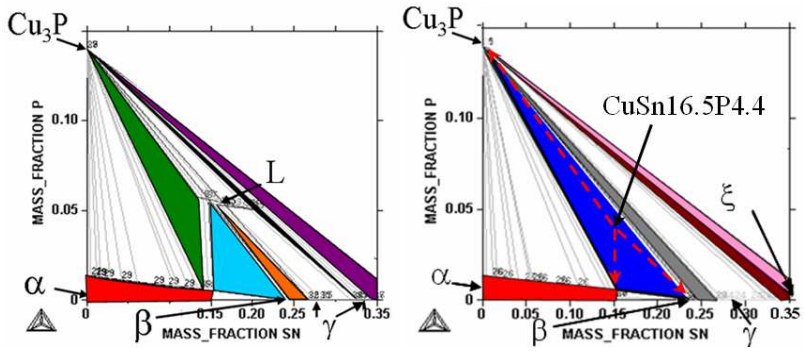

Figure 3-47: Isothermal sections of the Cu rich corner of the Cu-Sn-P system are displayed at a) T_a = 648 °C and b) T = 640 °C. The red broken arrows indicate the expected concentration of the remaining solidifying liquid (measured 16.5 wt.% Sn and 4.4 wt.% P in the center of the annealed sample). The isothermal sections are calculated with Thermo-Calc.

The first sample was annealed at 648 °C for 6 days to ensure that liquid forms. After annealing it was quenched in cold water and prepared for the SEM measurements. *Figure 3-46* shows an overview of the observed phase distribution described in chapter 3.2.3. *Figure 3-47* shows two isothermal sections, one at 648 °C and one at 640 °C.

It can be seen that the calculatios with Thermo-Calc propose a liquid region at 648 °C near the applied sample concentrations. The isothermal section at 640 °C is taken just below the expected ternary eutectic point to gain information about the expected concentrations and phase fractions of the solidified liquid.

It appears that the actually observed phase distribution of the sample is caused by a solidification sequence during the 6 days of annealing as described in the following.

The outer Cu tube has a melting temperature of T_{lCu} = 1084°C and is therefore expected to stay solid during annealing (*Figure 3-48a (1)*). The ternary alloy CuSn20P6 of the inner cylinder (*Figure 3-48a (2)*) consists of δ-Cu_3P and Cu_3P and lies at the applied annealing temperature within the two phase region Cu_3P and liquid (*Figure 3-48b (3)*). Therefore Cu_3P is not expected to melt during annealing. However, the dendritic shape of Cu_3P observed in the unnealed sample is not conserved after the heat treatment (*Figure 3-22*). Sn and P are detected in the Cu tube close to the boundary to the ternary diffusion partner (*Figure 3-48b (1)*). This leads to the formation of α with a Sn content up to 15 wt.% Sn and a P content of up to 2 wt.% P (*Figure 3-48b (2)*).

Due to the diffusion of Sn and P out of the ternary inner cylinder into the outer Cu tube, a lack of Sn and P develops at the solid-liquid interface of the inner sample (*(2)-(3)* interface in *(b)*). This leads to an increase in liquid temperature and therefore α is expected to grow at this interface (*Figure 3-48c (1)*). As the concentration of the two phase region in thermodynamic equilibrium is reached, Cu_3P stays in equilibrium with α (*Figure 3-48c (2)*).

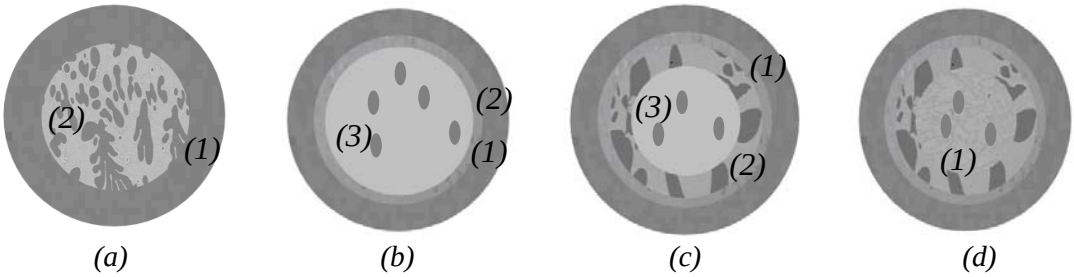

Figure 3-48: Schematical drawing of the diffusion and melting/solidification sequence of the annealed sample. (a) displays the diffusion sample before annealing. (b) The solid Cu shell shows diffusion of Sn and P (2). In the inner cylinder CuSn20P6 (3) a two phase region is expected at T_a = 648 °C where Cu_3P and liquid L is in equilibrium. (c) marks the expected diffusion of Sn and P out of the ternary inner cylinder into the outer Cu cylinder (1) which induces a decrease of Sn and P at the solid-liquid interface and leads to an increase in liquid temperature. α and Cu_3P grow as soon as the necessary concentration for the two phase region of thermodynamic equilibrium is reached (2). In the center the liquid is depleted in Sn and P but still liquid. (d) Quenching leads to rapid solidification of the liquid and ternary eutectic (α, β, Cu_3P) is formed.

Another feature could have happened due to density differences in the mush. Since Cu_3P has a lower density than the surrounding P poor liquid (*Figure 3-48b (3)*), it moved upwards in the sample. This could be one process that led to the observed Cu_3P enrichment at the bottom of *Figure 3-27* (the sample is displayed upside down). Additionally, as quenching took place, it is possible that the liquid itself got stirred by the process of taking the sample out of the stove and putting it into cold water. At the solid and liquid interface, solidification started very rapidly during quenching which led to a fine imbedding of Cu_3P at the grain boundaries of α. *Figure 3-32* (*Figure 3-49a)* display for example one Cu_3P droplet which is surrounded by a two phase eutectic region (Cu_3P and α, white rectangle) on the upper side. This could show that thermodynamics tried to balance the concentration at the boundary of the Cu_3P droplet. In addition, a three phase region with not clearly defined boundaries is occurring close to it. Attached to it, a second two phase region with eutectic structure of Cu_3P and β is observed (*Figure 3-49a,* red rectangle). Those examples indicate that the liquid was cooled rapidly and therefore the thermodynamic equilibrium was not reached. The three phase regions in *Figure 3-34* (*Figure 3-49b)* and *Figure 3-35* (*Figure 3-49c)* show a rather fine distribution which is thought to be caused by the fast solidification during quenching (*Figure 3-48d, (1)*). The observed average concentration of the three phase region in the center of the sample should show the concentration of the liquid just before solidification (*Figure 3-47a*, *Figure 3-47b*).

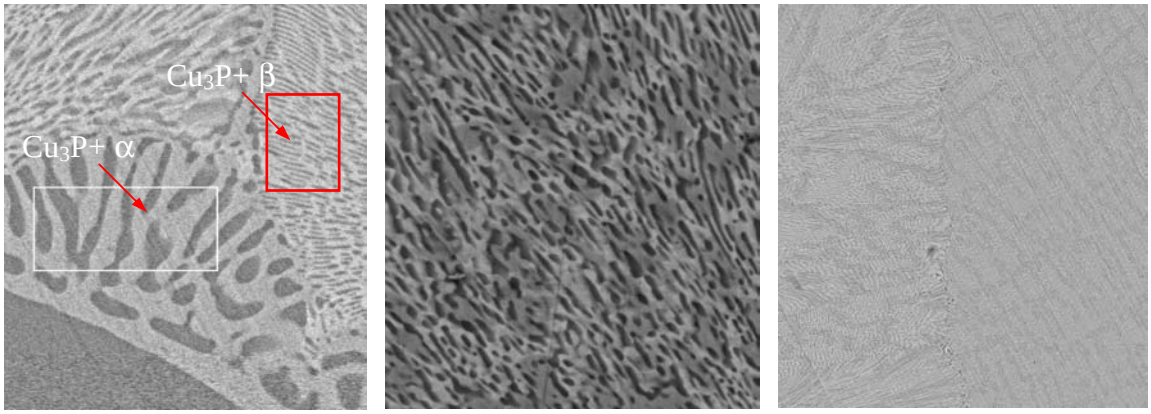

(a) *(b)* (c)

Figure 3-49: (a) shows a detail of Figure 3-32, (b) of Figure 3-34. Here Sn depletet melt at the solid liquid interface is expected. Occruing phases: α, β, Cu_3P. (c) shows a detail of of Figure 3-35 where a higher Sn content than in the area displayed in (b) is observed. This region lies in the center of the sample. Occruing phases: α, β, Cu_3P. White rectangle: two phase region Cu_3P+α, red rectangle: two phase region Cu_3P+ β.

Figure 3-50 shows the isothermal section at T = 640 °C. The green labels are the detected concentrations and phase distributions for the two and three phase regions of the annealed sample at T_a = *648 °C*, whereas the red labels are the detected concentrations of the one phase regions. The observed phase distributions agree with the proposed by computational thermodynamics. The P content in the two and three phase regions lies around 4.5 wt.% whereas the Sn content varies between 10 to 17 wt.% Sn. The measured concentration in the center of the sample is shown in *Figure 3-51* (blue dot) in the isopleth calculation at 4.4 wt.% P with database CuSn1. The expected concentrations of the phases at the ternary eutectic point are, according to the phase diagram information, 15 wt.% Sn and 0.55 wt.% P for α, 0 wt.% Sn and 14 wt.% P for Cu_3P, and 23.5 wt.%Sn for β. The measured concentrations as shown in *Figure 3-50* are, concerning the uncertainties of the detection of P with EDS/WDS of $\Delta c^P \sim \pm 0.5$ wt.%, in good agreement with the assessed data used in the database CuSn1 (see isopleth in *Figure 3-51*). Based on the fact that the sample is thought to have been liquid during annealing and with that convection has taken place, the radial element distribution does not show a radial diffusion path. In addition, the appearing phases give different diffusion conditions for the two alloying elements. Therefore, further interpretation of this diffusion experiment is not possible at the present stage.

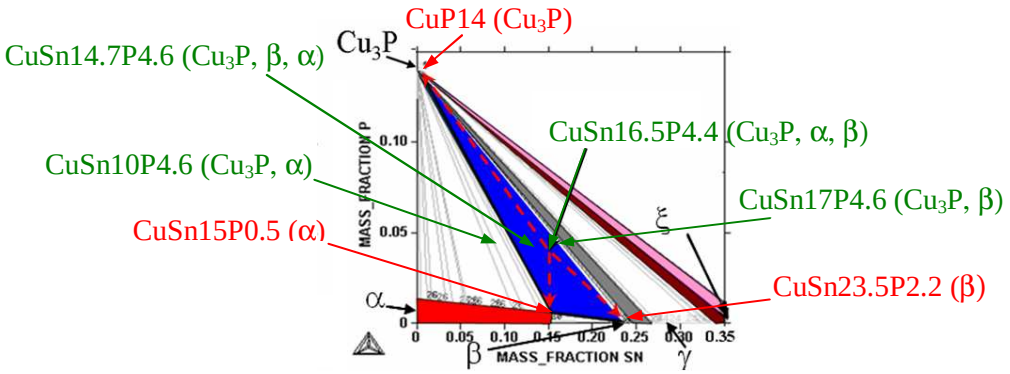

Figure 3-50: Isothermal sections of the Cu rich corner of the Cu-Sn-P system are displayed at T = 640 °C. The red broken arrows indicate the expected concentration of the remaining solidifying liquid (measured 4.4 wt.% P and 16.5 wt.% Sn in the center of the annealing sample). The isothermal section is calculated with Thermo-Calc. The black arrows show the different detected concentrations in the solidified sample T_a = 648 °C. It is visible that the P content is about the same in all of the two or three phase regions, whereas the Sn content varies significantly. Green lables show the two and three phase regions/concentrations measured by SEM, and red lables the concentration of the single phases.

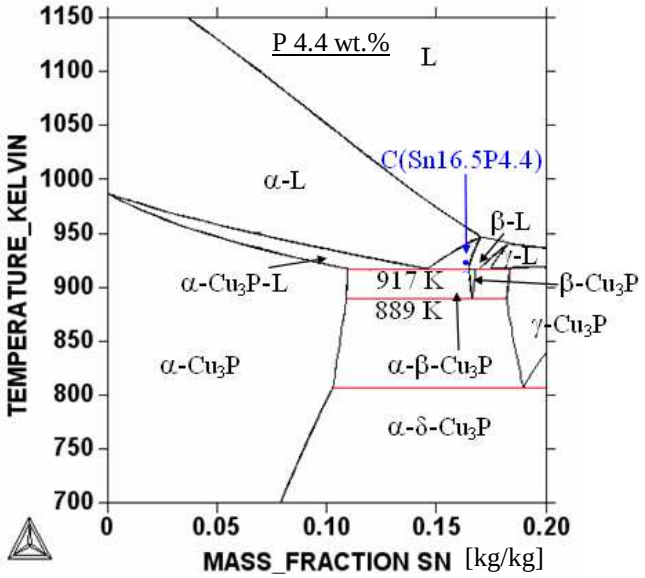

Figure 3-51: Vertical section (isopleth) of the ternary phase diagram Cu-Sn-P at 4.4 wt.% P calculated with the database CuSn1. The blue dot marks the average concentration detected in the center of the annealed sample at T_a = 648 °C for t_a = 6 days (Figure 3-27 (iv)).

The second sample was annealed at T_a = 644 °C for t_a = 6 days to go close to the eutectic temperature of the system. After annealing it was quenched in cold water and prepared for the SEM measurements. *Figure 3-52* shows an overview of the observed phase distribution as described in chapter 3.2.3. *Figure 3-52a* shows the phase distribution before annealing and *Figure 3-52b* the observed phases after quenching. A diffusion area at the sample interfaces (red broken line) is observed in the Cu tube and slightly in the inner CuSn20P6 cylinder. P is enriched in the porous area between the two sample partners. While α is formed in the outer tube, the attached Sn depleted area of the ternary diffusion partner forms a two phase region of α and Cu_3P.

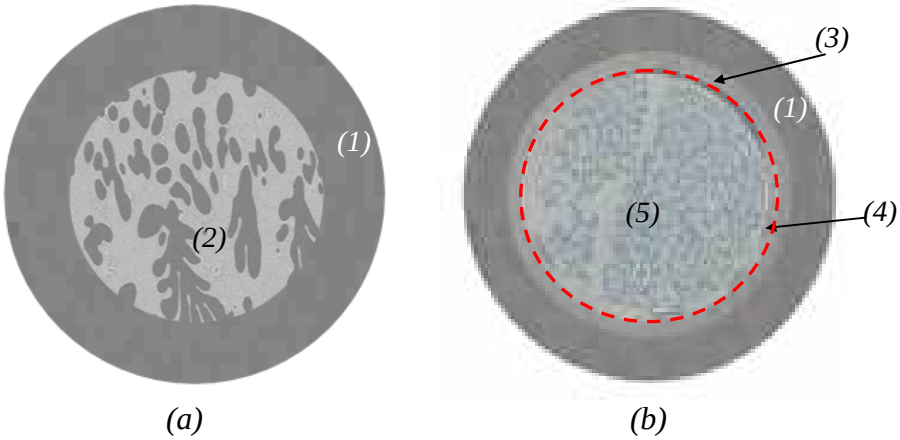

Figure 3-52: Schematical drawing of the diffusion sequence of the annealed sample at T_a = 644 °C. (a) displays the diffusion sample before annealing. Here (1) indicates the pure Cu (α^*) tube and (2) the ternary CuSn20P6 cylinder. (b) shows the sample after annealing. (1) is α^*, (3) is the diffusion area of Sn into the outer sample partner (α^*), (4) marks the small Sn depletet area in the CuSn20P6 cylinder, whereas (5) indicates the two phase region in the center of the sample. The red broken line is the porous, P rich boundary between the two diffusion partners.

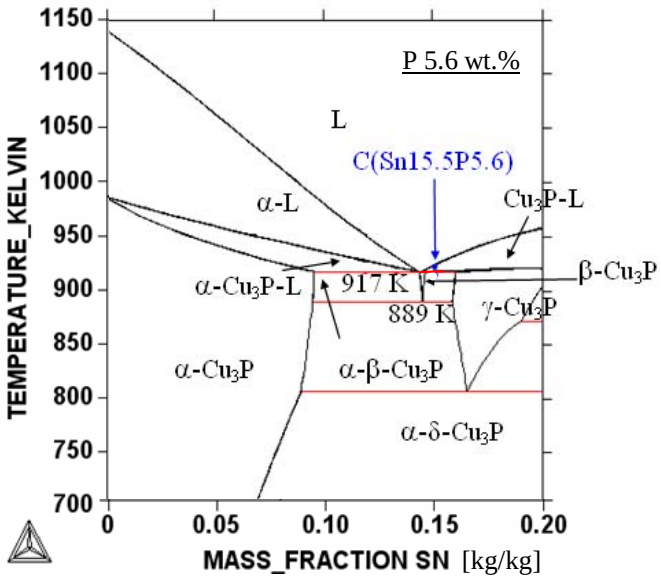

Figure 3-53: Vertical section (isopleth) of the ternary phase diagram Cu-Sn-P at 5.6 wt.% P calculated with the database CuSn1. Blue dot marks the average concentration in the center of the annealed sample at T_a = 644 °C for t_a = 6 days (Figure 3-36 (iii)).

After a small three phase region of α, β, and Cu_3P the two phase region of β and Cu_3P is observed in the center of the ternary sample. *Figure 3-53* displays the isopleth at 5.6 wt.% P to compare the measured concentration (15.5 wt.% Sn and and 5.6 wt.% P) and the phase distribution in the center of the sample with phase diagram calculations. The calculated phase diagram indicates that the concentration of the annealed sample at T_a = 644 °C lies in the two phase region Cu_3P-L. This indicates that besides the solid Cu_3P dendrites a high viscous or even almost liquid phase was present during annealing. It is thought that under this condition the diffusion of P is rather fast and with that the

present Cu_3P dendrites tend to form big dendrites. These are surrounded by β in the solid sample (see *Figure 3-38*).

According to the isothermal section, three phases should be present in this sample, but the γ phase is not observed. One reason for that could be that the sample itself is relatively inhomogenuous. The phase boundaries, at and slightly below, the ternary eutectic point lie within a small range and the calculation accuracy in this area shows some uncertainties. Therefore, a shift in concentration of the sample of about 2 wt.% Sn leads already to the absence of γ and the presence of α phase, and inbetween just β-Cu_3P is expected. The same is valid for depletion of P of about 0.05 wt.% P.

The third sample was annealed at T_a = 642 °C for t_a = 6 days. After annealing it was quenched in cold water and prepared for the SEM measurements. *Figure 3-54* shows an overview of the observed phase distribution described in chapter 3.2.3. *Figure 3-54a* shows the phase distribution before annealing and *Figure 3-54b* the observed phases after quenching. A diffusion area at the sample interfaces (red broken line) is observed in the Cu tube and in the inner cylinder. P is enriched in the porous area between the two sample partners. While α is formed in the outer tube the attached Sn depleted area of the ternary diffusion partner forms a two phase region of α and Cu_3P.

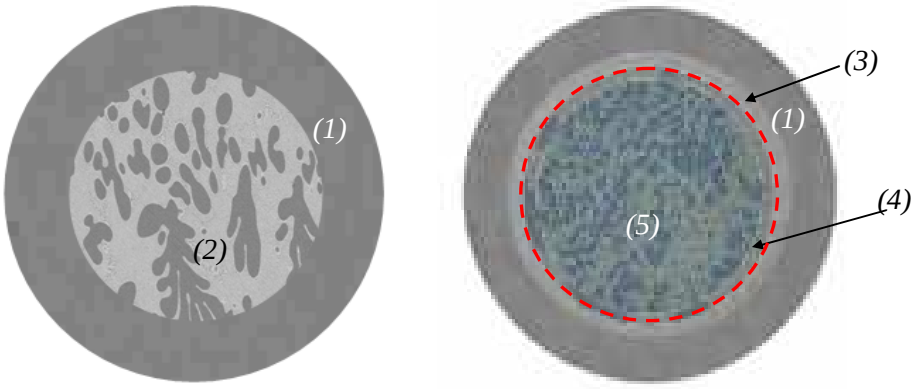

Figure 3-54: Schematical drawing of the diffusion sequence of the annealed sample at T_a = 642 °C. (a) displays the diffusion sample before annealing. Here (1) indicates the pure Cu (α^*) tube and (2) the ternary CuSn20P6 cylinder. (b) shows the sample after annealing. (1) is α^*, (3) is the diffusion area of Sn into the outer sample partner, (4) marks the small Sn depletet area in the CuSn20P6 cylinder, whereas (5) indicates the three phase region of the sample. The red broken line is the porous, P rich boundary between the diffusion partners.

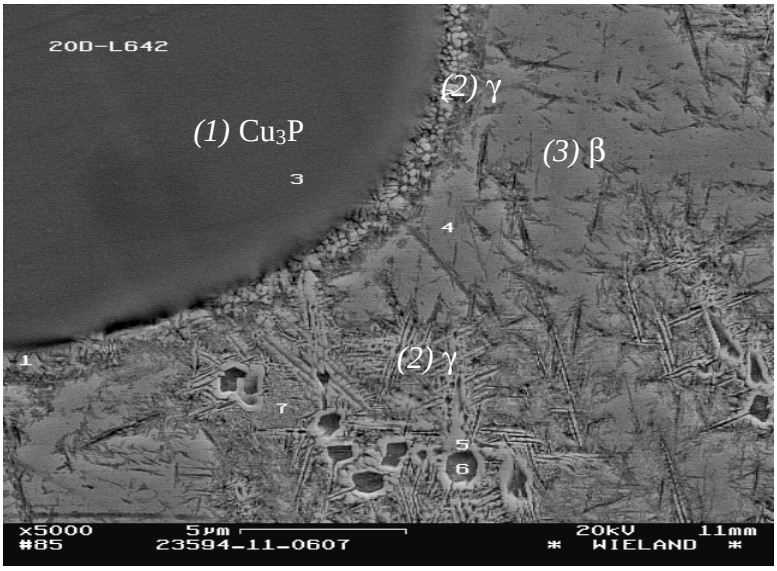

Figure 3-55: SEM picture of the diffusion sample annealed at T_a = 642 °C for t_a = 20 days as described in chapter 3.2.3. (1) marks a Cu_3P corn at the left hand side of the picture, (2) γ, which shows a "needle" structure, and (3) β, which appears to be a little bit darker color than γ. The small numbers 1-7 show the position of the different measurement points as described in [GRUBER 07B]. Measurment point 6 is located in a deeper etched area.

Attached to it, the three phase region of β, γ, and Cu_3P is observed in the ternary sample (*Figure 3-55*). The visible microstructure in *Figure 3-55* shows that β seems to transform to the needle-like γ phase, especially at grain boundarys, as for example around the Cu_3P grain. The detected concentration in point 6, which was located in a dark, and appearingly, deeper area than the surrounding, shows a Sn content of about 20 wt.% Sn and almost no P. This indicates that in this area α phase starts to form. Due to the limitation of the resolution of the SEM measurements the concentration in this area is questionable. In addition the etching and the uneven surface have a certain influence on the concentration distribution and with that this is a rough interpretation.

Figure 3-56 displays the isopleth at 6.4 wt.% P. Based on the measured concentration (14.2 wt.% Sn and and 6.4 wt.% P, *Figure 3-56*, blue dot) the expected phase distribution in the center of the annealed sample at T_a = 642 °C is compared with phase diagram calculations. The detected concentration lies close to the ternary eutectic temperature in the three phase region of Cu_3P, β and γ. The observed phase distribution shows good agreement with the phase diagram calculations.

In conclusion, it has to be mentioned that the experimental observations described in the last chapter show good agreement with the proposed ternary phase diagram of [Miettinen 01]. The observation of γ in the annealing experiment at T_a = 642 °C for t_a = 20 days is in good agreement with the thermodynamic calculations but controvers to the absence of γ in the DTA measurements of [TAKEMOTO 87]. The observed phase distribution especially in the annealing sample at T_a = 648 °C indicates that the phase transition as proposed by [EFFENBERG 07] ($L+\alpha \rightarrow \beta+Cu_3P$) should rather be a transition of $L \rightarrow \alpha+\beta+Cu_3P$.

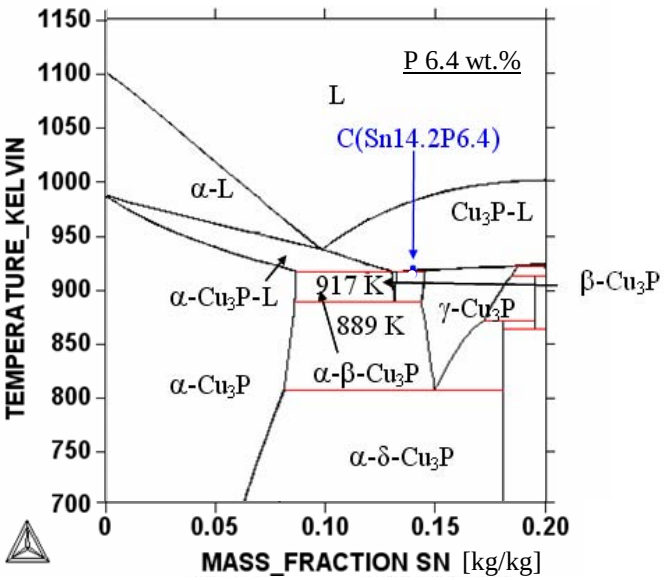

Figure 3-56: Vertical section (isopleth) of the ternary phase diagram Cu-Sn-P at 6.4 wt.% P (calculated with the database CuSn1). Blue dots mark show the measured average concentration in the center of the sample annealed at T_a = 642 °C for t_a = 6 days (Figure 3-39, ii).

The ε phase could not be observed in the experimental study which seems to justify the exclusion of this phase for phase predictions of "as-cast" conditions. So far the obtained temperatures in the DSC measurements and the concentrations of the annealing experiments indicate that the database CuSn1 allows the prediction of thermodynamics in the Cu rich corner of the ternary system Cu-Sn-P in an appropriate way.

The observed diffusion pattern in the performed experimental work does not allow proposing quantitative numbers for different diffusion coefficients. The main reason is that the diffusion interface is quite rough. Besides further studies have to be done to optimize the preparation of the samples to ensure homogenuous diffusion conditions. Since there is still a lack in values for diffusion coefficients and mobility values for the ternary Cu-Sn-P system, further work has to be performed to induce the ability to use numerical calculations for the prediction of phase distribution.

4 Multiphase Solidification Simulation for Continuous Casting of Sn/P – Bronzes

In the presented work, a Euler-Euler multiphase solidification model is applied to model solidification in continuous casting of bronze. For the numerical calculations the computational fluid dynamic (CFD) software FLUENT (Fluent Inc. USA) is used coupled with UDF's (User Defined Functions). The following description of the Euler-Euler multiphase solidification model of FLUENT is based on [WU 07]. In addition results and discussion include parts of publications during the last years [GRUBER 05, GRUBER 06, GRUBER 07, GRUBER 07A, LUDWIG 06A, LUDWIG 06B].

4.1 Basics and State of the Art

4.1.1 The Euler-Euler Multiphase Model

Basics

FLUENT is a CFD software with a finite volume differential (FVD) solver. The basic element is a representative volume element of a multiphase system as shown in *Figure 4-1*. In each volume element up to three phases, liquid, gas, and solid phase, are considered in this example. The definition of a phase differs to the one in thermodynamis and is used to identify the corresponding fluxes occuring based on the conservation equations. The term "phase" is not necessarily limited to the physical state. It can be extended to a certain class of fluid (for example primary fluid, group of gas bubbles, or moving solid particles) sharing the same thermophysical, hydrodynamic and thermodynamic properties or behaviors. The description of Eulerian multiphase fluids is based on the fact that the different phases are handled as interpenetrating continua. For that the different phases are thought to have a certain volume fraction, denoted here by f_q. The subscript q indicates here, for example, liquid, gas, or solid phases (1, 2, … n) [WU 07].

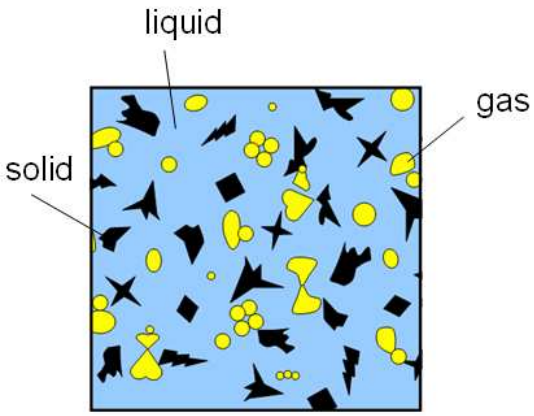

Figure 4-1: A representative volume element of a multiphase system [WU 07]. In this case three phases are present in the volume element, that is solid, liquid, and gas.

The sum of the volume fractions of all n phases in one volume element adds up to one

$$\sum_{q=1}^{n} f_q = 1. \tag{4-1}$$

The mass conservation has to be satisfied for each phase

$$\frac{\partial}{\partial t}\left(f_q \rho_q\right) + \nabla \cdot \left(f_q \rho_q \vec{u}_q\right) = \sum_{p=1}^{n} M_{pq}, \tag{4-2}$$

where ρ_q and $\vec{u}_q$ are the density and velocity of phase *q*. M_{pq} is the interphase mass transfer rate ($kgm^{-3}s^{-1}$) from phase *p* to *q*, and $M_{pq} = -M_{qp}$. The momentum balance for each phase is fullfiled by

$$\begin{aligned} &\frac{\partial}{\partial t}\left(f_q \rho_q \vec{u}_q\right) + \nabla \cdot \left(f_q \rho_q \vec{u}_q \otimes \vec{u}_q\right) = \\ &- f_q \nabla P + \nabla \bar{\bar{\tau}}_q + \vec{F} + f_q \rho_q \vec{g}_q + \sum_{p=1}^{n} K_{pq}\left(\vec{u}_p - \vec{u}_q\right) + \sum_{p=1}^{n} M_{pq} \vec{u}_{pq}. \end{aligned} \tag{4-3}$$

Where $\bar{\bar{\tau}}_q$ is the stress-strain tensor of phase *q* and $\vec{F}$ the source term for other body forces (e.g. lift force, virtual mass force,..), $\otimes$ is a dyadic product, and *P* is the pressure shared by all phases. $\vec{u}_{pq}$ is the interphase velocity, if $M_{pq} > 0$, which is for example the case if the mass of phase *p* is transferred to phase *q*, then $\vec{u}_{pq} = \vec{u}_p$. On the other hand, if $M_{pq} < 0$, which means $M_{qp} > 0$, then $\vec{u}_{pq} = \vec{u}_q$ and general $\vec{u}_{pq} = \vec{u}_{qp}$. The interphase momentum exchange coefficient, depending on friction, pressure, cohesion, and other effects is defined by $K_{pq} (= K_{qp})$.

The energy (enthalpy) conservation equation can be described as

$$\frac{\partial}{\partial t}\left(f_q \rho_q h_q\right) + \nabla \cdot \left(f_q \rho_q \vec{u}_q h_q\right) = \nabla \cdot \left(f_q k_q \nabla T_q\right) + \sum_{p=1}^{n} H_{pq}\left(T_p - T_q\right), \tag{4-4}$$

where h_q is the specific enthalpy of phase *q*, which is defined as

$$h_q = \int_{T_{ref}}^{T_q} c_{p(q)} dT_q + h_q^{ref}. \tag{4-5}$$

Here $c_{p(q)}$ is the specific heat of phase *q*, and h_q^{ref} the enthalpy at the reference temperature T^{ref} of phase *q*. In equation 4-4, k_q is the thermal conductivity of phase *q*, and H_{pq} the volume heat exchange coefficient between the phases *p* and *q*.

The species transport in each phase *i* in a multicomponent system can be described as

$$\frac{\partial}{\partial t}\left(f_q \rho_q c_q^i\right) + \nabla \cdot \left(f_q \rho_q \vec{u}_q c_q^i\right) = \nabla \cdot \left(f_q \rho_q D_q^i \nabla c_q^i\right) + C_q^i, \tag{4-6}$$

where c_q^i is the weight fraction of species *i* in phase *q*, D_q^i is the diffusivity of species *i* in phase *q*, and C_q^i [kgm^{-3}s^{-1}] is the rate of production or destruction of species *i* in phase *q*. Based on this the species exchange between phases during solidification is modeled according to the solidification rate and the solute partitioning or diffusion laws at the interface between the phases. If additional exchange terms are necessary to define specific values for the model, it is possible to solve additional transport equations for any arbitrary scalar in the same way as the above described transport equations. The general form of the arbitrary scalar ϕ_q^j of phase *q* is

$$\frac{\partial}{\partial t}\left(f_q \rho_q \phi_q^j\right) + \nabla \cdot \left(f_q \rho_q \vec{u}_q \phi_q^j\right) = \nabla \cdot \left(f_q \rho_q D_q^j \nabla \phi_q^j\right) + S_{\phi_q^j}. \tag{4-7}$$

Here D_q^j is the diffusion coefficient and $S_{\phi_q^j}$ the source term for the j^{th} scalar quantity in phase *q*.

Fundamentals about the solution methods for the described multiple equation system can be found in different sources [BRENNEN 05, FLUENT 05, FLUENT 06, KOLEV 02, PATANKAR 72, PATANKAR 80, SPALDING 72]. The methods for solving the Eulerian multiphase flow are available, but there are big differences in their infancy and timecosts. Each of the methods has its advantages depending on the application area of the flow pattern. There is no universal method for integrating systems of partial differential equations describing all multiphase flow patterns [WU 07]. The method applied in the presented work is based on that implemented in the CFD software FLUENT (Fluent Inc. USA).

State of the Art

As mentioned by [Wu 07], Beckermann and Viskanta developed the theoretical fundamentals of multiphase solidification models in the 1990's [BECKERMANN 88, BECKERMANN 93]. Based on this several two- or three-phase models with different assumptions have been published and applied [BECKERMANN 94, GANESAN 90, NI 91, NI 93, NI 95A, NI 95B, WANG 95]. These models have separate volume-averaged equations for mass, momentum, energy, and species conservation which are derived for a solid and a liquid phase. This development is the basic for the treatment of disparate solid and liquid velocity, thermal and solutal non-equilibrium, interfacial momentum, and heat and species exchange. The inclusion of interfacial transfer terms offered the possibility to integrate microscopic features like nucleation models, stereological formulations, or microsegregation features. Those microscopic and also macroscopic phenomena, as for example the formation of fragments and transport of equiaxed crystals (*Figure 4-2*) [NI 95A], and the dendritic morphology of the crystals [BECKERMANN 96, WANG 93, WANG 96A, WANG 96B] are still based on simplified assumptions.

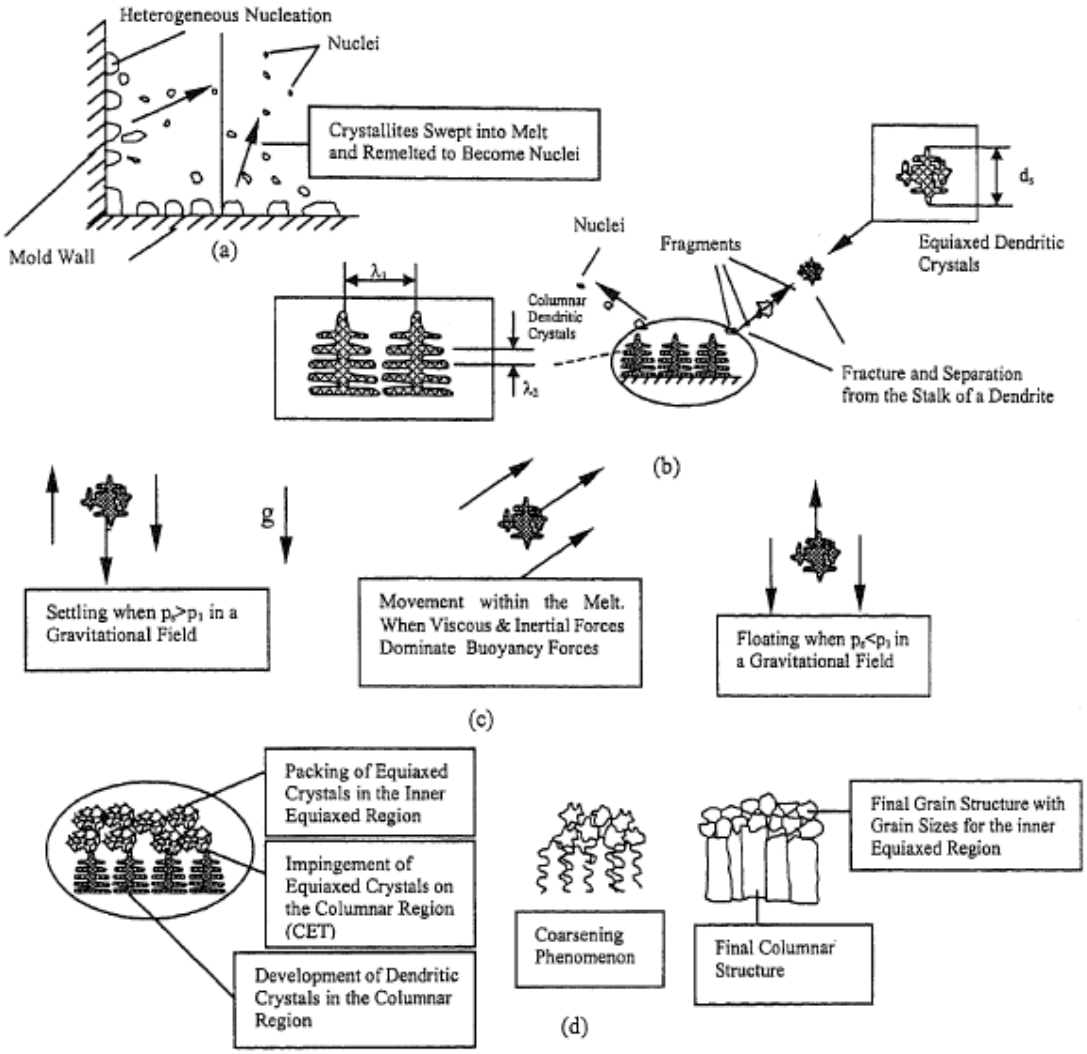

Figure 4-2: Illustration of the development and transport of solid structures [NI 95A]. a) Heterogeneous nucleation, b) generation of fragments and equiaxed crystals, c) transport of solid crystals, d) packing impingement, coarsening, and final solid structures.

However, they can be described for at least qualitativley. There are still some uncertainties included in the model assumtions. Therefore there is a need in further development of the physical models based on experimental research [Wu 07]. Such physical phenomena are for example a realistic physical nucleation model, or detailed volumetric heat and mass transfer coefficients, and a correct stereological formulation for interfacial area concentrations [ILEGBUSI 00, NI 95A, NI 95B, WANG 95]. *Figure 4-2* gives an overview about the main mechanisms taking part in nucleation. However, only some of them may occure under special circumstances during solidification. As explored by Beckermann and his coworkers [BECKERMANN 93, BECKERMANN 96, NI 93, WANG 96A, WANG 96B], there are a number of phenomena which are not included in for example continuum mixture models [WU 07]. The application for these models is mainly limited to a few benchmark cases as displayed in *Figure 4-3*. Further research efforts and experimental verifications are still demanded.

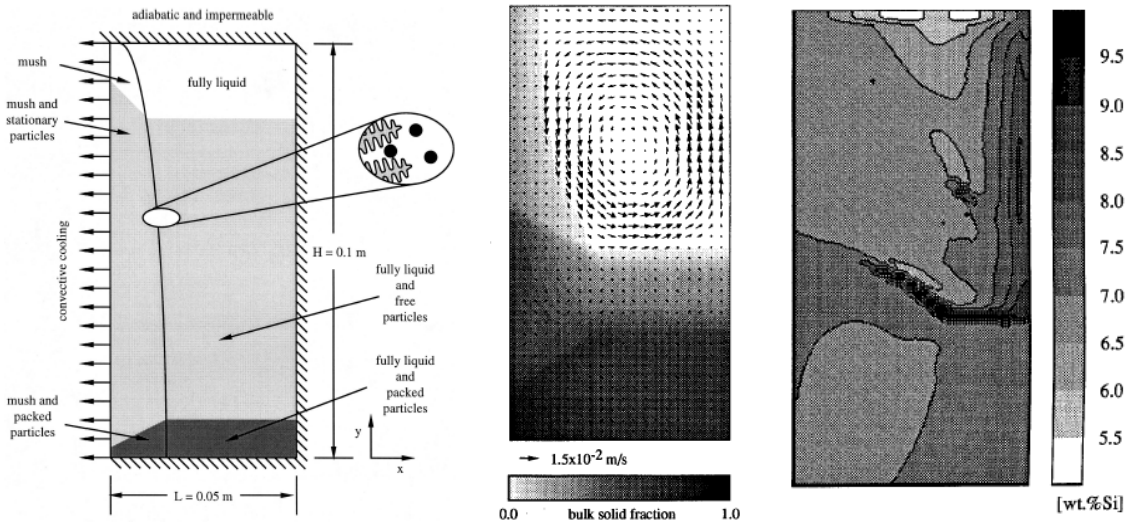

(a) *(b)* *(c)*

Figure 4-3: 3-phase (convective melt, stationary solid, movable SiC particle) model was developed to model the solidification of metal matrix particulate composites (MMPCs) [FELLER 97]. (a) Illustration of domain and boundary conditions used for the simulation. (b) Solid fraction (grey scale) and liquid velocity field at 100 s (arrows). (c) Predicted final macrosegregation pattern of Si.

Besides, studies on the influence of different flow phenomena on the flow field in the mushy zone were performed for Al-Cu alloys [DU 05, DU 06, ZALOZNIK 05, ZALOZNIK 06]. Zaloznik applies the Bennon-Incopera one-phase mixture model to study the influence of casting parameters in direct-chill casting of Al-Cu strands on the formation of macrosegregation [ZALOZNIK 05]. But for the simulation of macrosegregations a mixture model does not have the great advantages as the already described multi-phase models. Du and Eskin apply a multi-phase model for equiaxed solidification in Al-Cu direct-chill casting [DU 05, DU 06]. Here detailed studies on the influence of flow phenomena like forced convection, feeding flow, thermo-solutal buoancy flow, and grain sedimentation were taken into accont.

[MAYER 07, WU 06, WU 07] use the multiphase model of Ludwig and Wu [LUDWIG 02, LUDWIG 05, MAYER 07, WU 03A, WU 03B, WU 06, WU 07] to describe two and three phase solidification for ingot casting and continuous casting of steel. The main objective in these studies is the prediction of macrosegregation pattern in steel production.

For continuous casting of bronze studies on the numerical description of solidification have been published during the last three years by the author and coworkers [GRUBER 05, GRUBER 06, GRUBER 07A, LUDWIG 06A, LUDWIG06B]. The applied physical model for multiphase flow is the same as developed and published by Ludwig, Wu and coauthors from 2002-2006 [LUDWIG 02, LUDWIG 05, MAYER 07, WU 03A, WU 03B, WU 06, WU 07]. The basic features of the solidification process occurring in continuous casting of bronze are (i) fluid dynamics in the liquid and mushy zone, (ii) solidification for the transition from liquid to solid, (iii) definition of the growth mechanisms taking place during solidification, (iv) inclusion of thermodynamic features appearing during solidification, and (iiv) influence of different convection mechanism like forced convection, feeding flow and thermo-solutal flow.

Since technical alloys usually consist of more than two elements macrosegregation studies imply the need for taking thermodynamics of ternary or higher order systems into account. Most of the previous mentioned work was done for binary systems. A few studies were performed on multicomponent systems using simplified thermodynamics. Usually linearized phase diagrams with constant liquidus slope and constant partitioning coefficients are included [SCHNEIDER 95A, SCHNEIDER 95B]. Since the pioneer work of Kaufman and Bernstein in 1970 [KAUFMAN 70], the calculation of phase diagrams has become a widely used tool for predicting thermodynamic information by computational techniques. This method is known as the CALPHAD method (CALculation of PHAse Diagrams) [ANDERSSON 02, SUNDMAN 85]. Nowadays, more and more groups have started to combine numerical solidification simulations with CALPHAD calculations [BOETTINGER 00, GRAFE 00, GREVEN 99, KATTNER 97]. Since then it is possible to predict phase evolution and the according solidification path based on the CALPHAD method by taking into account effects of cooling rate, back diffusion, and coarsening [JIE 05, KRAFT 97, LAROUCHE 07]. [ESKIN 07] discusses formation of macrosegregation for a ternary Al-alloy based on a two phase model for equiaxed solidification. It is mentioned that direct coupling between a thermodynamic and a CFD software is rather time consuming for real casting processes. Therefore it is proposed to use tabulation moduls for the thermodynamic input.

Ludwig and co-workers recently proposed a new method [LUDWIG 06B, LUDWIG 07], developped partly in the presented work, to couple the thermodynamic data with the multiphase solidification model, where a way of coupling solidification kinetics with thermodynamics in multiphase solidification was presented. Since direct coupling of a thermodynamic software, like Thermo-Calc with a CFD software, like FLUENT, is very time consuming, the coupling is done by providing access to thermodynamic data through either linerarization methods or the tabulation and interpolation technique ISAT (In-Situ Adaptive Tabulation) [ISHMURZIN 08]. The presented calculations have been performed for columnar solidification.

4.1.2 Columnar Solidification

General Assumptions

During solidification of continuous casting of bronze, both, equiaxed and columnar dendritic growth is observed depending on the applied casting conditions. The physical model for multiphase flow, as described in the following, has been developed and published by Ludwig, Wu and coauthors from 2002-2006 [LUDWIG 02, LUDWIG 05, WU 03A, WU 03B, WU 06, WU 07, MAYER 07]. For the simulation of macrosegregation features the growth of equiaxed grains is denied as a first approximation. The main assumptions of the used model can be briefly summarized as follows:

- Columnar dendrites are thought to start growing at the mold wall as soon as the temperature drops below the liquidus temperature.
- The columnar dendrites are assumed to have an ideal cylindrical morphology (cellular dendrite-like).
- A shell-like growth driven by diffusion is assumed around the cylinder.
- Nucleation and growth of equiaxed grains are ignored.
- Two phases are defined: the liquid phase *l* as the primary and the columnar as the secondary phase *c*. The corresponding phase fractions are given as volume fraction of the liquid phase f_l and volume fraction of the columnar phase f_c with $f_l + f_c = 1$.
- The primary phase is thought to be a moving phase for which the corresponding Navier-Stokes equations are solved. The columnar phase is assumed to start growing from the mold wall, and to move with the constant and predefined casting velocity $\vec{u}_{castt}$. Thus, no momentum conservation equation for the columnar phase is considered.
- Corresponding source terms are included to account for thermo-solutal buoyancy driven flow.
- Shrinkage is modelled by feeding flow occurring due to the density difference between columnar and liquid phase ($\rho_c > \rho_l$).
- Mechanical interaction between mush and flowing melt is calculated via Darcy's law.
- The Blake-Kozeny permeability approach [BIRD 60, LUDWIG 02, LUDWIG 06A] is applied to model the mush permeability.
- Thermodynamic information for the binary Cu-Sn system is approximated by using a constant redistribution coefficient *k* and a constant liquidus slope *m*. For the ternary calculations of Cu-Sn-P the model published in [ISHMURZIN 08, LUDWIG 06B, LUDWIG 07] is applied. Here precalculated thermodynamic data is coupled with computational fluid dynamics (CFD) and therefore used for the calculation of the interfacial concentration of Sn and P.
- A constant value for the primary arm spacing of columnar dendrites, λ_1, is assumed.

Mass Conservation and Growth Kinetics

The mass conservation equations for the liquid and the columnar phase are given by

$$\frac{\partial}{\partial t}(f_l\rho_l)+\nabla\cdot(f_l\rho_l\vec{u}_l)=M_{cl}, \tag{4-8}$$

$$\frac{\partial}{\partial t}(f_c\rho_c)+\nabla\cdot(f_c\rho_c\vec{u}_c)=M_{lc}. \tag{4-9}$$

Here, ρ_l, ρ_c are the densities and $\vec{u}_l$, $\vec{u}_c$ the volume-averaged velocities of the two phases. The source terms, $M_{lc}(=-M_{cl})$, represent the net mass transfer rates from the liquid to the columnar phase [kg·m^{-3}·s^{-1}], which is positive for solidification and negative for melting. To define the net mass transfer rate, the diffusion controlled growth kinetics around a cylindrical dendrite trunk is modeled by considering the growth velocity *v* in the radial direction:

$$v = \frac{dR_c}{dt} = \frac{D_l}{R_c}\frac{\tilde{c}_l - c_l}{\tilde{c}_l - \tilde{c}_c}\ln^{-1}\left(\frac{R_f}{R_c}\right). \tag{4-10}$$

Here, $\tilde{c}_l$ and $\tilde{c}_c$ are the equilibrium liquid and solid concentrations adjacent to the solid/liquid interface, for which in a binary linearized phase diagram $\tilde{c}_c = k\tilde{c}_l$ and $\tilde{c}_l = (T - T_f)/m$, where *k* is the solute redistribution coefficient and *m* is the slope of the linearized liquidus line of the phase diagram, c_l is the average concentration in the liquid, *T* volume average temperature, and T_f the liquidus temperature of pure Cu. D_l is the diffusion coefficient in the liquid and $R_c = d_c/2$ is the average radius of a cylindrical dendrite trunk, d_c is the dendrite diameter, *v* is the radial growth velocity of the dendrite trunk. The far field radius is $R_f = d_{max}/2$ where d_{max} is the maximum dendrite trunk diameter in case where no liquid is thought to be left for the applied arranagement. With equation 4-11 we can define the volume-averaged net mass transfer rate by combining the total surface area of columnar dendrite trunks per volume in case of hexagonal arrangement $S_A = \pi d_c/\lambda_1^2$ for 2D, where λ_1 is the primary dendrite arm spacing, and the impingement factor f_{imp} to become

$$M_{lc} = \rho_c v \frac{2\sqrt{3}\pi d_c}{3\lambda_1^2} f_{imp}, \tag{4-11}$$

with

$$f_{imp} = \begin{cases} f_l, & 0 < d \le \lambda_1, \\ f_{l,crit}, & \lambda_1 < d \le d_{max} \end{cases} \text{ with}$$

$$f_{l,crit} = 1 - \frac{\sqrt{3}\pi}{6} \text{ for cylindrical growth.} \tag{4-12}$$

Here $f_{l,crit}$ is the critical volume fraction which is reached when the dendrite trunks are touching each other [MAYER 07]. In case of a hexagonal dendrite area $d_{max} = 1.05\lambda_1$.

This condition assumes that the entire residual melt is consumed by the growing cylinders. With equation 4.10 this leads to

$$M_{lc} = \frac{D_l}{(d_c/2)(1-k)}\left(1-\frac{c_l}{(T-T_f)/m}\right)\ln^{-1}\left(\frac{\lambda_1}{d_c}\right)\frac{2\sqrt{3}\pi d_c}{3\lambda_1^2}\rho_c f_{imp}\,. \qquad (4\text{-}13)$$

This approach leads to a positive mass transfer as soon as the temperature dependent interface concentration in the liquid $\tilde{c}_l = (T-T_f)/m$, exceeds the average liquid concentration c_l available in the corresponding volume element [MAYER 07].

Momentum Conservation and Viscous Interaction between Phases

The velocity field of the melt is obtained by solving the Navier-Stokes

$$\frac{\partial}{\partial t}(f_l\rho_l\vec{u}_l)+\nabla\cdot(f_l\rho_l\vec{u}_l\otimes\vec{u}_l) = -f_l\nabla p+\nabla\bar{\bar{\tau}}_l+f_l\rho_l\vec{g}+\vec{U}_{cl}\,, \qquad (4\text{-}14)$$

with

$$\bar{\bar{\tau}}_l = \mu_l f_l\left(\nabla\otimes\vec{u}_l+(\nabla\otimes\vec{u}_l)^T\right) \qquad (4\text{-}15)$$

being the stress-strain tensor of the liquid phase and

$$\rho_l(T,c) = \rho_l^{ref}\left[1+\beta_T(T^{ref}-T_l)+\beta_c(c^{ref}-c_l)\right] \qquad (4\text{-}16)$$

the temperature and concentration dependent density. The momentum exchange between the melt and the columnar dendrites includes two contributions: (i) due to the phase transition, $\vec{U}_{lc}^{\,p}$, and (ii) due to the drag force between liquid and solid, $\vec{U}_{lc}^{\,d}$. Thus, we have $\vec{U}_{lc} = \vec{U}_{lc}^{\,p}+\vec{U}_{lc}^{\,d}$. The contribution due to phase change is described by $\vec{U}_{lc}^{\,p} = \tilde{\vec{u}}M_{lc}$ with $\tilde{\vec{u}} = \vec{u}_l$ for solidification and $\tilde{\vec{u}} = \vec{u}_c$ for melting. The momentum exchange due to drag is modeled by using the Blake-Kozeny approach [BIRD 60, LUDWIG 02, LUDWIG 06A]

$$\vec{U}_{lc}^{\,d} = K_{lc}(\vec{u}_l-\vec{u}_c)\,. \qquad (4\text{-}17)$$

The drag coefficient is given by

$$K_{lc} = -\frac{f_l^{\,2}\mu_l}{K} \qquad (4\text{-}18)$$

and a permeability taken as

$$K = K_0\frac{f_l^{\,3}}{(1-f_l)^2}\,, \qquad (4\text{-}19)$$

with $K_0 = \overline{K_0}\lambda_1^2$, where the pre-factor $\overline{K_0}$ is assumed to be constant. Further details on the applied momentum exchange approach can be found in former publications [LUDWIG 02, LUDWIG 05A, WU 03A, WU 03B, WU 06, WU 07].

Species Conservation and Solute Partitioning at the Solid/Liquid Interface

The volume-averaged concentration of liquid phase c_l and of columnar phase c_c are obtained by solving the species concentration

$$\frac{\partial}{\partial t}\left(f_l \rho_l c_l\right) + \nabla \cdot \left(f_l \rho_l \vec{u}_l c_l\right) = \nabla \cdot \left(f_l \rho_l D_l \nabla c_l\right) + C_{cl}, \tag{4-20}$$

$$\frac{\partial}{\partial t}\left(f_c \rho_c c_c\right) + \nabla \cdot \left(f_c \rho_c \vec{u}_c c_c\right) = \nabla \cdot \left(f_c \rho_c D_c \nabla c_c\right) + C_{lc}, \tag{4-21}$$

where D_c is the diffusion coefficient in the solid.

The solute exchange among liquid and solid is caused by solute partitioning at the solid/liquid interface. It is straight forward, that the corresponding exchange term is given by $C_{lc} = \tilde{c}_c M_{lc}$ and $C_{cl} = \bar{c}_c M_{cl}$, where we assume $\tilde{c}_c = k \cdot \tilde{c}_l$ for binary solidification and $\tilde{c} = \bar{c}_c$ for melting.

Enthalpy Conservation

We solve the enthalpy conservation equation for each phase:

$$\frac{\partial}{\partial t}\left(f_l \rho_l h_l\right) + \nabla \cdot \left(f_l \rho_l \vec{u}_l h_l\right) = \nabla \cdot \left(f_l k_l \nabla T_l\right) + Q_{cl}, \tag{4-22}$$

$$\frac{\partial}{\partial t}\left(f_c \rho_c h_c\right) + \nabla \cdot \left(f_c \rho_c \vec{u}_c h_c\right) = \nabla \cdot \left(f_c k_c \nabla T_c\right) + Q_{lc}, \tag{4-23}$$

where the enthalpies are defined via

$$h_l = \int_{T_{ref}}^{T_l} c_{p(l)} dT + h_l^{ref} \tag{4-24}$$

and

$$h_c = \int_{T_{ref}}^{T_c} c_{p(c)} dT + h_c^{ref} \tag{4-25}$$

with the specific heat of the liquid being $c_{p(l)}$ and that of the solid phase being $c_{p(c)}$. T_{ref}, h_l^{ref} and h_c^{ref} are defined in a way that the enthalpy difference between the liquid and the solid, $(h_l - h_c)$, is equal to the latent heat of fusion. The source term for the enthalpie conservation equation is based on the sum of the release of latent heat Q_{lc}^p and the enthalpy exchange between the phases Q_{lc}^d as $Q_{lc} = Q_{lc}^p + Q_{lc}^d$. The release of latent heat between the phases is treated by $Q_{lc}^p = h_l M_{lc}$ for solidification and $Q_{cl}^p = h_c M_{cl}$ for melting. By solving the above described conservation equations (equation 4-22 and equation 4-23), two different temperatures, T_l and T_c are gained. A quite large volume heat exchange coefficient of $\tilde{H} = 10^8$ W·m^{-3}·K^{-1} is used to balance the temperatures between the two phases ($T_l \approx T_c$). Thus, a volume heat exchange of $Q_{lc}^d = \tilde{H}(T_l - T_c)$ is obtained. In [RAPPAZ 90] it was verified that the calculated temperature difference in

the mushy zone between liquid and solid, where a large amount of latent heat is released, is about 0.2 K.

Auxiliary Quantities

In order to study macrosegregation quantitatively the mixture concentration c_{mix} is defined according to

$$c_{mix} = \frac{c_l \rho_l f_l + c_c \rho_c f_c}{\rho_l f_l + \rho_c f_c}. \tag{4-26}$$

The volume averaging approach relates the volume fraction of the cylindrical dendrites to the ratio of the average cross section area of a single trunk, $\pi(d_c/2)^2$, to the highest available area for a hexagonal dendrite area

$$f_c = \frac{\sqrt{3}\pi}{6} \frac{{d_c}^2}{{\lambda_1}^2}. \tag{4-27}$$

This geometrical relationship is used to determine the volume-averaged dendrite trunk diameter d_c. Here, f_c is known from the corresponding mass conservation equation, and λ_1 is given. For the presented results the primary dendrite arm spacing is thought to be constant at $\lambda_1 = 150\ \mu\text{m}$.

Thermodynamic Description for the Ternary Model

The way of coupling ternary and higher componential phase diagram information with the multiphase solidification approach proposed by [ISHMURZIN 08, LUDWIG 05, LUDWIG 06B] is used for the ternary calculation. A brief model description based on [LUDWIG 06B] is presented here.

The above described two-phase volume averaging model considers two interpenetrating continua: the liquid *l*, and the columnar dendrite trunks *c*. At the solid-liquid interface the dendrites have an average species mass fraction of $\tilde{c}_l^{\,j}$ in the liquid and $\tilde{c}_c^{\,j}$ in the cylindrical solid. The assumption of a quasi-steady state diffusion field around growing cylindrical dendrites of diameter d_c leads to the following expression for the solute gradient, $\tilde{G}_l^{\,j}$, for cylindrical growth of the *j*-species in the liquid at the interface

$$\tilde{G}_l^{\,j} = -\frac{\tilde{c}_l^{\,j} - c_l^{\,j}}{d_c/2} \ln^{-1}\left(\frac{d_{max}}{d_c}\right) \text{ for cylindrical growth, } j = \text{Sn, P} \tag{4-28}$$

Neglecting solute diffusion from the interface into the solid, the solute flux balance at the interface leads to an expression for growth velocities v_j

$$v_j\left(\tilde{c}_l^{\,j} - \tilde{c}_c^{\,j}\right) = -D_{lj}\tilde{G}_l^{\,j} \quad \Rightarrow \quad v_j = \frac{2D_{lj}}{d} \frac{\tilde{c}_l^{\,j} - c_l^{\,j}}{\tilde{c}_l^{\,j} - \tilde{c}_c^{\,j}} \ln^{-1}\left(\frac{d_{max}}{d}\right), \ j = \text{Sn, P.} \tag{4-29}$$

Here D_{lj} is the diffusion coefficient of the *j*-species in the liquid. In case of strong convection, equation 4-29 has to be modified by including the Sherwood-Number. Note that equation 4-29 is valid for all considered species, in case of the ternary system Cu-

Sn-P j = Sn, P. However, to estimate the growth velocity one equation is sufficient. Hence, the two equations can be combined to express the equality of both growth velocities:

$$v = v_1(\tilde{c}_l^{Sn}, c_l^{Sn}, \tilde{c}_c^{Sn}) = v_j(\tilde{c}_l^{P}, c_l^{P}, \tilde{c}_c^{P}) \ , \tag{4-30}$$

where these functions have the form defined in equation 4-29. Knowing growth velocity v, the mass transfer M_{lc}, can be expressed in equation 4-11. For the estimation of v via equation 4-29, the interface species mass fraction, $\tilde{c}_l^{\,j}$ and $\tilde{c}_c^{\,j}$ with j = Sn, P have to be determined from the following thermodynamic considerations. As in most practical situations, local thermodynamic equilibrium at the solid/liquid interface can be assumed and as in the volume averaging consideration the mean curvature undercooling is approximately zero, the solid/liquid interface temperature is given by the corresponding liquidus temperature

$$T = T_L\left(\tilde{c}_l^{Sn}, \tilde{c}_l^{P}\right). \tag{4-31}$$

In addition to that, thermodynamics also relates the liquid and solid interface concentrations by corresponding tie-line functions

$$\tilde{c}_c^{Sn} = f_{Sn}\left(\tilde{c}_l^{Sn}, \tilde{c}_l^{P}\right) \tag{4-32}$$

$$\tilde{c}_c^{P} = f_{P}\left(\tilde{c}_l^{Sn}, \tilde{c}_l^{P}\right). \tag{4-33}$$

Here $\tilde{c}_l^{Sn}$ is the interfacial average species mass fraction of Sn and $\tilde{c}_l^{P}$ of P in the liquid. The n-1 (for ternary n = 2) equations (equation 4-32 and 4-33) and the n equations (equation 4-30) together with equation 4-31 yield a nonlinear system of equations, which can be used to estimate the 2n interface quantities $\tilde{c}_l^{Sn}, \tilde{c}_l^{P}, \tilde{c}_c^{Sn}, \tilde{c}_c^{P}$ (thermodynamic-related quantities) from the n+1 bulk quantities c_l^{Sn}, c_l^{P}, T (process-related quantities). Note that the n+1 bulk quantities are determined from solving the corresponding conservation equations [ISHMURZIN 08].

4.2 Multiphase Modelling in Continuous Casting of Bronze

4.2.1 Numerical Implementation

The conservation equations are numerically solved using the control-volume based finite difference CFD software FLUENT, version 6.2 (FLUENT is a trademark of Fluent Inc. USA). In the Euler-Euler model all phases share a single pressure field *P*. The pressure correction equation is obtained from the sum of the normalized mass continuity equations using a so-called Phase Coupled SIMPLE (PC-SIMPLE) algorithm [FLUENT 05].

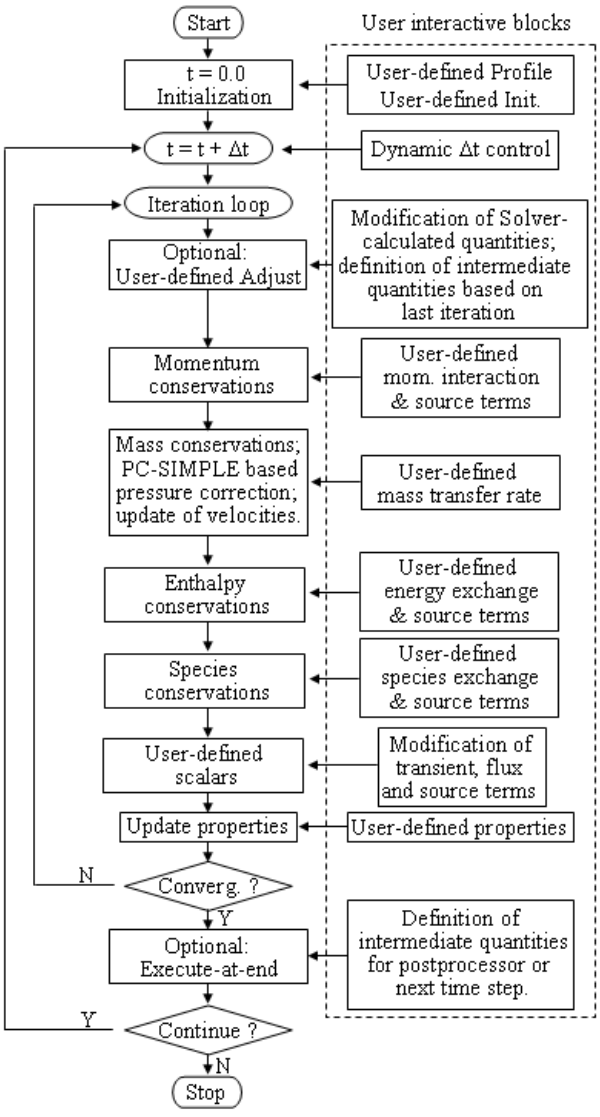

Figure 4-4: Flow chart of the solution procedure [WU 07].

Figure 4-4 shows a flow chart of the solution procedure applied in FLUENT. Carrying out transient calculations, for each time step several iterations are calculated to decrease the normalized residuals of c_l, c_c, f_c, $\vec{u}_l$, and P. On each iteration some intermediate (auxiliary) quantities, as for example the user defined property mixture concentration c_{mix}^{i}, are defined and updated first. Based on the quantities of the last iteration the ex-

change terms and the source terms are calculated. Finally, the conservation equations for the corresponding momentum, masses, enthalpies, and species are solved considering the amount of the different phases and the exchange terms.

The FLUENT formulation is fully implicit, so there is no stability criterion that has to be met. However, due to the complexity of the present problem, the time step, Δt, should not be too large in order to meet convergence. The optimal time step must be determined empirically by test simulations. Further discussion about calculation accuracy and the effect mesh quality/size can be found in previous publications [LUDWIG 02, WU 03A, WU 03B].

For the defined conditions, transient calculations have been carried out. Three types of calculation procedures have been compared. *Figure 4-5* shows the mixture concentration fields c_{mix} for *(a)* a pseudotransient calculation with time step $\Delta t = 1\text{s}$ and 1 iteration per time step, *(b)* a transient calculation with time step $\Delta t = 0.02\,\text{s}$ and 25 iterations per time step and no convergence criteria, and *(c)* a transient calculation with time step $\Delta t = 0.02\,\text{s}$, 25 iterations per time step and considering convergence limits of 10^{-4} for all parameters but 10^{-7} for h_l and h_c. The three calculations have been run for the same wall clock time, namely for three days. ① indicates the isotherm for the liquidus temperature of CuSn6 $T_{liquidus}$ and ② the isotherm of the temperature where solidification ends T_{end}. For the presented case, as described in details in chapter 4.2.2, the second calculation procedure shows the best calculation behaviour. In case of the pseudotransient calculation numerical errors occure which leads to strips in the liquid region (I) in the macrosegregation profiles that do not occure in the other calculations. In case *(b)* the most homogenuous macrosegregation distribution was reached. In case where convergence criteria are used to speed up the calculation, the simulation needs more time to find the steady state than in the case where a specific iteration number is given. This is indicated by a strong change in the macrosegregation distribution vertically below T_{end} (II) where no major changes are expected for a steady state solution. The displayed macrosegregation distribution in *Figure 4-5b* seems to satisfy a steady state solution the most. For sure, it has to be mentioned that this statement is just valid for this benchmark and the applied conditions in combination with the used UDF's.

For the results presented in the following a time step of $\Delta t = 0.02\,\text{s}$ was taken. In some cases it was adjusted to $\Delta t = 0.002\,\text{s}$ at a later stage to increase numerical stability. For each time step 25 iterations have been calculated without checking convergence. This is a possibility that offers relatively short calculation times (3-4 days) for the 2D simulations as described in 4.2.2. Since the interpretation is based on the steady state results it is not necessary to reach convergence in every time step.

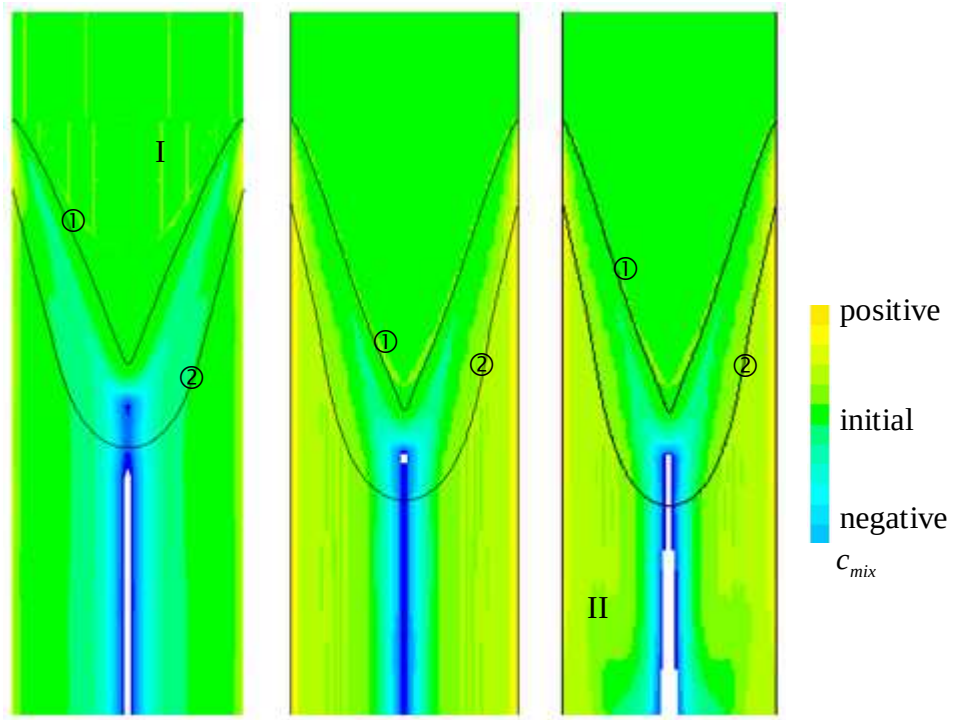

Figure 4-5: Mixture concentration c_{mix} of Sn for (a) a pseudotransient calculation with Δt = 1s and 1 iteration per time step, (b) a transient calculation with Δt = 0.02 s and 25 iterations per timestep and no convergence criteria, and (c) a transient calculation with Δt = 0.02 s, maximum 25 iterations per timestep with convergence limits of 10^{-4}, and for h_l and h_c of 10^{-7}. The three cases were run for 72 hours. Since different numerical settings were applied, the real time of the different cases varies significantly.

To check if a steady state solution is reached, several parameters are monitored as integrated average volume values during the calculation with FLUENT. In case of calculations for continuous casting, a steady state can be defined for example when the volume average of the mixture concentration c_{mix} of Sn reaches the original alloy concentration based on the mass/species conservation. *Figure 4-6* shows the monitored volume average development of the mixture concentration c_{mix} of a calculation for CuSn6 (geometrie and boundary conditions as described in 4.2.2). The red arrow shows the timestep where steady state is thought to be reached. Here the average volume value meets the alloy concentration according to the conservation equations. In addition *Figure 4-7* displays the residuals of the same calculation for the first 1000 iterations. For these results a time step of $\Delta t = 0.02$ s was applied with a maximum of 25 iterations per timestep and no convergence limits set. After the maximum at the beginning, the residuals are decreasing within each timestep. Since the steady state itself is thought to be the only real solution, the variation in the average volume mixture concentration and sometimes relativley high values of the residuals are accepted at the beginning of the calculation. The numerical settings and material data for the different calculations are given in chapter 8.

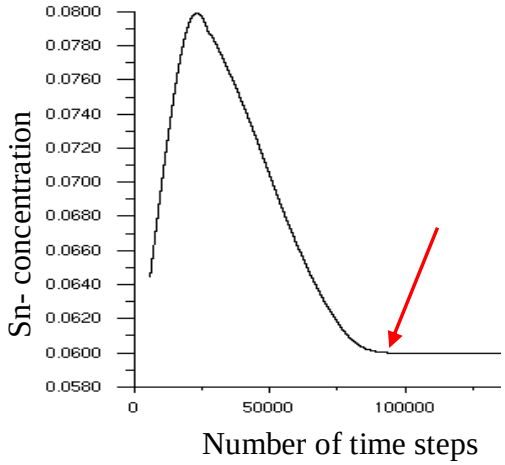

Figure 4-6: Monitored integrated volume average mixture concentration c_{mix} of Sn in a calculation for CuSn6 (geometrie and boundary conditions are described in 4.2.2). When the average concentration reaches the constant value of the initial alloy concentration, steady state is thought to be reached (red arrow indicates the time step).

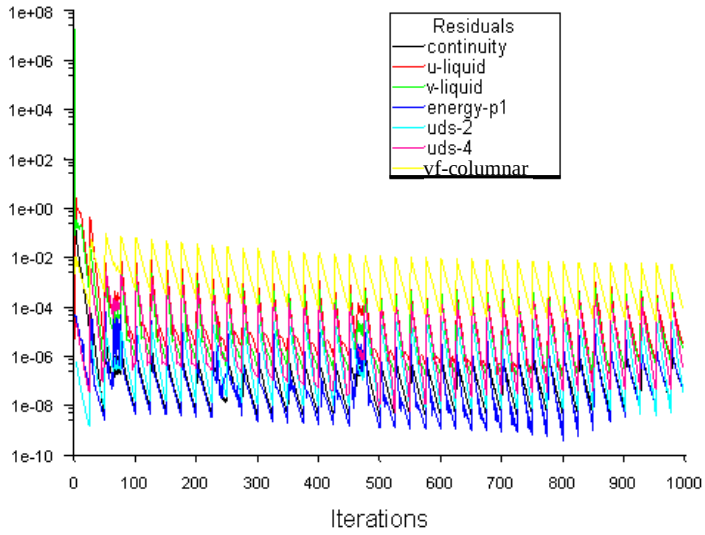

Figure 4-7: Residuals of the calculation of the first 1000 iterations of a calculation for CuSn6 (geometrie and boundary conditions are described in 4.2.2). The residuals are displayed for continuity (pressure field), velocity vector of the liquid in u and v direction (u-liquid, v-liquid), energy of the liquid (energy-p1), concentration of liquid (uds-2), concentration of the columnar phase (uds-4), and volume fraction columnar (vf-columnar).

The link between mathematics and physics is the numerical implementation that tries to meet natural conditions as accurate as possible. However, a model has to be defined including many approaches to get a numerical stable program and converging results. Up to now it is possible to calculate solidification and the corresponding macrosegregation qualitativley. But nevertheless further development of both, model details and implementation is necessary to go step by step closer to reality.

4.2.2 2D Axis Symmetric Simulations for CuSn6

In the following numerical simulation results are presented for binary CuSn6 continuous casting. Two types of calculations have been performed: (i) 2D axis symmetric calculations were done for cylindric mold geometry as cast in industry. To adjust the original 3D process to a 2D axis symmetric calculation some details were adjusted as for example position and complexity of the inlet. Nevertheless, the results are thought to be close to the casting process in mind. Various studies on macrosegregation of Sn have been performed for this binary case. In addition (ii) 3D simulations were performed to study the macrosegregation pattern of Sn for a rectangular geometry of laboratory scale.

Geometrie and Boundary Conditions

For all 2D calculations the same geometry and boundary conditions were applied to allow an accurate comparison of the different case studies. For the process simulation a casting velocity of $\vec{u}_{cast} = 1.92$ mm·s^{-1} and a casting temperature of T_{cast} = 1389 K are used. Since the mold is of a cylindrical shape, an axis symmetric simulation has been chosen. *Figure 4-8* displays a schematic sketch of the mold of the considered DC casting process where ① indicates the position of the inlet in the nozzle, ② marks the surface on the top. ③ assigns the upper part of the mold which is assumed to be insulating, and ④ shows the lower part of the graphite mold which is surrounded by a copper mold including a water cooling system ⑤. *Figure 4-9* displays a shematical sketch of the grid with the applied boundary conditions. Here ① gives the position of the inlet, where a pressure inlet is taken. A heat transfer coefficient (HTC) of h = 50 W·m^{-2}·K^{-1} and a temperature of T_{SEN} = 1292 K are considered for the submerged entry nozzle (SEN) region. For ② the HTC and the temperature have a value of h = 50 W·m^{-2}·K^{-1} and $T_{surface}$ = 325 K. For ③ almost ideal insulation is assumed with h = 10 W·m^{-2}·K^{-1} and T_{upper_mold} = 1292 K. For ④ h = 3000 W·m^{-2}·K^{-1} and T_{lower_mold} = 550 K and for ⑤ h = 1000 W·m^{-2}·K^{-1} and T_{water} = 300 K are considered. The constant casting velocity $\vec{u}_{cast} = 1.92$ mm·s^{-1} is taken at the outlet where a velocity outlet is applied ⑥. For the nozzle and for the surface slip condition is used for both phases whereas the mold wall is considered to move with casting velocity. Therefore, a slip condition for the liquid phase and a non-slip condition for the columnar phase are applied. The grid has a size of 9016 cells and 9296 nodes. As initial conditions, hot melt (T_{init} = 1292 K) at rest ($\vec{u}_l = 0$ mm·s^{-1}) is assumed. The presented results are taken after reaching steady state.

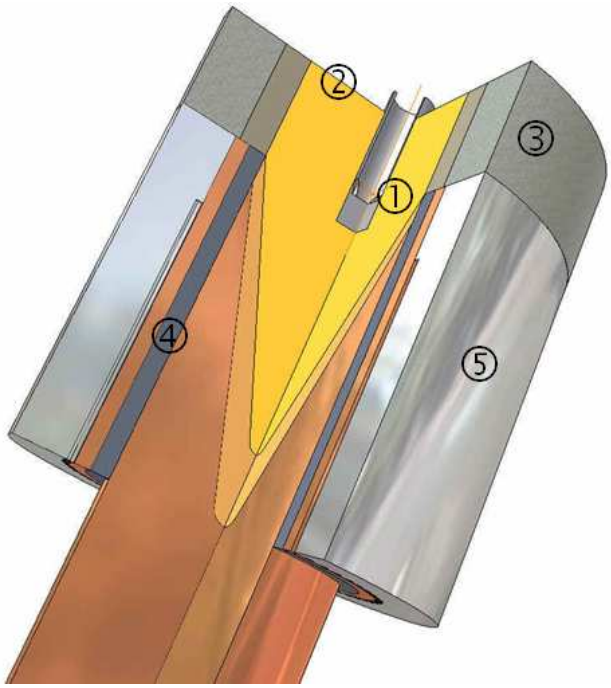

Figure 4-8: Sketch of the considered DC casting process: ① indicates the position of the nozzle, ② the surface, and ③ the graphite mold with isolation (upper part of the mold). The primary cooling zone is marked with ④ for the graphite/copper part, and ⑤ for the steel mold with included water cooling (lower part of the mold).

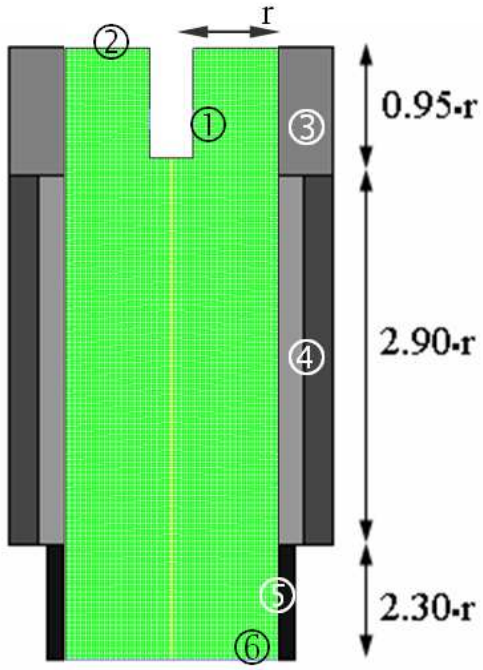

Figure 4-9: Grid and interfaces for the boundary conditions. ① marks the position of the inlet (pressure inlet), ② of a surface without cooling or isolation, ③ the graphite mold with isolation (upper part of the mold), ④ the graphite/copper mold of the primary cooling zone (lower part of the mold), ⑤ the secondary cooling zone with direct water cooling, and ⑥ the velocity outlet.

Case Description

In order to estimate the relative importance of feeding flow, thermal and solutal buoyancy flow, and inlet flow depending on the mush permeability, the simulation results of 10 different cases are discussed. Two different values for the empirical factor in the Blake-Kozeny expression (equation 4-19) are considered, namely i) $\overline{K}_0 = 1.4 \cdot 10^{-3}$ and ii) $\overline{K}_0 = 1.4 \cdot 10^{-5}$. The five cases, discussed for both mush permeabilities, can be described as follows:

- Case A: Just forced convection (inlet flow) is taken into account. No thermal and solutal buoyancy flow and no feeding flow are considered.

- Case B: Here solutal buoyancy flow is considered in addition to the forced convection. The solutal expansion coefficient was chosen to be $\beta_C = 0.11\,\text{wt.\%}^{-1}$ (calculated after [MIETTINEN 06]).

- Case C: Here thermal buoyancy flow is considered in addition to the forced convection. The thermal expansion coefficient was chosen to be $\beta_T = 8.6 \cdot 10^{-5}\,\text{K}^{-1}$ (calculated after [MIETTINEN 06]).

- Case D: For this simulation feeding flow is considered in addition to the forced convection. Liquid density ρ_l and solid density ρ_s are assumed to be constant independent of temperature and concentration, but different. During solidification the higher solid density leads to a shrinkage-induced feeding flow (ρ_l = 7810 kg·m^{-3} and ρ_s = 8565 kg·m^{-3}).

- Case E: This simulation includes thermal and solutal buoyancy flow in addition to feeding induced flow and forced convection (same constants as in the above described cases).

To distinguish between low and high permeability calculations, the different cases are labelled with L for low permeability or H for high permeability. All figures include the three isotherms $T_{liquidus}$ = 1289 K (①), $T_{solidus}$ = 1230 K (②), and T_{end} =1072 K (③) if nothing further is mentioned.

The General Process

The studied continuous casting process of a CuSn6 alloy starts with the melt preheated to the casting temperature of T_{cast} = 1389 K. The hot melt enters the mold through one nozzle in the center of the casting. Due to the fact that the upper part of the mold is thought to be isulating, cooling starts where the hot melt reaches the water cooled graphite mold. *Figure 4-10a* shows the calculated steady state temperature field of Case A-L. Solidification starts at the liquidus temperature of CuSn6, namely at $T_{liquidus}$ = 1289 K (①, *Figure 4-10a*) and is completed at the end temperature of T_{end} =1072 K (③, *Figure 4-10*). This temperature represents the first peritectic temperature of the binary CuSn system. The third black line between the before mentioned two lines shows the isotherm of the solidus temperature of CuSn6, $T_{solidus}$ = 1230 K (②, *Figure 4-10a*). In *Figure 4-10b* the estimated concentration field of the liquid phase c_l^{Sn} is shown. Based on the model assumptions, the last liquid solidifies with a concentration of 25.5 wt.% Sn at T_{end}. *Figure 4-11a* shows the volume fraction of the columnar phase in Case A-L. It can be seen that in the columnar mushy zone, extending from $T_{liquidus}$ to T_{end}, the volume fraction of the solid varies from 0 to 1. The solid fraction

close to the peritectic temperature ($\alpha+L\rightarrow\beta$) reaches about f_c = 0.95-0.98. Based on the fact that the casting reaches a solid fraction of about f_c = 0.95 at T_{end}, and because the model for the peritectic reactions is still under development, the remaining liquid is assumed to solidify over a small temperature interval at T_{end}.

As the mush is considered to be permeable, melt-flow occurs through the mush. *Figure 4-11b* displays the velocity magnitude field of the continuous casting process simulated in Case A-L. It can easily be seen that the flow velocities in the mush are much smaller compared to the inlet flow velocities. The incoming melt reveals a velocity as high as $\vec{u}_{in}$ = 25 mm·s^{-1}. This large value is a consequence of the constant outlet velocity $\vec{u}_{cast}$ and the overall mass conservation. The developing flow pattern shows a strong inlet jet that reaches the wall almost horizontal (I). Then the jet bends inwards towards the center while slowing down and creating one large vortex on each side of the casting (II). *Figure 4-12* shows on the left hand side the temperature field (as displayed in *Figure 4-10a*) and on the right hand side the velocity vector field of Case C-L overlaid by volume fraction of solid. The colored arrows indicate the integrated flow direction. The growing dendrites in the mushy zone force the flow to slow down by interaction with the liquid. After achieving a certain solid content, the liquid is forced to move with the same velocity as the solid phase due to the drag force acting between the liquid and the columnar phase (III) and the influence of the jet diminishes in the center of the casting (*Figure 4-12*). Although the velocity regime does not create turbulent flow ($\mathrm{Re} \approx 900$), the developing jet plays an important rule for the solute depletion and accumulation during solidification.

Due to microsegregation the Sn concentration in the liquid between the dendrites changes during the solidification process. Since the solute is enriched in the liquid phase, the intensity of the flow field has a huge impact on the alloy distribution in the solidified casting. In general three cases have to be mentioned [FLEMINGS 67A, FLEMINGS 67B, FLEMINGS 67C]:

(i) No relative fluid flow occurs in the interdendritic region. In this case the mixed concentration of the solidified casting is the same as the original alloy concentration.

(ii) The relative velocity of the liquid in the interdendritic region is higher than the casting velocity, and the growing solid is fed by non segregated fresh melt. This situation causes negative macrosegregations.

(iii) The growing dendrites are fed with already segregated melt: Here positive macrosegregation, the so called inverse macrosegregation, occurs.

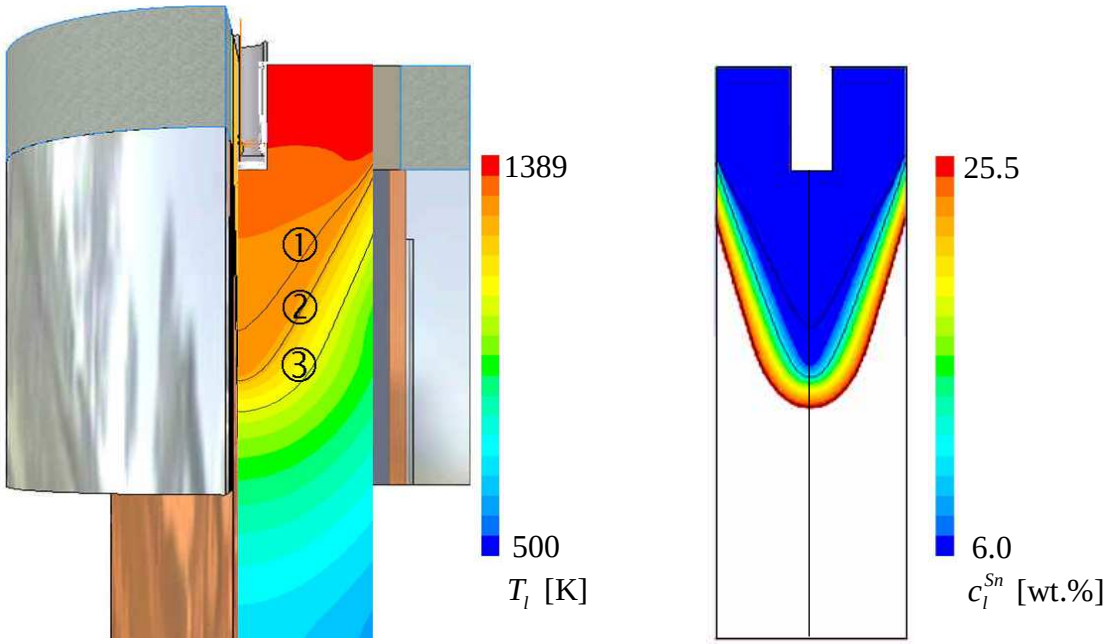

Figure 4-10: (a) Temperature field of the casting T_l is displayed in the case where just inlet flow is considered (Case A-L). (b) Liquid concentration c_l^{Sn} of the casting [wt.%] is shown in the case where just inlet flow is considered (Case A-L). Color scale shows red 25.5 wt.% Sn, and blue 6 wt.% Sn. Black lines: $T_{liquidus}$ =1289 K, $T_{solidus}$ = 1230 K, T_{end} =1072 K.

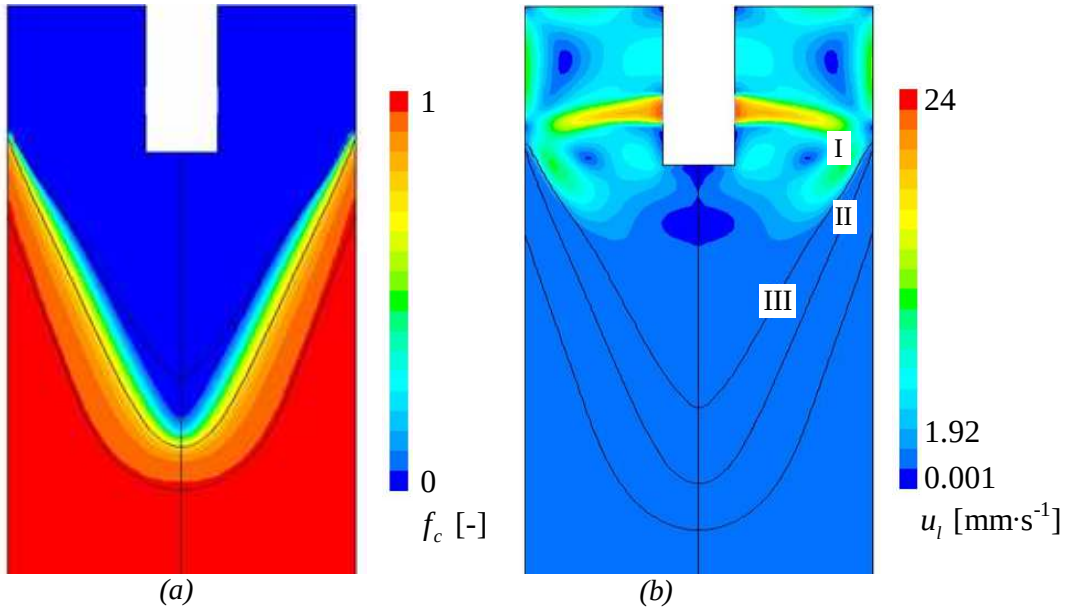

Figure 4-11: (a) Volume fraction of the columnar phase f_c [-] is shown in the case where just inlet flow is considered (Case A-L). (b) Velocity field of the casting [mm·s^{-1}] is displayed for Case A-L. I marks the position where the inlet jet is forming in the inlet region by bending back at the wall. II indicates the region where the vortex reaches into the mushy zone, and III assigns the regions where casting velocity $\vec{u}_{cast}$ is obtained. Black lines: $T_{liquidus}$ = 1289 K, $T_{solidus}$ = 1230 K, T_{end} = 1072 K.

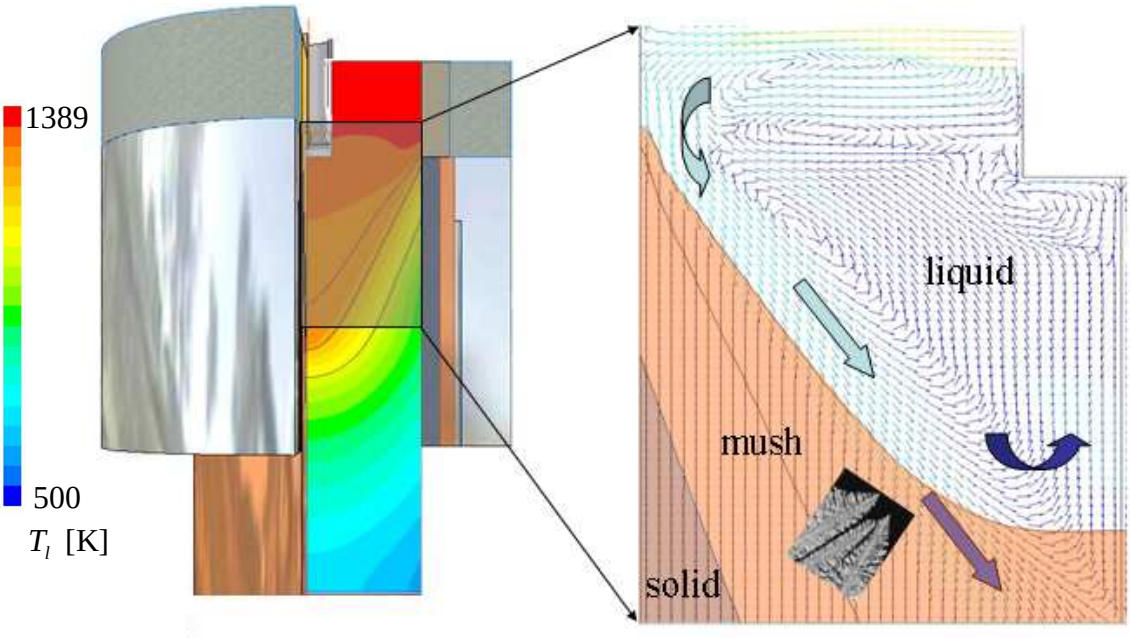

Figure 4-12: *Temperature field T_l as shown in Figure 4-10 and the velocity vector field of the liquid $\vec{u}_l$ in Case C-L, overlaid by the volume fraction of the columnar phase. The big arrows indicate the integrated flow direction. The growing dendrites force the flow to slow down until it reaches casting velocity $\vec{u}_{cast}$. Black lines: $T_{liquidus}$ = 1289 K, $T_{solidus}$ = 1230 K, T_{end} = 1072 K.*

The temperature fields of Case A-L, B-L, C-L, D-L, and E-L are displayed in *Figure 4-23* to compare the obtained temperature distributions. *Figure 4-24* shows the macrosegregation pattern for the cases with low mush permeability (Case A-L, B-L, C-L, D-L, and E-L) and *Figure 4-25* for the cases with high mush permeability (Case A-H, B-H, C-H, D-H, and E-H) as already described. Each field includes arrows indicating the global vector velocity directions.

Jet-Mush Interaction

The simulation of the casting process, where only forced convection is taken into account, shows the influence of the relatively high velocities of the inlet jet on the temperature distribution, the velocity field and the macrosegregation. As mentioned earlier, the inlet jet hits the mold wall close to the region where the first solid is formed, there it bends inwards and forms corresponding vortices. *Figure 4-13* shows the temperature field achieved in Case A-L (*Figure 4-13a*) and Case A-H (*Figure 4-13b*), whereas *Figure 4-14* displays the velocity magnitude of both cases (Case A-L: *Figure 4-13a*, Case A-H: *Figure 4-13 b*). The differences in the position of the isotherms of T_{liquid} = 1289 K (①, *Figure 4-13*) and T_{end} = 1072 K (②, *Figure 4-13*) in both cases are a direct result of the change in the velocity field due to the change in mush permeability. Note that with higher mush permeability (Case H), the vortices caused by the inlet jet are slightly wider and to some extend larger. As a consequence the liquidus isotherm is shifted upwards in the center of the casting. The isotherm representing the end of solidification stays at almost the same level (*Figure 4-11*). *Figure 4-14* shows that the inlet region is the part of the casting that has a velocity magnitude up to $\vec{u}_l \approx 30$ mm·s^{-1}. As soon as the mushy zone is reached, the jet slows down. Now the velocity of the liquid is governed more and more by the casting speed (①, *Figure 4-14*) due to the applied drag force between the columnar phase and the liquid phase.

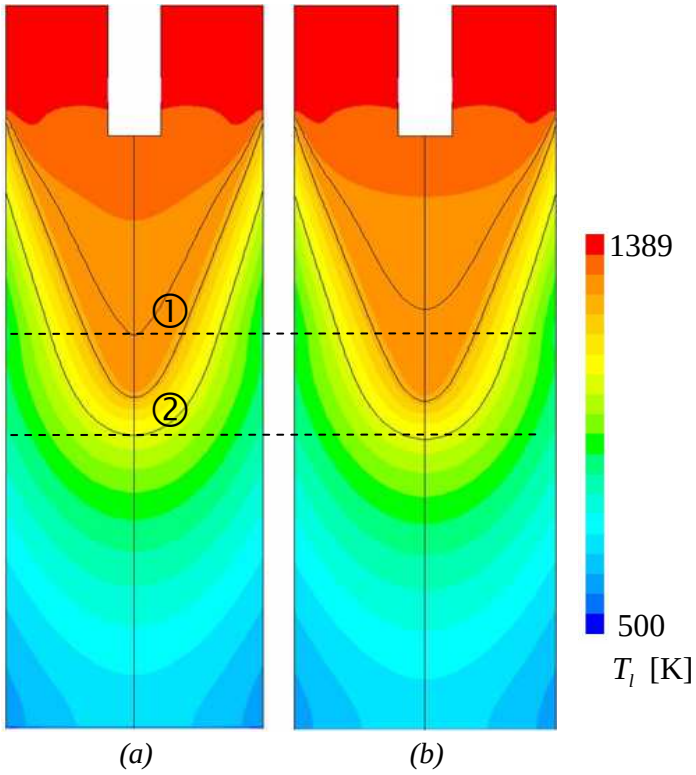

Figure 4-13: Temperature field of the casting T_l in (a) Case A-L and (b) Case A-H. As guidance, the broken lines show ① the position of $T_{liquidus}$ = 1289 K and ② the position of T_{end} = 1072 K in the center of the casting for Case A-L and compare the position of the isotherms for both permeability cases. Black lines: $T_{liquidus}$ = 1289 K, $T_{solidus}$ = 1230 K, T_{end} = 1072 K.

Because of the chosen $\overline{K}_0$, the vortices of the inlet jets penetrate into the mushy zone differently for the L and H cases. In Case A-H the high permeability of the mush allows the liquid to reach deeper into the mush (②, *Figure 4-14*). Therefore, segregated melt is removed from the mushy zone and replaced by non-segregated, 'fresh' melt from the jet vortices. This 'jet-mush' interaction phenomenon takes place in all cases (labeled with I in *Figure 4-24*, *Figure 4-25* for all cases). Its strength depends on the velocity of the jet on the one hand and on the permeability of the mush on the other hand. The higher the mush permeability, the more intensively the jet can meet the mushy zone and wash out an increasing amount of segregated melt. This then results in strong negative surface macrosegregations and more significant positive 'bulk' macrosegregations (*Figure 4-24*, *Figure 4-25*).

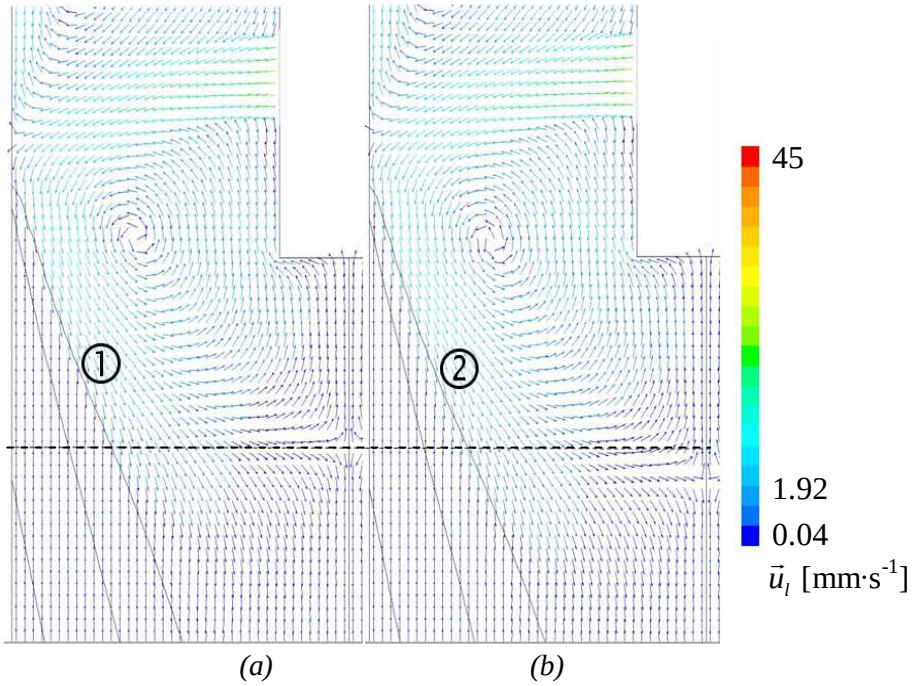

Figure 4-14: Velocity field of the upper part of the casting $\vec{u}_l$ in (a) Case A-L and (b) Case A-H (just inlet flow). With higher mush permeability (Case H), the vortices caused by the inlet jet are slightly wider and to some extend larger and the liquidus isotherm is shifted upwards in the center of the casting (dotted line). The isotherm representing the end of solidification stays at almost the some level. Black lines: $T_{liquidus}$ = 1289 K, $T_{solidus}$ = 1230 K, T_{end} = 1072 K.

Solutal Buoyancy

In addition to the inlet jet, solutal buoyancy convection is taken into account in Case B-L and B-H (labeled with IIa in *Figure 4-16b*, *Figure 4-25b*). The solutal buoyancy driven flow shows no significant influence at the temperature field in Case B-L (*Figure 4-15a*). But, increasing the mush permeability offers more freedom to the flow and therefore changes the temperature distribution in Case B-H (*Figure 4-15b*), which results in a slightly lower isoline for $T_{liquidus}$ = 1289 K (①, *Figure 4-15b*) in comparison to Case B-L, whereas T_{end} = 1072 K (②, *Figure 4-15b*) stays at almost the same level. During solidification the liquid in the mushy zone becomes enriched in solute and thus tends to rise upwards through the mush by solutal buoyancy (labeled with IIa in *Figure 4-16b*). In Case B-L the liquid is not able to move easily between the solidifying dendrites because the low permeability decreases the possibility of convection (*Figure 4-16a*). Hence, in this case an upward motion is not observed and therefore the macrosegregation pattern is not significantly different from that of Case A-L, the jet causes negative segregations right at the wall (*Figure 4-25a*) and slightly positive segregation occurs in the bulk of the casting (which can hardly be seen in *Figure 4-25*, due to the applied color scale). In Case B-H the high mush permeability allows solutal buoyancy flow to occur and therefore the macrosegregation pattern is influenced (labeled with IIa in *Figure 4-25b*).

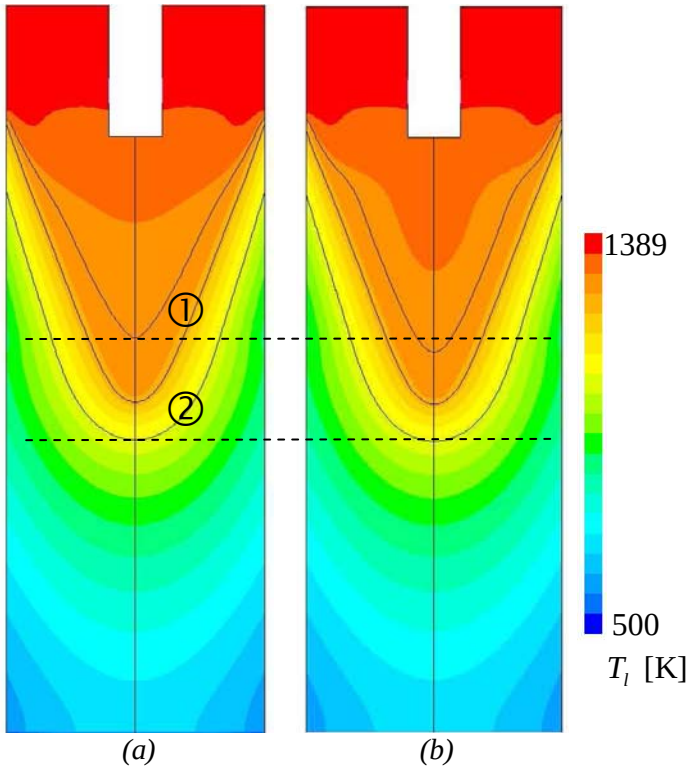

Figure 4-15: Temperature field of the casting T_l in (a) Case B-L and (b) Case B-H. The broken lines mark ① the position of $T_{liquidus}$ = 1289 K and ② the position of T_{end} = 1072 K in the center of the casting in Case B-L. The two lines compare the position of the isotherms for both permeability cases. Black lines: $T_{liquidus}$ = 1289 K, $T_{solidus}$ = 1230 K, T_{end} = 1072 K.

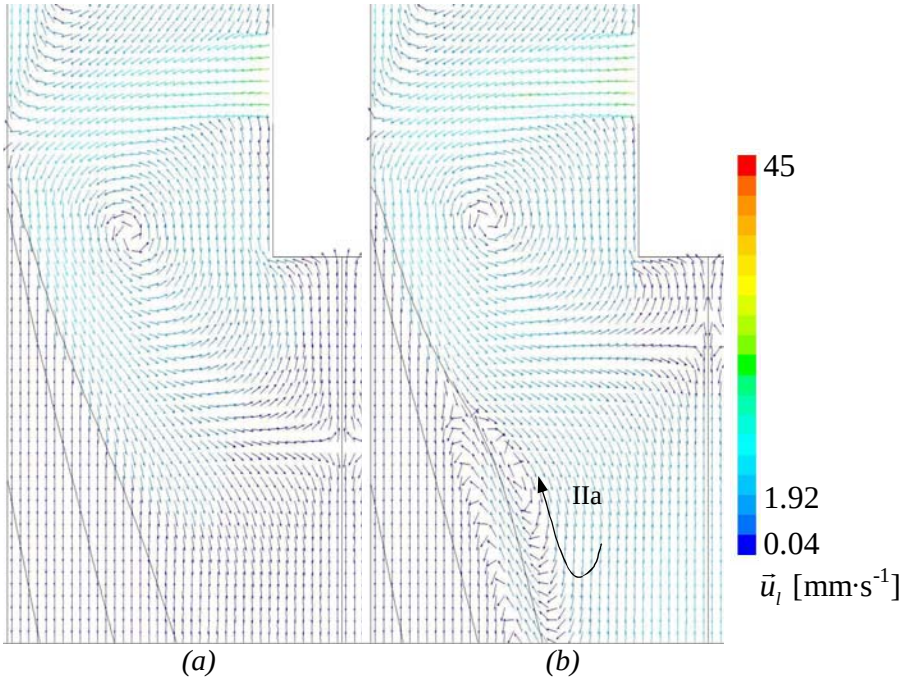

Figure 4-16: Velocity field of the casting $\vec{u}_l$ in (a) Case B-L and (b) Case B-H where inlet flow and solutal convection are considered. IIa marks the upward rising liquid due to solutal buoyancy flow. Black lines: $T_{liquidus}$ = 1289 K, $T_{solidus}$ = 1230 K, T_{end} = 1072 K.

Thermal Buoyancy

In addition to the inlet jet, thermal buoyancy convection is taken into account in Case C-L and Case C-H. This additional flow phenomenon changes the temperature field in the casting noticeably (*Figure 4-17a, b)*. The reason for this is the fact that thermal buoyancy flow strengthens the inlet jet vortex where the cooled melt flows down along the solidification front (labeled with II in *Figure 4-18a, b*). The thermal buoyancy driven downward flow induces an upward flow in the center of the casting. Thus, melt is carried from deep down the melt pool upwards (labeled with III in *Figure 4-18a,b*; *Figure 4-24c*, *Figure 4-25c*) and so the liquidus isoline $T_{liquidus}$ = 1289 K (①, *Figure 4-17b*) is shifted up in comparison to the first two discussed cases, whereas T_{end} = 1072 K (②, *Figure 4-17b*) stays at about the same position as in Case A-L *Figure 4-23*. This enlarges the mushy zone in comparison to Case A. As a consequence the 'jet-mush' interaction is increased and more segregated melt is washed out, which in turn leads to more extensive negative surface macrosegregations compared to Case A (*Figure 4-24a, c, Figure 4-25a,c*). The washed-out segregated melt is then accumulated in the middle of the casting by the flow, which is the reason for the positive macrosegregations in the 'bulk' of the strand (labeled with II in *Figure 4-18a,b; Figure 4-24c*, *Figure 4-25c*). All these effects of the velocity field are strengthened in Case C-H. *Figure 4-18* shows the velocity fields of the upper part of the calculation domain of Case C-L (*Figure 4-18a*) and Case C-H (*Figure 4-18,b*) including the "depth of penetration", indicated by broken black lines. The "depth of penetration" empirically defines the border between areas, where the velocity of the liquid is significantly different from that of the solid phase and those where, both phases move with almost the same speed and direction; that's where the drag caused by the columnar dendrites dominates. The "depth of penetration" corresponds to about f_c = 0.5 of the columnar fraction in Case C-H and f_c = 0.2 in Case C-L. Due to a large "flown-through" mush area, the distribution of the macrosegregations is much more pronounced in Case C-H. In the cases considered so far macrosegregations are frozen below the "depth of penetration" (broken black line in *Figure 4-24c, Figure 4-25c*).

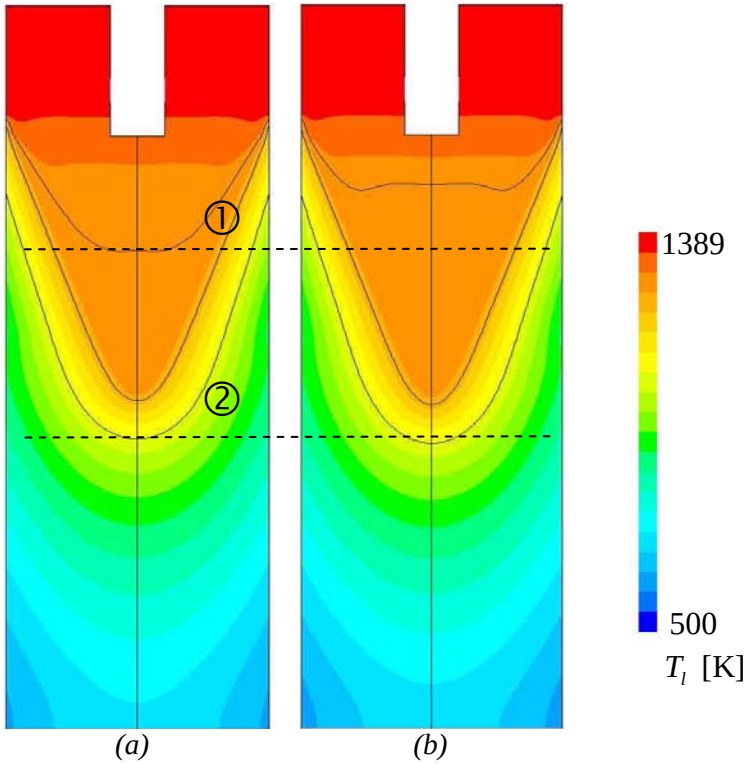

Figure 4-17: Temperature field T_l (a) in case with thermal buoyancy flow (Case C-L), and (b) in case with higher permeability (Case C-H). The broken lines show ① the position of $T_{liquidus}$ = 1289 K and ② the position of T_{end} = 1072 K at the center of the casting in Case C-L. The two lines compare the position of the isotherms for both permeability cases. Black lines: $T_{liquidus}$ = 1289 K, $T_{solidus}$ = 1230 K, T_{end} = 1072 K.

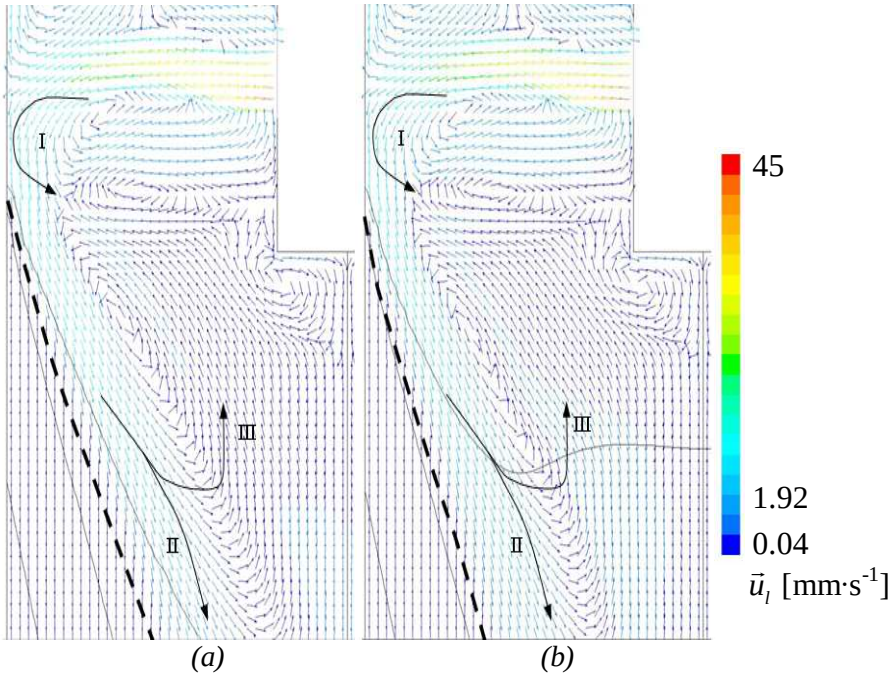

Figure 4-18: Velocity field $\vec{u}_l$ (a) in the case with thermal buoyancy flow (Case C-L), (b) the same case with a higher permeability (Case C-H). Broken black lines indicate the "depth of penetration". Black lines: $T_{liquidus}$ = 1289 K, $T_{solidus}$ = 1230 K, T_{end} = 1072 K.

Feeding Flow

Including feeding flow in Case D-L and Case D-H (*Figure 4-19* and *Figure 4-20*) in addition to the forced convection of the inlet flow, the flow pattern changes in a way that a second higher velocity field appears in the mushy zone, right in the middle of the casting. This also induces a significant change in the temperature fields of both cases shown in *Figure 4-19*. The isotherms are moved downwards (*Figure 4-19*) compared to Case A-L due to the fact that more liquid is needed to feed the solidification shrinkage (*Figure 4-23*). In Case D-H the high mush permeability causes a broadening of the mushy zone, which is shown by an upward movement of $T_{liquidus}$ (① in *Figure 4-19* and *Figure 4-20*). In addition the flow field shows a deeper penetration of the flow into the mushy zone in Case of D-H in comparison to Case D-L.

Up until now, surface macrosegregations are predicted to be negative and macrosegregations within the casting are predicted to be either negative or positive. However, if shrinkage-induced feeding flow is included and thermo- solutal buoyancy driven flow is ignored, the situation changes. In Case D-L the surface macrosegregations turned out to be positive and the macrosegregations in the center negative (*Figure 4-25d*). Feeding flow is always directed from the dendrite tip towards its roots and thus carries segregated melt into the mush. Since the early work of Flemings in 1967 [FLEMINGS 67A, FLEMINGS 67B, FLEMINGS 67C], this phenomenon is known to produce positive macrosegregation at the surface of a casting, the so-called inverse segregation. Exactly this happens in Case D-L (labeled with IV in *Figure 4-24d*). However, in Case D-H the influence of the jet is so high that negative macrosegregations still occur at the wall and the positive ones are moved to adjacent zones (labeled with IV in *Figure 4-25d*). At the center of the cylindrical casting the dendrite tips approach each other and form a ring which closes as solidification proceeds. Besides, a relatively large mush area is solidifying at the center and thus a huge amount of melt is needed to feed the corresponding shrinkage. This feeding flow causes the melt to be sucked into the solidifying mush through the closing 'ring of dendrites' and a strong relative downward velocity occurs in the center of the casting (labeled with V in *Figure 4-24d*). That is why the solidifying dendrites are fed with less- or non-segregated 'fresh' melt from the melt pool and negative macrosegregations occur in the central region of the casting. In addition, heat is carried downwards with the feeding flow which results in a lower position of the isotherms, especially at the casting center. Due to the low permeability in Case D-L this phenomenon is more pronounced compared to Case D-H. In the latter case, the large $\overline{K}_0$ makes feeding through the mush easier. Therefore, the central downward flow is significantly broader and slower, which broadens and decreases the negative center line segregation (labeled with V in *Figure 4-25*).

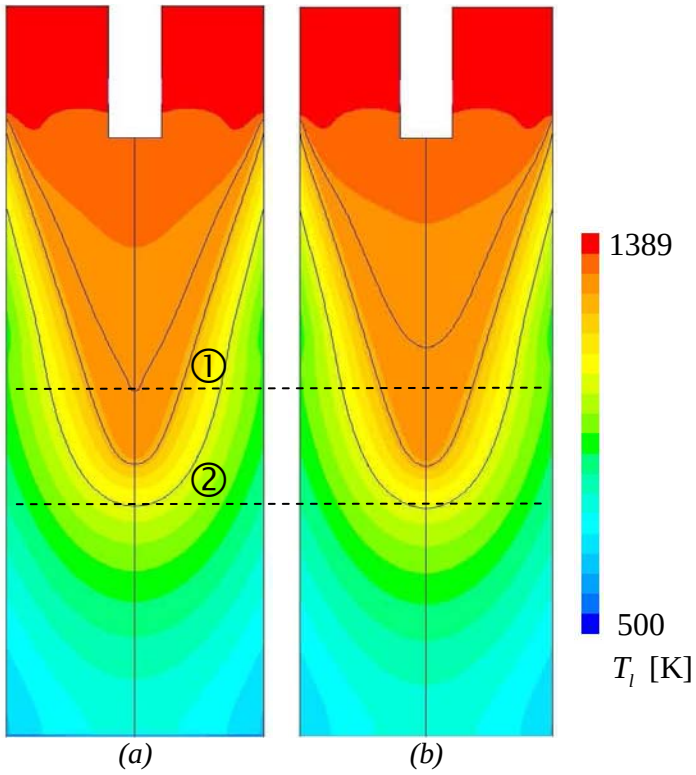

Figure 4-19: Temperature field T_l (a) in the case with feeding flow (Case D-L), (b) the same case with a higher permeability (Case D-H), the broken lines show ① the position of $T_{liquidus}$ = 1289 K and ② the position of T_{end} = 1072 K in the center of the casting in Case D-L. The two lines compare the position of the isotherms for both permeability cases.
Black lines: $T_{liquidus}$ = 1289 K, $T_{solidus}$ = 1230 K, T_{end} = 1072 K.

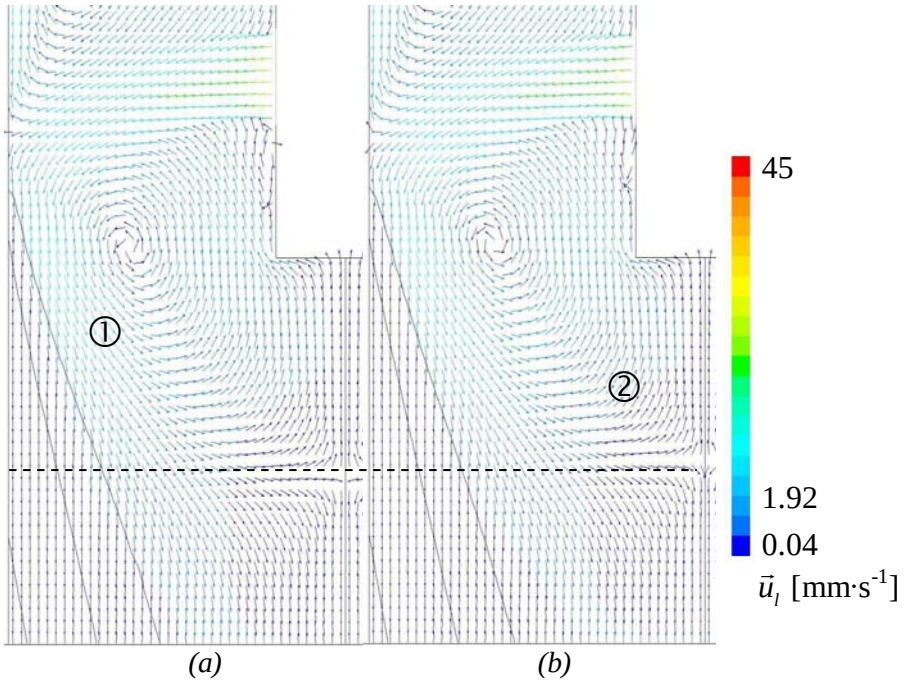

Figure 4-20: Velocity field $\vec{u}_l$ (a) in the case with feeding flow Case D-L, (b) and Case D-H. Black lines: $T_{liquidus}$ = 1289 K, $T_{solidus}$ = 1230 K, T_{end} = 1072 K.

Relative Importance of the Different Phenomena

So far, the presented cases give separate sets of information about the influence each considered convection phenomenon has on the solidification process. For simulations including thermo-solutal buoyancy and feeding flow in addition to the forced convection of the inlet jet, superposition of the different phenomena is expected, which indeed can be seen in Case E-L and Case E-H (*Figure 4-21*, *Figure 4-22*). The isolines in Case E-L (*Figure 4-21a*) reflect a strong influence of both, thermal convection and feeding flow. Hence, the melt pool is broadened and the liquid has more freedom to move, which can be seen by looking at the flow field in *Figure 4-22a*. In Case E-H (*Figure 4-21b*) all four studied flow phenomena are strengthened due to the higher permeability. In this case the solutal buoyancy driven flow plays an additional role in solidification. However, an upward flow caused by solutal buoyancy within the mush is not observed in the combined case. It seems that the opposite downward thermal buoyancy has overwhelmed the upward solutal buoyancy. This can also be seen in the position liquidus isotherm of Case E-H (*Figure 4-21*) being shifted upwards in the center of the casting, but not as much as in the purely thermal case, Case B-H (compare *Figure 4-16*). It is obvious that this change in the flow pattern has a huge effect on the solute distribution in the solidified casting. In Case E-L positive surface macrosegregations are predicted (*Figure 4-24e*).

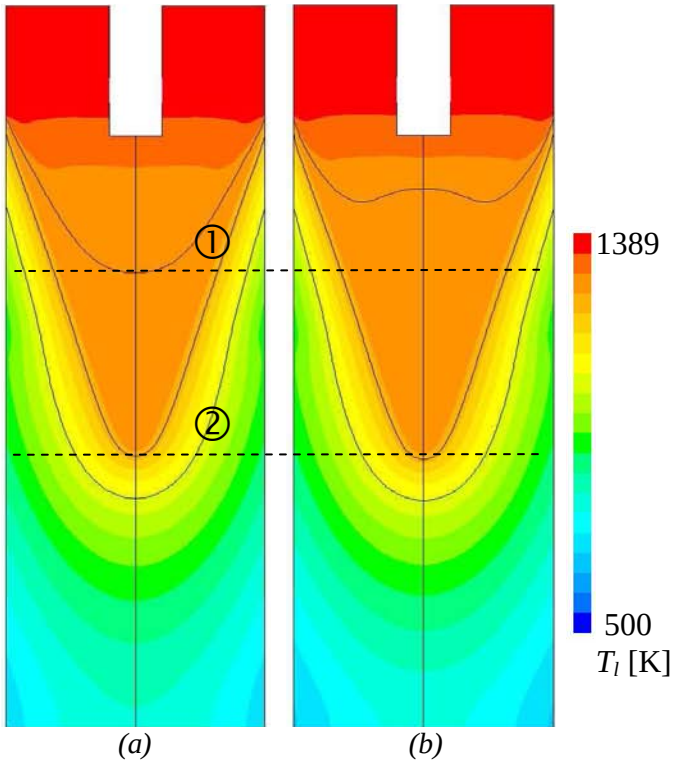

Figure 4-21: Temperature field of the casting T_l (a) in the combined case which considers inlet jet, solutal and thermal buoyancy, and feeding flow (Case E-L), (b) the same case with a higher permeability (Case E-H), the broken lines show ① the position of $T_{liquidus}$ = 1289 K and ② the position of T_{end} = 1072 K in the center of the casting in Case E-L and compare therefore the position of the isotherms for both permeability cases. Black lines: $T_{liquidus}$ = 1289 K, $T_{solidus}$ = 1230 K, T_{end} = 1072 K.

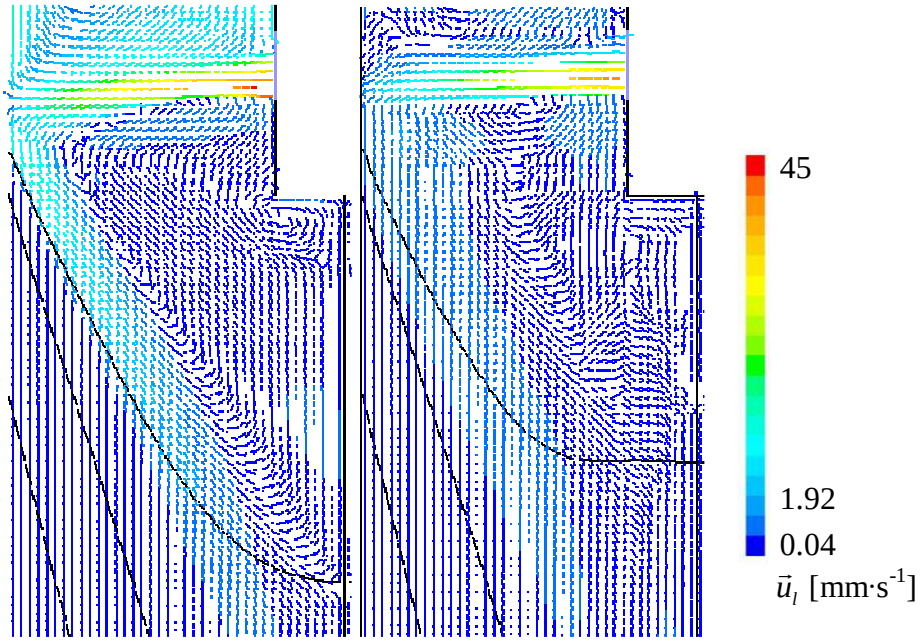

Figure 4-22: Velocity field at the inlet region $\vec{u}_l$ [mm·s^{-1}] (a) for the case which considers inlet jet, solutal and thermal buoyancy, and feeding (Case E-L), (b) for the same case with a higher permeability (Case E-H). Black lines: $T_{liquidus}$ = 1289 K, $T_{solidus}$ = 1230 K, T_{end} = 1072 K.

Here, the impact of the feeding flow on its formation is decreased by the inlet jet and the thermal buoyancy flow. Right at the center line strong negative macrosegregations appear which are caused by the feeding flow but smoothed by the additional effect of thermal convection. In Case E-H the influence of the jet is so high that the negative surface macrosegregation is not overwhelmed by the effect of feeding flow. Therefore, in this case the macrosegregation pattern results in negative surface and centerline segregations and positive ones in the bulk of the casting (*Figure 4-25e*).

Impact of Mush Permeability on the Formation of Macrosegregations

In the implemented case two different values of $\overline{K}_0$ have been considered for the calculation of the Blake-Kozeny-type mush permeability. Since no values for Copper alloys are available, those values are approximated from measurements on Aluminum alloys [APELIAN 74]. *Figure 4-24* and *Figure 4-25* show the computed macrosegregation patterns of the studied cases for a mush permeability assumed to be characterized by $\overline{K}_0 = 1.4 \cdot 10^{-5}$ and $\overline{K}_0 = 1.4 \cdot 10^{-3}$. By comparing these two figures it can be seen that, in general, an increase of $\overline{K}_0$ leads to more pronounced macrosegregations.

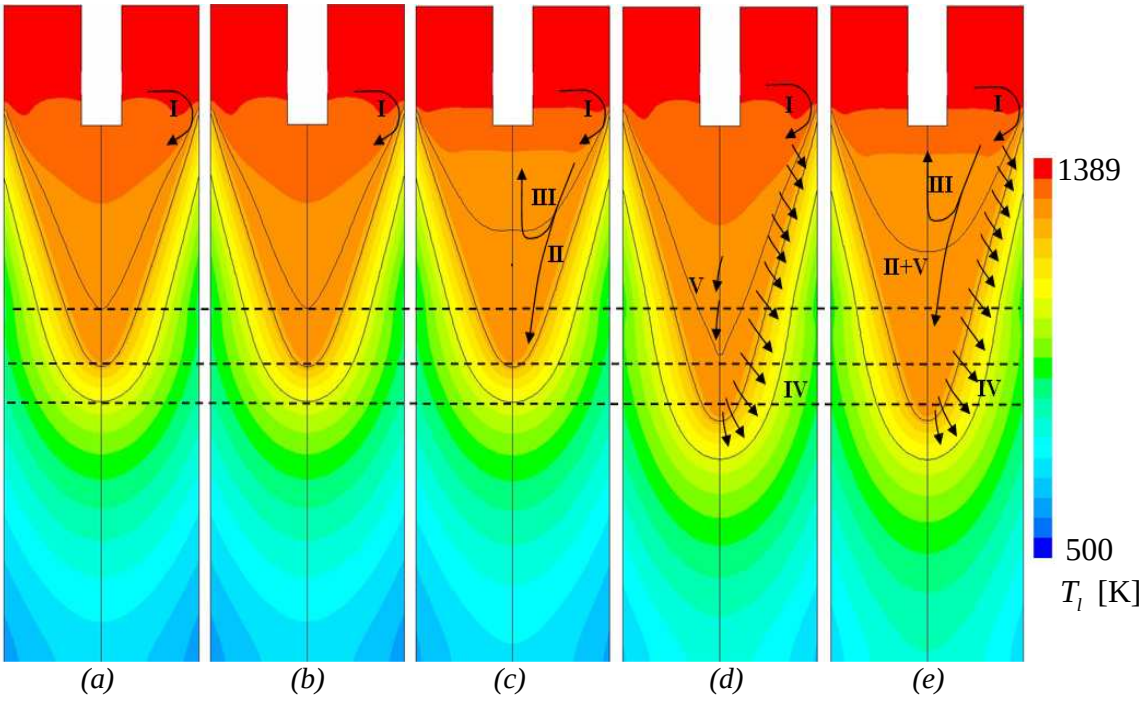

Figure 4-23: Steady-state distributions of the liquid temperature T_l are displayed for the five different cases with lower Blake-Kozeny-type mush permeability where $\overline{K}_0 = 1.4 \cdot 10^{-5}$: (a) without feeding and thermo-solutal buoyancy flow (Case A-L); (b) only solutal buoyancy flow (Case B-L); (c) only thermal buoyancy flow (Case C-L), and (d) only feeding flow (Case D-L), (e) including feeding and thermo-solutal buoyancy flow (Case E-L). The broken lines show the position of $T_{liquidus}$ = 1289 K, $T_{solidus}$ = 1230 K and T_{end} = 1072 K at the center of the casting for Case A-L and compare therefore the position of the isotherms for all Cases. Black lines: $T_{liquidus}$ = 1289 K, $T_{solidus}$ = 1230 K, T_{end} = 1072 K.

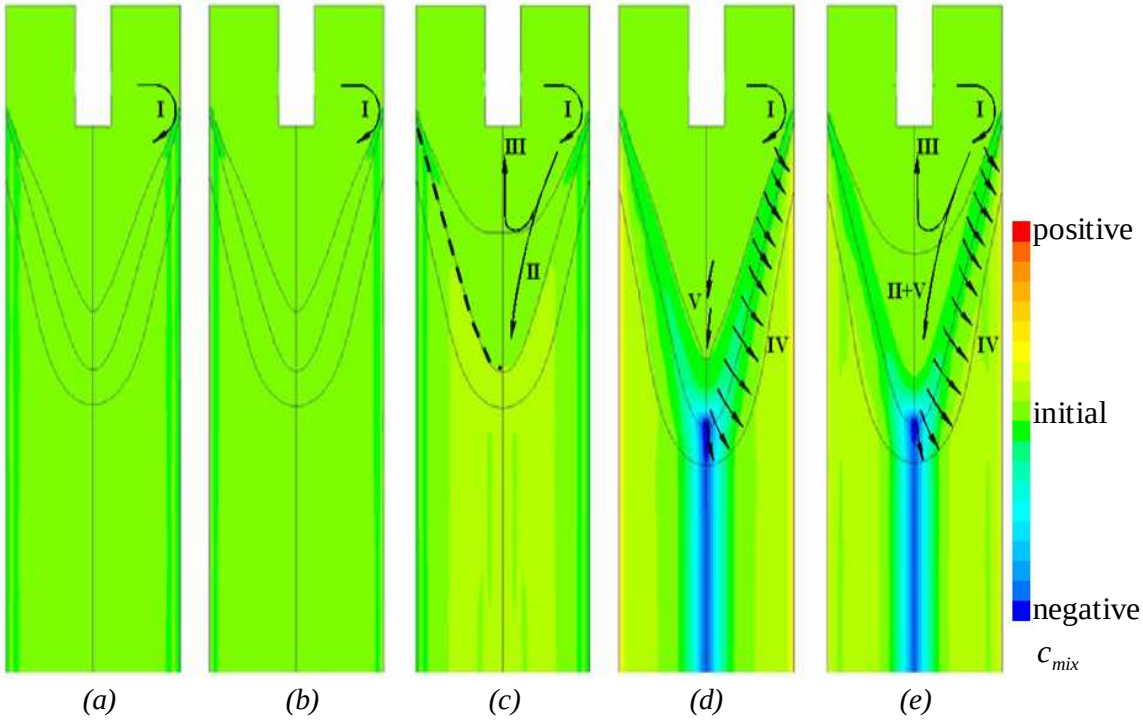

Figure 4-24: Steady-state distributions of the mixture concentration c_{mix} of Sn in the five different cases with low Blake-Kozeny-type mush permeability ($\overline{K}_0$ = 1.4 10^{-5}). The displayed range is c_{mix} = 5.425-6.575 wt.% Sn. (a) without feeding and thermo-solutal buoyancy flow (Case A-L), (b) with solutal buoyancy flow (Case B-L), (c) with thermal buoyancy flow (Case C-L) and (d) with feeding flow (Case D-L). Case E-L in (e) includs feeding and thermo-solutal buoyancy driven flow. Bright green represents the initial alloy concentration, yellow to red represents positive, and blue negative macrosegregations. The flow pattern is indicated by arrows.Dark lines are the isotherms of $T_{liquidus}$ = 1289 K, $T_{solidus}$ = 1230 K, T_{end} = 1072 K.

The flow from the jet and the flow caused by the withdrawal of the strand are the only convection mechanisms present. However, even in these two cases the negative surface macrosegregations and the slightly positive 'bulk' macrosegregations can be observed with the applied color scale. The comparison only shows very small positive segregations in Case A-L, but more significant ones in Case A-H. Solutal buoyancy does not affect the macrosegregation pattern in case of low $\overline{K}_0$ (*Figure 4-25a*). In Case B-H the high mush permeability enables the enriched liquid to move upwards through the mush till it impinges on the jet flow (labeled with IIa in *Figure 4-25b*). This causes positive macrosegregations at the corresponding position. The solutal buoyancy driven flow out of the middle of the strand causes negative center line segregations (labeled with IIa in *Figure 4-25b*) positive macrosegregations at the corresponding position.

When considering thermal buoyancy flow in Case C-L and C-H, the 'jet-mush' interaction is strengthened. This stronger flow pattern leads to more extensive negative surface macrosegregations compared to Case A (*Figure 4-24a, c, Figure 4-25a, c*). The washed-out segregated melt from the surface areas is accumulated by the flow in the middle of the casting. Thus, positive macrosegregations in the 'bulk' of the strand are predicted (labeled with II in *Figure 4-24c* and *Figure 4-25c*). The thermal buoyancy driven downwards flow induces upward flow in the center of the casting. With larger mush permeability, this even leads to upward transportation of washed-out alloying elements. Besides, in Case C-H (*Figure 4-25c*) the high mush permeability leads to significantly

stronger macrosegregations for both, negative ones at the wall and positive ones in the casting's center.

The simulation of Case D-L (labeled with IV in *Figure 4-24d*) predicts positive macrosegregations, namely inverse macrosegregations, at the wall, and negative ones in the center of the casting which is described in more details later. In Cases A, B, and C, the increase of the mush permeability was the reason for the strengthening of the forming macrosegregations. However, in Case D the increased mush permeability causes a total change in the macrosegregation pattern! On the one hand the influence of the jet is so high that negative macrosegregations occur at the wall and the positive ones are moved to adjacent zones (labeled with IV in *Figure 4-24d*), and on the other hand, the higher permeability makes feeding through the mush easier, and therefore the area between the solidifying dendrites in the center of the casting is not as small in Case D-H as in Case D-L. This leads to less pronounced but broadened negative macrosegregations in the center line (labeled with V in *Figure 4-25c*).

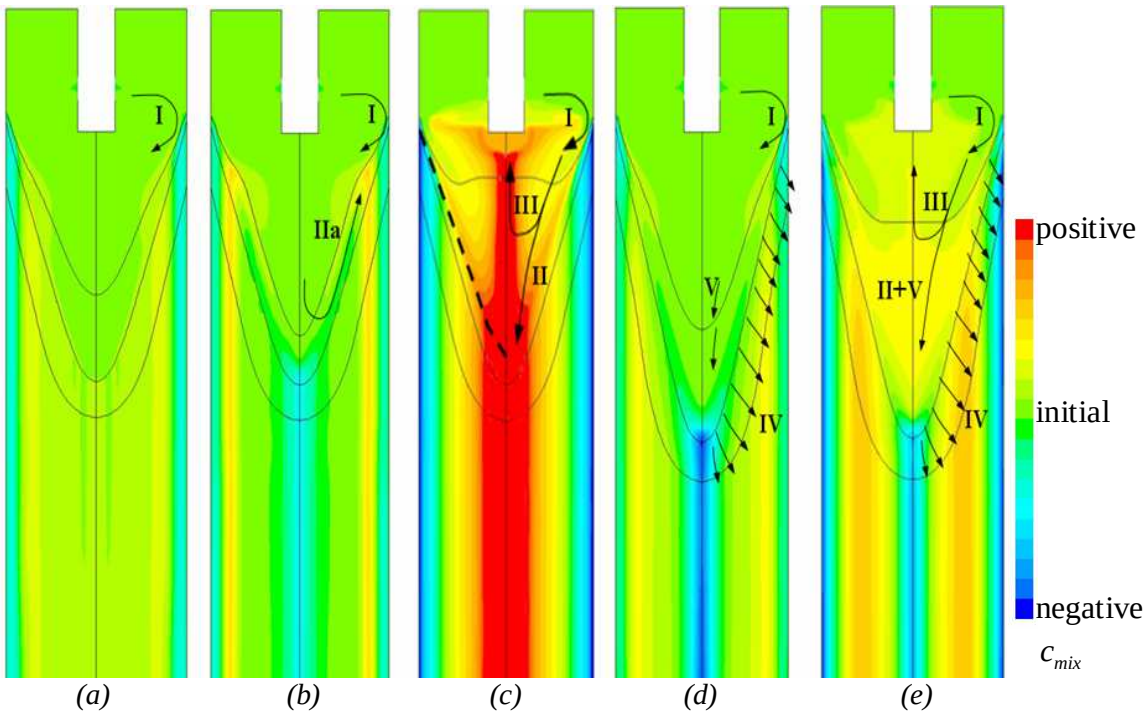

Figure 4-25: Steady-state distributions of the mixture concentration c_{mix} of Sn in the five cases with a higher Blake-Kozeny-type mush permeability ($\overline{K}_0$=1.4·10^{-3}). The displayed range is c_{mix} = 5.425-6.575 wt.% Sn. (a) without feeding and thermo-solutal buoyancy flow (Case A-H), (b) only solutal buoyancy flow (Case B-H), (c) only thermal buoyancy flow (Case C-H) and (d) only feeding flow (Case D-H), (e) including feeding and thermo-solutal buoyancy flow (Case E-H). Bright green represents the initial alloy concentration; yellow to red represents positive and blue negative macrosegregations. Flow patterns are indicated by arrows. Dark lines are the isotherms of $T_{liquidus}$ = 1289 K, $T_{solidus}$ = 1230 K, T_{end} = 1072 K.

In Case E all four flow phenomena are included. This leads to the prediction of positive macrosegregations at the surface and negative ones at the center line in Case E-L. Here, the impact of feeding flow on the formation of macrosegregation is decreased by the inlet jet and the thermal buoyancy flow. Case E-H shows three significant differences compared to Case E-L. Firstly, the influence of the inlet jet is so large that negative surface segregations can be observed. Secondly, the observed positive macrosegregations

in the bulk are stronger and broader compared to Case E-L. This is caused by a strengthening of the macrosegregations due to thermo-solutal buoyancy flow. Thirdly, the negative center line macrosegregations are not as pronounced as in Case E-L. In the center line of Case E-H, the strong positive macrosegregations caused by thermal convection (*Figure 4-25c*) are overwhelmed by feeding flow (*Figure 4-25b, d*).

Further permeability studies

Since the permeability of the mushy zone has a big impact on the macrosegregation in the solidified strand further studies have been performed to study the influence of the value $\overline{K}_0$ for the bronze continuous casting and to see if the already discussed tendency of macrosegregation is valid for an expanded range of $\overline{K}_0$. Therefore two additional values for the empirical factor in the Blake-Kozeny expression (equation 4.19) have been considered, which are $\overline{K}_0 = 1.4 \cdot 10^{-2}$ and $\overline{K}_0 = 1.4 \cdot 10^{-4}$, in addition to the already used ones $\overline{K}_0 = 1.4\ 10^{-5}$ and $\overline{K}_0 = 1.4 \cdot 10^{-3}$. The simulations include thermal and solutal buoyancy flow in addition to feeding induced flow and forced convection. The solutal expansion coefficient and the thermal expansion coefficient are chosen as before and the discussion is based on the results taken after reaching steady state. *Figure 4-26* shows the steady state distributions of the mixture concentration c_{mix} of Sn for the four permeability cases: (a) $\overline{K}_0 = 1.4 \cdot 10^{-5}$ (low), (b) $\overline{K}_0 = 1.4 \cdot 10^{-4}$ (medium), (c) $\overline{K}_0 = 1.4 \cdot 10^{-3}$ (high), and (d) $\overline{K}_0 = 1.4 \cdot 10^{-2}$ (highest). Green color represents the initial alloy concentration, yellow to red color positive and blue color negative macrosegregations. In general it can be seen that macrosegregation observed in the first two permeability studies is confirmed. Namley, that the lower the permeability of the mush is considered to be, the lower are the observed maximum and minimum macrosegregations. *Figure 4-27* shows the macrosegragation profiles at the outlet of the four cases as displayed in *Figure 4-26*. All cases in spite of the case with the low permeability result in negative macrosegregations at the wall due to the string influene of the inlet jet. Besides, the influence of feeding is large enough to keep negative macrosegregations in the center line for all cases. However, with higher permeability feeding is easier in the center and the negative segregations are decreased. The influence of the other phenomena like thermo-solutal convection and forced inlet convection are increased with increasing mush permeability and therefore the overall macrosegregation in the strand gets more inhomogenuous. According to the performed study, the lowest mush permeability shows the best agreement with the observed macrosegregation pattern in industry as discussed in chapter 4.3 which is the reason that the following studies for 2D ternary and 3D binary cases are performed with this permeability value.

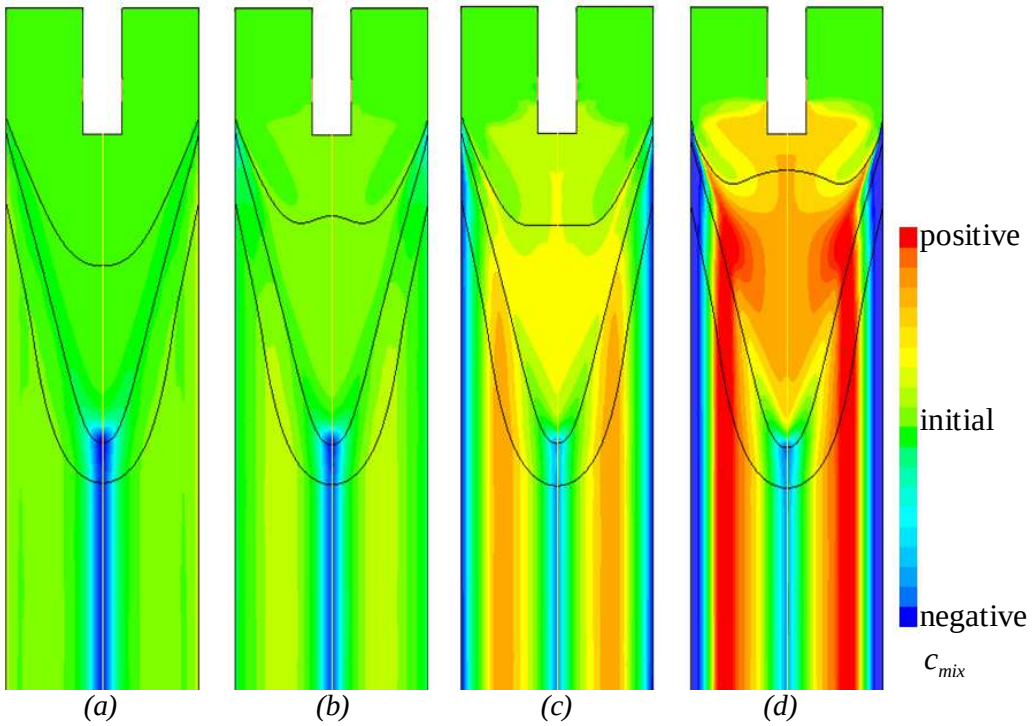

Figure 4-26: Steady-state distributions of the mixture concentration c_{mix} of Sn for four permeability cases in the range of $\underline{c}_{mix}$ = 5.425-6.575 wt.% Sn. (a) $\overline{K}_0 = 1.4 \cdot 10^{-5}$ (low), (b) $\overline{K}_0 = 1.4 \cdot 10^{-4}$ (medium), (c) $\overline{K}_0 = 1.4 \cdot 10^{-3}$ (high), and (d) $\overline{K}_0 = 1.4 \cdot 10^{-2}$ (highest). Bright green represents the initial alloy concentration, red represents positive, and blue negative macrosegregations. Black lines: $T_{liquidus}$ = 1289 K, $T_{solidus}$ = 1230 K, T_{end} = 1072 K.

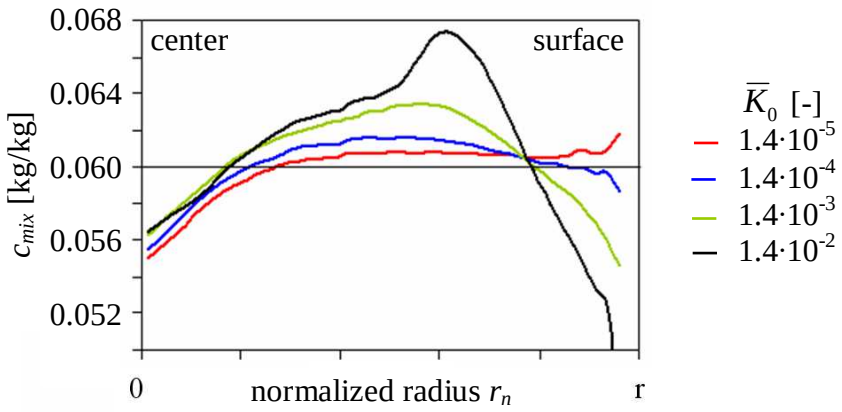

Figure 4-27: Comparison of c_{mix} profiles at the outlet of the solidified strand for the four applied $\overline{K}_0$ values as shown in Figure 4-26. Higher permeability leads to stronger negative and positive macrosegregations in the solidified strand. Since the influence of the inlet jet is increasing with higher mush permeability, the former positive inverse segregation at the wall is turned to negative macrosegregation.

Influence of the Casting Velocity on the Macrosegregation Destribution

Additionally a study has been performed to estimate the relative importance of the casting speed on the macrosegregation pattern (here $\overline{K}_0 = 1.4 \cdot 10^{-5}$). To ignore the influence of the inlet jet, the inlet is thought to be at the top of the geometry lasting over the whole diameter of the calculation domain (①, *Figure 4-28*). Besides, the insulating condition at the upper part of the mold was ignored and with that the calculations start to cool direct at the corner of inlet and wall (②, *Figure 4-28*). For these calculations the end of solidification is not at T_{end}, as in the permeability study, but at a defined volume fraction of the columnar phase, namely at $f_c = 0.99$. That is the reason why there are still changes in the mixture concentration visible below the last shown isoline T_{end}.

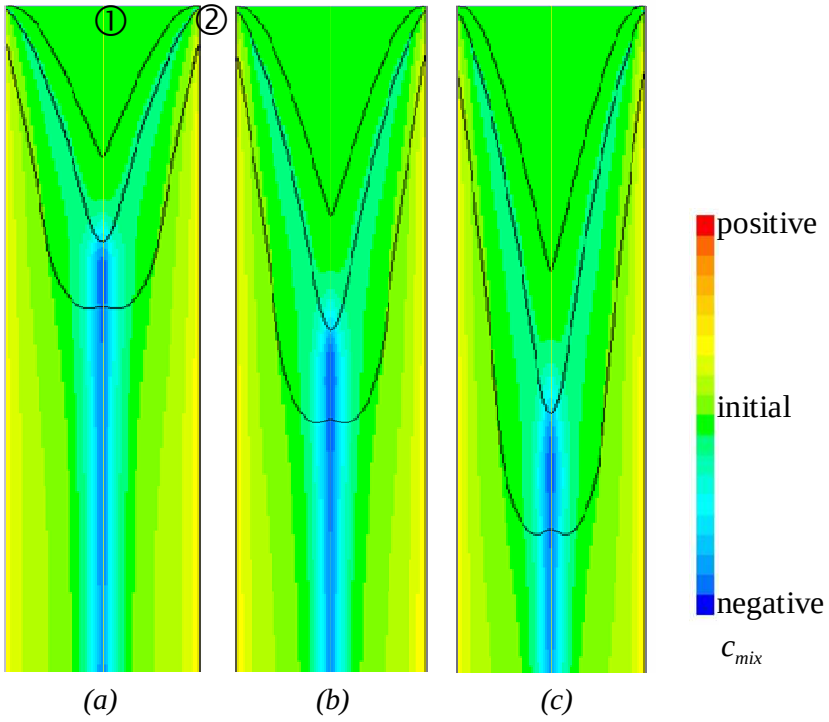

Figure 4-28: Steady-state distributions of the mixture concentration c_{mix} of Sn for three different casting velocities $\vec{u}_{cast}$ = (a) 1.44 mm·s^{-1}, (b) 1.92 mm·s^{-1}, and (c) 2.40 mm·s^{-1}. For these calculations just feeding flow is considered. Bright green represents the initial alloy concentration, red represents positive, and blue negative macrosegregations.
Black lines: $T_{liquidus}$ = 1289 K, $T_{solidus}$ = 1230 K, T_{end} = 1072 K.

For the study on the influence of the casting velocity three calculations have been performed which consider just feeding flow (as described in Case D, permeability study). For these cases a casting velocity of $\vec{u}_{cast}$ = *(a)* 1.44 mm·s^{-1}, *(b)* 1.92 mm·s^{-1}, and *(c)* 2.40 mm·s^{-1} is considered. *Figure 4-28* displays the steady-state distributions of the mixture concentration c_{mix} of Sn for the three cases. Bright green color represents the initial alloy concentration, red color positive and blue color negative macrosegregations. *Figure 4-29* shows a comparison of the c_{mix} profiles of Sn at the outlet of the casting for the three applied casting velocities as displayed in *Figure 4-28*. Based on this study it can be seen that the strength of macrosegregation in the center of the casting decreases with casting speed for the three applied casting velocities. The strength of the positive macrosegregation at the wall is not appearantly influenced by the casting speed in the studied cases (*Figure 4-29*).

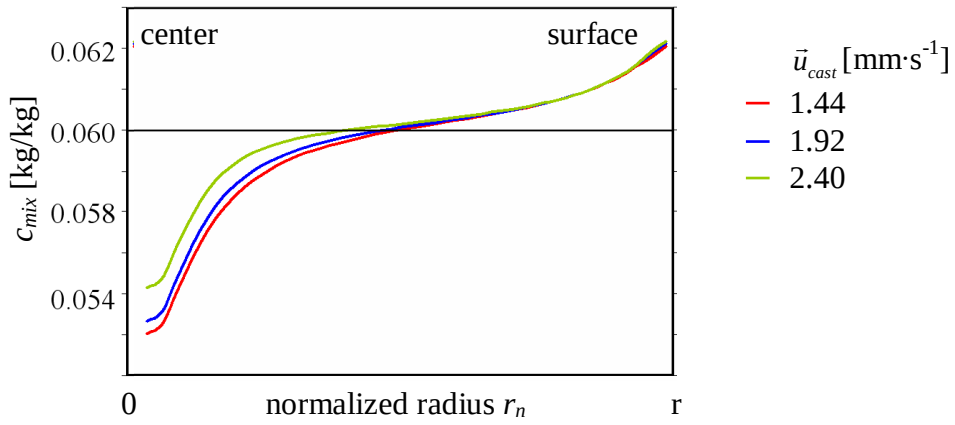

Figure 4-29: Comparison of the c_{mix} distribution of Sn at the outlet for the three applied casting velocities as displayed in Figure 4-28. For these calculations just feeding flow is considered as described before. The strength of the macrosegregation in the center of the casting decreases with casting speed, the positive segregation at the wall is not affected significantly by the change in casting speed.

4.2.3 3D Axis Symmetric Simulations for CuSn6

In industry besides round formats rectangular molds are used for continuous casting of bronze. An important part of the production is based on a process where rectangular two meter long semi continuous casting blocks are cast. This specific industrial process is studied by performing experimental investigations in a laboratory scale. The numerical simulations discussed in the following are based on this laboratory process. Due to the fact that the geometry has a rectangular shape, the simulations have been performed in 3D using the same numerical model as described in chapter 4.1.2.

Definition of the Benchmark

For the 3D calculations a casting velocity of $\vec{u}_{cast}$ = 1.66 mm·s^{-1} and a casting temperature of T_{cast} = 1523.5 K were taken. *Figure 4-30* displays the mold and *Figure 4-31* the grid and the boundary conditions where ① indicates the position of the inlet where a pressure inlet is taken. ② shows the first part of the mold where a temperature T_{cast} = 1523.5 K is applied at the wall. ③ indicates the second part of the mold which is assumed to be adiabatic, ④ marks the third part of the mold where a temperature T_{wall} = 1248 K is taken, and ⑤ assigns a second adiabatic region. ⑥ indicates the position of the start of the secondary cooling zone. For this part a heatflux of H_1 = -789000 W·m^{-2} was applied at the wall. The following two parts ⑦ and ⑧, have two different heatflux values at the wall which are H_2 = - 645000 W·m^{-2} and H_3 = -463000 W·m^{-2}. ⑨ shows the position of the outlet where a velocity outlet with $\vec{u}_{cast}$ = 1.66 mm·s^{-1} has been considered. The mold wall is assumed to move with casting velocity with slip condition for the liquid phase and non-slip condition for the columnar phase.

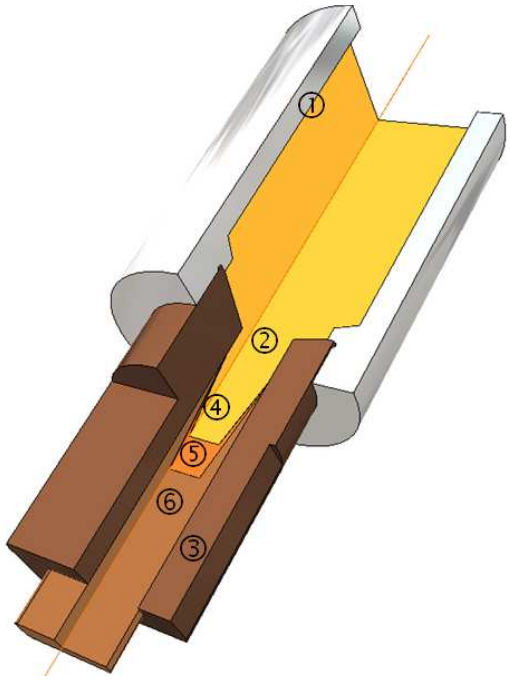

Figure 4-30: Laboratory geometry. Here ① marks the copper mold, acting as a tundish, ② the position of the inlet of the calculation, and ③ the secondary cooling zone. ④ indicates the liquid region, ⑤ the mushy zone, and ⑥ the solidified strand.

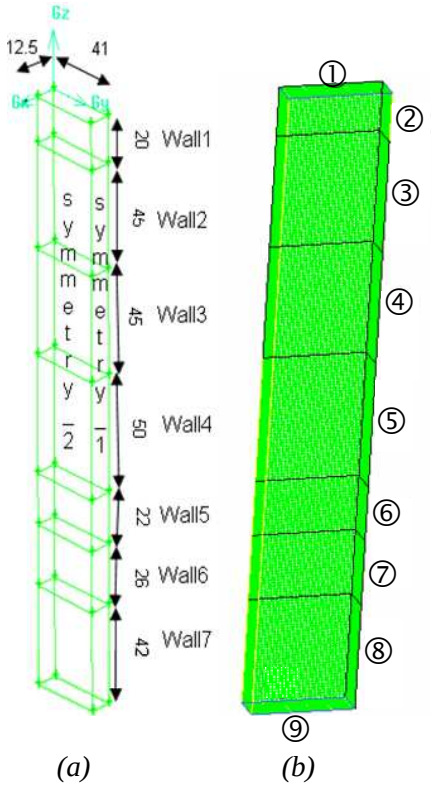

Figure 4-31: (a) and (b) display the grid of the geometry [mm]. ① marks the position of the inlet, ② to ⑤ indicate the mold where primary cooling takes place. ⑥ to ⑧ show the position of the secondary cooling zone and ⑨ of the outlet.

For the calculation one quarter of the 3D geometrie is calculated and therefore two symmetrie planes are considered. The grid has a size of 66330 cells and the simulation was started with hot melt T_{init} = 1523.5 K and a casting speed of $\vec{u}_{cast}$ =1.66 mm·s^{-1}. The presented results are taken after reaching a steady state. Feeding flow, thermal and solutal buoyancy flow, and inlet flow are taken into account. For the empirical factor in the Blake-Kozeny expression from equation 4-19 $\overline{K}_0$ = 1.4·10^{-5} has been considered. The material data and numerical settigs are applied as in the 2D simulation (see chapter 8).

Results and Discussion

The simulated continuous casting process of CuSn6 starts with the melt preheated to the casting temperature of T_{cast} = 1523.5 K. The following two figures visualize the estimated temperature distribution in steady state. *Figure 4-32a* shows the laboratory casting mold with the calculated temperature field that indicates the location of the calculation domain within the casting process. *Figure 4-32b* displays the calculated temperature field T_l [K] at the symmetry planes in the center of the geometrie (depth and width). Here ① indicates the iso-surface of the liquidus temperature of the casted alloy $T_{liquidus}$ = 1289 K, ② the iso-surface of the columnar volume fraction f_c = 0.5, ③ the iso-surface of f_c = 0.95, and ④ the iso-surface of f_c = 0.99 at the symmetrie planes.

The hot melt flows from the tundish above the mold of the laboratory continuous casting directly into the mold. Since the upper part of the mold (①, *Figure 4-32a*) is kept at casting temperature, cooling of the melt begins in the second part of the mold (②, *Figure 4-32a*) where adiabatic boundary conditions are assumed. The columnar dendrites start to grow at the mold wall as liquidus temperature of CuSn6

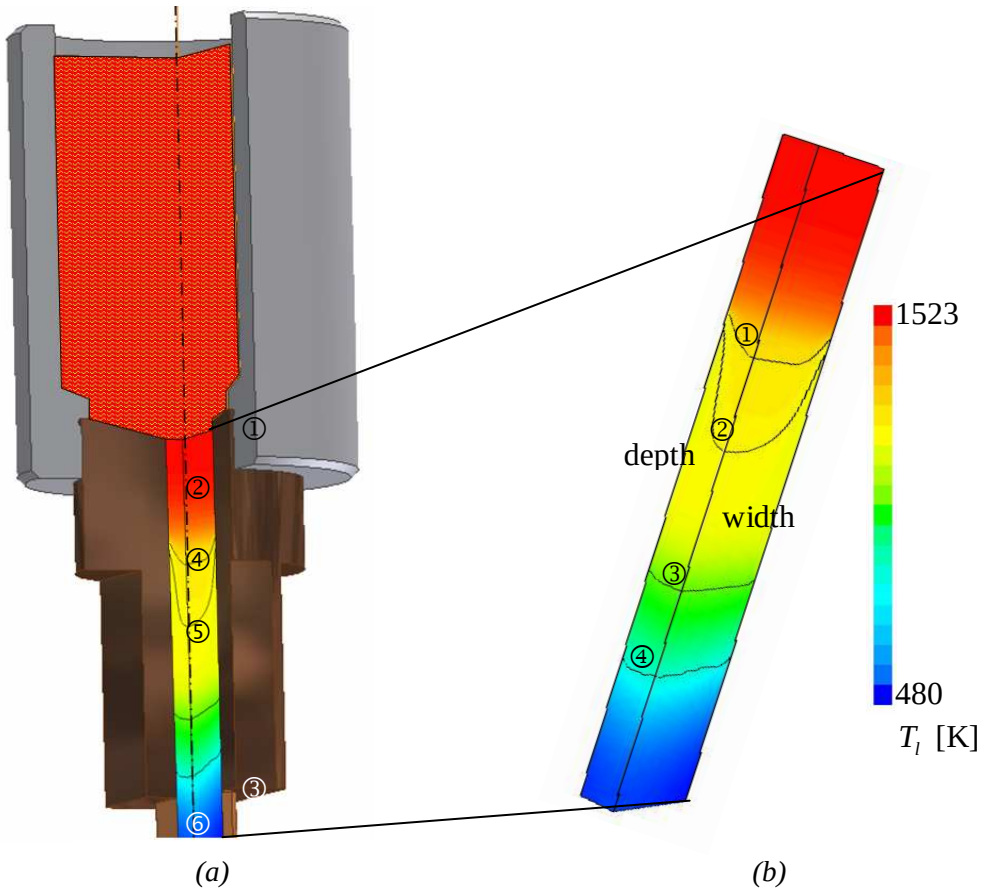

Figure 4-32: (a) The laboratory geometry with the calculated temperature field T_l [K] displayed for the 3D laboratory casting. ① indicates the copper mold acting as a tundish, ② the position of the inlet, and ③ the secondary cooling zone. ④ marks the liquid region, ⑤ the mushy zone, and ⑥ the solidified casting. (b)The temperature field T_l [K] is shown at the symmetry planes of the 3D laboratory casting process. ① marks the isoline of $T_{liquidus}$ = 1289 K, ② of f_c = 0.5, ③ of f_c = 0.95, and ④ of f_c = 0.99.

$T_{liquidus}$ = 1289 K (①, *Figure 3-31b*) is reached. Slightly below the iso-surface of $T_{liquidus}$ a volume fraction solid f_c = 0.5 is reached (②, *Figure 3-31*) at the wall. The following mold part is kept at adiabatic boundary condition which leads to lower cooling velocity in this part.

The iso-surface of f_c = 0.95 is reached where the secondary cooling zone starts (③, *Figure 4-32b*) with the three already described different cooling zones. The last shown iso-surface is f_c = 0.99 (④, *Figure 4-32b*). These four iso-surfaces are all displayed in the following figures. *Figure 4-33a* pictures the volume fraction field for the columnar phase as already described. It can be seen that in the columnar mushy zone, extending from $T_{liquidus}$ to f_c = 0.99, the volume fraction of the solid varies from f_c = 0 to f_c = 0.99. *Figure 4-33b* shows the liquid concentration c_l at the symmetry planes in a range from blue c_l^{Sn} = 6 wt.% Sn to red c_l^{Sn} = 53 wt.% Sn.

In comparison to the 2D axis symmetric simulation, where the rest of the liquid was thought to solidify below T_{end} in a small temperature interval, in the 3D case masstransfer and with that solidification is finished at a certain liquid volume fraction, in this case f_l = 0.01. This leads to an enrichment of Sn in the melt over the values observed in the 2D calculations due to the linear phase diagram assumption. Even though the value of

c_l^{Sn} is very high at this volume fraction, its influence on the macrosegregation is rather low due to the low volume fraction liquid in these areas. *Figure 4-34a* shows the columnar concentration c_c^{Sn} at the symmetry planes in a range from blue (3.2 wt.% Sn) to red (5.8 wt.% Sn).

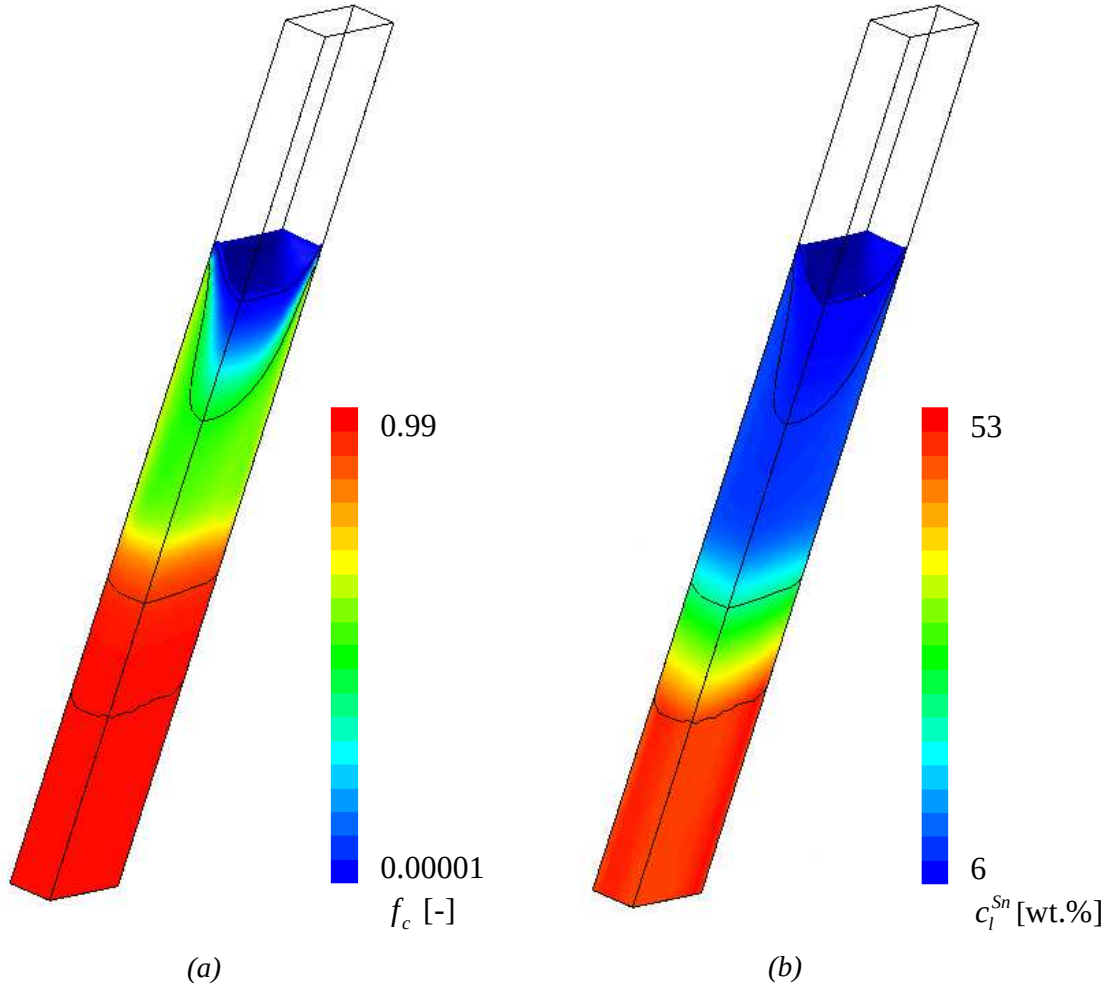

Figure 4-33: (a) The volume fraction columnar f_c and (b) the liquid concentration c_l^{Sn} is displayed at the symmetry planes of the 3D laboratory casting. Black lines: iso-surface $T_{liquidus}$ = 1289 K, f_c = 0.5, f_c = 0.95, f_c = 0.99.

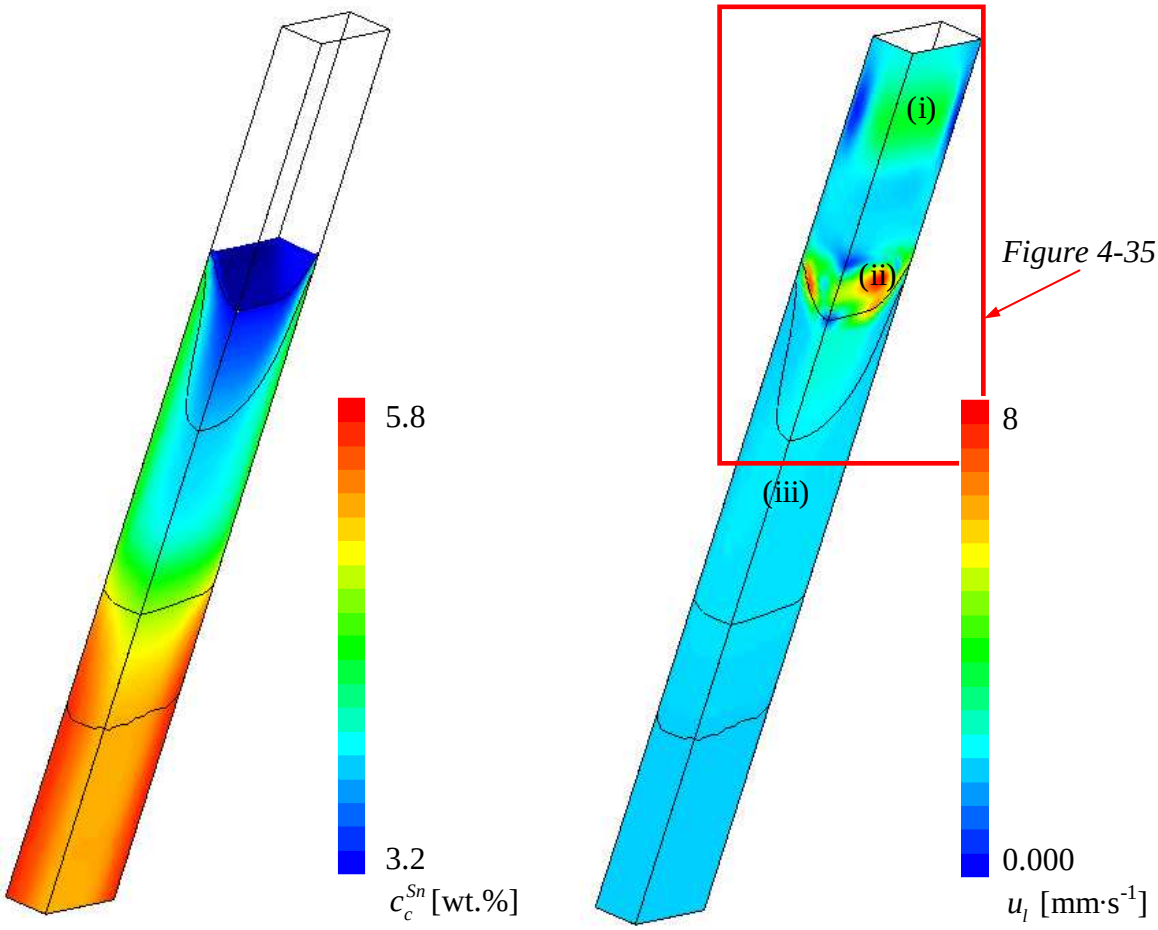

Figure 4-34: (a) The columnar concentration c_c^{Sn} and (b) the liquid velocity magnitude u_l displayed at the symmetry planes of the 3D laboratory casting. (i) marks the high velocity field developing in the upper region and (ii) a vortex occurring in the center of the casting. The strand itself moves with u_{cast} (iii). Black lines: iso-surface $T_{liquidus}$ = 1289 K, f_c = 0.5, f_c = 0.95, f_c = 0.99.

As we considered the mush to be permeable, melt-flow occurs through the mush. In *Figure 4-34b* liquid velocity magnitude u_l is displayed at the symmetry planes, where the blue color indicates low velocity regions and red ones high velocity regions. *Figure 4-35* shows the same liquid velocity $\vec{u}_l$ at the symmetry planes as vector field for the region defined by the red rectangular window assigned in *Figure 4-34b*. Again, blue indicates low velocities and red high. *Figure 4-35b* displays liquid velocity $\vec{u}_l$ at the symmetry planes as a vector field for the region defined by the red rectangular window marked in *Figure 4-35a* in the same color scale.

The flow field has two higher velocity regions: (i) the green region in the upper part of the casting, where a slightly higher velocity than the casting velocity $\vec{u}_{cast}$ is observed (*Figure 4-34b*, *Figure 4-35* (i)). A vortex develops in front of the solidification front which touches the broad side of the casting and the thin side at the symmetry planes (*Figure 4-34b*, *Figure 4-35* (ii)) because the down flowing melt is bent inwards due to the shape of the solidification front in combination with the considered convection mechanisms. In the center an upwards flow is observed which is in return the reason for the higher velocity observed in the upper part of the casting (*Figure 4-34b*, *Figure 4-35* (i)). Since just the two symmetry planes are displayed in the figures, this

motion is not visible. Deep in the mushy zone the velocity of the liquid is decreased because of its interaction with the solidifying dendrites. After achieving a certain solid content, the liquid is forced to move with the same velocity as the solid phase due to the drag force acting between the liquid and the columnar phase (*Figure 4-34b*, *Figure 4-35* (iii)). This seems to happen at least after reaching the isoline of f_c = 0.5.

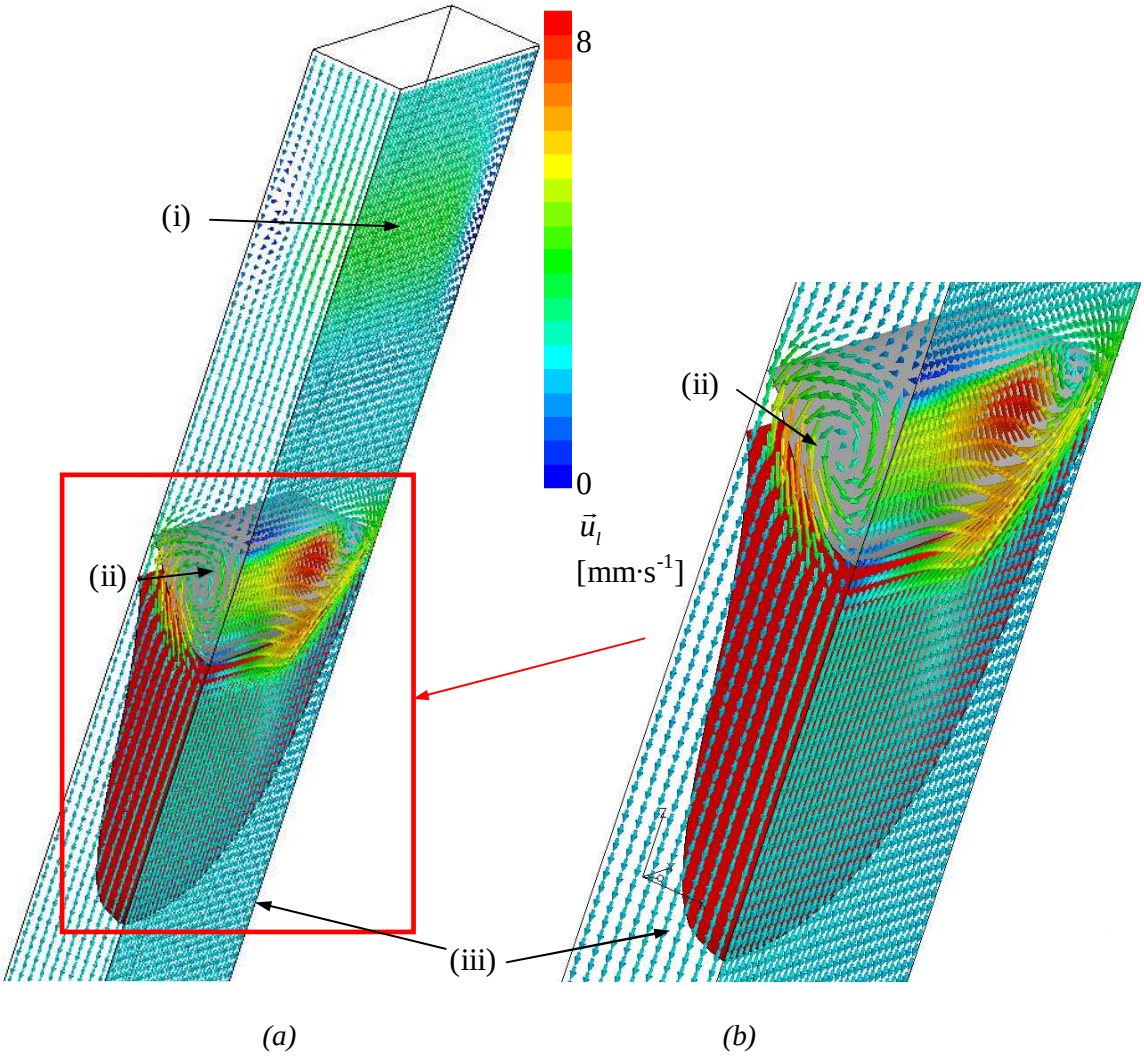

Figure 4-35: The liquid velocity vector field $\vec{u}_l$ of the region marked with the red rectangle in Figure 4-34 is displayed (a) and (b) for the region close to the mushy zone assigned by the red rectangle in (a). (i) marks a relatively high velocity field in the upper region and (ii) a vortex occurring in the center of the casting. The strand itself moves with $\vec{u}_{cast}$ (iii). Black lines: iso-surface $T_{liquidus}$ = 1289 K, f_c = 0.5, f_c = 0.95, f_c = 0.99.

Study of macrosegregation in 3D

The distribution of the macrosegregation pattern throughout the calculated 3D strand is displayed in *Figure 4-36* and *Figure 4-37*. For this calculation mush permeability was considered to be $K_0 = 1.4 \cdot 10^{-5}$ while forced convection, feeding flow and thermo-solutal convection were considered in the simulation. The displayed surfaces in the casting are the iso-surface $T_{liquidus}$ = 1289 K (gray surface), f_c = 0.5 (red surface), f_c = 0.95 (blue surface), and f_c = 0.99 (purple surface). Bright green color shows the initial alloy concentration, yellow positive and blue negative macrosegregations in the strand. Since the same flow mechanisms are considered for the 3D as before for the 2D geometry, the same tendency of the macrosegregation pattern is observed. Due to the applied geometry the flow is relatively uniform in the upper part of the casting and no strong influence of the inlet flow shows up. In this case feeding flow seems to be the most important feature. Therefore, low positive macrosegregations are forming at the walls and slightly negative ones in the center of the casting, as expected.

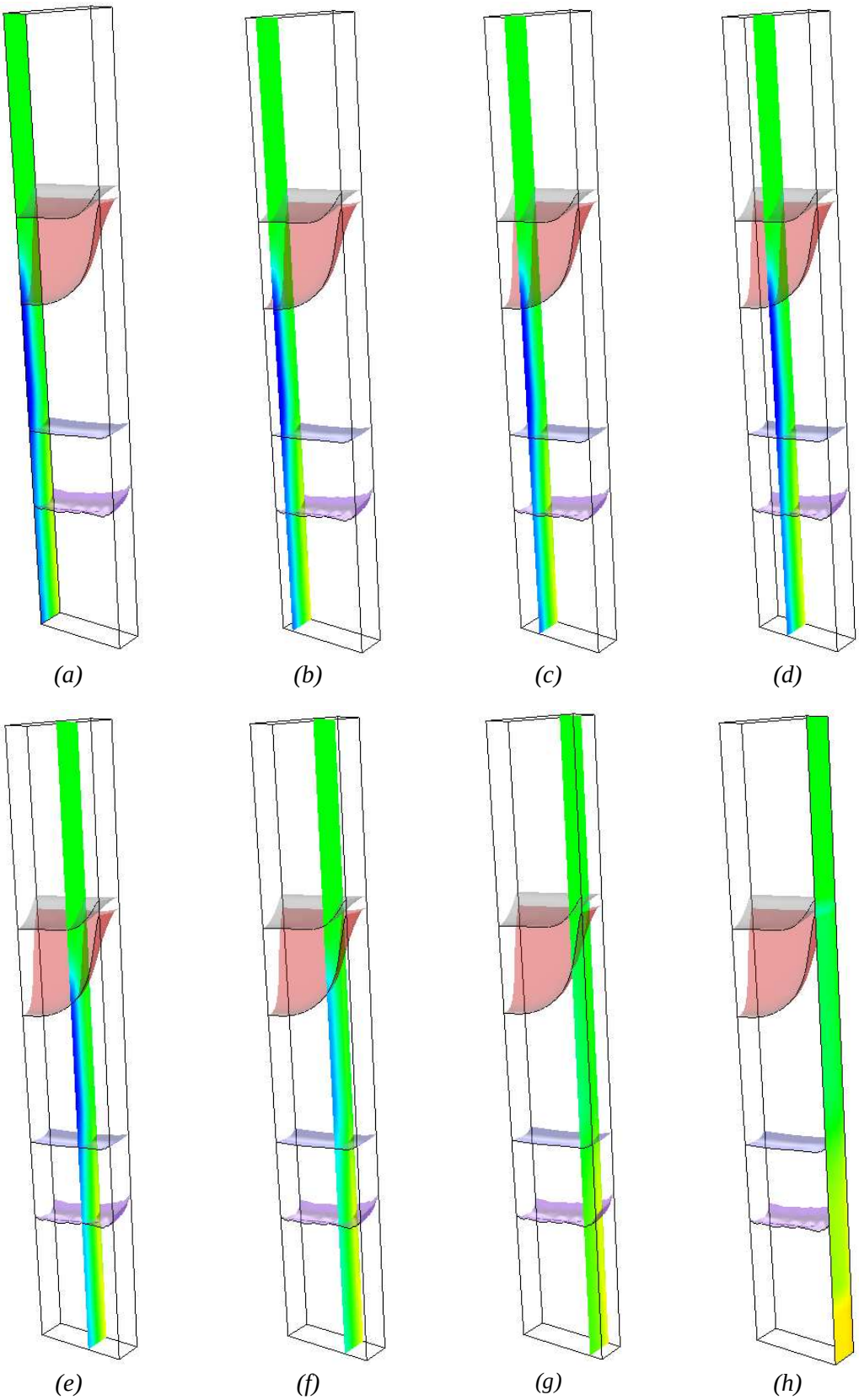

Figure 4-36: 3D steady-state distribution of the mixture concentration c_{mix} of Sn with $\overline{K_0}$ =1.4·10^{-5} and including forced convection, feeding flow, and thermo-solutal convection. Bright green: initial alloy concentration, yellow positive, and blue negative macrosegregations. Iso-surfaces: $T_{liquidus}$ = 1289 K, f_c = 0.5, f_c = 0.95, f_c = 0.99.

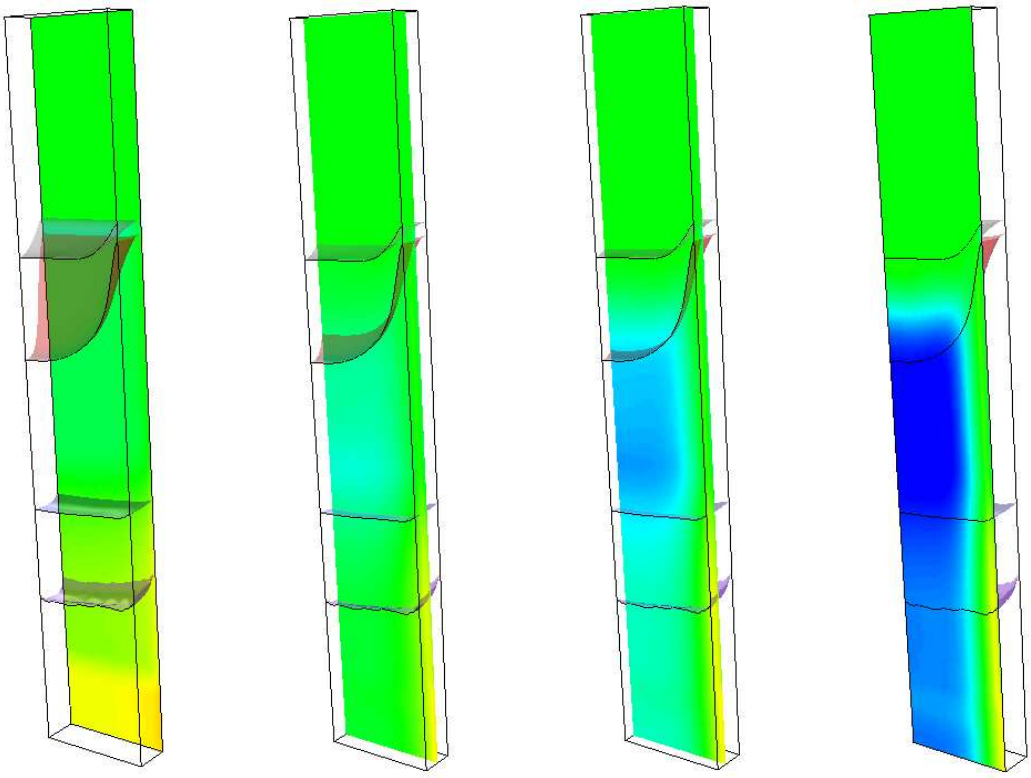

(a) *(b)* *(c)* *(d)*

Figure 4-37: Steady-state distribution of the mixture concentration c_{mix} of Sn with $\overline{K_0} = 1.4 \cdot 10^{-5}$ including forced convection, feeding flow, and thermo-solutal convection. Bright green: initial alloy concentration, yellow positive, and blue negative macrosegregations. Iso-surfaces: $T_{liquidus} = 1289$ K, $f_c = 0.5$, $f_c = 0.95$, $f_c = 0.99$.

Figure 4-38 shows the macrosegregation at the two walls where light gray shows the initial alloy concentration, white positive and dark gray negative segregated areas. In addition one plane at the end of the casting strand is shown in green/blue. In this plane the discussed cross plots of *Figure 4-39* and *Figure 4-40* are located. *Figure 4-39* shows the macrosegregation from the back to the front symmetry plane (x = 0 mm (at the back wall) to x = 12 mm (front symmetry plane)) and *Figure 4-40* from the left to the right (y = 0 mm (symmetry plane on the left hand side) to y = 40 mm (wall on the right)). On both walls slightly positive segregated areas are observed whereas in the center of the casting the macrosegregation pattern is negative. Anyway, the macrosegregation in the presented 3D case for the laboratory geometry is smaller as the one observed for the 2D axis symmetric case.

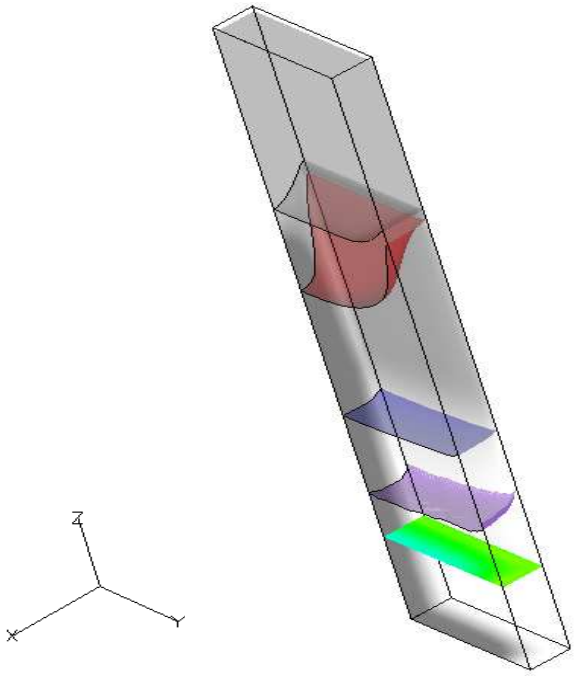

Figure 4-38: Steady-state distribution of the mixture concentration c_{mix} of Sn with $\overline{K_0} = 1.4 \cdot 10^{-5}$ and including forced convection, feeding flow, and thermo-solutal convection at the displayed surfaces of the geometry. Initial alloy concentration (light gray), positive macrosegregations (white), and negative macrosegregations (dark gray) are shown. The plane for the c_{mix} plots of Sn is displayed in green/blue. Displayed iso-surfaces are $T_{liquidus}$ = 1289 K, f_c = 0.5, f_c = 0.95, f_c = 0.99.

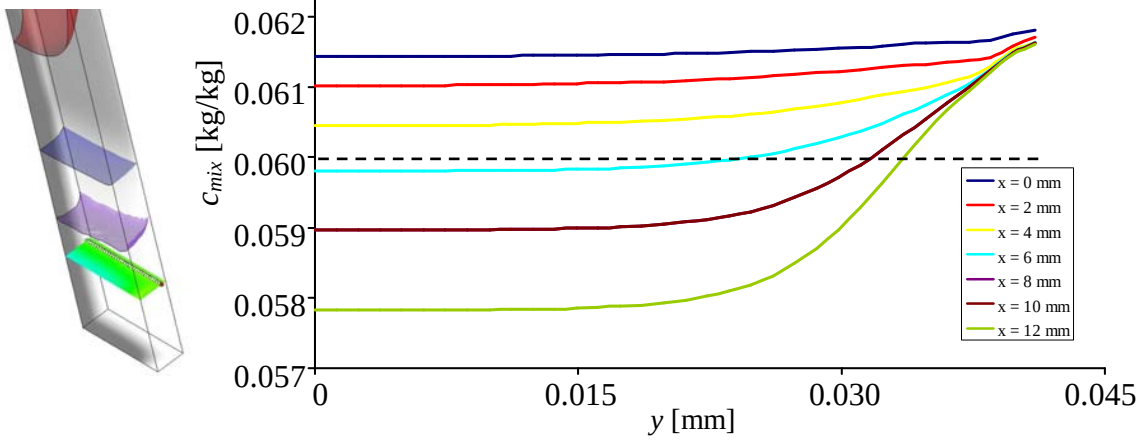

Figure 4-39: c_{mix} profiles of Sn along the width in the plane of the presented crosssection in Figure 4-38 for x = 0 mm (at the back wall) to x = 12 mm (front symmetry plane).

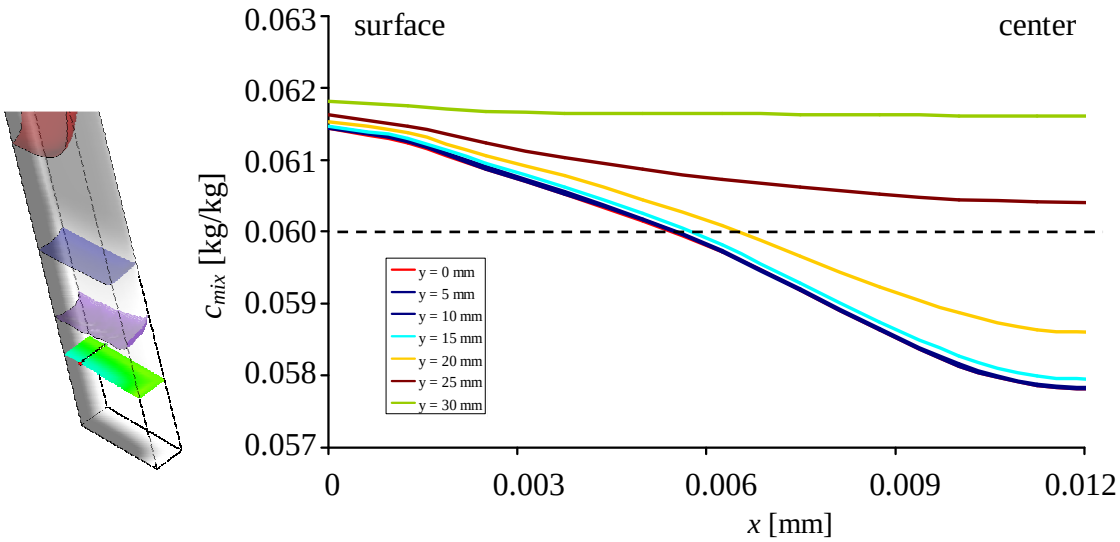

Figure 4-40: c_{mix} profiles of Sn along the depth in the plane of the presented crosssection in Figure 4-38 for y = 0 mm (symmetry plane on the left hand side) to y = 40 mm (wall on the right).

4.2.4 2D Axis Symmetric Simulations for CuSn6P0.5

Since technical bronze alloys as cast in industry are multicomponental alloys, the binary calculations have been expanded to include P. For the first studies as shown in the following the 2D axis symmetric geometrie was taken as described in chapter 4.2.1.

Thermodynamic information

The model published in [ISHMURZIN 08, LUDWIG 06B, LUDWIG 07] and described in chapter 4.1.3 is applied to simulate DC-casting of the alloy CuSn6P0.5. *Figure 4-41* shows the liquidus surface including the monovariant lines of the occurring phases in the Cu rich corner of the ternary phase diagram for Cu-Sn-P as mentioned in chapter 3.2.1.

Figure 4-42a-c shows the liquidus surface, $T = T_L(\tilde{c}_l^{Sn}, \tilde{c}_l^{P})$, and the solibility of alloying components in the solid, $\tilde{c}_c^{Sn} = f_c^{Sn}(\tilde{c}_l^{Sn}, \tilde{c}_l^{P})$ and $\tilde{c}_c^{P} = f_c^{P}(\tilde{c}_l^{P}, \tilde{c}_l^{Sn})$, calculated with the software Thermocalc based on the database CuSn1 and plotted in the Cu rich corner of the Cu-Sn-P system. Point c_0 in the pictures is the location of the initial alloy concentration of 0.06 mass fraction of Sn and 0.005 mass fraction of P whereas point B indicates the end of solidification (0.01 mass fraction Sn/P corresponds to 1 wt.% Sn/P where wt.% means weight percent of a certain element).

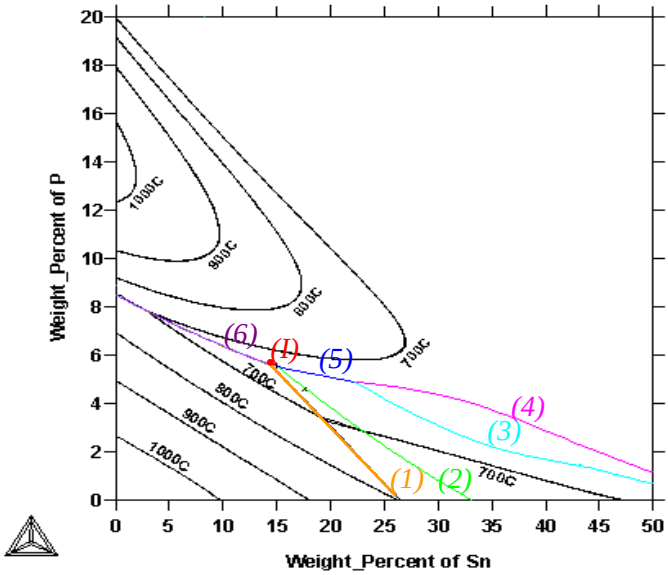

Figure 4-41: Rectangular liquidus surface projection of the Cu rich corner for the ternary phase diagram Cu-Sn-P up to 50 wt.% Sn and 20 wt.% P based on calculations with Thermo-Calc (database CuSn1). The colored lines are the monovariant lines of the liquidus surface and the black lines are isotherms. Orange line (1) is the monovariant line corresponding to the peritectic reaction L + α → β, green line (2) is the monovariant line corresponding to the peritectic reaction L + β → γ, bright blue line (3) is the monovariant line corresponding to the reaction γ + L → ε, pink line (4) is the monovariant line corresponding to the eutectic reaction L → Cu_3P + ε, blue line (5) is the monovariant line corresponding to the eutectic reaction L → Cu_3P + γ, purple line (6) is the monovariant line corresponding to the eutectic reaction L → Cu_3P + α, and red point (I) is the ternary eutectic point.

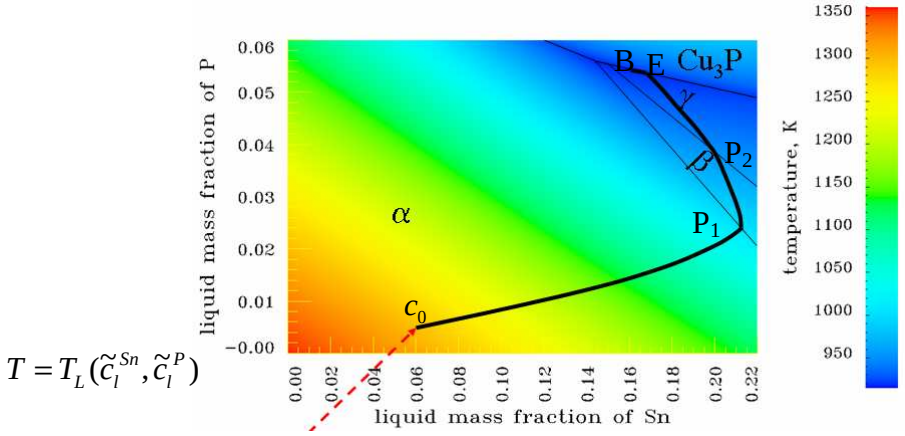

$T = T_L(\tilde{c}_l^{Sn}, \tilde{c}_l^{P})$

(a)

c_0 : CuSn6P0.5

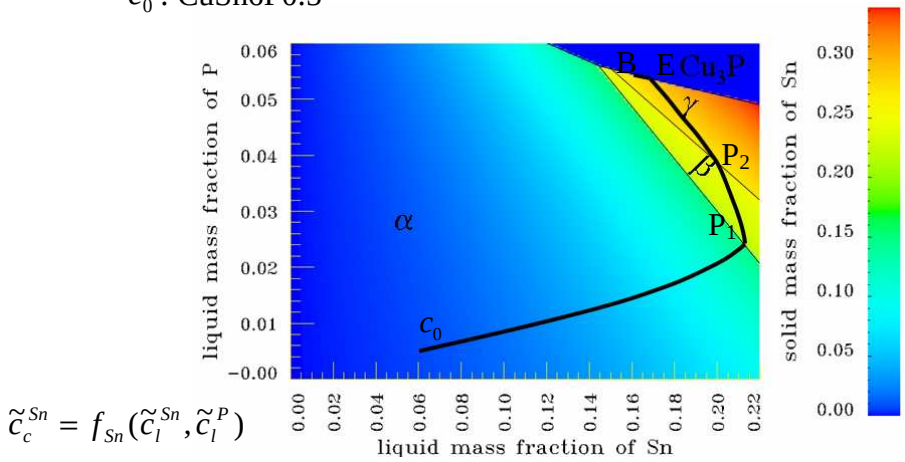

$\tilde{c}_c^{Sn} = f_{Sn}(\tilde{c}_l^{Sn}, \tilde{c}_l^{P})$

(b)

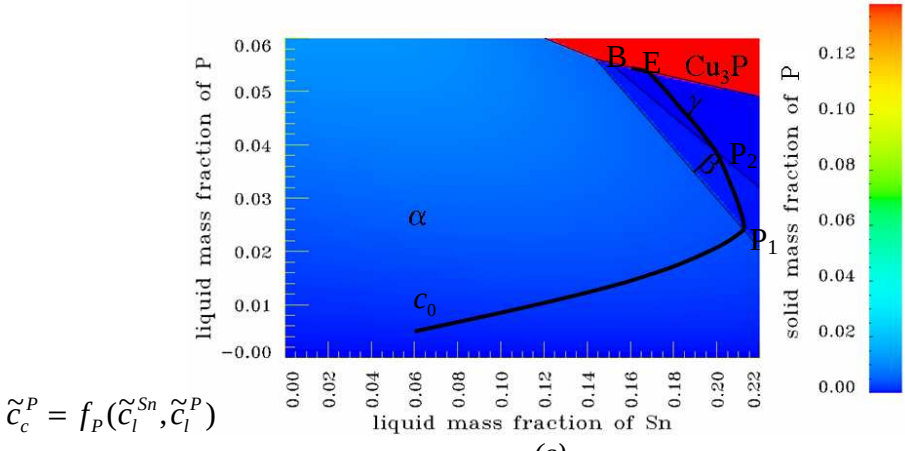

$\tilde{c}_c^{P} = f_P(\tilde{c}_l^{Sn}, \tilde{c}_l^{P})$

(c)

Figure 4-42: The contour plots of (a) the liquidus surface $T = T_L(\tilde{c}_l^{Sn}, \tilde{c}_l^{P})$, (b) the tie-line information of Sn $\tilde{c}_c^{Sn} = f_{Sn}(\tilde{c}_l^{Sn}, \tilde{c}_l^{P})$, and (c) the tie-line information of P $\tilde{c}_c^{P} = f_P(\tilde{c}_l^{Sn}, \tilde{c}_l^{P})$ are displayed based on a calculation with Thermo-Calc for the ternary Cu-Sn-P system. In each plot the black line marks the estimated solidification path of the alloy CuSn6P0.5 (marked by the red arrow) based on Scheil calculations. c_0 : initial alloy concentration, B: end of solidification according Thermo-Calc, P_1, P_2: first and second peritectic groove, E: eutectic groove.

Solidification of such bronze alloys starts with the formation of α dendrites according to thermodynamics as displayed in *Figure 4-41*. The black line in *Figure 4-42a-c* shows the solidification path calculated with the Thermo-Calc Scheil model. As, during solidification, the first peritectic groove is crossed (P_1, *Figure 4-42a-c*), β is formed due to the peritectic reaction L + α → β. Further cooling leads to the formation of γ after reaching the second peritectic groove (P_2, *Figure 4-42a-c*) according to the peritectic reaction L + β → γ. The remaining melt starts to solidify in the eutectic groove of γ and Cu_3P (E, *Figure 4-42a-c*). From here the solidification path follows the eutectic groove further on to the eutectic groove of β and Cu_3P. According to Thermo-Calc Scheil calculations, solidification ends here (*Figure 4-42a-c*, B). The very last melt is, according to the Scheil model, expected to solidify with the ternary eutectic concentration of 15 wt.% Sn and 5.5 wt.% P. But the calculation with the Thermo-Calc Scheil model (*Figure 4-42a-c*, B) stops already before the ternary eutectic point due to the low remaining liquid volume fraction.

All three functions T_L, $\tilde{c}_c^{Sn}$, and $\tilde{c}_c^{P}$ can be approximated by using their point wise Thermo-Calc tabulations. Generally, any suitable interpolation can be applied. For the following up scaling of the model to industrial dimensions the three thermodynamic functions equation 4-31 to equation 4-33 were linearized around the initial composition (c_0, *Figure 4-42a-c*).

In a first approximation and due to the fact that the volume fraction of solid at the first phase transition is about $f_c = 0.8$ just one set of linear interpolation functions around point c_0 is applied. Due to the fact that the phase transformation L + α → β is not taken into account in the model up to now, the presented results take into account only the formation of α. For details of the applied routine the reader is referred to [ISHMURZIN 08, LUDWIG 06B, LUDWIG 07].

Results and Discussion

A 2D axis symmetric geometry was taken for the simulation as described in chapter 4.2.2. The first simulation considers forced convection (inlet jet) and and the second one in addition shrinkage flow, which is modeled by different constant densities for the columnar and the liquid phase. The study of the ternary solidification is based on the calculation including just forced convection (*Figure 4-43-Figure 4-46*). Additional calcalculations have been performed including feeding flow since feeding flow contributes significantly to the occurring macrosegregation distribution under these specific process conditions. Other flow phenomena like thermo-solutal convection are ignored as a first approach (*Figure 4-47*). Material properties were the same as for the binary cases. In the presented solidification simulation permeability was taken into account by a $\overline{K_0} = 1.4 \cdot 10^{-5}$ according to the permeability study described in chapter 4.2.2. $T_{inlet} = 1398$ K and the initial temperature $T_{init} = 1300$ K whereas the casting velocity was considered to be $\vec{u}_{cast} = 1.92$ mm·s^{-1} and was with that the initial velocity of the melt.

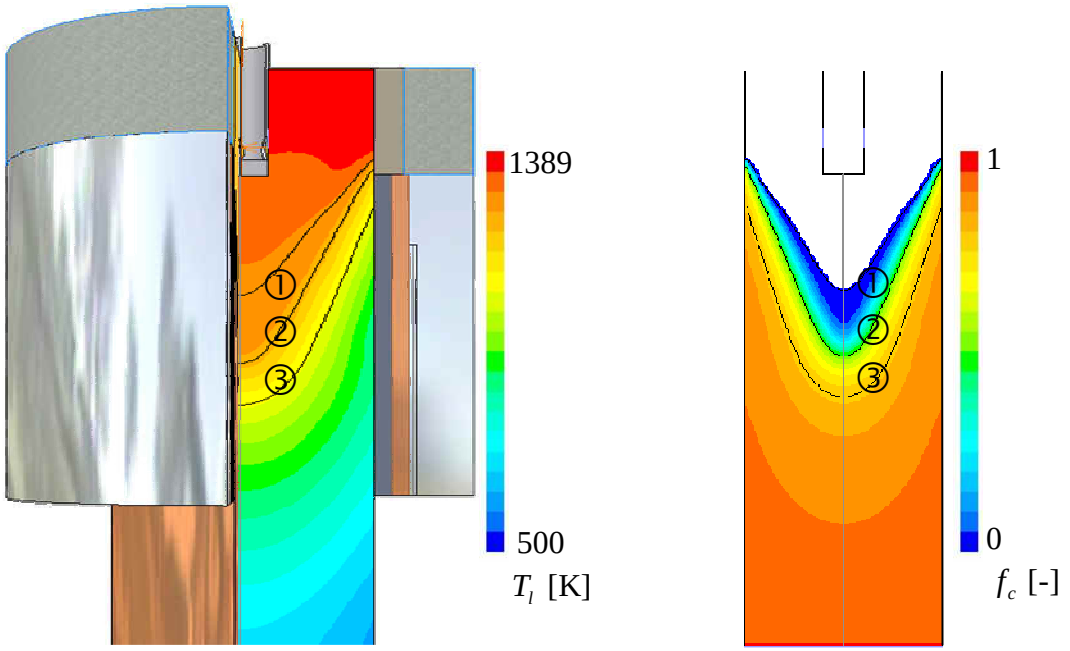

(a) *(b)*

Figure 4-43: (a) The temperature field of the casting T_l is displayed with the casting mold. (b) The columnar volume fraction distribution f_c for the ternary alloy CuSn6P0.5 in the case where inlet flow is considered. Black lines are ① $T_{liquidus}$ = 1295.5 K, ② f_c = 0.5 and ③ f_c = 0.8.

In the following, the results of this ternary simulation are discussed based on flow and thermodynamic parameter distributions gained from the ternary solidification simulation after reaching a steady state. *Figure 4-43a* shows temperature field T_l, *Figure 4-43b* columnar volume fraction f_c, *Figure 4-44a* liquid concentration for P c_l^P, and *Figure 4-44b* liquid concentration for Sn c_l^{Sn}. In *Figure 4-45* the velocity distribution in the melt is displayed *(a)* as velocity magnitude u_l and *(b)* as vector field $\vec{u}_l$.

Figure 4-46 shows the macrosegregation pattern c_{mix} for both alloying elements P *(a)* and Sn *(b)* in the case where inlet flow is considered, and *Figure 4-47* in the case where feeding flow is taken into account. Here the highest and the lowest values displayed correspond to positive and negative deviations of ± 5 % from the initial alloy composition. Above a columnar volume fraction f_c = 0.83, the results are meaningless, since the linearized thermodynamic functions do not take into account the additional occurring phase changes (P_1, P_2 in *Figure 4-42a-c*) and therefore have to be ignored. This is the reason why the distributions below this volume fraction are not displayed in the following figures. The three isolines displayed in every contour plot are corresponding to ① $T_{liquidus}$ = 1295.5 K, ② f_c = 0.5, and ③ f_c = 0.83.

Columnar volume fraction f_c (*Figure 4-43b*) and liquid concentrations c_l^P and c_l^{Sn} (*Figure 4-44a, b*) show that solidification starts at $T_{liquidus}$ and that the columnar volume fraction is f_c = 0.83 when the first peritectic groove is reached where c_l^{Sn} = 22.5 wt.% Sn and c_l^P = 1.9 wt.% P. The concentration of P in the liquid phase, c_l^P, is lower in the prediction with FLUENT than the one of Thermo-Calc which proposes a value of c_l^P = 2.5 wt.% P at the first peritectic groove.

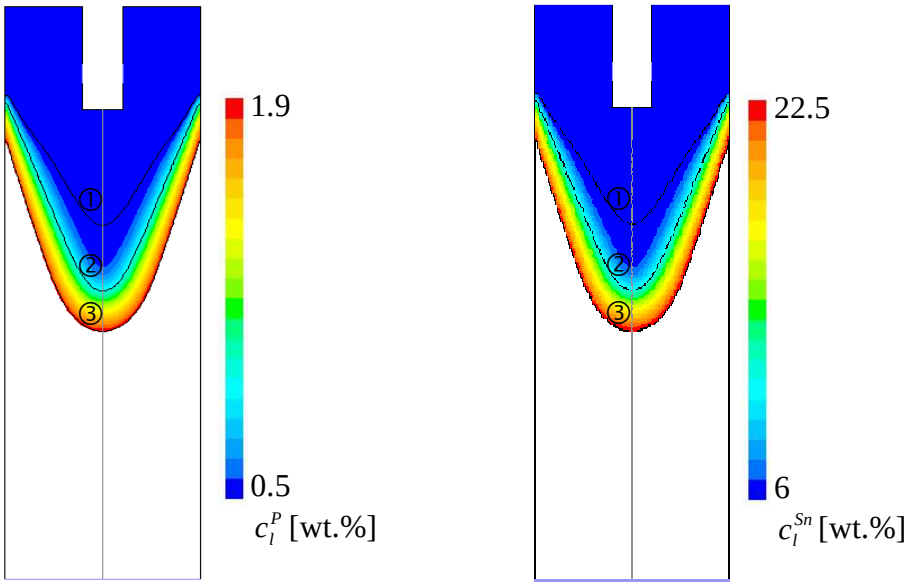

(a) *(b)*

Figure 4-44: Liquid concentration c_l^P for P (a) and c_l^{Sn} for Sn (b) for the ternary alloy CuSn6P0.5 in the case where just inlet flow is considered. The black lines are ① $T_{liquidus}$ = 1295.5 K, ② f_c = 0.5, and ③ f_c = 0.8.

This difference is due to linearization of the thermodynamic functions from the real ones (equation 4-31 to equation 4-33). Due to the fact that the phase transformation L + α → β was not taken into account, the results show the volume fraction for α.

In the presented case the inlet jet is the only flow phenomenon that causes the development of the big vortex in the upper region of the mold (①, *Figure 4-45*) and induces with that slightly negative macrosegregations at the wall of the casting *Figure 4-46* for both elements and very low positive macrosegregation in the bulk of the casting.

In the case including feeding flow presented in *Figure 4-47*, the inlet jet causes, the development of a big vortex with relatively high velocity in the upper region of the mold (I, *Figure 4-47*). In addition, there is a second higher velocity region occurring due to feeding flow deep in the mushy zone (II, *Figure 4-47*). The strand with a columnar volume fraction above f_c = 0.83 moves with casting velocity (III, *Figure 4-47*). In these regions the applied drag force (described in [LUDWIG 06A]) causes entrapment of the remaining liquid between the dendrite network. Therefore columnar phase and liquid phase move with the same casting velocity. *Figure 4-47* shows that macrosegregations are positive at the surface of the strand and negative in the center for c_{mix}^P and c_{mix}^{Sn}.

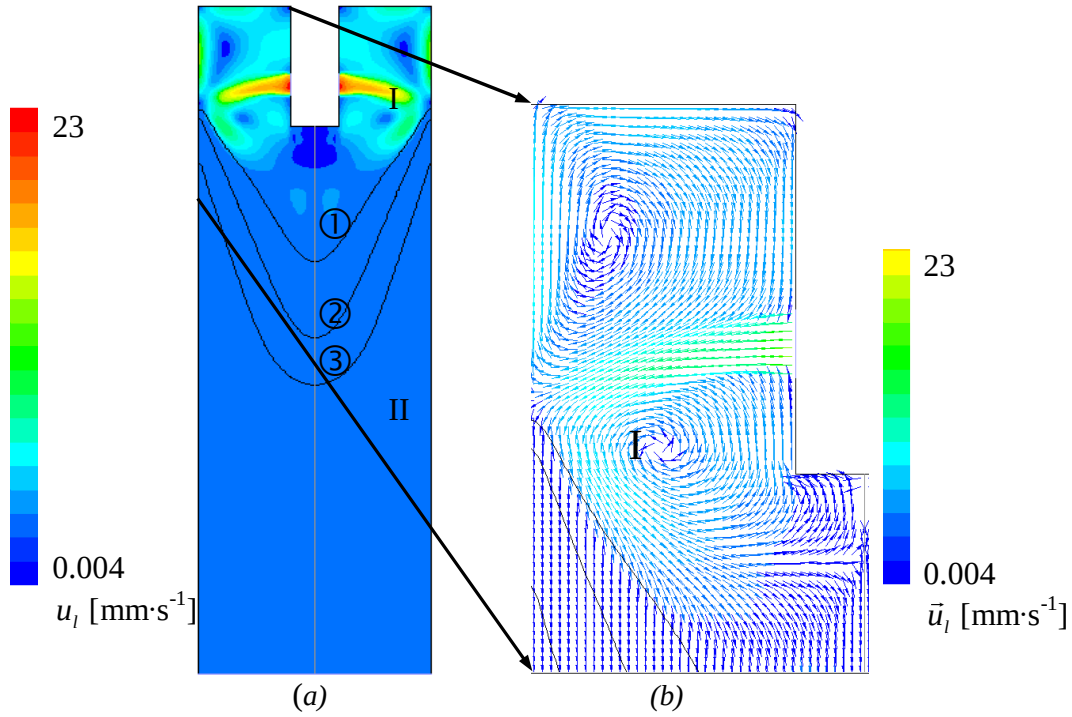

Figure 4-45: Liquid velocity field for the ternary alloy CuSn6P0.5 in the case where just inlet flow is considered. (a) velocity magnitude u_l in the whole geometry, (b) velocity vector field $\vec{u}_l$ in the upper part of the casting. A vortex develops at the inlet (I), the solidified strand moves with $\vec{u}_{cast}$ (II). The black lines are ① $T_{liquidus}$ = 1295.5 K, ② f_c = 0.5 and ③ f_c = 0.8.

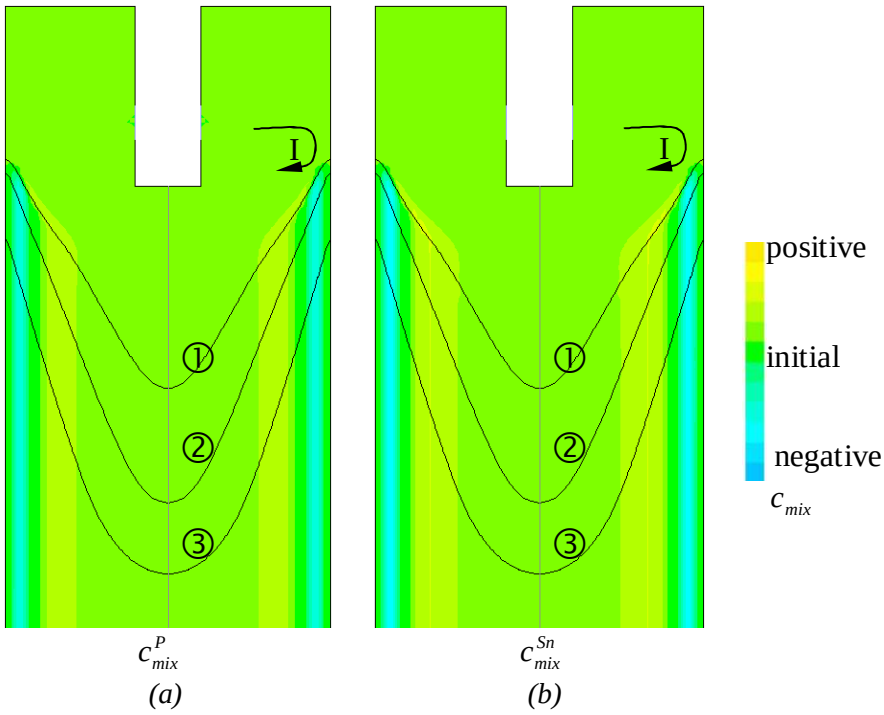

Figure 4-46: Steady-state distribution of the mixture concentration c_{mix} (a) c^P_{mix} = 0.49 - 0.51 [wt.% P], (b) c^{Sn}_{mix} = 5.9 - 6.1 [wt.% Sn] with $\overline{K_0}$ = 1.4·10^{-5} including forced convection. The inlet jet causes negative segregations adjacent to the wall. Black lines mark ① $T_{liquidus}$ = 1295.5 K, ② f_c = 0.5, and ③ f_c = 0.8.

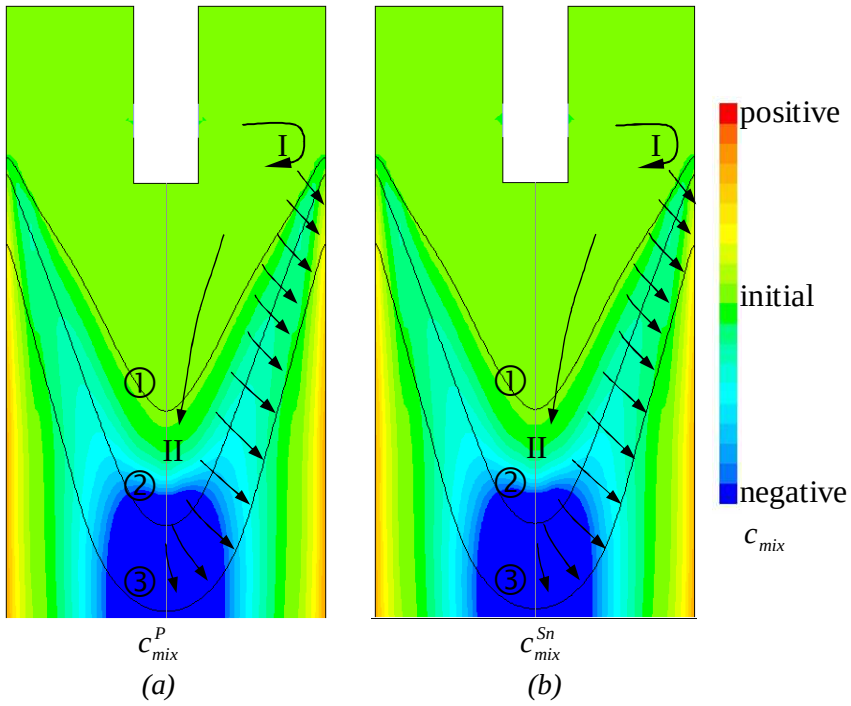

Figure 4-47: Steady-state distribution of the mixture concentration c_{mix} (a) c_{mix}^{P} = 0.45 - 0.55 [wt.% P], (b) c_{mix}^{Sn} = 5.4 - 6.6 [wt.% Sn] with K_0 =1.4·10^{-5} including forced convection and feeding flow. The inlet jet causes slightly negative segregations adjacent to the wall. But since the influence of feeding flow is significantly stronger, there are positive macrosegregations occurring at the wall and negative ones in the center of the strand. Black lines mark ① $T_{liquidus}$ = 1295.5 K, ② f_c = 0.5, and ③ f_c = 0.8.

4.3 Discussion

4.3.1 Development of Macrosegregation in the Continuous Casting Strand

To understand the macrosegregation distribution in the solidified strand, the development of the macrosegregation pattern within the mushy zone is of interest to estimate the influence of different casting parameters on the solute destribution in the scale of the casting. *Figure 4-48* shows a schematical picture of growing dendrites where three different zones are considered: the liquid in front of the solidifying region, followed by the mushy zone with liquid and solid developing to a totally solidified zone.

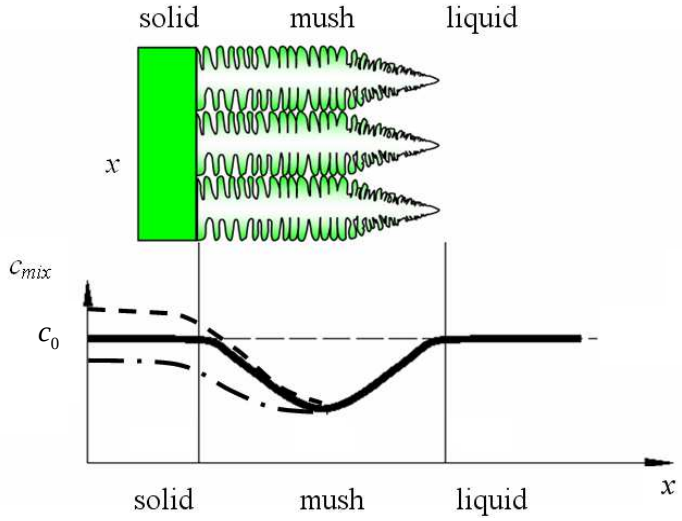

Figure 4-48: Expected one dimensional c_{mix} profile (black line) through the mushy zone after Flemings [FLEMINGS 67A, FLEMINGS 67B, FLEMINGS 67C]. c_0 shows the original alloy concentration (thin dasched line). The thick dashed line shows the expected mixture concentration defelopment for increasing mushy zone width (positive macrosegregations), and the thick dashed-dotted line the c_{mix} profile for decreasing mushy zone width (negative macrosegregations). For constant mush thickness during solidification a non segregated solid will be formed for 1D only considering feeding flow (thick black line).

After Flemings study for steady state of the one dimensional case, the concentration profile has negative c_{mix} values in the mush whereas in the solidified casting no macrosegregation appears (black line, *Figure 4-48*). This expectation is based on a situation where the isotherms of $T_{liquidus}$ and $T_{solidus}$ in a solidifying casting move parallel to each other due to the considered constant temperature gradient. Equation 4.3.1 shows Flemmings "Local Solute Redistribution Equation" (LSRE) [FLEMINGS 67A, FLEMINGS 67B, FLEMINGS 67C].

$$\frac{\partial f_l}{\partial c_l} = -\left(\frac{1-b}{1-k}\right)\left(1+\frac{u}{v_T}\right)\frac{f_l}{c_l}, \text{ with } b = \frac{\rho_c - \rho_l}{\rho_c} \text{ and } v_T = -\frac{\dot{T}}{G_T} \qquad (4.3.1)$$

Here k is the solute redistribution coefficient, u the independent melt velocity, v_T the velocity of the isotherms, b relates the density of the liquid and the solid, G_T the temperature gradient and $\dot{T}$ the cooling rate. If the temperature gradient is not constant width of the mushy zone may change. In the case of an increasing temperature gradient, the mushy zone width decreases and negative macrosegregation forms (dashed-dotted line, *Figure 4-48*). In the case of a decreasing temperature gradient, the mushy zone width increases and positive macrosegregation forms (dashed line, *Figure 4-48)*. These results from Flemings LSRE (equation 4.3.1) can be understood as explained in the following based on a Scheil solidification curve as shown in *Figure 4-49*. The melt enters a volume element with a concentration c_l^{in} and leaves the volume element with a concentration c_l^{out}. During solidification, the melt becomes enriched in solute (microsegregation) and therefore c_l^{out} is expected to be larger than c_l^{in} (dilution). However, due to solidification the volume flow of the liquid entering the volume element is larger than the volume flow of the liquid leaving the volume element (enrichment). This leads to accumulation of solute. For low solid fraction the dilution is dominant compared to the enrichment (decreasing c_{mix}), for large solid fraction it is the reverse (increasing c_{mix}).

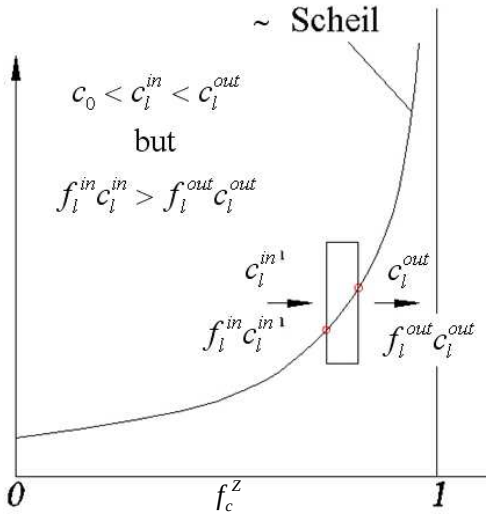

Figure 4-49: Solidification in a cell during Scheil-type solidification. The diagram shows liquid concentration c_l versus columnar volume fraction f_c. If the volume flow of the liquid $f_l^{in}\, c_l^{in}$ entering the volume element is larger than the volume flow of the liquid leaving the volume element $f_l^{out}\, c_l^{out}$ solute is accumulated in the cell.

Flemings one dimensional case can be compared with the calculation taking just feeding flow into account. Therefore the calculation results of the already discussed Case D-L are studied in detail to gain more information about the macrosegregation development in the casting. *Figure 4-50* displays on the left hand side a contour plot of the calculated macrosegregation pattern. The green color shows no macrosegregation whereas the yellow areas (at the wall of the casting) indicate positive and the blue areas (in the center of the casting) negative macrosegregations. On the right hand side several horizontal profiles are presented which were taken at 0.15, 020, 0.25, and 0.30 m depth of the casting. The last concentration profile is taken before the isotherm of $T_{liquidus}$ reaches the center of the casting. The horizontal slashed lines in the profiles show the position of the original alloy concentration (6 wt.% Sn). The specific negative mixture concentration profile in the mushy zone is developed similar as the curves shown in *Figure 4-48*. The high positive macrosegregation at the mold wall forms because of the accumulation of solute at

the beginning of solidification. Additionally, a plateau of slightly positive segregated solid forms attached to the inverse segregation. This positive macrosegregation is induced by the increasing mushy zone width in this area due to a decreasing temperature gradient.

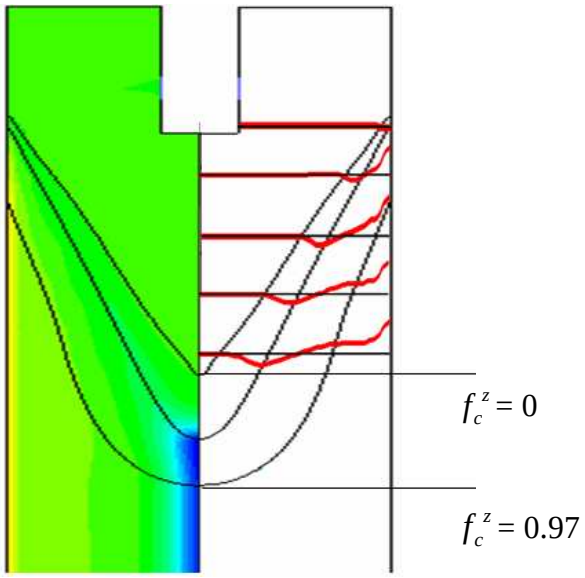

Figure 4-50: On the left a steady-state distribution of the mixture concentration c_{mix} of Sn in case with $\overline{K}_0 = 1.4 \cdot 10^{-5}$ considering only feeding flow. Bright green represents the initial alloy concentration, yellow positive and blue negative macrosegregations. Black lines show the isotherms of $T_{liquidus}$ = 1289 K, $T_{solidus}$ = 1230 K, and T_{end} = 1072 K. On the right c_{mix} profiles are displayed at 0.15, 020, 0.25 and 0.30 m depth of the casting (red curves). f_c^Z = 0: columnar volume fraction is 0 at the center, f_c^Z = 0.97: columnar volume fraction is 0.97 at the center.

Figure 4-51 gives a more detailed view on the macrosegregation pattern between $f_c^Z = 0$ (volume fraction solid in the center of the casting) and $f_c^Z = 0.97$ at a depth of 0.310, 0.320, 0.330, 0.340, 0.345, 0.350, 0.355, 0.360, 0.365, 0.375, 0.375, 0.380, 0.385, 0.390, 0.395, 0.400, and 0.405 m. On the right hand side a vertical profile along the center of the casting is displayed. *Figure 4-52* shows all the profiles overlaid in a c_{mix} plot of Sn versus distance *x* form the center of the strand. When reaching $T_{liquidus}$ ($f_c^Z = 0$) in the center of the casting, the two developed minima (left side and right side) in the mushy zone touch each other and in the following the negative values of macrosegregation at the center increase up to a depth of 0.375 m (*Figure 4-51* and *Figure 4-52*). Looking at the profiles between 0.375 m and 0.405 m, it can be seen that c_{mix}^Z is increasing again slightly to values below c_0.

The reason for this is the fact that the center of the casting is fed by almost ”fresh”, less segregated melt until c_{mix}^Z reaches a minimum at 0.375 m. Subsequently, the zone below this depth is fed by already segregated melt and therefore c_{mix}^Z increases again up to the depth of 0.405 m where the strand is fully solidified.

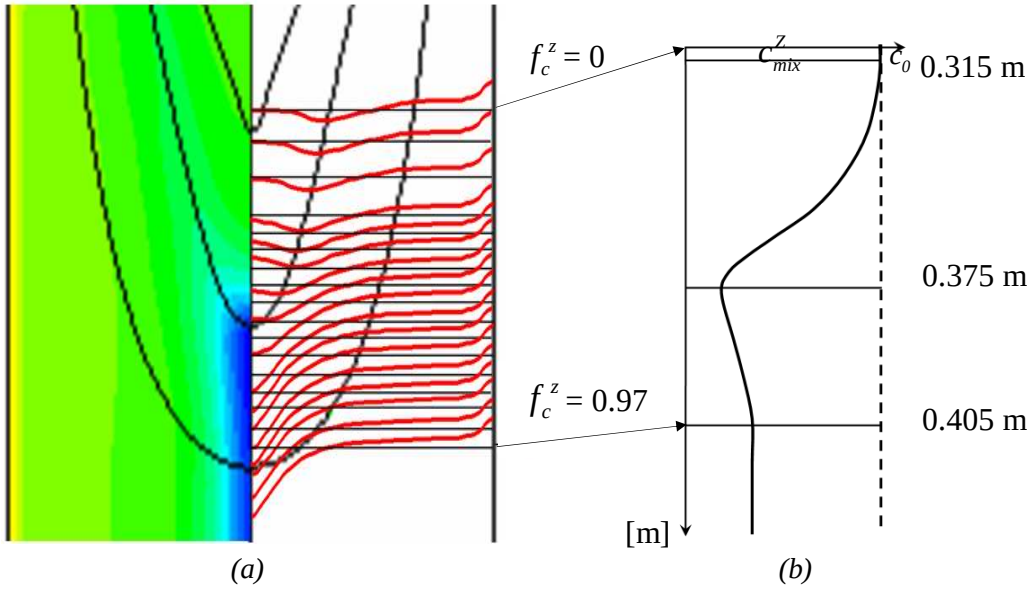

Figure 4-51: (a) left: steady-state distribution of the mixture concentration c_{mix} in case with low Blake-Kozeny-type mush permeability ($\overline{K_0}$ =1.4·10^{-5}) considering only feeding flow. Bright green represents the initial alloy concentration, yellow positive and blue negative macrosegregations. Black lines: isotherms of: $T_{liquidus}$ =1289 K, $T_{solidus}$ = 1230 K, T_{end} =1072 K. Right: the red curves show c_{mix} profiles of the calculation at 0.310, 0.320, 0.330, 0.340, 0.345, 0.350, 0.355, 0.360, 0.365, 0.375, 0.375, 0.380, 0.385, 0.390, 0.395, 0.400, and 0.405 m depth of the casting, f_c^z = 0: columnar volume fraction is 0 at the center, f_c^z = 0.97: columnar volume fraction is 0.97 at the center.

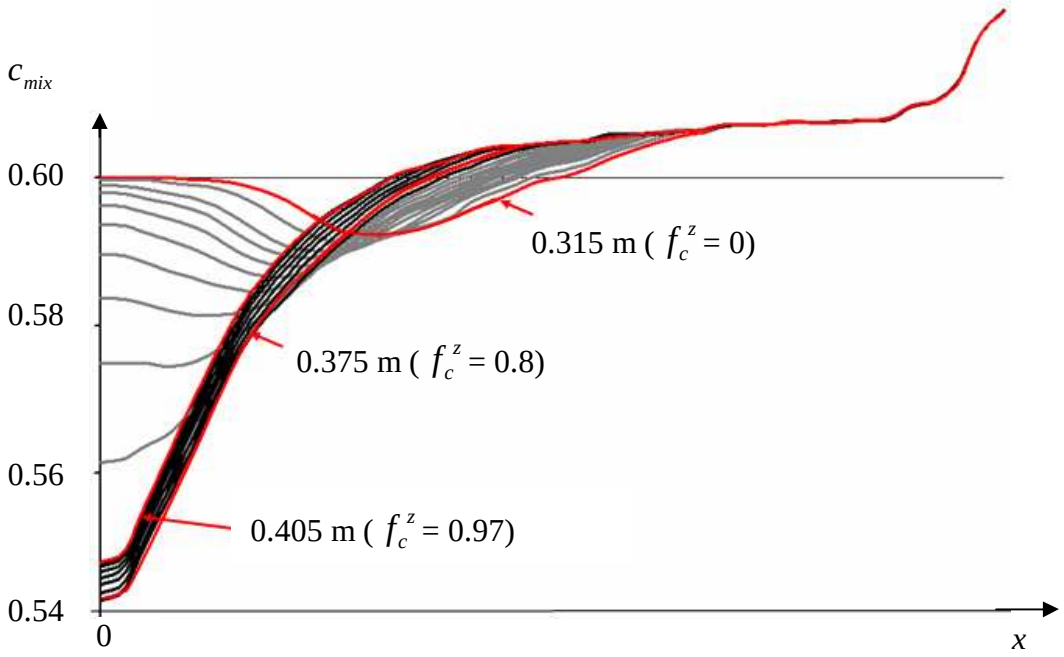

Figure 4-52: c_{mix} distribution of Sn over the casting length and the casting radius x. Red lines show the c_{mix} profiles indicated by the red arrows at 0.315 m, 0.375 m and 0.405 m depth, gray lines show the c_{mix} profiles between 0.315 m and 0.375 m depth, black lines show the c_{mix} profiles between 0.375 m and 0.405 m depth.

4.3.2 Verification of the Simulation Results

To verify the simulation results presented in chapter 4.2, experimentally obtained macrosegregation distributions are combared with calculated ones. The experimental measurements have been performed by Wieland in the solidified strand with XRF (X-Ray Fluorescence Method) with an measurement accuracy to 0.1 wt.%. For the 2D and 3D binary simulations, experimental concentrations and calculated ones are compared and discussed. Since the ternary model is still under development the verification of the simulation of these simulation results is performed by discussing the predicted species concentration with respect to expected Scheil calculations.

(i) 2D Binary

Figure 4-53 shows a typical, experimentally obtained macrosegregation distribution of Sn in a solidified strand of a CuSn7.6P0.22 round strand. Since in industrial praxis ternary or higher order alloys are cast, a strand containing very low P content is taken for the comparison with the binary case study. For the presented simulations the binary alloy CuSn6 was taken. Since for the experimental investigation no CuSn6 alloy was present, the simulation results are compared with slightly higher concentrated alloys. Therefore the comparison of the experimental and simulation concentration profiles is based on relative concentrations.

The experimentally detected Sn distribution and the calculated c_{mix} profile (*Figure 4-54*) for the case with low permeability show good qualitative agreement. In both distributions, positive segregated areas are obtained at the walls and negative ones in the center of the strand. Hence, there has to be discussed that a W-form is observed in the center of the casting. This effect is not observed in the simulation results. One reason for that could be that nucleation and sedimentation of the equiaxed grains are not taken into account yet in the simulation. Another reason could be that solidification does not stop at $f_c = 1$ columnar volume fraction but at $f_c = 0.97$ and additional phase transformations (as described in chapter 3.2.4) are not considered up to now. As equiaxed grains are usually obtained in the center of the strand, the two phase model excluding this additional phase has a certain error. In addition, solid deformation of the strand is not taken into account which is thought to have an important influence on the high Sn content at the surface of the strand.

Figure 4-55 shows the four Sn c_{mix} profiles at the outlet for the four cases with different permeabilities as displayed in *Figure 4-26*. It is visible, that deviation of the numerical macrosegregation prediction from the experimential profile increases with increasing permeability. In the case where the highest mush permeability is considered, the Sn distribution shows strong negative macrosegregation at the surface. This is not observed in industrial productions.

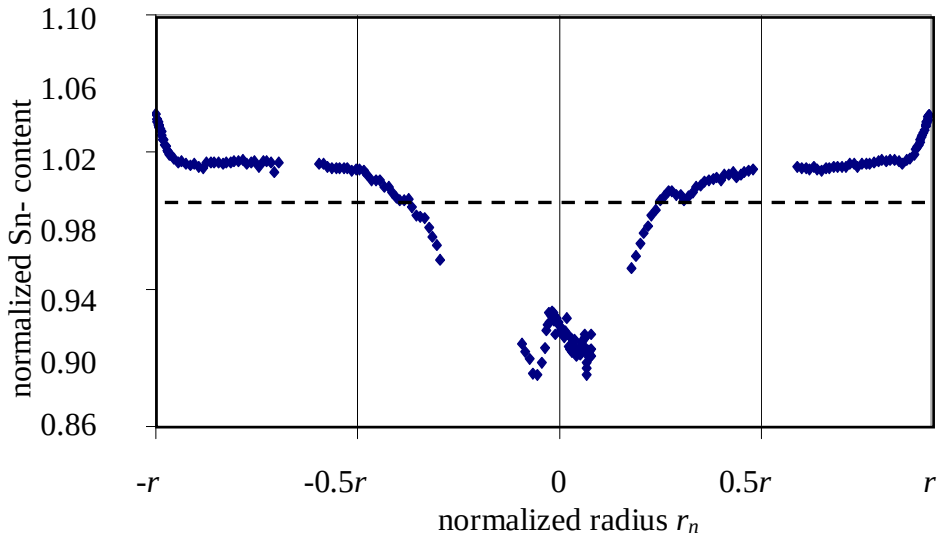

Figure 4-53: Typical surface-to-surface Sn distribution in a CuSn7.6P0.022 round strand.

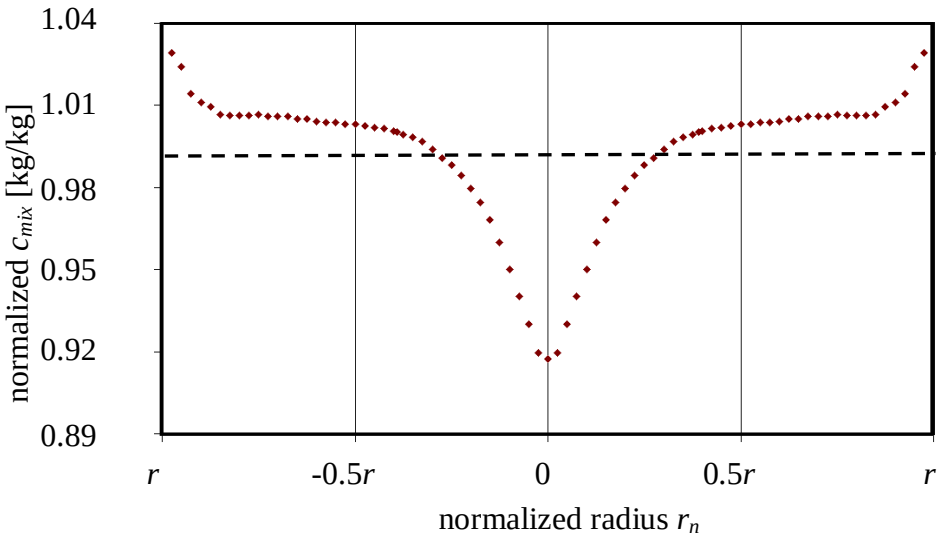

Figure 4-54: Calculated c_{mix} Sn distribution in a CuSn6 round strand in case of including forced convection, feeding flow, and thermo-solutal convection for low permeability. In both, experimental and simulation results, positive macrosegregations are observed at the wall and negative ones in the center of the casting.

The reason for that is that the inlet jet has an increasing influence with increasing permeability at the beginning of solidification. This indicates that it could be easier to obtain a homoghuous element distribution in the solidified strand if the relative flow in the mushy zone is kept as small as possible. Additionally, this implies the importance of the position of the inlet with respect to the beginning of the mushy zone. Based on the recent study, it can be statet that the inlet should be located in a way that the occurring flow does not reach the solidification front to minimize macrosegregation. But for special situations, for example strong inverse segregation at the wall, the inlet could be used to reduce this undesired effect.

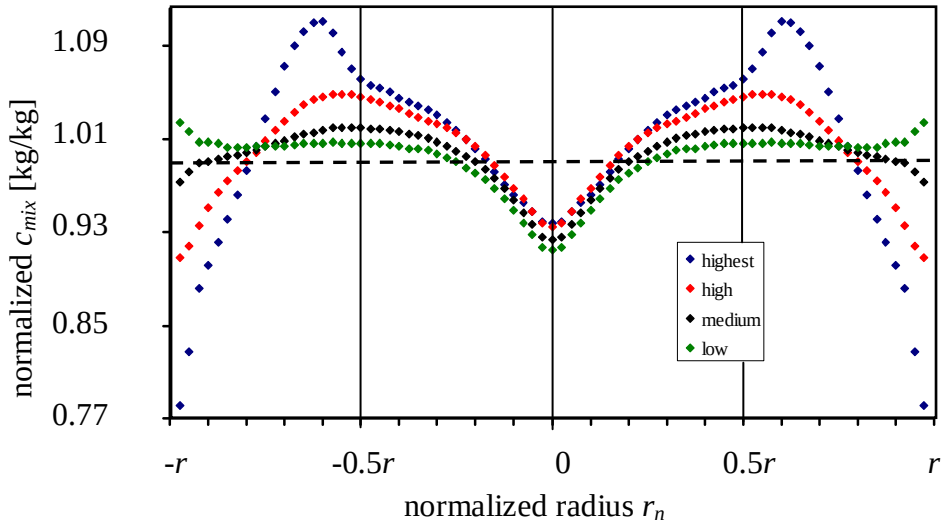

Figure 4-55: Comparison of Sn c_{mix} profiles at the outlet of the solidified strand for the four applied permeability values as shown in Figure 4-26 Higher permeability leads to stronger negative and positive macrosegregations in the solidified strand. Red dots: $\overline{K_0}$ =1.4·10^{-5}), blue dots: $\overline{K_0}$ = 1.4·10^{-4}, green dots: $\overline{K_0}$ =1.4·10^{-3}, black dots: $\overline{K_0}$ = 1.4·10^{-2}.

(ii) 3D Binary

The predicted macrosegregation distribution of the 3D laboratory continuous casting calculation (*Figure 4-57*, *Figure 4-58*) is compared with the experimentally observed Sn distribution shown in *Figure 4-56*. *Figure 4-57* displays the macrosegregation profile for the depth of the casting (*x*) and *Figure 4-58* for the width (*y*). The experimental profile is shown for the depth of the casted strand where positive macrosegregation is observed at the wall and negative ones in the center of the casting. Again, as already seen in the round strand, the experimental macrosegregation profile has a broad W- form in the center of the casting which is not obtained in the simulation results. However, the general behaviour seems to be well predicted. In comparison to the 2D axis symmetric simulations, it has to be mentioned, that the macrosegregations in the 3D geometry is lower in both, positive and negative concentrations.

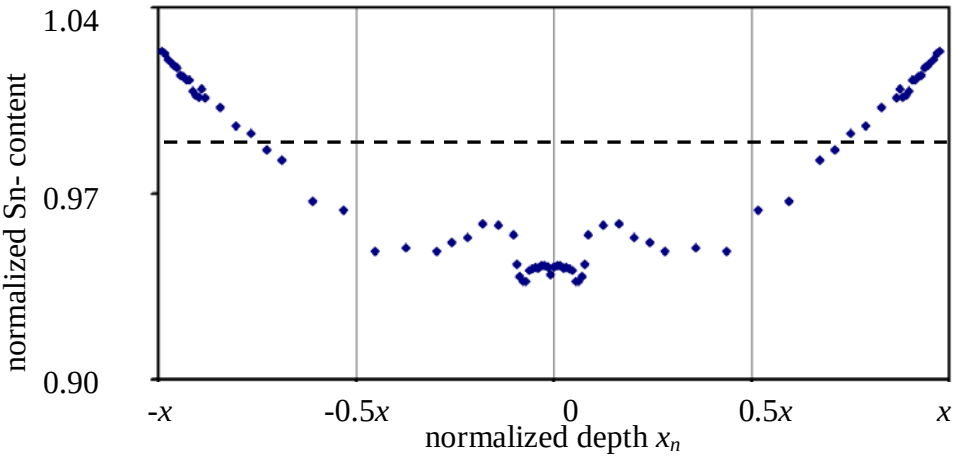

Figure 4-56: Measured profile of Sn distribution in a CuSn8.2P0.46 3D rectangular laboratory continuous casting strand (depth).

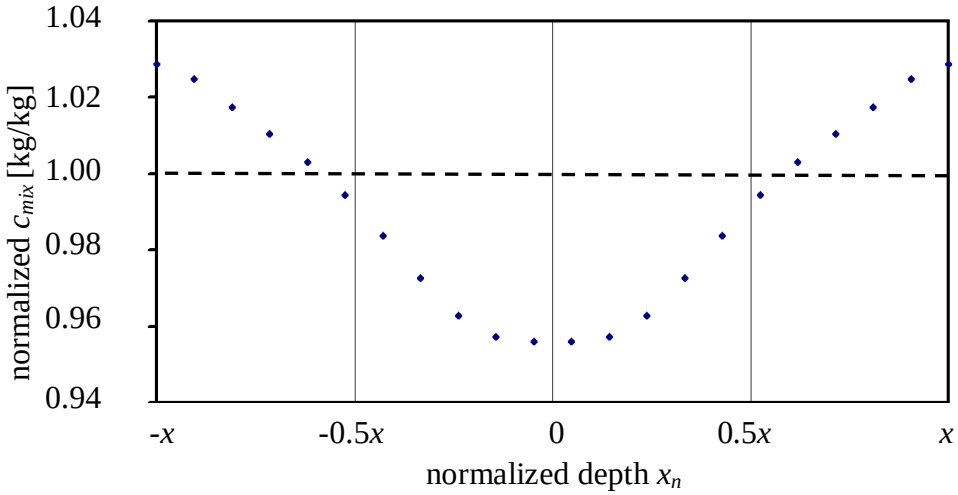

Figure 4-57: Calculated crosssection of the Sn c_{mix} profiles at the outlet in the CuSn6 3D rectangular laboratory continuous casting geometry (depth). The comparison of experiment and simulation result show the same tendency as already observed in the 2D case. Again, the W-form in the center is not predicted by the simulation results.

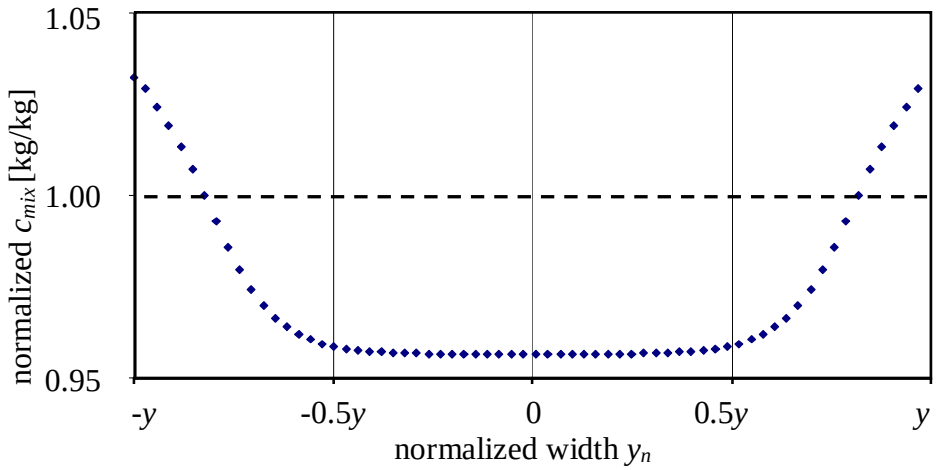

Figure 4-58: Calculated crosssection of the Sn c_{mix} profile at the outlet in the CuSn6 3D rectangular laboratory continuous casting geometry (width).

This could be caused by the fact that the 3D geometry is smaller than the 2D one, but also on the fact that the cooling conditions vary in the different cases. Besides, the 3D calculation has an inlet over the whole geometry, where the melt is entering the mold direct from the tundish. Based on this fact the velocity of the melt is not as fast as in the case of the 2D geometry where the inlet jet directly hits the mushy zone. In addition there is no special cooling taking place in the upper part of the 3D casting.

Figure 4-59 shows the macrosegregation distribution where the initial alloy concentration has green color, yellow areas indicate regions with positive macrosegregations, and blue areas are regions with negative macrosegregations. In addition macrosegregation is displayed for six different cutting planes of the casting. As already discussed, positive macrosegregations are formed at the mold wall and negative ones in the center of the continuous casting strand. The two lines in *Figure 4-59* mark the tracer lines for a negative segregated area (line 1) and a positive segregated one (line 2). The diagram on the right in *Figure 4-59* displayes average columnar concentration $\bar{c}_c$ versus volume fraction columnar f_c for the two tracer lines and compare them with the calculated cumulative Scheil curve for CuSn6P0.5. The comparison between CFD calculation and Scheil shows that the simulated curve differs slightly from the Scheil curve in the regions where negative macrosegregation is observed and significantly where positive macrosegregation is formed. Since Scheil does not consider concentration changes due to the flow, the deviation shows the important influence of the flow field occurring during solidification. Since resently the simulation ends at a volume fraction solid of 0.99, the expected tendency of the three curves to or even above the original alloy concentration is not reached in the cumulative solid concentration. In industry, deviations in the microstructure are observed between Sn enriched and depleted areas. The micrograph (right, *Figure 4-59*) shows highly Sn enriched areas where the probability of the presence of the δ phase (black small interdendritic regions) is increased. It is possible to gain information about microstructure distributions by relating the output of CFD calculations for macrosegregation with thermodynamic equilibrium calculations at the interesting temperature range [GRUBER 08].

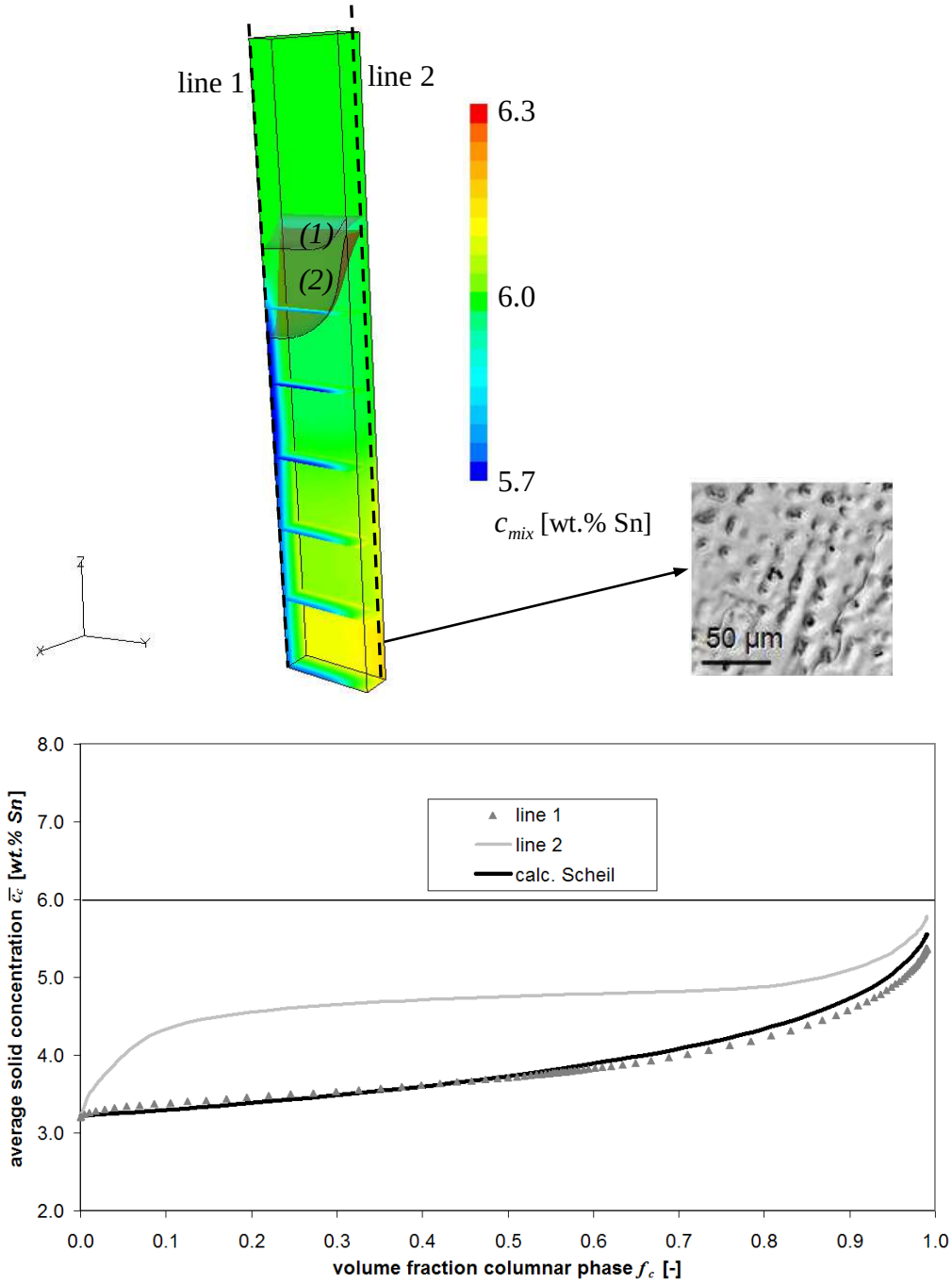

Figure 4-59: Macrosegregation distribution in the simulated continuous casting geometry is shown in color scale at the top of the figure. Yellow areas are positive and blue areas are negative segregated. Green indicates regions with original alloy concentration. The first displayed gray surface (1) is the isosurface of $T_{liquidus}$ = 1289 K whereas the red one (2) is the isosurface of f_c = 0.5. The other horizontal surfaces display the macrosegregation distribution for six horizontal planes. The micrograph on the left of the macrosegregation distribution shows obtained eutectoid of δ phase (dark regions) and α dendrits (gray to white) [GRUBER 07A]. The average concentration of Sn in the columnar phase is plotted versus the volume fraction of the columnar phase in the diagram on the bottom of the figure. The solid concentration obtained along the two lines as indicated in the geometry on the top are compared with the expected concentrations according to cumulative Scheil calculation. Black straight line is the initial alloy composition.

(iii) 2D Ternary

To verify the proposed ternary solidification model, a "0D" solidification simulation of the CuSn6P0.5 alloy was performed. Temperature T is assumed to decrease linearly with time, starting from the initial temperature T_0 with a given constant cooling rate $\dot{T}_0$. This Initial Value Problem was integrated using the CFD-solver FLUENT with appropriate settings. The thermodynamic functions (equation 4-31 to equation 4-33) were interpolated based on tabulated Thermo-Calc data for the Cu-Sn-P system. Initial values were taken as follows: $f_c(0) = 10^{-5}$, for the columnar volume fraction and $c_l^{Sn}(0) = 6.0$ wt.% and $c_l^{P}(0) = 0.5$ wt.% for the mass fractions of Sn and P in the liquid phase. Inital temperature was set to $T_0 = 1297$ K and the cooling rate $\dot{T}_0 = 1\ \mathrm{K \cdot s^{-1}}$. *Figure 4-60* shows the Scheil-curves resulting from the ternary solidification simulation in comparison with appropriate Scheil-curves calculated with Thermo-Calc. Since the Thermo-Calc-Scheil model implies an infinite diffusion coefficient in the liquid but the proposed model uses a finite one, the diffusion coefficient for the "0D" model was increased to make comparison with Thermo-Calc results possible. Nevertheless minor differences are observed, as shown in the small windows in *Figure 4-60*. Discrepancies also occur at high columnar volume fraction (B in *Figure 4-60*). Here the presented model is not valid since it models only the formation of one solid phase from the liquid, whereas there are two solid phases forming directly from the liquid during the eutectic reaction. Apart from the differences mentioned, the curves produced by the proposed model are in good agreement with those calculated with Thermo-Calc [ISHMURZIN 08].

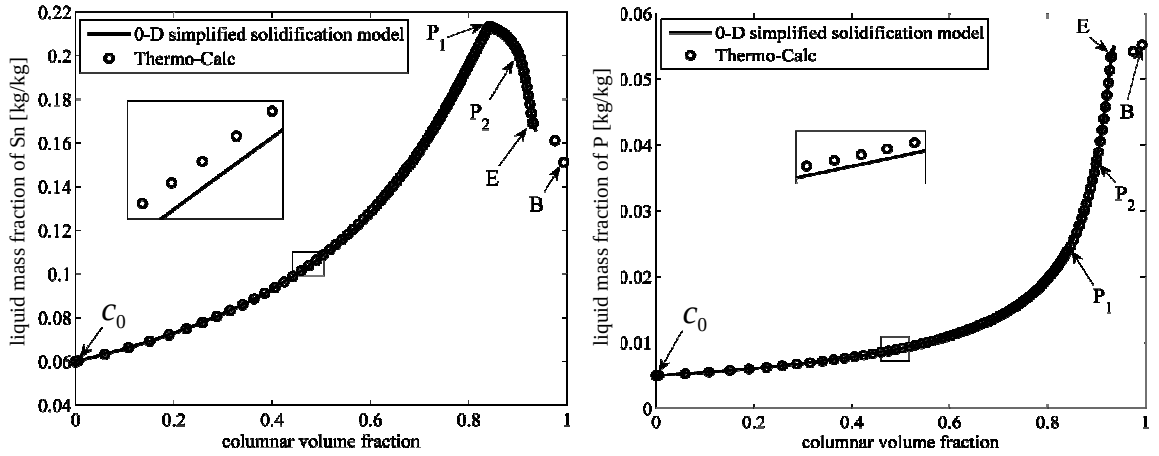

(a) *(b)*

Figure 4-60: Scheil curves calculated for the alloy CuSn6P0.05 for (a) Sn and (b) P with the"0D simplified solidification model" (black line) and compared with a Thermo-Calc Scheil calculation (circles). Here c_0 is the initial alloy concentration, P_1 corresponds to the beginning of the first peritectic reaction L + $\alpha \rightarrow \beta$, P_2 to the beginning of the second peritectic reaction L + $\beta \rightarrow \gamma$, E to the beginning of the eutectic groove, and B to the end of solidification according to the Thermo-Calc Scheil model [ISHMURZIN 08].

Figure 4-61 shows the liquidus surface projection as already described in chapter 4.2.4 including the expected solidification path according to ThermoCalc Scheil calculations (thick black line). The black broken line is the linearized solidification path used for the calculations. It is visible that at higher Sn and P concentrations the linearization causes a certain error.

Principally, all three functions T_L (equation 4-31), $\tilde{c}_c^{Sn}$ (equation 4-32), and $\tilde{c}_c^{P}$ (equation 4-33) can be approximated using their pointwise Thermo-Calc tabulations. Generally, any suitable interpolation can be applied. For the following up-scaling of the model to industrial dimensions the three thermodynamic functions (equation 4-31 to equation 4-33) were linearized around the initial composition (point c_0, *Figure 4-60*).

The presented ternary calculations predict macrosegregation for the two solute elements, Sn and P. Since the P content of this study was considered to be higher than usually applied in industrial continuous casting of a round strand of bronze, no comparable experimental measurements are available at the moment. To validate the already obtained macrosegregation distributions, the simulation results just considering forced convection are compared with concentrations predicted by Scheil calculations. The broken line in *Figure 4-61* indicates the solidification path according to the linearization. It is visible that at higher Sn and P concentrations the linearization causes a certain error.

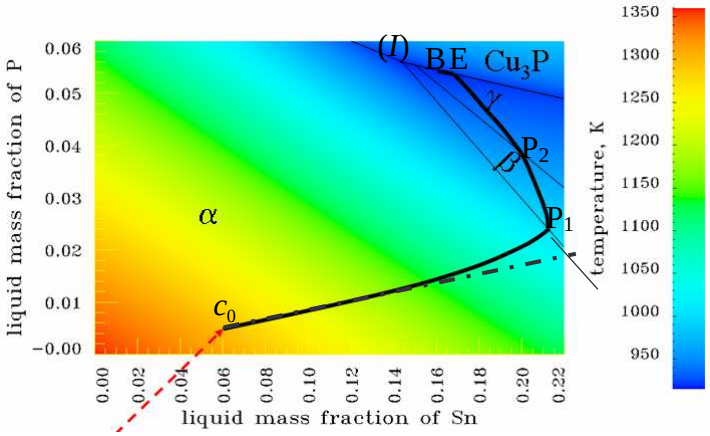

c_0 = CuSn6P0.5

Figure 4-61: Rectangular 2D liquidus surface projection of the Cu rich corner for the ternary phase diagram Cu-Sn-P up to 22 wt.% Sn and 6 wt.% P based on calculations with Thermo-Calc (database CuSn1).The black thick line shows the solidification path predicted by a Scheil calculation for CuSn6P0.5. The black thin lines assign the monovariant lines of the liquidus surface. The color scale displays the temperature of the liquidus isosurface. P_1 marks the monovariant line corresponding to the peritectic reaction L + $\alpha \rightarrow \beta$, P_2 the monovariant line corresponding to the peritectic reaction L + $\beta \rightarrow \gamma$, E the monovariant line corresponding to the eutectic reaction L $\rightarrow Cu_3P + \varepsilon$, B the end of solidification predicted by the Scheil calculation (Thermo-Calc, database CuSn1), and (I) the ternary eutectic point. The black broken line is the linearized solidification path of the ternary model.

To verify the simulated mixture concentration with concentrations expected by thermodynamics $\bar{c}_c$ and c_l are compared with corresponding concentrations according to a Scheil calculation performed with Thermo-Calc. The Scheil model is based on the assumptions that no diffusion is consideren in the solid and indefinite fast diffusion in the liquid.

If both phases, liquid and solid phase, have the same density the mixture concentration c_{mix} is simply given by

$$c_{mix} = \bar{c}_c f_s + c_l f_l . \qquad (4.3.2)$$

Here $\bar{c}_c$ is the averaged solid concentration corresponding to the shell wise growth during solidification. For this comparison the case without feeding is studied because these results should show a concentration field close to the expected curve according the Scheil model. However, in the discussed case the influence of the inlet jet is still present.

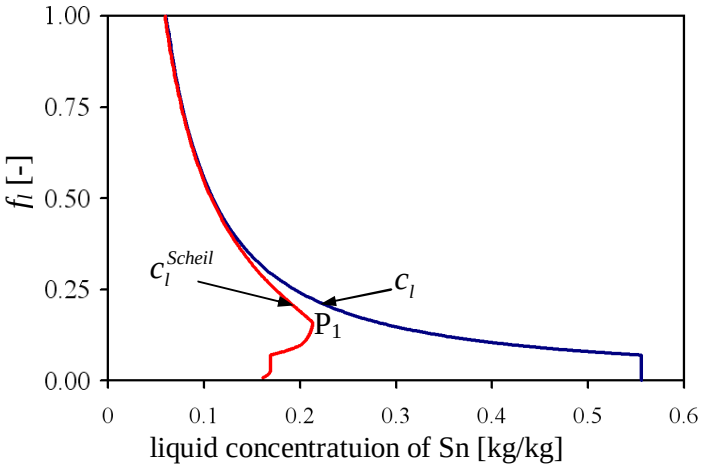

Figure 4-62: Scheil concentration for Sn (red curve) calculated with ThermoCalc (database CuSn11) compared to f_l versus c_l of the FLUENT calculation (dark curve) of CuSn6P0.5 for Sn. c_l^{Sn} starts to deviate from c_l^{Scheil} below a volume fraction liquid of approximatley f_l = 0.4. The first peritectic groove is reached at f_l = 0.17 (P_1). The calculated concentrations below this volume fraction show to high values and are so far away from expected concentrations.

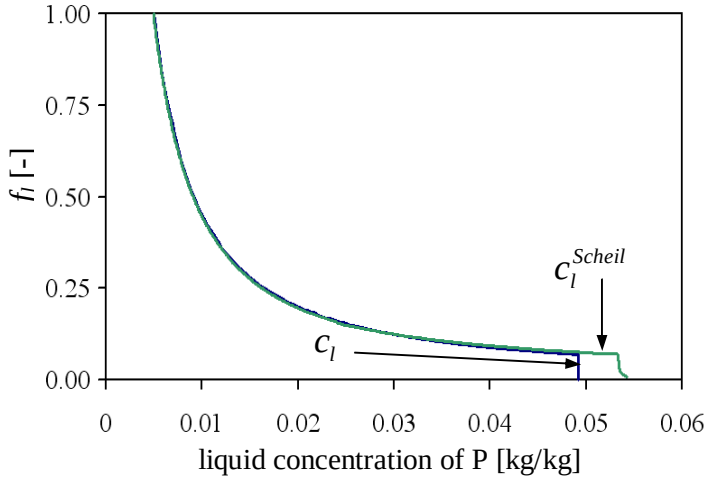

Figure 4-63: Scheil concentration for P (green curve) calculated with ThermoCalc (database CuSn1) compared to f_l versus c_l of the FLUENT calculation (dark curve) of CuSn6P0.5 for P. The calculated Scheil curve and the simulated one do not differ significantly at higher volume fraction. Therefore, there is a deviation observed at the end of solidification, where the Scheil curve predicts higher enrichment of P in the liquid than the simulation does.

Figure 4-62 and *Figure 4-63* show liquid concentrations c_l for Sn and P plotted versus volume fraction liquid for CuSn6P0.5 and the propsed values by Scheil calculations performed with Thermo-Calc c_l^{Scheil}. Since a linearization around the alloy concentration c_l^0 is applied for the ternary process simulation, the calulated liquid concentration c_l^{Sn} (dark line, *Figure 4-62*) starts to deviate from c_l^{Scheil} (red line, *Figure 4-62*) at a volume fraction liquid of around $f_l = 0.40$. The first peritectic groove is reached at $f_l = 0.17$ (point P_1). Below this point the calculation predicts far too high liquid concentrations.

For c_l^P the linearization approach does not have that big influence as for c_l^{Sn}, here the calculated Scheil curve (green line, *Figure 4-63*) and simulated one (dark line, *Figure 4-63*) do just differ significantly at high volume fraction. Anyhow, the strong enrichment in the liquid does not have a big influence on the c_{mix} field because of its low volume fraction. With that its contribution to equation 4.3.2 is rather low. The reason for the enrichment of Sn in the liquid is caused by the fact that just the Sn poor α phase is considered. As already shown in *Figure 4-60* taking into account the first or even the second peritectic transformation, the concentration profile fits more the expected thermodynamic prediction.

To compare the average $\bar{c}_c$ of the simulation results with Scheil calculations preformed with ThermoCalc (database CuSn11), an cumulated $\bar{c}_c^{Scheil}$ is calculated by using

$$\bar{c}_c^{Scheil} = \frac{1}{f_c} \sum c_c^{Scheil} \Delta f_c^{Scheil}, \tag{4.3.3}$$

where c_c^{Scheil} is the given columnar concentration and Δf_c^{Scheil} the change in the columnar volume fraction according to Scheil calculations.

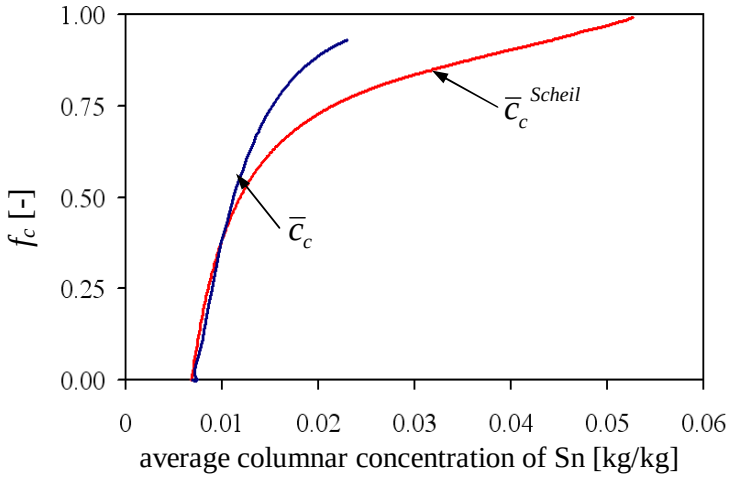

Figure 4-64: Cumulative Scheil curve $\bar{c}_c^{Scheil}$ (red line) calculated with ThermoCalc and combared with average columnar concentration of solidification simulation $\bar{c}_c$ (dark curve) for Sn in CuSn6P0.5. The calculated Scheil curve (red line) and the simulated one (blue line) do not differ significantly until a volume fraction solid of about 0.4 is reached. Due to the fact that the tin rich phases are not considered up to now in the solidification simulation, a significant deviation is observed for higher columnar volume fractions.

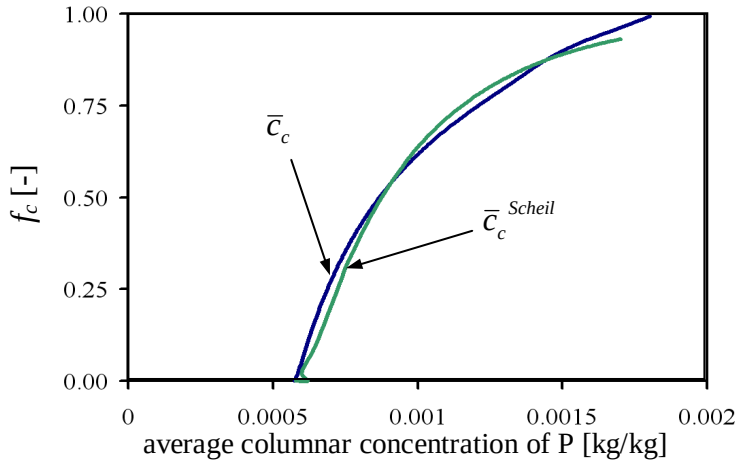

Figure 4-65: Cumulative Scheil curve $\bar{c}_c^{\,Scheil}$ (green line) calculated with ThermoCalc and combared with average columnar concentration of solidification simulation $\bar{c}_c$ (dark curve) for P in CuSn6P0.5. The calculated Scheil curve and the simulated one differ slighlty.

Figure 4-64 and *Figure 4-65* show $\bar{c}_c$ and c_c^{Scheil} plotted versus volume fraction solid for Sn (*Figure 4-64*) and for P (*Figure 4-65*) of the FLUENT calculation with CuSn6P0.5 and the propsed values by cumlative Scheil calculations based on ThermoCalc. It is shown that the Sn concentration of the average columnar concentration and with that the macrosegregation is underestimated in the simulation for higher volume fractions. Further development of the model is strongly demanded to include the peritectic reactions for the prediction of macrosegregations. Anyway, the P content of the columnar phase in the simulation is close to that predicted by Scheil calculations.

Figure 4-66 and *Figure 4-67* show the simulated macrosegregation profiles for Sn and P in the solidified strand for the case including feeding flow. The c_{mix} profiles indicate positive macrosegregations at the wall and negative ones at the center for both, Sn and P. This tendency is comparable to the observed macrosegregation in the binary cases.

Gernerally it can be stated that the magnitude of the predicted macrosegregation for Sn and P is qualitatively almost the same. One reason for this could be that for both alloying elements the same diffusion coefficient in the liquid $D_l^{Sn} = D_l^P$ was considered, since exact values are not known precisely. In addition, both alloying elements are enriched almost linearly during solidification because of the observed linear solidification path in the α region. Of course, the macrosegregation distribution between the two elements would differ significantly if the peritectic reactions were taken into account.

Since the phase transformation of the peritectic reaction is ignored and therefore the thermodynamics is still simplified, the simulation results for the ternary Cu-Sn-P system are not comparable to experiments at the moment. In addition the exclusion of the equiaxed phase might have an addition impact on the predicted macrosegregation distribution under as-cast conditions.

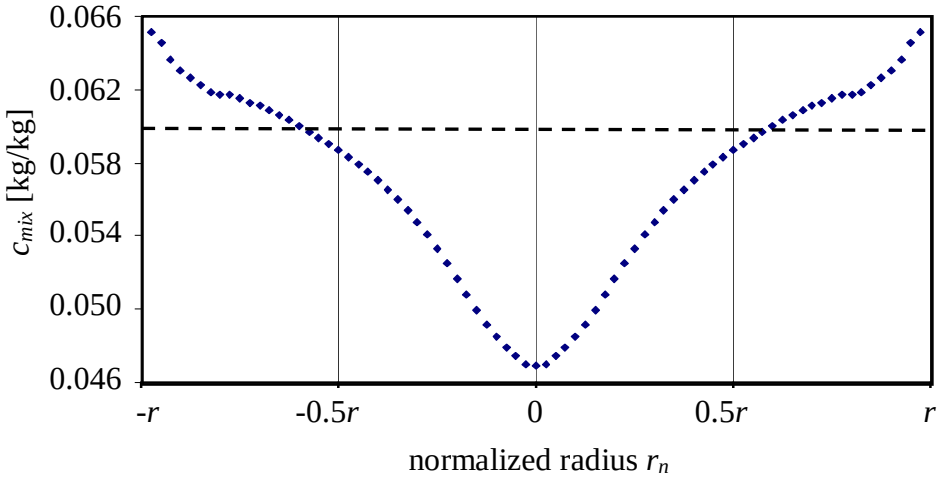

Figure 4-66: c_{mix} profile of Sn distribution in a CuSn6P0.5 round strand (calculation with feeding flow and forced convection).

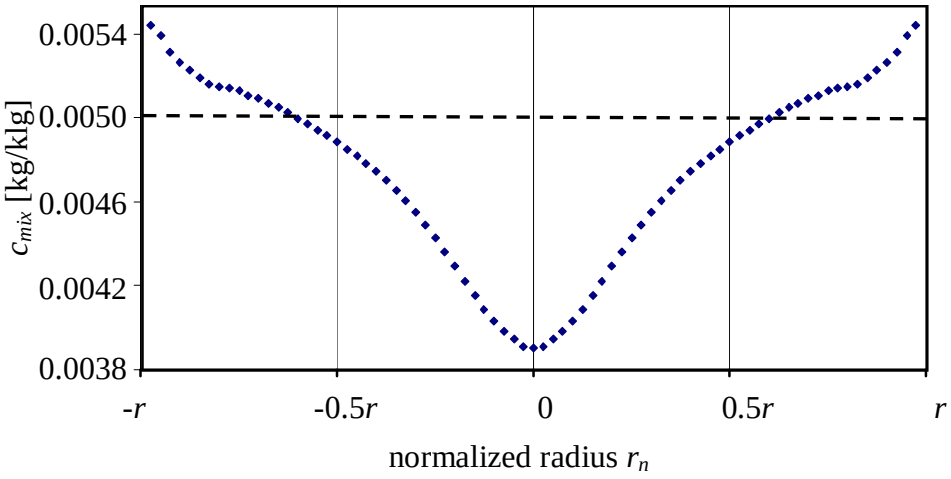

Figure 4-67: c_{mix} profile of P distribution in a CuSn6P0.5 round strand (calculation with feeding flow and forced convection).

5 Conclusions and Future Needs

Formation of macrosegregation in technical bronze alloys is studied in the presented work for both areas, thermodynamics of the included Cu-Sn-P system and numerical simulation. In addition, the numerical results are compared with experimental measurements of the real solidified strand.

The presented experimental study is based on DSC measurements and diffusion experiments coupled with SEM investigatins. The obtained results show good agreement with published and essessed data for the binary phase diagram as well as the ternary one. The achievements of the presented work are as follows:

- The phase appearance proposed by literature was confirmed by the measurements.

- The presented diffusion experiments indicate that there is a ternary eutectic point in the Cu-Sn-P system at approximately CuSn15P5. Thermo-Calc (database CuSn1) and Miettinen [MIETTINEN 01] propose this point at around 644 °C. Based on the observed phase distributions up to now, this point can be confirmed to lie between 648 °C and 644 °C.

- The ε phase was not observed in the presented study, neither in the DSC measurements nor in the diffiusion experiments. Since, this phase occurs, according to literature and industry, after very long transformation times, it is reasonable to ignore it in simulations for technical applications.

- The γ phase was detected in a ternary sample in the presented study. In former experimental work performed for the ternary system by Takemoto [TAKEMOTO 87] the γ phase was not observed at all.

- It has to be mentioned that there are some discrepances between different statements in literature, Thermo-Calc calculations, and the performed experimental work, as for example the liquidus curve of the CuP system and the occurring phases around the ternary eutectic point in the ternary system. However, since the P amount used in industry is rather low, as a first attemt the database CuSn1 is sufficient accurate to use it for ternary process simulation.

Based on the observations of the presented experimental study the following is suggested for future work:

- The preperation of the diffusion samples is rather difficult due to the high rigidity of the Cu_3P phase. According to this, further work has to be done to improve the sample preperation for alloys with high P contents.

- The presence of the γ phase in the presented work is in contrast to the observations of [TAKEMOTO 87]. Further studies on the conditions of the occurance and stability of the γ phase are a challanging subject.

Macrosegregations in DC casting are generally caused by a relative motion between the solid and the liquid. The present numerical study of the continuous casting process investigates how the formation of macrosegregations in DC casting of columnar solidifying Sn or SnP bronze is influenced by different phanomena, as the 'inlet jet-mush' interaction, the thermo-solutal buoyancy driven flow and the shrinkage-induced feeding flow. Simulations were performed to investigate the influence of high and low permeable mushy zones. In addition, the influence of the casting speed on the macrosegregation distribution in the solidified strand was investigated. For this, two different geometries, a round and a rectangular strand have been investigated. The round strand was studied for the binary CuSn6 and the ternary CuSn6P0.5 alloy and the rectangular geometry for the binary CuSn6 alloy.

The highlights gained by the presented study are as followed.

- For all used permeability values and geometries, the 'jet-mush' interaction leads to negative macrosegregations on the surface and positive ones in the bulk of the casting if feeding flow is ignored. Here higher permeability leads to more pronounced segregation than lower one.

- Solutal buoyancy driven flow is negligible for the used axis symmetric case with low mush permeability. Considering higher permeabilities, negative segregations occure at the wall due to the jet-mush interaction, and in the middle of the casting due to solutal buoyancy. An enrichment of solute is predicted close to the solute-poor region near to the casting wall because solutal buoyancy convection forces the solute-rich fluid to rise through the higher permeable mush.

- For all used permeability values, thermal buoyancy driven flow and its interaction with the inlet jet and the mushy zone plays an important role for the 2D axis symmetric case. If additional phenomena are ignored, the negative surface macrosegregations and the positive bulk macrosegregations are more pronounced in comparison to the case where just inlet flow is considered. For higher mush permeability, the larger mushy zone enables an increase in macrosegregations throughout the whole casting.

- Shrinkage-induced feeding flow causes positive macrosegregations at the surface for the 2D axis symmetric case. In case of higher mush permeability the interaction with the jet is stronger than in the case with lower permeability. Therefore, solute poor solid is formed at the wall, followed by a positive segregated area and a negative segregated solid in the centre.

- The 2D axis symmetric cases which include feeding flow, thermo-solutal buoyancy flow and forced inlet flow show the expected superposition of the different phenomena. In the case with lower permeability, positive macrosegregations are predicted at the wall and strong negative ones in the centre. Higher permeability causes significant changes in the macrosegregation pattern, namely negative segregations at the wall (caused by the inlet jet) and in the centre (mainly influenced by feeding flow), while for the rest, positive macrosegregations are predicted.

- The 3D calculations of the rectangular laboratory geometry show similar behaviour as already discussed for the 2D axis symmetric geometry, namely positive segregations occuring close to the surface and negative ones in the center of the casting. However, in the discussed 3D case the macrosegegation pattern is not as pronounced as in the 2D axis symmetric case.

- The results show the high dependency of macrosegregations on the flow pattern, and hence on the permeability of the mushy zone. Generally, it can be stated that higher permeability increases the possibility of fluid movement in the mushy zone which goes hand in hand with more pronounced macrosegregations in the casting.

- The ternary "0-D case" shows that the model is able to reproduce the solidification path proposed by Thermo-Calc Scheil calculations.

- The presented 2D axis symmetric ternary simulation results based on the simplified thermodynamic assumption so that only solidification of α phase is considered. Here, the same trend of the macrosegreation is observed for both alloying elements. In the ternary case calculations the β phase has a major impact on the solid concentrations as comparisons with Scheil calculations show.

- The comparison of measured macrosegregation distributions with simulated ones shows good qualitative agreement for the binary cases discussed. Nevertheless, the W-formed of negative center macrosegregation could not be observed in the simulation work up to now.

- A coupling between thermodynamics and CFD could give a possibility to predict microstructure distributions based on macrosegregation calculations.

The model based on current assumptions provides a numerical tool for qualitative study of macrosegregations. Although good qualitative agreement is obtained by comparing the simulation result with the experimental measurement, quantitatively further refinements/improvements of the current model are necessary. Further more, boundary conditions as well as material properties for the simulations could be improved. Some important points are discussed as follows.

- As studied in this work, permeability is one of the most important parameters influencing the macrosegregation in the continuous casting. Some efforts on this topic have been already done in last decades (for example [APELIAN 74, GOYEAU 99, SCHNEIDER 95]). Based on the presented study, further work is required to model the permeability of the mushy zone for specific processes.

- It is of evidence that equiaxed solidification and grain sedimentation plays an important role in the formation of macrosegregation. In the presented two phase model, nucleation, growth and sedimentation of equiaxed crystals are ignored. For further studies the mixed columnar-equiaxed solidification model (CET), recently suggested by Ludwig and Wu [WU 06], could be applied to take the third phase into account.

- In addition, exudation has not been taken into account in the current model. For this a coupling between CFD and stress and distortion simulation (Finite Element Methode (FEM)) is necessary but at the moment not available.

- The current model is based on the assumption of a shell-type growth driven by diffusion around the cylinder. In the mushy zone, the local average concentration of the interdendritic liquid, c_l, is supposed to be different from the local average equilibrium concentration at the solid/liquid interface, $\tilde{c}_l$. This difference is taken as the driving force for growth of the columnar phase. In a previous publication by Wu and Ludwig [WU 06], detailed parameter studies on the c_l and $\tilde{c}_l$ in the mushy zone were performed. In a 1D unidirectional solidification, the species in the mushy zone is predicted to be gradually enriched with the evolution of the solid phase. Although c_l is predicted to be somehow smaller than $\tilde{c}_l$, especially in the region near to the columnar tips, the predicted $c_l - f_c$ curve is quite close to the $\tilde{c}_l - f_c$ curve according to the Scheil assumption (ideal diffusion in the liquid). There was a simulation done with an artificially increased D_l and it was found that both the simulated $c_l - f_c$ curve and the Scheil $\tilde{c}_l - f_c$ curve are almost identical [WU 07]. This indicates that although a shell-type growth driven by diffusion around the cylinder is assumed, it reproduce closely the classical Scheil type mushy zone behaviour.

- As for the considered case the typical Reynolds-number is not larger than $\mathrm{Re} \approx 900$, the simulation results presented in this study did not include any turbulence flow. The highest Reynolds-numbers are found in the upper part of the pool region near the entry nozzle. Inside the pool and especially in the mushy zone the Reynolds-numbers are smaller by orders of magnitudes.

- The presented ternary results are only reliable for low volume fraction solid. It is shown that the model works in CFD, but further development, which is out of the scope of this work, has to be done. Applying the ternary model in the way that the peritectic reactions are taken into account might lead to significant differences in the Sn and P macrosegregation profiles.

- The numerical predictions depend strongly on the considered geometry and other casting properties. Therefore, any changes in casting conditions can influence the macrosegregation results significantly.

6 Summery

During the last decades industrial production of technical bronzes was more and more supported by numerical description of the applied manifacturing processes and the physics behind. Bronze tends to form microsegregations and, in combination with relative flow between the phases, macrosegregations during DC-casting due to the particular thermodynamic properties and kinetics of phase transformation. Therefore, the research in respect to this area was be pushed forward by the presented study. Due to the observed heterogeneous cast microstructure, tin rich phases form, which are brittle at room temperature as well as at hot working temperature. This could lead to a decrease in workability during a subsequent production process. As known from industrial praxis, the extent of macrosegregations in DC-casting can be effectively influenced by casting parameters like casting velocity, primary cooling or inlet geometry which in fact change the relative flow between the melt and the forming solid.

This work presents a detailed study on the thermodynamics of the ternary system Cu-Sn-P, which can roughly be considered to describe technical bronze alloys. Therefore computational thermodynamics and diffusion experiments have been performed together with DSC and SEM measurements. The obtained experimental data was compared with published and calculated data based on literature. Here in general good agreement was obtained with already assessed data for the ternay phase diagram. One major point is that it was possible to observe the γ phase in this ternary system which was not possible up to now. However, there are still some points that need further studies to verify the system in more details.

In addition to the experimental investigations, numerical studies have been performed to describe the physical processes taking place during continuous casting of bronze. To understand the influence and interaction of the related phenomena, simulation methods are applied to 2D and 3D geometries, for binary and ternary alloys. The solidification of a strand as well as the formation of macrosegregation is simulated with a two phase volume averaging model. The velocity field of the melt flow is explicitly calculated by solving the corresponding momentum conservation equation. Within the mushy zone the local formation of microsegregations in the presence of feeding and buoyancy flow is estimated. The thermodynamics of the Cu-Sn system in the case of the binary simulations is accounted for by a linearization of the binary real phase diagram and in the ternary calculations the Cu-Sn-P system is included by a thermodynamic model. In both cases it is distinguished explicitly between the solid/liquid interface and average melt concentrations.

Since it is known that the flow field in the mushy zone contributes to the macrosegregation pattern in the whole strand, the influence of different flow phenomena (thermosolutal buoyancy flow, feeding flow and forced convection) on the formation of macrosegregations was investigated. Based on simulations with a 2D axis symmetric geometry and a binary CuSn6 alloy, the results of case studies are discussed by separating the different convection mechanisms and combining them. Additionally, a study on the influence of the Blake-Kozeny-type mush permeability on the macrosegregation pattern has been performed. With that, it is demonstrated that the individual flow phenomena contributes differently to the final macrosegregation distribution. In addition it was shown that the casting speed influences the macrosegregation distribution in the solidi-

fied strand. Ternary calculations have been performed for the 2D axis symmetric geometry and give qualitative predictions for both, P and Sn macrosegregations in a round strand. The studies show that the flow field in the mushy zone has a major impact on the macrosegregation distribution, whereas the flow field itself can be influenced by, for example, the geometry, the casting velocity, or the applied cooling conditions.

It was possible to obain good qualitative agreement between the predicted macrosegregation distributions with measured element distributions of casting processes for the binary simulations. Nevertheless, based on the presented work it can be stated that for the ternary simulations further development of the model has to be done. Therefore, for future work further development and adjustment of the presented model and the process description is necessary.

Based on the recent study, it was shown that strong flow locally in the mushy zone induces strong macrosegregation. In addition, an increase of mush premeability leads to a higher interaction of the flow with the mush and causes therefore changes in the solute distribution. It can be stated that microsegregation in combination with relative velocity between liquid and solid phase induces macrosegregation.

7 References

[AGREN 02A] J. Agren, F.H. Hayes, L. Höglund, U.R. Kattner, B. Legendre, R. Schmid-Fetzer, Zeitschrift für Metallkunde, 93, 2, 2002.

[AGREN 02B] J. Agren, Scripta Materialia, 46, 2002, 893-898.

[AGREN 07] J. Agren, pers. com., 2006.

[AMBERG 05] G. Amberg, J. Shiomi, Fluid Dyn. Mater. Proc., 1, 2005, 81-96.

[ANCHORBRONZE 07] http://www.anchorbronze.com

[ANDERSSON 02] J.O. Andersson, T. Helander, L. Höglund, P. Shi, B. Sundman,Calphad, 26, 2002, 273-312.

[ANDERSSSON 92] J.-O. Anderssson, J. Agren, J. Appl. Phys., 72, 1992, pp. 1350.

[APELIAN 74] Apelian, M.C. Flemings, R. Mehrabian, Metall. Trans., 5, 1974, 2533-2537.

[ATKINS 82] P.W. Atkins, Oxford University Press.

[BAUER 30] O.Bauer, M. Hansen, Z. Metallkunde, 22, 1930, 367-391.

[BECKERMANN 88] Beckermann, C. and Viskanda, R., *PhysicoChemical Hydrodynamics*, 10, 1988, pp. 195.

[BECKERMANN 93] C. Beckerman, R. Viskanta, Appl. Mech. Rev., 46, 1993, pp. 1.

[BECKERMANN 94] C. Beckermann, C.Y. Wang, JOM, 46, 1994, pp. 42.

[BECKERMANN 96] C. Beckermann, C.Y. Wang, Metall. Mater. Trans. A, 27A, 1996, pp. 2784.

[BECKERMANN 02] C. Beckermann, Inter. Mater. Reviews, 47, 2002, pp. 243.

[BHADESHIA 02] H. K. D. H. Bhadeshia, http://www.msm.cam.ac.uk/phase-trans/2002/Thermal2.pdf, University of Cambridge, Materials Science & Metallurgy, 2002.

[BIRD 60] R.B. Bird, W.E. Steward, E.N. Lightfoot, Transport Phenomena, New York, John Wiley & Sons, NY, 1960.

[BLUMENAUER 94] H. Blumenauer, Werkstoffprüfung, Deutscher Verlag für Grundstoffindustrie, Leipzig-Stuttgart, 1994.

[BOETTINGER 00] W.J. Boettinger, S.R. Coriell, A.L. Greer, A. Karma, W. Kurz, M. Rappaz, R. Trivedi, Acta Mater. 48, 2000, 43-70.

[BRENNEN 05] C.E. Brennen, Fundamentals of Multiphase Flow, Cambridge University Press, 2005.

[BRUNNER 90] H. Brunner, K. Flessel, F. Hiller, Meyers Lexikonverlag, Mannheim, 1990.

[CARSLAW 59] H. S. Carslaw, J. C. Jaeger, Oxford University Press, London, 2, 1959, pp. 28.

[CHADWICK 39] R. Chadwick, J. Inst. Met., 64, 1939, 331-346.

[CIA-AN 87] Q. Cia-An, J. Zhan-Peng, H. Pei-Yun, Experiments to be published, 1987.

[COGAN 84] S. F. Cogan, S. Kwon, J. D. Klein, R. M. Rose, J. Mater. Sci, 19, 1984, pp. 447.

[COOK 41] M. Cook and W. G. Tallis, J. Inst. Met., 67, 1941, 49-65.

[COSTA E SILVA 06] A. Costa e Silva, J. Agren, M.T. Clavaguera-Mora, D. Djurovic, T. Gomez-Acebo, B.J. Lee, Z.K. Liu, P. Miodownik, H.J. Seifert, Science Direct, 31, 2007, 53-74.

[DAYANANDA 89] M.A. Dayananda, Materials Sci.&Eng., A121, 1989, pp. 351.

[DAYANANDA 96A] M.A. Dayananda, Metall. Mater. Trans., 27A, 1996, pp. 2504.

[DAYANANDA 96B] M.A. Dayananda, Y.H. Sohn, Scripta Mater., 35, 1996, pp. 684.

[DEAN 95] J. A. Dean, The Analytical Chemistry Handbook. New York. McGraw Hill, Inc., 15.1-15.5, 1995.
[DICTRA 05] Dictra, users guide, 2005.
[DIES 67] K. Dies, Kupfer und Kupferlegierungen in der Technik, Springer Verlag, Berlin/Heidelberg/New York, 1967.
[DU 05] Q. Du, D.G. Eskin, L. Katgerman, Mat. Sci. Eng. A, 413-414, 2005, 144-150.
[DU 06] Q. Du, D.G. Eskin, L. Katgerman, MCWASP-XI, 2006, 235-242.
[EBERLING 68] R. Eberling, H. Wever, Z. Metallkd., 59, 1968, pp. 222.
[EFFENBERG 07] G. Effenberg, S. Ilyenko, Landolt-Börnstein-Group IV Physical Chemisty, 2007, 355-367.
[EINSTEIN 05] A. Einstein, Annalen der Physik, 17, 1905, 549-560.
[ESKIN 07] D. G. Eskin, Q. Du, R. Nadella, A.N. Turchin, L. Kagerman, Proc. of the 5th Dec. Int. Conf. on Solid. Proc., 2007, 437-441.
[FELLER 97] R.J. Feller, C. Beckermann Metall. Mater. Trans., 28B, 1997, pp. 1165.
[FICK 55A] A. Fick, Poffensdorf's Ann., 94, 1855, 59-86.
[FICK 55B] A. Fick, Philos. Mag., 10, 1855, pp. 30.
[FIDOS 70] H. Fidos, H. Schreiner, Z. Metallkd., 61, 1970, pp. 225.
[FLEMINGS 67A] M.C. Flemings, G.E. Nero, Trans. Metall. Society AIME, Vol. 239, 1967, 1449-1461.
[FLEMINGS 67B] M.C. Flemings, R. Mehrabien, G.E. Nero, Trans. Metall. Society AIME, Vol. 242, 1967, 41-49.
[FLEMINGS 67C] M.C. Flemings, G.E. Nero, Trans. Metall. Society AIME, Vol. 242, 1967, 50-55.
[FLEMINGS 00] M.C. Flemings, ISIJ Intern., 40, 2000, pp. 833.
[FLEWITT 94] P.E.J. Flewitt, R.K. Wild, Physical Methods for Materials Characterisation, Chapter 6, IOP Publishing, Bristol, 1994.
[FLUENT 05] Fluent 6.2 User's Guide, Fluent Inc., Lebanon, NH, USA, 2005.
[FLUENT 06] Fluent 6.3 User's Guide, Fluent Inc., Lebanon, NH, USA, 2006.
[FROHBERG 81] M.G. Frohberg, Deutscher Verl. für Grundstoffind., Leipzig, Stuttgart, 1981.
[GANESAN 90] S. Ganesan, D.R. Poirier, PhysicoChemical Hydrodynamics, 12, 1990, 195-213.
[GLICKSMAN 00] M.E. Glicksman, Wiley Inter Science, New York, 2000.
[GOYEAU 99] B. Goyeau, T. Benihaddadene, D. Gobin, M. Quintard, Metall. Mater. Trans., 30B, 1999, pp. 613.
[GRAFE 00] U. Grafe, B. Böttger, J. Tiaden, S. G. Fries, Scripta Mater. 42, 2000, 1179-1186.
[GRAHAM 29] T. Graham, Quarterly Journal of Science, Literature and Art, 27, 1829, 74-83.
[GRAHAM 33] T. Graham, Philosophical Magazine, 2, 1833, 175-190.
[GRAHAM 50] T. Graham, Philosophical Transactions of the Royal Society of London, 140, 1850, 1-46.
[GREVEN 99] K. Greven, A. Ludwig, T. Hofmeister, P.R. Sahm, Solidification of Metallic Melts in Research and Technology, ed. A. Ludwig, publisher Wiley-VCH, Weinheim, 1999, pp. 119.
[GRUBER 05] M. Gruber-Pretzler, F. Mayer, M. Wu, A. Ludwig, ed. H.R. Müller, Wiley-VCH, 2005, 219-225.

[GRUBER 06] M. Gruber-Pretzler, F. Mayer, M. Wu, A. Ludwig, H.A. Kuhn, J. Riedle, 11th Modeling of Casting, Welding and Advanced Solidification Processes (McWASP XI), France, eds. C. A. Gandin, M. Bellet, Warrendale, Pennsylvania, A Publication of TMS, 2006, 799-806.

[GRUBER 07A] M. Gruber-Pretzler, M. Wu, A. Ludwig, J. Riedle, U. Hofmann, Proceedings of COM/Cu2007, Canada, I, eds. J. Hugens, K. Sadayappan, J. Spooner, L.D. Smith, et al., A publication of the Canadian Institute of Mining, Metallurgy and Petroleum, 2007, 265-279.

[GRUBER 07B] M. Gruber-Pretzler, Arbeitsbericht CD Modul 2, Montanuniversität Leoben, 2007.

[GRUBER 08] M. Gruber-Pretzler, F. Mayer, A. Ishmurzin, L. Könözsy, M. Wu, A. Ludwig, BHM, 2008, submitted.

[HALLSTEDT 07] B. Hallstedt, N. Dupin, M. Hillert, L. Höglund, H.L. Lukas, Computer Coupling of Phase Diagrams and Thermochemistry, 31, 2007, 28-37.

[HANSON 51] D. Hanson, W.T. Pell-Walpole, Edward Arnold & Co., London, 1951, 60-64.

[HANSON 58] M. Hanson, K. Anderko, McGraw-Hill Book Comp. Inc., New York-Toronto-London, 1958, 633-638.

[HELANDER 99] T. Helander, J. Agren, Acta Metall., 47, 1999, pp. 1141.

[HILLERT 97] M. Hillert, CALPHAD, 21, 2, 1997, 143-153.

[HILLERT 01] M. Hillert, Journal of Alloys and Compounds, 320, 2001, 161-176.

[HILLERT 04] M. Hillert, L. Höglund, Scripta Materialia, 50, 2004, 1055-1059.

[HILLERT 05] M. Hillert, L. Höglund, J. Agren, J. Appl. Phys., 98, 2005.

[HILLERT 98] M. Hillert, University Press, Cambridge, 1998, 60-166.

[HISHINO 80] K. Hishino, Y. Iijima, K. Hirano, Trans Jpn. Inst. Met., 21, 1980, pp. 674.

[HISHINO 82] K. Hishino, Y. Iijima, K. Hirano, Acta Metall., 30, 1982, pp. 265.

[HOFMANN 05] U. Hofmann, A. Bögel, H. Hölzl, H.A. Kuhn, Prakt. Metallogr. 42, 7, 2005, 339-364.

[HÖHNE 96] G. Höhne, W. Hemminger, H.-J. Flammersheim, Differential Scanning Calorimetry-An Introduction for Partitioners. Springer-Verlag, Berlin-Heidelberg, 1996.

[HUNGER 95] H.J Hunger, Deutsch. Verl. für Grundstoffind., Leipzig-Stuttgart, 1995.

[ILEGBUSI 00] Q.J. Ilegbusi, and Mat, M.D., J. Mater. Processing & Manufacturing Sci., 8, 2000, pp. 188.

[ISHMURZIN 08] A. Ishmurzin, M. Gruber-Pretzler, F. Mayer, L. Könözsy, M. Wu, A. Ludwig, IJMR, 2008, submitted.

[JIE 05] W.Q. Jie, R. Zhang, Z. He: Mater. Sci. Eng. A. 413-414, 2005, 497-503.

[KASCHNITZ 07] E. Kaschnitz, pers. Com., 2007.

[KATTNER 00] U. Kattner, G. Erickson, P. Spencer, M. Schalin, R. Schmid-Fetzer, B. Sundman, B. Jannson, B. Lee, T. Chart, A. Costa e Silva, CALPHAD, 24, 1, 2000, 55-94.

[KATTNER 97] U. Kattner, JOM 49, 1997, 14-19.

[KAUFMAN 70] L. Kaufman, H. Bernstein, Computer Calculation of Phase Diagrams with Special Reference to Refractory Metals, New York: Academic Press, 1970.

[KAWANAMI 97] Y. Kawanami, S. Yoshida, N. Takeuchi, M. Kajihara, T Mori, ISIJ International, 37, 6, 1997, 590-595.

[KOLEV 02] N. Kolev, Springer-Verlag, Berlin, 2002.

[KRAFT 97] T. Kraft, M. Rettenmayr, H.E. Exner, Progress in Mater. Sci., 42, 1997, 277-286.

[KUDASHOV 05] D.V. Kudashov, H.R. Müller, R. Zauter, ed. H.R. Müller, Wiley-VCH, 2005, pp. 256.

[KULKARNI 05] N. S. Kulkarni, C. V. Iswaran, R. T. DeHoff, Intrinsic diffusion simulation for single-phase multi component systems, Acta Materialia, 53, 2005, 4097-4110.

[LAN 05] C.W. Lan, B.C. Yeh, Fluid Dyn. Mater. Proc., 1, 2005, 33-44.

[LAROUCHE 07] D. Larouche: Computer Coupling of Phase Diagrams and Thermochemistry, 31, 2007, 490-504.

[LARSSON 06] H. Larsson, A. Engström, Acta Mater., 54, 2006, 2431-2439.

[LUBYOVA 75] Z. Lubyova, P. Fellner, K. Matiasovsky, Z. Metallkd., 66, 1975, pp. 179.

[LUDWIG 02] A. Ludwig, M. Wu, Metall. Mater. Trans., 33A, 2002, pp. 3673.

[LUDWIG 05] A. Ludwig, M. Wu, Mater. Sci. Eng., A413-414, 2005, pp. 109.

[LUDWIG 06A] A. Ludwig, M. Gruber-Pretzler, M. Wu, A. Kuhn, J. Riedle, Fluid Dyn. Mater. Proc., 1 4, 2006, 285-300.

[LUDWIG 06B] A. Ludwig, M. Gruber-Pretzler, F. Mayer, A. Ishmurzin, M. Wu, Mat. Sci. Eng. A, 413-414, 2005, 485-489.

[LUDWIG 07] A. Ludwig, A. Ishmurzin, M. Gruber-Pretzler, F. Mayer, M. Wu, Proceedings of the 5th Dec. Int. Conf. on Solid. Proc., 2007, 493-496.

[MADELUNG 90] O. Madelung, H. Bakker, H. P. Bonzel, C. M. Bruff, M. A. Dayananda, W. Beest, J. Horvath, I. Kacer, G. V. Kidson, A. D. Lee Claire, H. Mehrer, G. E. Murch, G. Neumann, N. Stollia, N. A. Stolwijk, Landolt-Börnstein, ed. H. Mehrer, III, 26, 1990.

[MASBERG 99] S. Masberg, Ruhr-Universität Bochum, Fakultät für Chemie, 1999.

[MASSALSKY 86] T.B. Massalsky, J.L. Murray, L.H. Bennet, H. Baker, American Society for Metals, Ohio, 1, 1986.

[MASSALSKY 90] T.B. Massalsky (Ed.), ASM International, Metals Park, Ohio, 2nd edition, 1990.

[MAYER 07] F. Mayer, M. Gruber-Pretzler, M. Wu, A. Ludwig, 2nd International Conference of Simulation & Modeling of Metallurgical Processes in Steelmaking (STEELSIM 2007), Austria, ed. A. Ludwig, 2007, 265-270.

[MEY 90] S. an Mey, P. J. Spencer, CALPHAD 14, 1990, pp. 265.

[MIETTINEN 01] J. Miettinen, Calphad, 25, 1, 2001, 67-78.

[MIETTINEN 06] J. Miettinen, Comp. Mater. Sci., 36, 4, 2006, 367-380.

[MORAN 98] M.J. Moran, H.N. Shapiro, John Wiley & sons, 1998.

[MÜLLER 97] M. Müller, Uni. Augsburg, Inst. F. Physik, 1997.

[NI 91] J. Ni, C. Beckermann, Metall. Trans. B, 22B, 1991, pp. 349.

[NI 93] J. Ni, C. Beckermann, J. Mater. Process. Mater. Sci., 2, 1993, pp. 217.

[NI 95A] J. Ni., F.P. Incropera, Int. J. Heat Mass Transfer, 38, 1995, 1271-1284.
[NI 95B] J. Ni., F.P. Incropera, Int. J. Heat Mass Transfer, 38, 1995, 1285-1296.
[OIKAWA 75] H. Oikawa, A. Hosai, Scr. Metall., 9, 1975, pp. 823.
[ONISHI 75] M. Onishi, H. Fujibuchi, Trans. Jpn. Inst. Met., 16, 1975, pp. 539.
[ONSAGER 31] L. Onsager, Phys. Rev., 37, 1931, pp. 405.
[ONSAGER 45] L. Onsager, Ann. N.Y. Acad. Sci., 46, 1945-46, pp. 241.
[PANZL 08] G. Panzl, Bachelor work, University of Leoben, 2008.
[PATANKAR 72] S.V. Patankar, D.B. Spalding, Int. J. Heat Mass Transfer, 1972, 15, 1787-1806.
[PATANKAR 80] S.V. Patankar, Numerical heat transfer and fluid flow, Hemisphere, New York, 1980.
[PERIODENSYSTEM 07] www.periodensystem.info.
[PREDEL 82] B. Predel, Steinkopf Verlag, Darmstadt, 1982.
[PRINZ 80] N. Prinz, H. Wever, Phys. Status Solidi, a 61, 1980, pp. 505.
[PUNGOR 95] E. Pungor, A Practical Guide to Instrumental Analysis. Boca Raton, Florida, 1995, 181-191.
[RAPPAZ 87A] M. Rappaz, Ph. Thevoz, Acta Metall., 35, 1987, pp.1487.
[RAPPAZ 87B] M. Rappaz, Ph. Thevoz, Acta Metall., 35, 1987, pp.2929.
[RAPPAZ 90] M. Rappaz, V. Voller, Metall. Mater. Trans., 21A, 1990, pp. 749.
[RAYNOR 49] G.V. Raynor, The Institute of Metals, London, 1949.
[REDDY 97] A.V. Reddy, C. Beckermann, Metall. Mater. Trans., 38, 1997, pp. 3455.
[RIEDLE 04] J. Riedle, Wieland Werke Ulm, per. com., 2004.
[RIEDLE 06] J. Riedle, Wieland Werke Ulm, pers. com. 2006.
[ROUSSET 95] P. Rousset, M. Rappaz, B. Hannart, Metall. Mater. Trans., 26A, 1995, pp. 2349.
[ROUX 84] H. Roux, A. Piquet, Surf. SCi. 141, 1984, pp. 301.
[SAMUEL 07] G. Samuel, www.npl.co.uk/materials, 2007.
[SAUNDERS 98] N. Saunders, Miodownik, A.P. Pergamon Materials Series, XVI, 1998.
[SCHNEIDER 95] M. Schneider, C. Beckermann, Inter. J. Heat Mass Transfer, 38, 1995, pp. 3455.
[SCHNEIDER 95A] M.C. Schneider, C. Beckermann: Metall. Mater. Trans. A. 26A, 1995, 2373-2388.
[SCHNEIDER 95B] M.C. Schneider, C. Beckermann: Int. J. Heat Mass Transfer. 38, 1995, 3455-3473.
[SCHUMANN 90] H. Schumann, Leipzig Dt. Verlag für Grundstoffind., neubearb. Aufl., Leipzig, 13, 1990, 504-576.
[SEILNACHT 07] www.seilnacht.com
[SEITH 55] W. Seith, Springer-Verlag, Berlin, 1955.
[SHIM 96] J.H. Shim, C.S. Oh, B.J. Lee, D.N. Lee, CuSn. Z. Metallkd., 87, 1996, 205-212.
[SHIM 96] J.H. Shim, C.S. Oh, B.J. Lee, D.N. Lee, Z. Metallkd., 87, 1996, 205-212.
[SHOWELL 51] D.G.D. Showell, unpublished, cited after D. Hanson, W.T. Pell-Walepole, London, 1951, 69-70.
[SKOOG 98] D. A. Skoog, F. J Holler, T. Nieman, New York, 1998, 905-908.

[SPALDING 72] D.B. Spalding, in Recent Advances in Numerical Methods in Fluids, Eds. Tayler C., Morgan, K., 1980, 139-167.
[SPINDLER 76] P. Spindler, K. Nachtrieb, Phys. Status Solidi, a 37, 1976, pp. 449.
[STARKE 64] E. Starke, H. Wever, Z. Metallkd., 55, 1964, pp. 107.
[STEUDEL 60] H. Steudel, VDI-Verlag GMBH, Düsseldorf, 1960, 1-10.
[SUNDMAN 85] B. Sundman, B. Jansson, J.O. Andersson, Calphad, 9, 1985, 153-190.
[TAKEMOTO 87] T. Takemoto, I. Okamoto, J. Matusumura, Trans. JWRI 16, 301, 1987, 73-79
[THERMOCALC 03] SGTE, ThermoCalc, 2003.
[THERMOCALC 05] ThermoCalc, "CuSn1 Database", 2005.
[THERMOCALC 06] ThermoCalc, Users Guide, 2006.
[THOMPSON 86] M.S: Thompson, J.E. Morral, Acta Metall., 34, 1986, pp. 339.
[UNITERRA 07] www.periodensystem.info.
[VERÖ 53] J. Verö, Zeitschrift anorg. allgem. Chemie, 213, 1953, 257-272.
[VILLARS 97] P. Villars, A. Prince, H. Okamoto, ASM International, 8, 1997, 9902-9908.
[VOLLER 89] V.R. Voller, A.D. Brent, C. Prakash, Inter. J. Heat Mass Transfer, 32, 1989, pp. 1719.
[VREEMAN 00A] J.C. Vreeman, M.J.M. Krane, F.P. Incropera, Inter. J. Heat Mass Transfer, 38, 2000, pp. 677.
[VREEMAN 00B] J.C. Vreeman, F.P. Incropera, Inter. J. Heat Mass Transfer, 43, 2000, pp. 687.
[WANG 93] C.Y. Wang, C. Beckermann, Metall. Trans., 24A, 1993, pp. 2787.
[WANG 95] C.Y. Wang, S. Ahuja, C. Beckermann, Groh III, H.C., Metall. Mater.
[WANG 96A] C.Y. Wang, C. Beckermann, Metall. Mater. Trans. A, 27A, 1996, pp. 2754.
[WANG 96B] C.Y. Wang, C. Beckermann, Metall. Mater. Trans. A, 27A, 1996, pp. 2765.
[WATSON 03] A. Watson, Wagner S, Lysova E., Rohkhlin L, MSIT Workplace, 2003.
[WIKIPEDIA 07] http://de.wikipedia.org.
[WU 03A] M. Wu, A. Ludwig, A. Bührig-Polaczek, M. Fehlbier, P.R. Sahm, Inter J. Heat Mass Transfer, 46, 2003, pp. 2819.
[WU 03B] M. Wu, A. Ludwig, Adv. Eng. Mater., 5, 2003, pp. 62.
[WU 06] M. Wu, A. Ludwig, Metall. Mater Trans., 37A, 2006, 1613-1631.
[WU 07] M. Wu, Habilitationsschrift, University of Leoben, 2007.
[YOKOTA 80] M. Yokota, M. Nose, H. Mitani, J. Jpn. Inst. Met., 44, 1980, pp. 1007.
[ZALOZNIK 05] M. Zaloznik, B. Sarler, Mat. Sci. Eng. A, 413-414, 2005, 85-91.
[ZALOZNIK 06] M. Zaloznik, B. Sarler, MCWASP-XI, 2006, 243-250.
[ZHANPENG 87] J. Zhanpeng, Changsha, China, 1987.

8 Attachment

Following the settings used in FLUENT for the calculations are listed as example for the 2D axis symmetric geometry.

Project : CD-Modul 2	Axis symetric Calculations 2D	
Grid file:	Grid_Cu_10_05_05.msh	
Define		
Models	solver	segregated/unsteady/1st order implicit
		axisymmetric/cell based
	multiphase	Eulerian/3 phase
	energie	yes
	viscous	laminar
	radiation	off
	species	off
	discrete phase	off
	solidification and melting	off
	acoustics	off
Materials	properties	
CuSn liquid; phase 1	density [$kg \cdot m^{-3}$]	7810
	specific heat capacity [$J \cdot kg^{-1} \cdot K^{-1}$]	454
	thermal conductivity [$W \cdot m^{-1} \cdot K^{-1}$]	96
	viscosity [$kg \cdot m^{-1} \cdot s^{-1}$]	user-def: liquid_viscosity
	molecular weight [$kg \cdot kg^{-1} \cdot mol^{-1}$]	28.966
	standard state enthalpy [$J \cdot kg^{-1} \cdot mol^{-1}$]	0
	reference temperature [K]	298.15
	UDS diffusivity [$kg \cdot m^{-1} \cdot s^{-1}$]	uds: uds-o: 0
CuSn equiaxed; phase 2	density [$kg \cdot m^{-3}$]	8565
	specific heat capacity [$j \cdot kg^{-1} \cdot K^{-1}$]	395
	thermal conductivity [$W \cdot m^{-1} \cdot K^{-1}$]	184
	viscosity [$kg \cdot m^{-1} \cdot s^{-1}$]	user-def: solid_viscosity
	molecular weight [$kg \cdot kg^{-1} \cdot mol^{-1}$]	28.966
	standard state enthalpy [$J \cdot kg^{-1} \cdot mol^{-1}$]	0
	reference temperature [K]	298.15
	UDS diffusivity [$kg \cdot m^{-1} \cdot s^{-1}$]	uds: uds-o: 0
CuSn columnar; phase 3	density [$kg \cdot m^{-3}$]	8565
	specific heat capacity [$J \cdot kg^{-1} \cdot K^{-1}$]	395
	thermal conductivity [$W \cdot m^{-1} \cdot K^{-1}$]	184
	viscosity [$kg \cdot m^{-1} \cdot s^{-1}$]	320
	molecular weight [$kg \cdot kg^{-1} \cdot mol^{-1}$]	28.966
	standard state enthalpy [$J \cdot kg^{-1} \cdot mol^{-1}$]	0
	reference temperature [K]	298.15
	UDS diffusivity [$kg \cdot m^{-1} \cdot s^{-1}$]	uds: uds-o: 0
Phases		
phase 1	primary phase	CuSn
phase 2	secondary phase	CuSn equiaxed
phase 3	secondary phase	CuSn columnar

Interaction		diameter [m]: constant; 1e-5
phase 1 and 2	drag	UDF: drag_force_E_L
	lift	none
	collisions	/
	slip	/
	heat	UDF: heat_x_udf_E_L
	mass	0
	reactions	/
	surface tension	/
phase 3 and 2	drag	UDF: drag_force_C_E
	lift	none
	collisions	/
	slip	/
	heat	UDF: heat_x_udf_C_E
	mass	0
	reactions	/
	surface tension	/
		/
phase1 and 3	drag	UDF: drag_force_C_L
	lift	none
	collisions	/
	slip	/
	heat	UDF: heat_x_udf_C_L
	mass	0
	reactions	/
	surface tension	/
Operating Conditions	pressure	1.00E+07 [Pa]
	gravity	no
	operating Temperature	/
	density	/
Boundary Conditions		
Mixture		
name;	mixture; thermal conditions;	momentum; species; uds
casting	fluid	stationary
default interior	interior	/
inlet	pressure-inlet	gauge total pressure: P = 100000 [Pa] /0 / normal
mold_lower	wall; convection; HTC = 3000 [$W \cdot m^{-2} \cdot s^{-1}$]; T = 550 K	moving wall /absolute / components/ u = 0.00192 [$m \cdot s^{-1}$]
mold_upper	wall; convection; HTC = 20 [$W \cdot m^{-2} \cdot s^{-1}$]; T = 1300 K	moving wall /absolute / components/ u = 0.00192 [$m \cdot s^{-1}$]
nozzel	wall; convection; HTC c = 5 [$W \cdot m^{-2} \cdot s^{-1}$]; T = 1300 K	stationary wall
outlet	velocity-inlet;	
surface	wall; convection; HTC = 10 [$W \cdot m^{-2} \cdot s^{-1}$]; T = 325 K	stationary wall
watercooling	wall; convection; HTC = 1000 [$W \cdot m^{-2} \cdot s^{-1}$]; T = 300 K	moving wall /absolute / components/ u = 0.00192 [$m \cdot s^{-1}$]

Phase 1	liquid	
casting	Source Terms:	
	mass [$kg \cdot m^{-3} \cdot s^{-1}$]	udf mass_phase1
	x-momentum [$N \cdot m^{-3}$]	udf mom_u_p1
	y-momentum [$N \cdot m^{-3}$]	udf mom_v_p1
	energie [$W \cdot m^{-3}$]	udf enthalpy_phase1
	UDS 0	udf UDS_s-p1
	UDS 2	udf CU_L_s_p1
default interior	interior	
inlet	pressure-inlet: T = 1389 K constant	
	UDS boundary condition	UDS boundary value
	UDS 0: specified value	UDS 0: 1e9; constant
	UDS 2: specified value	UDS 2: 0.06; constant
mold_lower	wall; casting; specified shear (X:0/Y:0)	
	UDS boundary condition	UDS boundary value
	UDS 0: specified flux	UDS 0: 0; constant
	UDS 2: specified flux	UDS 2: 0; constant
mold_upper	wall; casting; specified shear (X:0/Y:0)	
	UDS boundary condition	UDS boundary value
	UDS 0: specified flux	UDS 0: 0; constant
	UDS 2: specified flux	UDS 2: 0; constant
nozzel	wall; 10; casting; specified shear (*x*:0/*y*:0)	
	UDS boundary condition	UDS boundary value
	UDS 0: specified flux	UDS 0: 0; constant
	UDS 2: specified flux	UDS 2: 0; constant
outlet	velocity-inlet	axial velocity: 0.00192 [$m \cdot s^{-1}$] constant radial velocity: 0 [$m \cdot s^{-1}$] constant
	absolute; components	T = 500 K; constant
	UDS boundary condition	UDS boundary value
	UDS 0: specified flux	UDS 0: 0; constant
	UDS 2: specified flux	UDS 2: 0; constant
surface	wall; casting; specified shear (X:0/Y:0)	
	UDS boundary condition	UDS boundary value
	UDS 0: specified flux	UDS 0: 0; constant
	UDS 2: specified flux	UDS 2: 0; constant
watercooling	wall; casting; specified shear (X:0/Y:0)	
	UDS boundary condition	UDS boundary value
	UDS 0: specified flux	UDS 0: 0; constant
	UDS 2: specified flux	UDS 2: 0; constant
Phase 2	equiaxed	
casting	Source Terms:	
	mass [$kgm^{-3}s^{-1}$]	udf mass_phase2
	x-momentum [$N \cdot m^{-3}$]	udf mom_u_p2
	y-momentum [$N \cdot m^{-3}$]	udf mom_v_p2
	energie [$W \cdot m^{-3}$]	udf enthalpy_phase2
	UDS 1	udf UDS_s-p2
	UDS 3	udf CU_S_s_p2
default interior	interior	

inlet	pressure-inlet: T= 1389 K constant	volume fraction: 1E-06 constant
	UDS boundary condition	UDS boundary value
	UDS 1: specified value	UDS 1: 1e9; constant
	UDS 3: specified value	UDS 3: 0.032; constant
mold_lower	wall; casting; specified shear (x:0/y:0)	
	UDS boundary condition	UDS boundary value
	UDS 1: specified flux	UDS 1: 0; constant
	UDS 3: specified flux	UDS 3: 0; constant
mold_upper	wall; casting; specified shear (x:0/y:0)	
	UDS boundary condition	UDS boundary value
	UDS 1: specified flux	UDS 1: 0; constant
	UDS 3: specified flux	UDS 3: 0; constant
nozzel	wall; casting; specified shear (x:0/y:0)	
	UDS Boundary condition	UDS boundary value
	UDS 1: specified flux	UDS 1: 0; constant
	UDS 3: specified flux	UDS 3: 0; constant
outlet	velocity-inlet	axial velocity: 0.00192 [$m \cdot s^{-1}$] constant radial velocity: 0 [$m \cdot s^{-1}$] constant
	absolute; components;	T = 500 K; constant volume fraction: 1E-06 constant
	UDS Boundary condition	UDS boundary value
	UDS 1: specified flux	UDS 1: 0; constant
	UDS 3: specified flux	UDS 3: 0; constant
surface	wall; 3; casting; specified shear (x:0/y:0)	
	UDS Boundary condition	UDS boundary value
	UDS 1: specified flux	UDS 1: 0; constant
	UDS 3: specified flux	UDS 3: 0; constant
watercooling	wall; casting; specified shear (x:0/y:0)	
	UDS boundary condition	UDS boundary value
	UDS 1: specified value	UDS 1: 0; constant
	UDS 3: specified value	UDS 3: 0; constant
Phase 3	columnar	
casting	Source Terms; fixed values	
	mass [$kg \cdot m^{-3} \cdot s^{-1}$]	udf mass_phase3
	x-momentum [$N \cdot m^{-3}$]	udf mom_u_p3
	y-momentum [$N \cdot m^{-3}$]	udf mom_v_p3
	energie [$W \cdot m^{-3}$]	udf enthalpy_phase3
	UDS 4	udf CU_S_s_p3
default interior	interior; collumnar;	
inlet	pressure-inlet: T= 1389 K constant	volume fraction: 0 constant
	UDS boundary condition	UDS boundary value
	UDS 4: specified value	UDS 4: 0; constant
mold_lower	wall; casting; no slip	
	UDS boundary condition	UDS boundary value
	UDS 4: specified flux	UDS 4: 0; constant
mold_upper	wall; casting; no slip	
	UDS boundary condition	UDS boundary value
	UDS 4: specified flux	UDS 4: 0; constant

nozzel	wall; casting; specified shear (*x*:0/*y*:0)	
	UDS boundary condition	UDS boundary value
	UDS 4: specified flux	UDS 4: 0; constant
outlet	velocity-inlet	axial velocity: 0.00192 [m·s^{-1}] constant radial velocity: 0 [m·s^{-1}] constant
	absolute; components;	T = 500 K; constant volume fraction: 0.999 constant
	UDS boundary condition	UDS boundary value
	UDS 4: specified flux	UDS 4: 0; constant
surface	wall; casting; specified shear (*x*:0/*y*:0)	
	UDS boundary condition	UDS boundary value
	UDS 4: specified flux	UDS 4: 0; constant
watercooling	wall; casting; no slip	
	UDS boundary condition	UDS boundary value
	UDS 4: specified value	UDS 4: 0; constant
User Defined Functions:		ccp; 10000
	compiled: library name:	libudf
	manage: udf libraries:	libudf
Function hooks:		adjust_m_transfer_rate
Execute on Demand:	none	
User Defined Scalars	number of UDS	5
	flux function:	mass flow rate
	unsteady function:	default
	domains to solve in	
	scalar-0	phase 1
	scalar-1	phase 2
	scalar-2	phase 1
	scalar-3	phase 2
	scalar-4	phase 3
User Defined Memory:	20	

Solve	
Equations	
flow	on
volume fraction	on
energy	on
UDS 0	off
UDS 1	off
UDS 2	on
UDS 3	on
UDS 4	on
Under-Relaxation-Factor	
pressure	0.4
density	1
body forces	0.3
momentum	0.5
volume fraction	0.2
energy	0.95
UDS 0	1
UDS 1	1
UDS 2	0.3
UDS 3	0.3
UDS 4	0.3
Presure-Velocity Coupling	
simple	
discretization	
momentum	1st; upward
volume fraction	1st; upward
energy	1st; upward
UDS 0	1st; upward
UDS 1	1st; upward
UDS 2	1st; upward
UDS 3	1st; upward

Initialzation	
Compute Form	
all zones	
Initial Values	
pressure	100000
UDS 0	1.00E+09
UDS 1	1.00E+09
UDS 2	0.06
UDS 3	0.032
UDS 4	0.032
phase 1 *x*-velocity; liquid	0
phase 1 *y*-velocity; liquid	0
phase 1 *T*; liquid	1293
phase 2 *x*- velocity; equiaxed	0
phase 2 *y*- velocity; equiaxed	0
phase 2 volume fraction; equiaxed	1.00E-06
phase 2 *T*; equiaxed	1293
phase 3 *x*- velocity; columnar	0
phase 3 *y*- velocity; columnar	0
phase 3 volume fraction; columnar	0.0001
phase 3 *T*; columnar	1293

Iterate	
time step size	0.02
number of time steps	0
time step method	fixed
maximum iteration per time step	25
report interval	1
UDF update interval	1

9 List of Symbols

A	integreated area of the DSC measuring curve
B	number of additional conditions in Gibbs phase rule
B	end of solidification
b	solidification shrinkage in LSRE
C	independent chemical constituents in Gibbs phase rule
c	index for columnar phase
ΔC	concentration gradient [mol·m^{-4}]
$\tilde{c}$	concentration at the interface
C_0 , c_0	initial alloy concentration
c_c	volume average concentration in the columnar phase
$\overline{c}_c$	cumulative volume average concentration in the columnar phase
$\tilde{c}_c$	equilibrium columnar concentration adjacent to the solid/liquid interface
$\tilde{c}_c^{\,j}$	equilibrium columnar concentration of the *j*-species adjacent to the solid/liquid interface
$\tilde{c}_c^{\,P}$	equilibrium columnar concentration of P adjacent to the solid/liquid interface
c_c^{Sn}	columnar concentration of Sn
$\tilde{c}_c^{\,Sn}$	equilibrium columnar concentration of Sn adjacent to the solid/liquid interface
c_c^{Scheil}	columnar concentration according to Scheil
$\overline{c}_c^{\,Scheil}$	cumulative columnar concentration according to Scheil
C_{cl}	concentration exchange term for melting
C_{lc}	concentration source term for solidification
c_l	average mass fraction of the liquid phase
$\tilde{c}_l$	equilibrium liquid concentration adjacent to the solid/liquid interface
$c_l^{\,j}$	average species mass fraction of the *j*-species
$\tilde{c}_l^{\,j}$	average species mass fraction of the *j*-species adjacent to the solid/liquid interface
$c_l^{\,P}$	average species mass fraction of P
$c_l^{\,Sn}$	average species mass fraction of Sn
c_l^{Scheil}	liquid concentration according to Scheil
$\tilde{c}_l^{\,P}$	average species mass fraction of P at the solid/liquid interface
$\tilde{c}_l^{\,Sn}$	average species mass fraction of Sn at the solid/liquid interface
c_l^{in}	incoming melt concentration
c_l^{out}	outgoing melt concentration
c_{mix}	mixture concentration
c_{mix}^{i}	mixture concentration of species *i* in the ternary system
c_{mix}^{P}	mixture concentration of P in the ternary system
c_{mix}^{Sn}	mixture concentration of Sn in the ternary system
c_{mix}^{Z}	mixture concentration in the center of the casting
$c_{p(l)}$	specific heat capacity of the liquid phase
$c_{p(c)}$	specific heat capacity of the columnar phase

c^{ref}	reference concentration
$c_{p(q)}$	specific heat capacity of phase *q*
c_q^i	weight fraction of species *i* in phase *q*
C_q^i	rate of production/destruction of species *i* in phase *q* [kg·m^{-3}·s^{-1}]
Δc^P	measurement accuracy for P
D	diffusion coefficient [m^2·s^{-1}]
d	dimension of the casting
d_c	columnar dendrite trunk diameter
D_c	diffusion coefficient in the columnar phase
D_l	diffusion coefficient in the liquid phase
D_q^i	diffusivity of species *i* in phase *q*
D_{lj}	diffusion coefficient of the *j*-species in the liquid
D_l^{Sn}	diffusion coefficient of Sn in the liquid
D_l^P	diffusion coefficient of P in the liquid
d_{max}	maximum possible dendrite trunk diameter
d_n	normalized diameter
$D_{P\alpha}$	diffusion coefficient of P in α [m^2·s^{-1}]
D_{PP}	diffusion coefficient of P in CuSnP dependent on P [m^2·s^{-1}]
D_{PSn}	diffusion coefficient of P in CuSnP dependent on Sn [m^2·s^{-1}]
D_{SnP}	diffusion coefficient of Sn in CuSnP dependent on P [m^2·s^{-1}]
D_{SnSn}	diffusion coefficient of Sn in CuSnP dependent on Sn [m^2·s^{-1}]
$D_{Sn\alpha}$	diffusion coefficient of Sn in α [m^2·s^{-1}]
E	end of solidification
F	degrees of freedom in the Gibbs phase rule
$\vec{F}$	source term for other body forces
f_q	volume phase fraction of phase *q*
f_c	volume phase fraction columnar phase
f_c^Z	average volume fraction of the incoming melt
Δf_c^{Scheil}	change in the columnar volume fraction according to Scheil
f_l	volume phase fraction liquid phase
$f_{l,crit}$	critical volume fraction of the melt
f_l^{in}	average volume fraction of the incoming melt
f_l^{out}	average volume fraction of the outgoing melt
f_{imp}	impingement factor
f_P	function for P dependent on the liquid Sn and P content at the columnar/liquid interface
f_{Sn}	function for Sn dependent on the liquid Sn and P content at the columnar/liquid interface
$\vec{g}$	gravity vector
G_i	Gibbs energy for element *i*
G_A^α, G_A^β,G_B^α, G_B^β , G_C^α,G_C^β	Gibbs energy for element *A*, *B* and *C* and phase α, β
G_i^φ	Gibbs energy for element *i* and phase φ
$\tilde{G}_l^j$	solute gradient of the *j*-species in the liquid phase at the interface
$\vec{g}_q$	gravity vector of phase *q*
G_T	temperature gradient
h	heat transfer coefficient (HTC) [W·m^{-2}·K^{-1}]

$\tilde{h}$	enthalpy at the interface
$\tilde{H}$	volume heat exchange coefficient
ΔH	enthalpy of transition
h_c	enthalpy of the columnar phase
h_c^{ref}	reference enthalpy for the columnar phase
h_l	enthalpy of the liquid phase
h_l^{ref}	reference enthalpy for the liquid phase
h_q	specific enthalpy of phase *q*
h_q^{ref}	enthalpy at the reference temperature T_{ref} of phase *q*
H_{pq}	volume heat exchange coefficient between the phases *p* and *q*
i	running index
j	running index
$\vec{J}$	flux vector [mol·m^{-2}·s^{-1}]
$\vec{J}_{Sn}$	flux vector of Sn [mol·m^{-2}·s^{-1}]
$\vec{J}_P$	flux vector of P [mol·m^{-2}·s^{-1}]
K	permeability
k	redistribution coefficient
$\overline{K}_0$	pre-factor for the permeability (empirical factor in the Blake-Kozeny expression)
K_0	permeability factor dependent on $\overline{K}_0$
K_c	calorimetric constant
K_{lc}	drag coefficient between liquid and columnar phase
K_{pq}	interphase momentum exchange coefficient of phase *p* to *q*
K_{qp}	interphase momentum exchange coefficient of phase *q* to *p*
L, *l*	liquid phase
m	Slope of the liquidus line
M_{qp}	mass transfer rate phase *q* to *p*
M_{pq}	mass transfer rate phase *p* to *q*
M_{cl}	mass transfer rate columnar to liquid phase
M_{lc}	mass transfer rate liquid to columnar phase
n	running index
N	diffraction order
n^{φ}	number of particles of phase φ
n_i	number of particles of phase *i*
n_j	number of other particles
P	pressure
P_1	peritectic reaction L + α → β
P_2	peritectic reaction L + β → γ
P_p	number of present phases
p, q	phase indices
Q	heat flux [mW]
Q_{lc}	energy source term liquid to columnar
Q_{cl}	energy source term columnar to liquid
Q_{lc}^d	enthalpy exchange between liquid and columnar phase at the interface
Q_{lc}^p	release of latent heat between liquid and columnar phase at the interface

Q_{cl}^{d}	enthalpy exchange between liquid and columnar phase at the interface
Q_{cl}^{p}	release of latent heat between columnar and liquid phase at the interface
R	number of linear independent reactions
r	radius
R_c	radius of a cylindrical dendrite trunk
Re	Reynolds number
R_f	half of the primary dendrite arm spacing
R_m	ultimate tensile strength
S	entropy
S_A	total surface area of columnar dendrite trunks per volume
Sn_{ac}	actual Tin content
Sn_{mean}	average Tin content
$S_{\phi_q^j}$	source term for the j^{th} scalar quantity in phase q
T	temperature [K], [°C]
t	time [s], [days]
ΔT	deviation in temperature
Δt	time step
$\dot{T}$	cooling rate
T_a	annealing temperature
ΔT_a	deviation in the annealing temperature
t_a	annealing time
ΔT_{Al}	DSC measuring device deviation in temperature for Aluminum
ΔT_{Au}	DSC measuring device deviation in temperature for Aurum
T_c	temperature of the columnar phase
T_{ce}	extrapolated peak completion temperature
T_{cast}	casting temperature
ΔT_{Cu}	DSC measuring device deviation in temperature for Copper
T_{DSC}	phase transformation temperature detected by DSC
T_e	extrapolated peak onset temperature
T_E	ternary eutectic point
T_{end}	peritectic temperature of CuSn L +α to β transition
T_f	the liquidus temperature of pure Cu (linearized phase diagram)
T_{fp}	final peak temperature
T_i	first deviation from the baseline
T_{init}	initial temperature of the liquid phase
T_{inlet}	inlet temperature of the phases
T_l	volume averaged liquid temperature
T_L	function of the liquidus temperature dependent on liquid Sn and P content at the columnar/liquid interface
T_{lCu}	melting temperature of Cu
T_{lCu3P}	melting temperature of Cu_3P
$T_{liquidus}$	liquidus temperature of the initial alloy concentration
T_{lower_mold}	temperature of the lower part of the mold
$T_{Massalsky}$	phase transformation temperature of the phase diagram [MASSALSKY 86]

ΔT_{min}	minimum temperature difference
T_q	temperature of phase *q*
T_p	peak maximum interpolated baseline temperature
$T_l, T_s, T_\varepsilon, T_\gamma, T_\delta,$	phase transformation temperature of the different phases
T^{ref}	reference temperature
T_{SEN}	temperature of submerged entry nozzle (SEN)
$T_{solidus}$	solidus temperature of the initial alloy concentration
$T_{surface}$	surface temperature in the mold
T_{TC}	phase transformation temperature based on Thermo-Calc calculations
T_{upper_mold}	temperature of the upper part of the mold
T_{wall}	temperature of the mold wall
T_{water}	water temperature in the secondary cooling zone
U	internal energy
u	independent melt velocity
$\tilde{\vec{u}}$	volume average velocity at the interface
$\vec{u}_c$	volume average velocity vector of the columnar phase
$\vec{u}_{cast}$	casting velocity [mm·s^{-1}]
$\vec{u}_{in}$	inlet velocity [mm·s^{-1}]
u_l	volume average velocity of the liquid phase
$\vec{u}_l$	volume average velocity vector of the liquid phase
$\vec{U}_{lc}$	momentum source term liquid to columnar phase
$\vec{U}_{lc}^{\,d}$	momentum exchange between liquid and columnar dendrites due to the drag force
$\vec{U}_{lc}^{\,p}$	momentum exchange between liquid and columnar dendrites due to phase transition
$\vec{u}_q$	velocity of phase *q* [mm·s^{-1}]
$\vec{u}_p$	velocity of phase *p* [mm·s^{-1}]
$\vec{u}_{pq}$	interphase velocity
V	volume
v	growth velocity of the dendrite trunk
v_T	velocity of the isotherms
x	local variable in space
x_i	mole fraction of phase *i*
y	local variable in space
$\alpha, \alpha^*, \beta, \gamma, \gamma', \delta, \varepsilon, \xi$	phases in the phase diagram CuSn
β_C	volume concentration expansion coefficient
β_T	volume temperature expansion coefficient
λ	wavelength
λ_1	primary dendrite arm spacing
μ^φ	chemical potential of phase φ
μ_i	chemical potential of phase *i*
μ_A, μ_B, μ_C	chemical potential of component *A, B* and *C*
μ_l	viscosity of the liquid
φ	phase index
ρ_q	density of phase *q* [kg·m^{-3}]
ρ_c	density of the columnar phase [kg·m^{-3}]

ρ_l	density of the liquid phase [kg·m^{-3}]
ρ_l^{ref}	liquid density in reference state
Θ	reflexion angle
$\overline{\overline{\tau}}_q$	stress-strain tensor of phase q
$\overline{\overline{\tau}}_l$	stress-strain tensor of the liquid phase
ϕ_q^j	general form of the arbitrary scalar of phase q
bcc	body centered cubic
CET	Columnar to Equiaxed Transition
CFD	Computational Fluid Dynamics
CRT	Cathode Ray Tube
Cu	Copper
Cu_3P	component of the CuP system
CuSn1	thermodynamic database of the system Cu-Sn-P
DC	direct chill casting
DSC	Differential Scanning Calorimetrie
DTA	Differential Thermal Analysis
EDS/EDX	Energy Dispersive X-Ray
fcc	face centered cubic
FEM	Finite Element Method
FVD	Finite Volume Difference
HTC	Heat Transfer Coefficient
LSRE	Local Solute Redistribution Equation
P	Phosphorus
PT	Phase Transitions
SEM	Scanning Electron Microscope
SEN	Submerged Entry Nozzle
Sn	Tin
UDS	User Defined Subroutines
UDF	User Defined Functions
vol.%	volume percent
WDS/WDX	Wave length Dispersive X-Ray
wt.%	weight percent
XRF	X-Ray Fluorescence Method
0D	zero dimensional
1D	one demensional
2D	two demensional
3D	three dimensional
$\otimes$	Dyadic Product
∇	Nabla-Operator (gradient)
Δ	Laplace-Operator